ULTRAFAST SPIN DYNAMICS IN CONTINUOUS AND CONFINED MAGNETIC THIN FILM

THESIS SUBMITTED FOR THE DEGREE OF

DOCTOR OF PHILOSOPHY (SCIENCE)

IN

PHYSICS (EXPERIMENTAL)

BY

AMRIT KUMAR MONDAL

DEPARTMENT OF PHYSICS

UNIVERSITY OF CALCUTTA

2023

Abstract

The quest for advanced spin-based computational technology started as charge-based technology could not keep up with increasing demands for energy efficiency, tunability, and miniaturization. The continuous and confined magnetic thin films have emerged as strong contenders for next-generation spintronics and magnonics. In this thesis, we aimed to explore spin and spin-wave dynamics in various ferromagnetic thin film heterostructures and nanostructures, employing wave vector domain (conventional Brillouin light scattering), time domain (time-resolved magneto-optical Kerr effect microscopy), and frequency domain (broadband ferromagnetic resonance) measurement techniques.

We first examined the role of defect density over the Rashba shift in SLG/CoFeB/SiO_2 heterostructures from asymmetric spin-wave dispersion measurement. This revealed a significant defect-induced interfacial Dzyaloshinskii-Moriya interaction (iDMI) and spin-mixing conductance, demonstrating the potential of SLG for engineering interface magnetism.

Next, we investigated femtosecond laser-induced ultrafast demagnetization and transient magnetization enhancement (TME) of a $[Co/Pt]_{22}$ multilayer sample at in-plane saturated state, AC-demagnetized state and four different remanent domain states. We found that the spin-transport-driven magnetization dynamics undergo a phase transition from pure demagnetization to pure TME with a coexistence state, and can be tuned across domain walls.

Furthermore, we demonstrated reconfigurability of magnetization dynamics as well as avoided crossing by tuning magnetic field orientation (φ) in triangular-shaped $Ni_{80}Fe_{20}$ nanodot arrays. Here, two lower frequency modes showed mutual coherence due to anisotropic dipolar interaction, leading to significant modification in the magnetization dynamics for a range of in-plane orientations. Subsequently, we studied the magnonic band structure of a two-dimensional array of rounded rectangular nanodots made of $Ni_{80}Fe_{20}$ for three different spin textures. Especially for an identical field value, we achieved both "S" and shifted-core vortex states and observed a significant change in the magnonic band.

Finally, we investigated the spin-wave dynamics in a square artificial spin ice (ASI) nanostructure made of $Ni_{80}Fe_{20}$ by tuning φ. We observed a transition from *w*-shaped mode-softening to monotonous dispersion of low-frequency mode as φ changed from 0° to 45°. Additionally, we introduced type-III

ASI, and topological defects (magnetic vortices) into a type-II ASI system in five different ways. This allowed for precise control over mode frequency shifting, microstate-specific anti-crossing gap opening, and the number of dominating spin-wave modes.

List of Publications

- Included in the thesis:

1. "Spin-texture driven reconfigurable magnonics in chains of connected $Ni_{80}Fe_{20}$ submicron dots" **A. K. Mondal**, C. Banerjee, A. Adhikari, A. K. Chaurasiya, S. Choudhury, J. Sinha, S. Barman and A. Barman, *Phys. Rev. B* **2020,** *101* (22), 224426.
2. "Defect-Density- and Rashba-Shift-Induced Interfacial Dzyaloshinskii–Moriya Interaction and Spin Pumping in Single-Layer Graphene/$Co_{20}Fe_{60}B_{20}$ Heterostructures: Implications for New-Generation Spintronics" **A. K. Mondal**, S. Majumder, S. Sahoo, S. N. Panda, S. Sinha and A. Barman, *ACS Appl. Nano Mater.* **2022,** *5* (4), 5056-5063.
3. "Bias field orientation driven reconfigurable magnonics and magnon−magnon coupling in triangular shaped $Ni_{80}Fe_{20}$ nanodot arrays" **A. K. Mondal,** S. Majumder, B. K. Mahato, S. Barman, Y. Otani, A. Barman, *Nanotechnology* **2023**, 34 (13), 135701.
4. "Bias Field Orientation Driven Magnetic Microstates and Spin Wave Dynamics in Nanoscale Artificial Spin Ice System" **A. K. Mondal** *et al.* (*Manuscript to be submitted*).
5. "Femtosecond Laser-Induced Transient Magnetization Enhancement and Ultrafast Demagnetization Mediated by Domain wall Origami" **A. K. Mondal** *et al.* (*Manuscript under preparation*).

- Not included in the thesis:

6. "Large nonlinear ferromagnetic resonance shift and strong magnon-magnon coupling in $Ni_{80}Fe_{20}$ nanocross array" K. Adhikari, S. Sahoo, A. K. Mondal, Y. Otani and A. Barman, *Phys. Rev. B* **2020,** *101* (5), 054406.
7. "Direct measurement of interfacial Dzyaloshinskii–Moriya interaction at the $MoS_2/Ni_{80}Fe_{20}$ interface" A. Kumar, A. K. Chaurasiya, N. Chowdhury, A. K. Mondal, R. Bansal, A. Barvat, S. P. Khanna, P. Pal, S. Chaudhary, A. Barman and P. K. Muduli, *Appl. Phys. Lett.* **2020,** *116* (23), 232405.
8. "Voltage controlled on-demand magnonic nanochannels" S. Choudhury, A. K. Chaurasiya, A. K. Mondal, B. Rana, K. Miura, H. Takahashi, Y. Otani and A. Barman, *Sci. Adv.* **2020,** *6* (40), eaba5457.

9. "Observation of Coherent Spin Waves in a Three-Dimensional Artificial Spin Ice Structure" S. Sahoo, A. May, A. van Den Berg, A. K. Mondal, S. Ladak and A. Barman, *Nano Letters* **2021,** *21* (11), 4629-4635.
10. "Comparison of Spin-Wave Modes in Connected and Disconnected Artificial Spin Ice Nanostructures Using Brillouin Light Scattering Spectroscopy" A. K. Chaurasiya, A. K. Mondal, J. C. Gartside, K. D. Stenning, A. Vanstone, S. Barman, W. R. Branford and A. Barman, *ACS Nano* **2021,** *15* (7), 11734-11742.
11. "Anisotropic spin-wave propagation in asymmetric width modulated $Ni_{80}Fe_{20}$ nanostripes" A. Adhikari, C. Banerjee, A. K. Mondal, A. K. Chaurasiya, S. Choudhury, J. Sinha, S. Barman and A. Barman, *Mater. Sci. Eng. B* **2021,** *272*, 115385.
12. "Large Dzyaloshinskii-Moriya interaction and atomic layer thickness dependence in a ferromagnet-WS_2 heterostructure" S. Husain, S. Pal, X. Chen, P. Kumar, A. Kumar, A. K. Mondal, N. Behera, N. K. Gupta, S. Hait, R. Gupta, R. Brucas, B. Sanyal, A. Barman, S. Chaudhary and P. Svedlindh, *Phys. Rev. B* **2022,** *105* (6), 064422.
13. "Mechanism of Spin-Orbit Torques in Platinum Oxide Systems" J. Nath, A. V. Trifu, M. S. Gabor, A. Hallal, S. Auffret, S. Labau, A. Mahjoub, E. Chan, A. K. Chaurasiya, A. K. Mondal, H. Yang, E. Schmoranzerova, M. A. Nsibi, I. Joumard, A. Barman, B. Pelissier, M. Chshiev, G. Gaudin and I. M. Miron, *Adv. Electron. Mater.* **2022,** *8* (7), 2101335.

- **Review Articles:**

14. "Applications of nanomagnets as dynamical systems: I" B. Rana, A. K. Mondal, S. Bandyopadhyay and A. Barman, *Nanotechnology* **2021,** *33* (6), 062007.
15. "Applications of nanomagnets as dynamical systems: II" B. Rana, A. K. Mondal, S. Bandyopadhyay and A. Barman, *Nanotechnology* **2021,** *33* (8), 082002.

Acknowledgements:

The long journey of my doctoral research has finally reached its destination after crossing a few hundred of memory throughout the period since 2017. Coming from a small rural area (Sihar, Bankura, West Bengal), getting opportunities at a reputed institute like SNBNCBS for higher studies was indeed a remarkable achievement for me. It will be my pleasure to express my gratitude to all the people who were a part of my PhD life including the faculty from the CM&MP (CMP&MS) department of S N Bose Centre, our collaborators and our funding agencies.

First and foremost, I am deeply grateful and humbled to my PhD supervisor, Prof. Anjan Barman, for his unwavering patience, guidance, and support throughout my PhD research journey. I am particularly grateful for the opportunity to join his research group and work in his world-class laboratory. I also learned a great deal from him when our solid-state BLS laser stopped working shortly after the first Covid-19 lockdown. He put in immense effort to get a new laser and we finally received it about a year later. However, a month later, we had to send it back to France for repair. During this time, I was filled with fear that I would not be able to complete my PhD. Prof. Barman allowed me to explore TR-MOKE on Co/Pt domain wall samples, and I learned many great attitudes from his positive outlook. Most importantly, he taught me to never be afraid of pursuing a difficult problem and to never ignore any experimental result, even if it is noisy. Finally, he instilled the importance of research ethics with professionalism, which will stay with me forever.

I am immensely grateful to Dr. Saswati Barman for her assistance in the LLG Micromagnetic Simulator. I am especially thankful to Dr. Jaivardhan Sinha for his invaluable advice and for introducing me to some of the latest research activities. I would like to express my sincere appreciation to Dr. Olav Hellwig (HZDR, Germany), Dr. Will Branford (United Kingdom), Dr. Yoshichika Otani (Japan) and their respective research teams for providing various samples in collaboration and engaging in fruitful discussions.

I am especially grateful to Dr. Chandrima Banerjee and Dr. Avinash Kumar Chaurasiya for their mentoring and support during my first days in the lab. They trained me to align the tandem Fabry-Pérot interferometer and other optical alignments in the BLS Lab. I am also thankful to Dr. Samiran

Choudhury and Dr. Sucheta Mondal for their assistance and helpful conversations during different stages of my research.

I am also thankful to my senior group members Dr. Santanu Pan, Dr. Anulekha De, Dr. Bivas Rana, Dr. Sumona Sinha, Dr. Sandeep Agarwal, Dr. Arpan Bhattacharyya and Dr. Ajit Kumar Sahoo for their support and help. My sincere thanks to Dr. Sourav Sahoo and Mr. Kartik Adhikari for their friendly advice. I am also grateful to my batchmates Surya, Arundhati, Koustuv and Sudip for our interesting discussions and quality time spent together at various conferences in India. I deeply value the lessons I have learned from sharing my experiences (good and bad) with them. Furthermore, I am thankful to my juniors Pratap, Sreya, Soma, Payal, Suchetana, Chandan and Brikram for creating a research-friendly environment in the lab. Lastly, our lab was filled with joy while Gaurav, Shubham, Anuj, Gyandeep, Pankaj, Daisy, Kajal, Abhilash, Rajdeep, Prapti and Gaurav (NISER) worked on their projects.

I would like to express my sincere gratitude to Sayantan, Sourav Kanthal, Didhiti, Shubhadip, Paru, Koushik, Anirban, Arka, and Vishal at S N Bose centre. I have enjoyed many indelible memories with them during this period. I express my gratitude to my SNBNCBS seniors: Sadhu da, Indranil da, Semanti di, Diraj da, Rahul da, Imadul da, Saikat da, Parth da and juniors: Biswajit Pabi, Shubhrasis, Rafiqul, Saniyul, Biswajit Panda, Premasish, Krishnendu, Anirban Paul, Jayanta, Dhrubajyoti, Narayan, Sayan, Soumen, Riju, Sanuja and Shubham. I would like to extend my appreciation to the cooking team of SNB Canteen and SNB Mess.

A short paragraph cannot be sufficient for describing the contribution of my friends and family members. My parents, Gouri Mondal and Kartick Chandra Mondal, have always supported my decisions and provided me with the motivation to do my best. They never forced me to do anything. They taught me not to hesitate to express my failure to the owner if I have been unable to do some problems and not to expect anything from my owner after any prosperous work. They have taught me to be honest, humble, and kind and to focus on my goals regardless of the situation. I am specifically thankful to my uncle Debangshu Hazra (Mama), Himangshu Hazra (Mama), Arun Mondal (Kaka), cousin Sourav Mondal, Polash Ghosh, Sristi Koley, Rimjim Hazra and other family members for their unconditional love, unwavering support throughout my academic career. I express my heartiest gratitude to my childhood friend Indrajit Mondal and Arijit Majumder for their friendship and companionship throughout my life.

My sincerest gratitude and respect go to all of the teachers throughout my academic career who have provided me with the guidance and knowledge to reach this point. I would like to express my deepest gratitude to Dr. Abhijit Chakraborty, Prof. Sourangshu Mukhopadhyay, Prof. Bishnu Charan Sarkar, Dr. Abhighan Duttta and Dr. Tanmoy Banerjee from the University of Burdwan for their invaluable contributions.

I am grateful to those who have provided me with guidance and support throughout my research work, both directly and indirectly.

Last but not least, I would like to thank S. N. Bose National Centre for Basic Sciences for providing me with the privilege of conducting research and a fellowship to pursue my doctoral studies. Without their invaluable assistance, this would not have been possible. I am also thankful to the academic and technical personnel of the Centre for their help and support in facilitating the completion of my research. I am also deeply thankful to S. N. Bose National Centre for Basic Sciences for their generous financial support which enabled me to attend various national and international conferences in India.

Amrit Kumar Mondal

Department of Condensed Matter and Materials Physics,
S. N. Bose National Centre for Basic Sciences,
Block – JD, Salt Lake, Sector-III, Kolkata – 700106, INDIA

List of Abbreviations:

1D	:	One-dimensional
2D	:	Two-dimensional
3D	:	Three-dimensional
AFM	:	Atomic force microscopy
AOM	:	Acousto-optic modulator
ASI	:	Artificial spin ice
BBO	:	β-barium borate
BG	:	Bandgap
BLS	:	Brillouin light scattering
BZ	:	Brillouin zone
BV	:	Backward-volume
CD	:	Connected nanodot
CVD	:	Chemical vapour deposition
CW	:	Continuous wave
DE	:	Damon-Eshbach
(i)DMI	:	(Interfacial) Dzyloshinskii Moriya interaction
DOF	:	Depth of field
DW	:	Domain wall
EBL	:	Electron-beam lithography
EDX	:	Energy dispersive X-ray
EM	:	Edge mode
EY	:	Elliott-Yafet
FEBID	:	Focused electron beam ion deposition
FFT	:	Fast Fourier transformation
FM	:	Ferromagnet
FMR	:	Ferromagnetic resonance
FPI	:	Fabry-Pérot interferometer
fs	:	Femtosecond

GHz	:	Gigahertz
GMR	:	Giant magneto resistance
GSG	:	Ground-signal-ground
GVD	:	Group velocity dispersion
HDD	:	Hard disk drive
HM	:	Heavy-metal
HNB	:	Horizontal nanobar
HNC	:	Horizontal nanochannel
HWP	:	Half wave plate
InP	:	In-plane
IR	:	Infrared
LTB	:	Lithium triborate
MD	:	Multidomain
MFM	:	Magnetic force microscopy
MO	:	Microscope objective
MOD	:	Modulation of damping
MOF	:	Modulation of frequency
MOKE	:	Magneto-optical Kerr effect
MRAM	:	Magnetic random-access memory
MTJ	:	Magnetic tunnel junction
mW	:	Milliwatt
NA	:	Numerical aperture
NC	:	Nanochannel
ns	:	Nanosecond
OBD	:	Optical bridge detector
OOP	:	Out-of-plane
(P)BS	:	(Polarized) beam splitter
PMA	:	Perpendicular magnetic anisotropy
ps	:	Picosecond
PVD	:	Physical vapour deposition

PWM	:	Plane wave method
QM	:	Quantized mode
RR	:	Retro-reflector
rf	:	Radio-frequency
SAW	:	Surface acoustic wave
SC	:	Simple cubic
SEM	:	Scanning electron microscopy
SHE	:	Spin Hall effect
(i)SHE	:	(Inverse) spin Hall effect
SHG	:	Second harmonic generator
SOC	:	Spin-orbit coupling
SOI	:	Spin-orbit interaction
SOT	:	Spin-orbit torque
ST-FMR	:	Spin-torque ferromagnetic resonance
STT	:	Spin-transfer torque
SW	:	Spin wave
TFPI	:	Tandem Fabry-Pérot interferometer
TMR	:	Tunnelling magnetoresistance
TPL	:	Two-photon lithography
TR-MOKE	:	Time-resolved magneto-optical Kerr effect
UM	:	Uniform mode
UV	:	Ultraviolet
VNA	:	Vector network analyzer
VNB	:	Vertical nanobar
VNC	:	Vertical nanochannel
XRD	:	X-ray diffraction
μs	:	Microsecond
μBLS	:	Micro-BLS

List of Figures:

Figure 2.1: Schematic of Dzyaloshinskii-Moriya interaction at NM/FM interface.	13
Figure 2.2: (a) Broadside and (b) head to tail configuration for ferromagnetically coupled magnetic moments. The latter is lower in energy.	15
Figure 2.3: Ultrafast demagnetization and relaxation mechanisms according to the 3T-model.	19
Figure 2.4: Temperature evolution of electron (E), spin (S) and lattice (L) heat baths after laser excitation according to 3T-model (a) and modified 3T-model (b).	20
Figure 2.5: (a)-(b) Precessional motion of magnetization (M) around effective magnetic field (H_{eff}) without and with damping. (c) The dispersion relation for different types of magnetostatic SW modes.	23
Figure 2.6: Cartoon of spin wave propagation.	25
Figure 2.7: Schematic of the experimental geometry. The directions of the rf field (h_{rf}) is shown in the schematic.	29
Figure 2.8: Schematic representation of (a) two- and (b) one-port microwave excitation and detection systems. (c) A graphical representation of the scattering (S) parameters.	32
Figure 2.9: (a) Schematics of polar, longitudinal, and transverse MOKE geometries are shown. (b) The geometry of the Kerr rotation (θ_k) and Kerr ellipticity (ε_k).	33
Figure 3.1: Schematic of RF-DC magnetron sputtering unit.	37
Figure 3.2: Schematic of electron-beam evaporation.	38
Figure 3.3: Schematic of scanning electron microscope (SEM) and energy dispersive X-ray (EDX).	40
Figure 3.4: Schematic of X-ray diffractometer and diffraction of X-ray from the atomic planes.	41
Figure 3.5: Schematic of vibrating-sample magnetometer.	42
Figure 3.6: Schematic of magnetic force microscopy (AFM).	44
Figure 3.7: Schematic of the static-MOKE system presents in our laboratory at S.N. Bose national centre for Basic Sciences	45
Figure 3.8: Schematic of the (a) creation (stokes) and (b) annihilation (anti Stokes) scattering processes. (c) Schematic of the scattering of incident laser beam by surface and bulk magnons.	48

Figure 3.9: (a) Schematic illustration of the interaction between p-polarized incident beam and precessing magnetization. (b) Transmission Spectra of FP1 and FP2 and in tandem operation. 50

Figure 3.10: Schematic diagram of the BLS system present in our laboratory at S.N. Bose national centre for Basic Sciences. 51

Figure 3.11: Schematic diagram of the non-collinear TR-MOKE system present in our laboratory at the S. N. Bose National Centre for Basic Sciences, Kolkata. 59

Figure 3.12: Schematic diagram of the broadband VNA-FMR system present in our laboratory at S.N. Bose national centre for Basic Sciences. 61

Figure 3.13: A rectangular MC formed by circular ferromagnetic elements A embedded in matrix B. 65

Figure 4.1: (a) Cartoon of SLG/CoFeB bilayer showing the magnetic vector chirality due to DMI from the SLG interface. (b)-(c) AFM image of the SLG/CoFeB (1.5 nm)/SiO_2 and SLG/CoFeB (6 nm)/SiO_2 samples. (d) Variation of average roughness (R_a) extracted from the AFM images as a function of CoFeB thickness. (e) Magnetic hysteresis loops for SLG/CoFeB (1.5 nm)/SiO_2 and CoFeB (1.5 nm)/SiO_2 samples. (f) Variation of coercive field (H_C) as a function of CoFeB thickness. (g) Variation of saturation magnetization (M_S) as a function of CoFeB thickness. 73

Figure 4.2: (a) Raman spectra of CVD-grown SLG on Si/SiO_2 substrate (top panel), SLG/CoFeB (1.5 nm)/SiO_2 (middle panel) and SLG/CoFeB (4 nm)/SiO_2 (bottom panel). (b) Intensity profile of 2D and G peak of SLG. (c) Variation of defect density (n_D) and I_D/I_G as a function of inverse of CoFeB thickness. The error bars in n_D is calculated from the n_D expression. Symbols represent experimental data points and solid lines are the corresponding theoretical fits for (b)-(c). 74

Figure 4.3: (a) Schematic of the sample stack along with the BLS measurement geometry where the incident and scattered light beams lie in the z-x plane and are at an angle θ to the z-axis. Representative BLS spectra at (b) k = 8.07 rad/mm and (c) k = 20.45 rad/mm under oppositely oriented external magnetic fields B = 0.1 T. (d) Spin-wave dispersion for SLG/CoFeB (1.5 nm) sample at B = 0.1 T. Symbols represent the experimental data points, the solid curve shows the fit to the data points using Eq. (1) and the dotted curve shows the theoretical spin-wave dispersion in absence of DMI. (e) Representation of Δf vs. k for all 76

four SLG/CoFeB/SiO_2 samples. Symbols represent the experimental data points and solid lines are the fit using Eq. (2). (f) Plot of Δf as a function of B for SLG/CoFeB (1.5 nm)/SiO_2.

Figure 4.4: (a) Extracted DMI constant (D) vs inverse of CoFeB thickness for all four SLG/CoFeB/SiO_2 samples. (b) Variation of D as a function of defect density (n_D). (c) Plot of Rashba shift (k_R) vs inverse of CoFeB thickness for all SLG/CoFeB/SiO_2 samples. (d) Variation of k_R as a function of K_S for all four SLG/CoFeB/SiO_2. Symbols represent experimental data points and solid lines are the corresponding theoretical fits. 78

Figure 4.5: (a) Linewidth (FWHM: Δf_{res}) of BLS spectra in the SLG/CoFeB (1.5 nm)/SiO_2 sample as a function of wave-vector. (b) Variation of Δf_{res} as a function of B for SLG/CoFeB (1.5 nm)/SiO_2 and SLG/CoFeB(6 nm)/SiO_2 samples. (c) Extracted effective damping (a) as a function of inverse CoFeB thickness for SLG/CoFeB/SiO_2 and CoFeB/SiO_2 samples. (d) Plot of a vs. defect density (n_D) for all SLG/CoFeB/SiO_2 samples. Symbols represent experimental data points and solid lines are the corresponding theoretical fits. 80

Figure 5.1: (a)-(e) The magnetic force micrographs (MFMs) of five different domain configurations [S2], [S1], [S5], [S4], and [S3]. (f)-(j) Modulus of 2D Fourier transforms of images in (a)–(e), respectively. (k) Magnetic hysteresis loops when magnetic field is applied in-plane and out plane direction of sample plane. Coercive field as a function of azimuthal angle (l) and polar angle (m) of applied magnetic field. 86

Figure 5.2: (a) Schematic of the film stack along with TR-MOKE geometry. (b) Representative TR-MOKE trace where different temporal regions are marked. (c)-(d) The variation of ultrafast demagnetization time (τ_m) and magnetization quenching with laser fluence respectively. 89

Figure 5.3: (a) Representative TR-MOKE for [S2], [S5] and [S4] domain configurations for a fixed pump fluence 12.99 mJ cm^{-2}. (b)-(d) Representative TR-MOKE trace for [S2], [S5] and [S4] with laser fluences respectively. 90

Figure 5.4: (a)-(b) A schematic showing the processes involved in ultrafast demagnetization, transient magnetization enhancement (TME) and final magnetization recovery after laser bombardment onto the stripe domain configuration. 91

Figure 5.5: (a)-(b) The variation of different time constants and amplitudes with pump fluence for [S2]. (c)-(d) The variation of different time constants and amplitudes with pump fluence for [S5]. (e)-(f) The variation of different time constants and amplitude with pump fluence for [S4]. 93

Figure 5.6: (a)-(b) The variation of maximum magnetization quenching and demagnetization time (τ_m) with k_y/k_x. (c)-(d) The variation of transient magnetization enhancement amplitude and time (τ_{tme}) with k_y/k_x. 94

Figure 6.1: (a) Schematic of the experimental geometry. The directions of the rf field (h_{rf}) are shown in the schematic. (b)–(c) Scanning electron micrographs of $Ni_{80}Fe_{20}$ triangular nanodot arrays S1 and S2. The bias field orientation (φ), base length (*l*), and separation (*s*) are shown in (c). (d) Surface plot of bias-field-dependent SW mode frequencies for Py thin film of 20-nm thickness at excitation power of $P = -15$ dBm. The Kittel fit is shown by white line. 100

Figure 6.2: Simulated SW frequencies as a function of bias magnetic field at an orientation (φ) of 0º and P = -15 dBm for single regular triangle (a) and deformed triangle (b). Inset shows the representation of single triangle. Simulated SW spectra for regular triangular dot array (c) and deformed triangular dot array (d). Simulated SW frequency as a function of bias field at φ of 0º and P = -15 dBm for regular triangle dot array (e) and deformed triangle dot array (f). Inset shows representative magnified view of triangular dot array. 101

Figure 6.3: (a) Re(S_{11}) parameter as a function of bias magnetic field at φ = 0º and P = -15 dBm for sample S1. (b)-(e) Surface plots of bias-field-dependent SW mode frequencies for φ = (b) 0°, (c) 15°, (d) 165° and (e) 195°, respectively, at P = -15 dBm. Simulated SW frequencies are shown by symbols. The color map of experimental surface plot is shown at the bottom of the figure. 102

Figure 6.4: (a) Close in representation of Re(S_{11}) parameter at different values of φ = 10º, 15º and 20º at *P* = -15 dBm for sample S2. (b)-(e) Surface plots of bias-field-dependent SW mode frequencies for φ = (b) 0°, (c) 15°, (d) 165° and (e) 195°, respectively, at *P* = -15 dBm. Simulated SW frequencies are shown by symbols. The color map of experimental surface plot is shown at the bottom of the figure. 104

Figure 6.5: Simulated spatial distribution of power and phase of the SW modes during the avoided crossing (*H* = 900 Oe for S1 and 850 Oe for S2) at φ = 0°, 15°, and 165°. 105

Figure 6.6: Simulated spatial distribution of power and phase of the SW modes during the avoided crossing (*H* = 900 Oe for S1 and 850 Oe for S2) at φ = 0°, 15°, and 165°. 107

Figure 6.7: (a)-(b) Surface plots of bias-field-dependent SW mode frequencies for *P* = +5 dBm and 0 dBm, respectively, for φ = 15°. Simulated SW frequencies are shown by symbols. The color map of experimental surface plot is shown at the right side of the figure. (c) Variation of avoided crossing gap (δ_{FR}) as a function of *P* for sample S2. Inset shows representative magnetization at *P* = -15 dBm (left), and *P* = +5 dBm (right). (d) Variation of simulated stray magnetic field distribution with *P* for φ = 15°. 108

Figure 6.8: Simulated spatial distribution of power corresponding to two lowest frequency SW branches for sample S2 for φ = (a) 0°, (b) 15° (195°) and (c) 165°. 109

Figure 7.1: Scanning electron microscope (SEM) and (b) atomic force microscope (AFM) image of the sample. (c) Height of nanodot obtained from the AFM image along the dotted line in (b). (d) Roughness of various dots in the sample along with a high-resolution image taken from the dotted box in (b) is shown in the inset. (e) Experimental and (f) simulated magnetic force microscope (MFM) image of the sample in the AC demagnetized state. The arc arrows represent chirality of vortex found from the simulation. 114

Figure 7.2: (a)-(c) The Stokes side of BLS spectra taken at three different magnetic history, i.e., leaf state (H_1 = 850 Oe), 'S' state (H_2 = 330 Oe, when decreased from saturation field) and shifted-core vortex state (H_3 = 330 Oe, when increased from AC demagnetized state) at $k \approx 0$. The simulated magnetic states are shown in the insets. (d)-(f) The Stokes side of BLS spectra taken for leaf, 'S' and shifted-core vortex state, respectively at the first BZ boundary ($k \approx \pi/a$). (g) The Stokes side of BLS spectra taken for the leaf state at the second BZ boundary ($k \approx 2\pi/a$). The solid lines represent the Lorentzian fits to identify the peaks. (h) Schematic of BLS measurement in the Damon-Eshbach (DE) geometry. 115

Figure 7.3: (a)-(c) Magnonic band structure corresponding to three different magnetic states, i.e., leaf, 'S' and shifted core vortex state, respectively. Here, filled symbols represent BLS peak frequencies for different k values, the dashed vertical line is the boundary of the first BZ, while the band gap is shown by the shaded areas. The three-dimensional surface plots of the plane wave method calculated spin-wave dispersion is superposed on the experimental data in (a) and (b). The corresponding color map for (a)-(b) is shown at the right side of the figure. The simulated magnetization configuration in the spin-wave propagation channels for the three magnetic states are shown in the insets. 116

Figure 7.4: Spatial profiles of selected spin-wave modes (F1, F1', F2, F3, and F4) for two different magnetic states, namely the leaf and 'S' state at $k \approx 0$ and $k \approx \pi/a$. 117

Figure 7.5: (a) Simulated power maps showing spin-wave modes (F1, F1', F2, F3, and F4) profile for the shifted-core vortex state at $k = 0$. The corresponding color map is shown at the right side of the figure. (b) Simulated variation of normalized magnetization with applied magnetic field. Arrows represent the path of variation from one spin texture to another spin texture. Inset represents simulated spin-wave frequency vs. bias magnetic field along two different paths of magnetic field history. 119

Figure 8.1: (a)-(b) Scanning electron micrographs and energy dispersive X-Ray of $Ni_{80}Fe_{20}$ ASI nanobar array. (c)-(f) MFM images at remanence states for φ = 0°, 15°, 30° and 45°, respectively. (g)-(h) Experimental and simulated hysteresis loops. 124

Figure 8.2: Representative BLS spectra measured at wave vector $k \approx 0$ for different magnetic field strengths at φ = 0°, 15°, 30° and 45°, respectively. 125

Figure 8.3: Surface plots of bias-field-dependent SW mode frequencies for φ = 0° (a), 15° (b), 30° (c), 45° (d) and 90° (e). Simulated SW frequencies are shown by symbols. The color map of experimental result is shown at the side of the surface plots. (f) Schematic of the BLS measurement geometry. 126

Figure 8.4: (a)-(b) Simulated spatial distribution of power and phase of the SW modes for different magnetic fields at φ = 0° (a) and 45° (b), respectively. 127

Figure 8.5: (a)-(c) Linescans of the simulated demagnetization field component H_{dy} at φ = 0°, 15° and 45°, respectively. The linescans direction is shown in the inset of (b). (d)-(f) Linescans of the simulated demagnetization field component H_{dx} at φ = 0°, 15° and 45°, respectively. The linescans direction is shown in the inset of (e). The green rectangular dashed box indicates the inner region of the nanobars. 128

Figure 8.6: (a)-(e) MFM images for different ACD state such as [S1]-[S5] state, respectively. (f)-(j) Magnified views of those MFM images. (d)-(f) Representative BLS spectra measured at wave vector $k \approx 0$ for [S1]-[S5] states, respectively. 129

Figure 8.7: (a)-(e) Bias-field-dependent SW mode frequencies for [S1]-[S5] states. (f)-(h) Simulated SW field dispersion for pure vortex state, T3 and T2 ASI microstate. (i)-(k) Representative vortex, T3 and T2 microstate. 130

Figure 8.8: (a)-(b) Simulated spatial distribution of power and phase of the SW modes for vortex (a) and T3 ASI state (b) at H = -100 Oe and 0 Oe respectively. 131

Table of Contents:

Abstract i

List of Publications iii

Acknowledgements: v

List of Abbreviations: viii

List of Figures: xi

Table of Contents: xvii

1. Introduction 1

1.1 Interfacial Properties of Nonmagnet/Ferromagnet Heterostructure: 3

1.2 Femtosecond Laser-Induced Ultrafast Demagnetization and Transient Magnetization Enhancement: 4

1.3 Ferromagnetic Nanostructures: Dot and Connected Nanodot Lattice: 5

1.4 Nanoscale Ferromagnetic Spin Textures: Magnetic Domain, Vortex, Artificial Spin Ice: 6

1.4.1 Magnetic Domain: 7

1.4.2 Magnetic Vortex: 7

1.4.3 Artificial Spin Ice: 8

1.5 Objective of the Thesis: 9

2. Theoretical Background 10

2.1 Different Magnetic Energies: 10

2.1.1 Zeeman Energy (E_z): 11

2.1.2 Exchange Energy (E_{ex}): 11

2.1.3 Magnetic Dipolar Interaction (E_d): 14

2.1.4 Magnetic Anisotropy (E_{anis}) 14

2.2 Timescale of Magnetization Dynamics: 17

2.3 Ultrafast Demagnetization: 18

2.3.1 Three-temperature Model and Modification: 18

2.3.2 Mechanisms Involved Behind Ultrafast Demagnetization: 21

2.4 Precessional Magnetization Dynamics: 22

2.4.1 Magnetic Damping: 23

2.4.2 Spin Wave: 25

2.5 Ferromagnetic Resonance (FMR): 27

2.5.1 Microwave Excitation and Detection: 28

2.5.2 Vector Network Analyzer Incorporated Broadband FMR: 28
2.6 Magneto-optical Kerr Effect (MOKE): 32
2.6.1 Origin of MOKE: 33
3. Fabrication and Characterization Techniques 35
3.1 Fabrication Techniques: 36
3.1.1 Sputtering: 36
3.1.2 E-beam Evaporation (EBE): 37
3.2.3 E-beam Lithography (EBL): 38
3.2 Static Characterization Techniques: 39
3.3.1. Scanning Electron Microscopy (SEM): 39
3.3.2 Energy Dispersive X-ray: 39
3.3.3 X-ray Diffraction: 40
3.3.4 Vibrating Sample Magnetometer (VSM): 41
3.3.5 Atomic Force Microscopy (AFM) and Magnetic Force Microscopy (MFM): 43
3.3.6 Static Magneto-optical Kerr Effect (Static-MOKE) Magnetometer: 45
3.3 Spin Dynamics and Spin-wave Dynamics Measurements: 46
3.3.1 Brillouin Light Scattering (BLS) Technique: 46
3.3.2 Time-resolved Magneto-optical Kerr Effect (TR-MOKE) Magnetometry: 56
3.3.3 Broadband Ferromagnetic Resonance (FMR) Spectrometer: 60
3.4 Numerical Techniques: 63
4. Defect Density and Rashba Shift Induced Interfacial Dzyaloshinskii-Moriya Interaction and Spin Pumping in Single Layer Graphene/$Co_{20}Fe_{60}B_{20}$ Heterostructures: Implications for New Generation Spintronics 70
I. Introduction: 70
II. Experimental and Theoretical Methods: 72
III. Results and Discussions: 73
IV. Conclusions: 82
5. Femtosecond Laser-induced Transient Magnetization Enhancement and Ultrafast Demagnetization Mediated by Domain wall Origami 83
I. Introduction: 83
II. Experimental and Theoretical Methods: 85
III. Results and Discussions: 87
IV. Conclusions: 94

6. Bias Field Orientation Driven Reconfigurable Magnonics and Magnon-Magnon Coupling in Triangular Shaped $Ni_{80}Fe_{20}$ Nanodot Arrays 96
I. Introduction: 96
II. Experimental and Numerical Methods: 98
III. Results and Discussions: 99
IV. Conclusions: 110
7. Spin Texture Driven Reconfigurable Magnonics 111
I. Introduction: 111
II. Experimental and Theoretical Methods: 112
III. Results and Discussions: 113
IV. Conclusions: 120
8. Bias Field Orientation Driven Magnetic Microstates and Spin Wave Dynamics in Nanoscale Artificial Spin Ice System 121
I. Introduction: 121
II. Experimental and Theoretical Methods: 123
III. Results and Discussions: 124
IV. Conclusions: 132
9. Summary and Future Perspective 134
9.1 Summary: 134
9.2 Future Perspective: 137
Appendix A: Chapter 5 139
Appendix B: Chapter 6 142
Appendix C: Chapter 7 144
References: 147

Chapter 1

1. Introduction

The charge-based electronic industry is one of the most well-used industries in modern world and consumer electronics are products for daily use, most often in communications, entertainment, and office purpose [1]. The invention of the transistor was a revolution that made this technology inevitable in everyday life [2,3]. The concept of a field-effect transistor was first proposed in 1926. However, the discovery of the first working form of a transistor was made in 1947. The most widely accepted type of transistor is the metal–oxide–semiconductor field-effect transistor (MOSFET) since 1959. Here the main carrier is an electronic charge in the form of an electron or hole inside the semiconductor components. The number of transistors fabricated on the silicon-based wafer in the form of an integrated chip (IC) with metallic connectors almost doubled on a fixed chip area every 18 months following Moore's law successfully for decades [4]. Moore's law is coming to an end simply because the technocrats are unable to develop chips with smaller (and more numerous) transistors [5]. The integration of the thermal runway process of all transistors presents inside any IC circuit can generate enormous heat which is an additional and inherent drawback of charge-based technology [6].

The field of spintronics promises to solve the above-mentioned bottlenecks arising from change-based electronics [7-10]. The central idea behind this field is to utilize the spin degree of freedom of electron in a material for nanoscale signal processing and storage of information. Since spins can propagate without any Joule heating loss, this is the main advantage of spin over charge. The first experimental observation of electron spin was made by Stern and Gerlach in 1922 [11] and theorized by Uhlenbeck and Goudsmit in 1926 [12]. Later, Dirac explains the origin of spin as a consequence of the union of quantum mechanics and relativity with the help of the orbital motion of electrons in magnetism [13]. This rotational motion can either be clockwise (assumed to be the spin-down configuration) or anticlockwise (known to be the spin-up configuration) which can store one "bit" of information if used in a storage device. In 1958, a pioneering work on chiral spin texture by Dzyaloshinskii [14] and Moriya [15] opened a new field of research and it arises from the symmetry breaking at the ferromagnet (FM) and nonmagnet (NM) interface [16-21]. Later, the evolution of nanotechnology and nanoscience opened the path for the exploration of the universe of nanomagnets [22]. An important breakthrough in magnetic thin film research was the discovery of giant magnetoresistance (GMR) in 1988 by Fert [23] and Grunberg [24], for which they were awarded the Nobel prize in 2007. This discovery revolutionized the hard disk drive (HDD) where GMR is now used as a read head. Current HDD has a

data density of more than 1024 GB/in^2 [25]. The GMR deals with interactions between transported electron's spin and orientations of the magnetization for ferromagnetic elements and its dynamics in spintronics field have been triggered. This leads to the designing of another aspect of this field, the magnetic tunnel junction (MTJ) where two magnetic layers (reference and free layer) are separated by an insulating layer (metallic layer used in GMR) [26]. The MTJs has created opportunities for new types of non-volatile magnetic storage such as magnetic random-access memory (MRAM) and magnetic hard disk drives (HDDs), which could be used as primary memory in computers. Later, the introduction of spin transfer torque (STT) was made in 1996 where the flow of spin-angular momentum through a sample is not constant, but has sources or sinks [27]. The STT is a direct and effective method to switch magnetization and control the bit states in MRAM, like STT-MRAM [28,29]. The spin-orbit torque (SOT) is emerging as the transfer of angular momentum from the lattice to the magnetic layer(s) as an alternative for STT [30]. The hypothesis of SOT was first recognized for the modulation of magnetization dynamics in $Ni_{81}Fe_{19}$/Pt bilayers [31], and the modulation of magnetization switching in diluted magnetic semiconductor (Ga,Mn)As [32]. The low-power and high-speed switching using SOT are promising for SOT-MRAM [33]. The generation of SOT-induced spin current through (inverse) spin Hall effect ((I)SHE) [34,35], spin pumping effect [36], and spin Seebeck effect (SSE) [37] have added interesting perspectives where heavy metal, topological insulators and noncollinear antiferromagnet are promising elements for advanced development to the field of spintronics [38].

While spintronics deals with spin transport, magnonics deals with the wave motion of spins in a magnetic system. Magnonics has been considered a key candidate to meet some of these inherent drawback of charge-based technology using spin waves (SWs) (the quanta of SWs are called magnon with spin 1─ following Bose-Einstein statistics) [39,40], a coherent propagation of magnetic excitation originating from the collective precession of magnetic moments in an ordered magnetic system. The concept of spin wave was first proposed by F. Bloch in 1930 [41]. SWs, magnetic analogue of photon or phonon waves, show similar type of wave characteristics, namely: propagation [42,43], reflection and refraction [44], injection [42], interference [45], diffraction [46], tunnelling [47] and Doppler effect [48]. These wave properties of spin-waves have assisted the emergence of magnonic crystals (MCs), which is an artificially patterned periodic FM nanostructures, composed of two or more FM materials arranged in a periodic manner. These MCs can also be designed by periodic modulation of external parameters such as strain [49], electric current [50], voltage [51], and magnetic field [47]. Besides the fundamental interests, SWs exhibit a diversity of dispersion characteristics as opposed to other waves.

For example, the dispersion of dipolar-mediated SWs in continuous FM film depends on their propagation direction and applied magnetic field direction, giving rise to different SWs modes such as Damon-Eshbach mode, backward-volume mode and forward-volume mode. Overall, control and propagation of SW mode devoid of Joule heating, can potentially fulfil the ever-increasing demand for energy-efficient information carriers for information transmission and storage [40,52].

In the succeeding paragraphs, a brief overview of few aspects of spintronics and magnonics are presented which have motivated this doctoral thesis work.

1.1 Interfacial Properties of Nonmagnet/Ferromagnet Heterostructure:

The understanding and manipulation of interfacial effect at the FM/NM interface is an emerging topic due to various reasons such as the generation of pure spin current, spin-orbit torque and SW non-reciprocity [53]. To this end, Co, Fe, YIG, Ni, CoFe, $Co_{20}Fe_{60}B_{20}$ (CoFeB hereafter), Permalloy ($Ni_{80}Fe_{20}$, and $Ni_{81}Fe_{19,}$ Py hereafter), ferromagnetic Heusler alloys etc. are some well-used FMs, while Pt, Pd, Ta, W, Hf, two-dimensional materials such as graphene, WS_2, WSe_2, MoS_2, $MoSe_2$ and topological insulators are some important NMs that have attracted intense interest in engineering the interface magnetism [18,20,54-60]. These NM/FM heterostructures with large interfacial SOC can exhibit a range of interfacial phenomena such as spin pumping [36], spin Hall effect [61], inverse spin Hall effect [34,35], spin caloric effects, Rashba-Edelstein effect [18], inverse Rashba-Edelstein effect [62] etc. which are also crucial for generation of pure spin current for developing next-generation spin-orbitronic devices.

The interfacial Dzyaloshinskii-Moriya interaction (iDMI) is a phenomenon that introduces SW non-reciprocity in NM/FM system in presence of SOC and inversion symmetry breaking at the interface [17,54,55,63,64]. Several reports have been made to estimate the value of the iDMI constant for different HM/FM heterostructures which is a crucial parameter for stabilization of chiral spin textures, including magnetic skyrmions. Some popular HMs are Pt, Pd, Ta, W and Hf for hosting skyrmions [65-68]. Recently two-dimensional materials such as graphene, WS_2, WSe_2, MoS_2, $MoSe_2$ and topological insulators have attracted intense interest in engineering interface magnetism [18,20,54-57]. A monolayer graphene reveals long spin diffusion length (~ μm) [59,69,70] and prolonged spin relaxation time (~ μs) [71] at room temperature which helps spin angular momentum for long-distance propagation through graphene. Although graphene has low intrinsic SOC, its extrinsic SOC is highly sensitive to defects and impurities which can be controlled through processes like proximity to

ferromagnet (FM) [72], Rashba effect [18,73], absorption [74], intercalation [75], fluorination [76], hybridization [73] etc. The SOC of graphene gives rise to non-zero effective mass of electrons and induces a bandgap in its electronic dispersion. In addition, graphene/FM heterostructure shows SHE [77], anomalous Hall effect [72], iSHE [78], large PMA [79], enhancement of the Rashba SOC [18], spin-dependent Klein tunnelling [80], defect-induced iDMI [54], spin pumping [19] etc. which make these heterostructures important platforms for novel spintronic applications [59].

1.2 Femtosecond Laser-Induced Ultrafast Demagnetization and Transient Magnetization Enhancement:

The magnetization of an FM can be manipulated via different mechanisms such as optical inter-site spin transfer (OISTR) [81,82], ultrafast demagnetization [83] and transient magnetization enhancement (TME) [84-86]. The mechanisms of femtosecond laser-induced ultrafast demagnetization are still being debated over two decades since its discovery in 1996 by the pioneering experiment of Beaurepaire *et al.* in ferromagnetic nickel thin film [87]. A wide range of theoretical and experimental investigations of ultrafast demagnetization have been accomplished and several models have been developed by the researchers for developing an in-depth understanding of the contribution of the spin transport (ST) [84,86,88-90] and spin-flip scattering (SFS) [91-96] to ultrafast demagnetization. SFS events are originally considered to be the primary channel for angular momentum transfer at ultrafast timescales via Coulomb-scattering [91], Stoner excitations [95], phonon-mediated Elliott-Yafet processes [93,96], or relativistic quantum electrodynamic processes [94]. Koopmans *et al*. first explained ultrafast demagnetization via phonon-mediated Elliott-Yafet type of SFS (EYSFS) by spin-orbit coupling due to the transfer of angular momentum between the electrons and the lattice [93]. A large degree of tunability of the spin manipulation mechanism time has been achieved experimentally, varying from the femtosecond time scale to 100s of picoseconds by varying material parameters such as the degree of spin polarization and chemical ordering or experimental parameters such as the laser pulse width and excitation fluence. In 2008, Malinowski *et al.* first demonstrated a channel for ST to control ultrafast demagnetization in antiferromagnetically coupled $[Co/Pt]_n$ multilayers through an insulating NiO spacer and metallic Ru spacer [88]. Later, a new model based on super-diffusive spin transport (SST) [89] was proposed for layered structures such as ferromagnet (FM)/metal, FM/semiconductor (SC) [84] and FM/metal/FM [86] heterostructure. The ultrafast demagnetization through SST across the domain wall was found to be accelerated in nanoscale domain network as opposed to uniform

domain because of the direct transfer of spin angular momentum between neighboring domains [86,90,97]. Rudolf *et al.* reported that depending upon the longitudinal parallel and antiparallel spin configuration, transient enhancement of magnetization or decrement of magnetization occurs due to SST of excited spin majority electrons from the Ni layer to the buried Fe layer through the Ru spacer layer [86]. Moreover, TME has been reported in the Fe layer of a Ni/Ru/Fe layered structure due to SST when Ni layer was excited by femtosecond laser pulses [86]. Very recently, Jiang *et al.* have also demonstrated TME mechanism along with the demagnetization mechanism via SST in SC/FM systems from low conducting SC layer to FM layer [84]. Furthermore, the dynamic TME exhibits a maximum below the Curie temperature T_c due to the photoexcited thermalized hole-mediated ferromagnetic ordering and dominates over the demagnetization component close to T_c in GaMnAs [85]. A detailed understanding of these ultrafast mechanisms will play a key role in the technological development of spintronics devices in ultrafast timescales [98].

1.3 Ferromagnetic Nanostructures: Dot and Connected Nanodot Lattice:

Nanomagnetism is one of the subfields of magnetism dealing with the magnetic phenomena specific to size reduction, i.e., structures having dimensions in the submicrometer to nanometer range [99]. Patterning of those nanomagnets can lead to connected and disconnected structures such as nanodot, antidot, nanoring, bi-component, and binary nanostructures which have huge potential to act as building blocks of the magnonic devices. These structures are also known as magnonic crystals (MCs) in analogy with photonic or phononic crystals (PCs) which are the building blocks of optoelectronics or acousto-optics. MCs have several advantages over PCs in terms of lower heat dissipation, shorter wavelength, anisotropic properties, negative group velocity to name a few. Magnonics deals with the excitation, propagation, control, and detection of SWs through those MCs. In 2001, Nikitov *et al.* first named periodic multilayered structures with layers having the same thickness but different magnetization as the 1-D magnon crystal (1-D MC) [100]. A flurry of reports have been published on investigation of novel SW dynamics in a variety of nanostructures, such as 1-D MC, pseudo-1-D MC, 2-D MC, and 3-D MC [39,40,52]. These are important from the technological point of view to design magnonic waveguides [101], filters [102], splitters [103], grating couplers [104], SW emitters [105], SW amplifiers [106], SW multiplexers [107], transistor [108,109], logic gates [110], phase shifter [111] and SW interferometers [112]. In the case of reconfigurable or dynamic MC, which forms a fascinating class of MC, it is possible to realize universal data processing units with switchable SW properties.

The external magnetic field strength [113] and orientation [114], voltage [51], stain [49], electric field [115], spin-texture [116], element shape [117], lattice symmetry [118], base material, and lattice constant [118] are few important parameters which can introduce reconfigurabilities in SWs dynamics. Apart from those MCs, hybrid systems [119-124] form another important class of MC which are important for the fundamental development quantum information processing using a combination of different carriers such as superconducting qubits, phonons [125], plasmons [126,127], photons [128] and magnons [120]. During the last decades, a periodic arrangement of ferromagnetic nanodots and physically connected nanodots (known as connected dot, CD) have attracted intense interest in field of nanomagnetism due to their inherently large shape anisotropy aiding efficient transfer of energy [113,114,129]. The primary difference of the CD system from antidots (ADs) is that the latter generally does not have regular shaped connector channels. However, CD systems can sustain properties of dots as well as ADs the latter shows a relatively larger SW propagation velocity as well as a longer propagation wavelength [120]. Further studies promise different phenomena such as bang gap opening at the boundary of Brillouin zone, mode conversion, positive and negative group velocity of spin wave, mode hopping, mode crossover, mode softening, etc. which are important for transmission, storage, and processing of data. The year 2021 is remarkable for the field of magnonics because its progresses and perspectives in fundamental science as well as applications have been well documented in two road maps, namely “The 2021 Magnonics Roadmap” [40], and “The 2021 roadmap for noncollinear magnonics” [52].

1.4 Nanoscale Ferromagnetic Spin Textures: Magnetic Domain, Vortex, Artificial Spin Ice:

Magnetic spin textures are nonuniform, stable and flexible spin configurations, which possess a remarkable degree of tunability and scalability. Interactions between spin textures such as vortices, skyrmions, magnetic bubbles, merons, domain walls, monopole defects in artificial spin ice (ASI), and different types of quasi-uniform states (e.g., S state, leaf state, flower state, C state, onion state, etc.) with propagating SWs are important to reconfigure SW dynamics. The continuously increasing quantity of information poses a major challenge for data processing and storage. The spin texture-driven magnonics has the potential to handle this problem efficiently by creating on-demand magnonic crystals [116]. Furthermore, these spin textures allow for low-power operation due to their low SW impedance. This makes them attractive for use in low-power applications such as mobile devices [116].

1.4.1 Magnetic Domain:

In order to minimize the magnetostatic self energy $\overrightarrow{E_d} = \overrightarrow{H_d}.\vec{M}$ a magnetic material breaks into the "magnetic domains" [130]. When an external field is applied to a multi-domain ferromagnet, saturation magnetization is achieved through the motion of domain walls, which is energetically inexpensive compared to magnetization rotation, which carries a large anisotropy energy penalty. Domain walls are boundaries between two domains in which all the magnetic dipoles are aligned in the direction of the easy axis. The magnetic domain wall is mainly determined by the ratio of exchange constant and magnetic anisotropy of the system. Electric field-induced curving, bending, branching, and elongation of magnetic domains have been reported in various studies [131-133]. The magnetic domain wall and its motion can be play important role in SW propagation and the dynamics of SWs [134]. Recently, it has also been observed that periodic variations of magnetic domains can behave as a dynamic magnonic crystal [135,136]. Here, the spatial periodicity of this magnetization serves as a periodic magnetic potential for SW propagation, similar to the laterally confined geometry of MCs. Magnetic domain wall and its propagation can be controlled by the magnetic field, spin-polarized current pulse, spin-orbit torque, electric field and strain. So far, the formation and evolution of magnetic stripe domains and their SW excitations are reported for NiFe [137], Co [138], CoFeSiB [139], FeSiB [140], FeCoAlON [141], FeCoZr [142], and FePd [143] thin films. Furthermore, the interaction between magnetic domain walls and SWs can induce a phase change when they pass through domain walls [111], which can help nanoscale ferromagnetic devices to perform logical operations based on SW propagation.

1.4.2 Magnetic Vortex:

Magnetic vortex (topological charge = ±0.5 [144]) is a curling configuration in ferromagnetic materials with negligible magneto-crystalline anisotropy comes due to competition between exchange and demagnetization energy. In the curling spin configuration, the direction of spin changes gradually along the in-plane direction so as not to lose too much exchange energy, but to cancel the total dipolar energy and the out-of-plane vortex core is located at the centre of the system. Magnetic vortex can be used to store data, process logic operations, and act as transistors in magnonic circuits [109,145]. Many theoretical and experimental observations have shown that the magnetic vortex core polarity and chirality can be controlled by the excitation of SW, the geometry of nanodots, electric current pulse, resonant excitation with rf current and applied magnetic field [146,147]. So far, It has been observed that static properties are essentially independent of core polarization, while dynamical behavior can be

controlled by core polarization [148]. The time-resolved scanning transmission X-ray microscopy has reported the controlled manipulation of the vortex core polarization by excitation with small and short in-plane bursts of 4 ns of an alternating magnetic field [149]. More recently, Brillouin light scattering experiments and hybrid micromagnetic modelling have observed the presence of azimuthal SW modes in magnetic vortex states and backward volume-like modes in the saturated state in Py nanodots [150]. Further experiments revealed azimuthal mode splitting into doublet due to the coupling between SWs and the gyrotropic motion of the magnetic vortex core [151]. Later, the dynamical operation of SWs demonstrated the "transistors" like behaviour in three vortices system by controlling their relative core polarities [108,109,152]. It helped the efficient energy transfer mechanics via the interaction of the dynamical stray field mediated by antivortex soliton [145]. As a result, the utilization of vortex and SW interaction can be used to design similar operations to those of semiconductor operations for the next generation of low-power spintronics and magnonics devices [153].

1.4.3 Artificial Spin Ice:

ASIs are one type of metamaterial which recently attracted great interest to investigate the collective dynamics of SWs in order to expose a variety of properties that are not inherently present in their building blocks. Here lithographically patterned two-dimensional or three-dimensional ferromagnetic nanoislands nanomagnets are arranged in such a way that all possible interactions between the nanomagnets cannot be satisfied simultaneously [154]. As a result, it will create a topologically disordered ground state or frustration with macroscopic degeneracy in a well-ordered structure of an FM nanodot system. That frustrated magnetic monopole and anti-monopole pairs of spin texture (magnetic defect) are linked via effective 'Dirac strings' in an ASI lattice [155]. The possible lattice configurations to design ASI are the kagome [156], triangular [154], square–kite tessellation [157], square [158], pentagonal [159], quadrupolar [160] and brickwork arrangements [161]. The first work on geometrical frustration was reported in 1935 by Pauling to describe the zero-temperature entropy in water ice [162]. Later, Harris *et al.* explained geometrical frustration in the ferromagnetic pyrochlore $Ho_2Ti_2O_7$ where spins are located at the corners of tetrahedra [163]. Wang *et al.* first explained the possible interactions present in a square ASI nanomagnets and explore the effect of correlations between different pairs of the islands with lattice constant [158]. In the same year, the spin ice behaviour in a kagome ASI was also demonstrated [156]. Thereafter, researchers observed a wide variety of interesting phenomena in magnetic ASI including vertex-based frustration, magnetic monopoles, phase transitions and chiral dynamics [164-166]. ASIs are also important for SW dynamics

because of their potential applications as reprogrammable magnonic crystals [154]. Further, theoretical calculations predicted that the band structure tunability could be achieved via the topological states in a square ASI [167]. It was also observed that the SW modes were strongly influenced by the ASI geometry, in-plane field strength and angle due to a changes in the magnetic microstate [168] and that will open an additional reconfigurability in on-demands magnonic crystal [164,169].

1.5 Objective of the Thesis:

The objective of this thesis can be broadly described as to explore the different fundamental as well as technological aspects of the spin dynamics and SW dynamics in three different possible domains, i.e., wave vector domain (conventional Brillouin light scattering), time domain (time-resolved magneto-optical Kerr effect magnetometry) and frequency domain (broadband ferromagnetic resonance) for patterned magnetic nanostructures, magnetic thin films heterostructures and multilayers. The studied systems can be categorized as follows:

(I) Observation of interfacial Dzyaloshinskii-Moriya interaction and spin pumping in single-layer graphene/CoFeB heterostructure: Here we have studied the role of defect density and Rashba shift on interfacial Dzyaloshinskii-Moriya interaction and spin pumping in monolayer graphene/CoFeB heterostructures.

(II) Magnetic domain driven transient magnetization enhancement and ultrafast demagnetization mechanism: Here we have investigated the role of different magnetic domains in ultrafast demagnetization mechanism and transient magnetization enhancement in Co/Pt multilayer.

(III) Bias field orientation driven reconfigurable magnetization dynamics and magnon-magnon coupling in triangular shaped $Ni_{80}Fe_{20}$ nanodots: Here, we have presented the magnon-magnon coupling in $Ni_{80}Fe_{20}$ made triangular nanodot arrays with different in-plane bias field angles. In this case, the inhomogeneous distribution of magnetic stray field is found to be responsible for magnon mode repulsion for a range of in-plane angles.

(IV) Spin-texture driven reconfigurable magnonics: Here, we have demonstrated the ability to modify the magnonic band structure and band gap by bias-field manipulating spin texture in chains of submicron dots made of $Ni_{80}Fe_{20}$.

(V) Bias field dependent magnetic microstates and spin wave dynamics in nanoscale artificial spin ice system: Finally, we have observed the effect of magnetic-field reversal study on SW spectra for different in-plane field orientations in a square ASI system using BLS spectroscopy.

Chapter 2

2. Theoretical Background

A continuously evolving theoretical as well as experimental development is always complementary to the advancement in research. The discovery of two different ends or poles of lodestone by P. Peregrines in 1269 A.D. introduced the era of magnetism [170]. The initial concept of magnetism was explained with the help of the orbital angular momentum of an electron. After the discovery of magnetism from the s-band electron of a silver atom by Stern-Gerlach introduced another era of magnetism [171]. The modern concept of magnetization is based upon the number of unpaired electrons, their spin, and interactions of spin angular momenta with the orbital angular momenta. In magnetism, depending upon the response to magnetic field, materials can be classified into five main classes: diamagnet, paramagnet, ferromagnet, ferrimagnet, and antiferromagnet. Among those, only ferromagnet and ferrimagnet retain spontaneous magnetization in absence of a magnetic field. Later, the origin of spontaneous magnetization was described with the help of quantum mechanics by considering neighbouring spin-spin interaction and this is known as Heisenberg exchange interaction [172]. The concept of magnetic domain was developed by Weiss in 1906 and it describes the competition between the exchange interaction and the dipolar interaction created by the free magnetic poles on the surface and edges (demagnetizing field) leading to the creation of small domains in ferromagnet (FM) to minimize the free energy [173]. Later, with the introduction of nanomagnetism, the scenario has become different. Here, in addition to exchange and dipolar interactions, geometry, shape and dimension always play important roles to describe magnetization reversal and its dynamics. This thesis is based upon the properties of ferromagnetic thin films and nanostructures, where the above-mentioned interactions play an important role.

In the following section, an overview of different energies that affect the magnetization reversal and magnetization dynamics of ferromagnetic nanostructures is illustrated. Subsequently, several aspects of spin currents, magnon current and the underlying physics behind their generation and manipulation have been discussed. Following that, different phenomena of probing SWs have been be explained.

2.1 Different Magnetic Energies:

In general, any ferromagnetic system consists of the sum of four different energy terms in continuum limit such as Zeeman energy (E_z), exchange energy (E_{ex}), demagnetizing energy (E_{demag}) and anisotropy energy (E_{anis}). The competition between these energies helps the system to create static magnetization

state which, in turn, affects the dynamical properties. In the end, the magnetic system tries to achieve its ground or equilibrium state by minimizing its effective energy (E_{eff}) at any given condition.

2.1.1 Zeeman Energy (E_z):

The Zeeman energy is generated by the torque experienced on the magnetic system due to the interaction of the external magnetic field (H_0) and the magnetization (M). It can be written as

$$E_z = -\mu_0 \int_v M \cdot H_0 \, d\tau \tag{2.1}$$

where μ_0 and dτ are the free space magnetic permeability and volume element, respectively. In presence of H_0, M tries to align along H_0 to archive the ground state.

2.1.2 Exchange Energy (E_{ex}):

This is of quantum-mechanical origin and short-range magnetic interaction energy that satisfies both the Pauli exclusion principle and Coulomb interaction. The theory of exchange interaction was developed by Heisenberg based on the Heitler-London model for hydrogen atom. So, it is called the 'Heisenberg exchange' or 'isotropic exchange' interaction. The magnetic ordering of ferromagnet, in addition to ferrimagnet and antiferromagnet systems, can also be understood by this interaction.

The Heisenberg exchange Hamiltonian between two neighbouring spins S_i and S_{i+1} is given by [174]

$$H_{ex} = -2 \sum_i J_{i,i+1} S_i . S_{i+1} \tag{2.2}$$

Where J is the exchange integral between them. J is positive for parallel spin configuration (ferromagnet) and negative for antiparallel spin configuration. In the continuum limit, the above equation can be expressed as:

$$E_{ex} = A \int_0^V (\nabla m)^2 dV \tag{2.3}$$

Where m and A are normalized magnetization and exchange stiffness constant respectively. A can be expressed as:

$$A = \frac{n_u J S^2}{a} \tag{2.4}$$

The above exchange interaction is called a direct exchange interaction where the electrons of magnetic atoms interact with their nearest neighbours. However, there are few other interactions where itinerant electrons play the role of an intermediator to couple magnetic atoms over relatively larger distances, which is called indirect exchange interaction. Some indirect exchange interactions are listed below.

2.1.2.1 RKKY Exchange:

This is a type of indirect exchange, where there is little or no direct overlap between the neighbouring electrons and itinerant conducting electrons play a major role to couple them. This type of exchange is popularly known as the RKKY interaction named after Ruderman, Kittel, Kasuya and Yoshida [175,176].

2.1.2.2 Superexchange:

Here, the spins of the magnetic cations are exchange-coupled via different non-magnetic anions. Most of the antiferromagnetic insulators are transition metal oxides and the transition metal cations are separated by large oxygen anions. In this case, the hopping via the intermediate p-orbital of oxygen plays an important role to couple magnetic cations, which is commonly known as superexchange interaction [177,178].

2.1.2.3 Antisymmetric Exchange

This is one type of three-site exchange mechanism that originates mostly because of spin-orbit coupling and broken inversion symmetry leading to superexchange interaction and canting of spins by a small angle [17]. Here any two neighbouring ferromagnetic atoms are coupled via a three-site exchange mechanism that includes a non-magnetic atom.

2.1.2.3.1 Dzyaloshinskii Moriya Interaction:

Dzyaloshinskii Moriya Interaction (DMI) is an antisymmetric type indirect exchange interaction where any two neighbouring ferromagnetic atoms are coupled by an interfacial DMI (iDMI) vector via three-site exchange mechanism that includes a non-magnetic atom [14,15,58]. The iDMI can arise due to inversion symmetry breaking at the interfaces between a ferromagnetic layer and a nonmagnetic layer due to SOC in the system. The observation of iDMI opens new avenues for designing thin-film heterostructures based on nonmagnetic layers such as heavy metal, two-dimensional materials for controlling chiral spin structures such as skyrmions and bubbles, and magnetic domain-wall-based storage and memory devices. The DMI Hamiltonian between two spins S_i and S_j can be written as $H_{DM} = -D_{ij}.(S_i \times S_j)$ as shown in Fig. 2.1 and The DMI energy density is given by [179-181]

$$E_{DM} = \frac{D}{M_S^2}\left(M_y \frac{\partial M_x}{\partial x} - M_x \frac{\partial M_y}{\partial x} + M_y \frac{\partial M_z}{\partial y} - M_z \frac{\partial M_y}{\partial z}\right) \quad (2.5)$$

Where D is the iDMI constant and M_i is the i^{th} component of the magnetization. The magnetization

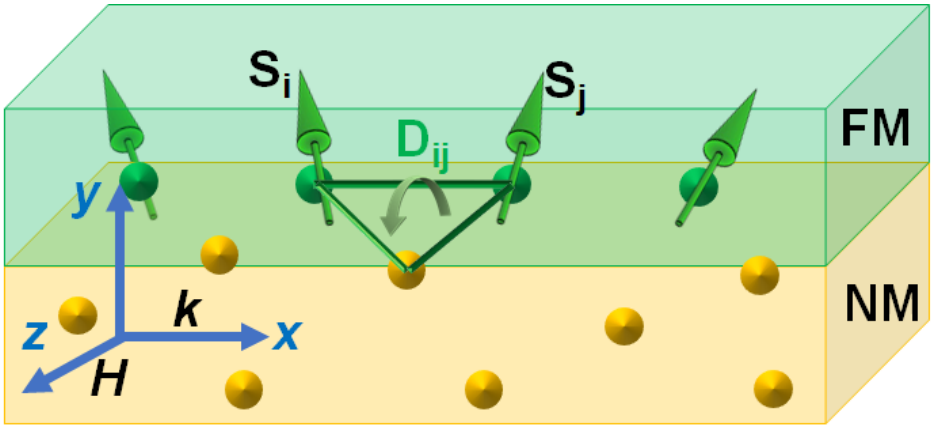

Figure 2.1: Schematic of Dzyaloshinskii-Moriya interaction at NM/FM interface.

of linear spin-wave (SW) can be written as $\frac{M(x,t)}{M_s} = m(x,t)$ where $m(x,t)$ is normalized magnetization direction which can be expressed as

$$m(x,t) = m_x\widehat{e_x} + m_y\widehat{e_y} - m_z\widehat{e_z} = m_{x0}e^{i(wt-kx)}\widehat{e_x} + m_{y0}e^{i(wt-ky)}\widehat{e_y} - \widehat{e_z} \quad (2.6)$$

Where m_{x0}, m_{y0} are much less than 1, $\widehat{e_x}$, $\widehat{e_y}$ and $\widehat{e_z}$ are the unit vectors co-directional with the coordinate axis. For SW travelling in the *x* direction, the expression of the field due to DMI is given by [182]

$$H_{DM} = -\frac{1}{\mu_0}\frac{\delta E_{DM}}{\delta M} = \frac{2D}{\mu_0 M_s}\left(\frac{\partial m_x}{\partial x}\widehat{e_x} - \frac{\partial m_x}{\partial x}\widehat{e_y}\right) \quad (2.7)$$

The total effective field is given by:

$$H_{eff} = -H\widehat{e_z} + J\nabla^2 M + H_{dip} + H_{ani} + H_{DM} \quad (2.8)$$

Where $J = 2A/\mu_0 M_S$ is the SW stiffness, A *is* the exchange constant and $H_{dip} = -M_s\xi(kL)m_x\widehat{e_x} - M_s(1-\xi(kL))m_y\widehat{e_y}$, where L is the magnetic film thickness, $\xi(kL) = 1 - (1 - \exp|-kL|)/|kL|$, the perpendicular magnetic anisotropy field $H_{ani} = \frac{2K}{\mu_0 M_s}m_y\widehat{e_y}$; Using the above expressions in the Landau Lifshitz Gilbert (LLG) equation:

$$\frac{dm}{dt} = -\mu_0\gamma m \times H_{eff} + \alpha m \times \frac{dm}{dt} \quad (2.9)$$

we end up with the following SW dispersion relation in the DE geometry:

$$\omega = \omega_o + \omega_{DM} = \mu_0\gamma\sqrt{[H + Jk^2 + \xi(kL)M_S][H - H_U + Jk^2 + M_S - \xi(kL)M_S]} - \frac{2\gamma}{Ms}Dk \quad (2.10)$$

The DMI-induced frequency shift of counter-propagating SWs is given by

$$\Delta f = \left\{\frac{\left[[f(-k, M_z) - f(k, M_z)] - [f(-k, -M_z) - f(k, -M_z)]\right]}{2}\right\}$$

$$\Delta f = [\omega(-k) - \omega(+k)]/2\pi = \frac{2\gamma}{\pi Ms}Dk \quad (2.11)$$

To extract the expression of the magnon linewidth, the linearized LLG equation can be solved by neglecting the high-order terms like O(α^2). The imaginary part of the angular frequency is given by:

$$\Delta f_{res} = 2Im[\omega] = 2\alpha_a\gamma\mu_0(H_0+Jk^2-H_u/2+M_s/2)\left[1 + \frac{\omega_{DM}(k)}{\omega_o(k)}\right] \quad (2.12)$$

The Brillouin intensity is given by:

$$I(\omega') \propto \left|m(\omega', k)\right|^2 \propto \frac{1}{(\omega' - Re[\omega]) + Im[\omega]^2} \quad (2.13)$$

where $m(\omega',k)$ is the Fourier transform of $m(x,t)$.

2.1.3 Magnetic Dipolar Interaction (E_d):

The magnetic dipolar interaction irrespective of whether ferromagnetic or not is present between any two magnetic moments m_1 and m_2 and associated magnetic energy can be expressed as [183]:

$$E_d = \frac{\mu_0}{4\pi r^3}[m_1.m_2 - \frac{3}{r^2}(m_1.r)(m_2.r)] \quad (2.14)$$

Where r is the separation between those two moments. In ferromagnets, this energy does not contribute to ferromagnetic ordering because of its long-range nature but plays a crucial role in the formation of domain and domain wall width, demagnetizing field distribution and SW behaviours in long wavelength regimes.

2.1.4 Magnetic Anisotropy (E_{anis})

While Heisenberg exchange energy is isotropic, ferromagnetic materials tend to have all their spins aligned along a particular crystallographic axis. These crystallographic axes, which encourage magnetization alignment, are known as easy axes, while the axes that resist magnetization saturation

are called hard axes. Deviation from these directions imposes an additional energy penalty on the system, known as the anisotropy energy [184,185]. There are mainly three primary sources of magnetic anisotropy, namely SOC, symmetry axes and long-range dipolar interaction. Some of the prominent magnetic anisotropies are described below:

2.1.4.1 Magnetocrystalline Anisotropy:

Magnetocrystalline anisotropy mainly originated from SOC and crystalline symmetry axis [186]. The electronic orbits depend upon the crystallographic axes and the spin-orbit interaction forces the

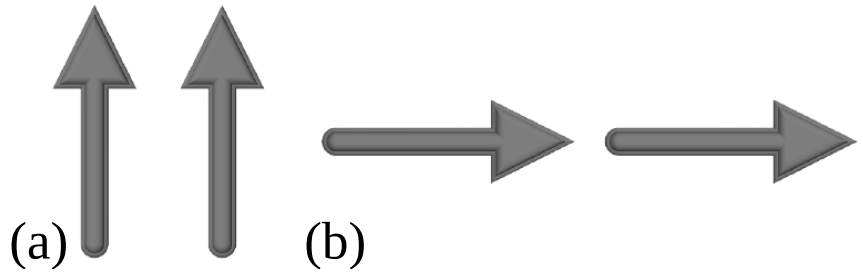

Figure 2.2: (a) Broadside and (b) head to tail configuration for ferromagnetically coupled magnetic moments. The latter is lower in energy.

electronic spins to be aligned along certain crystallographic axes. Two different spin configurations of ferromagnetically coupled magnetic moments are shown in Fig. 2.2. Further, the foldedness of the magnetic anisotropy is determined by the detailed symmetry of the lattice. Usually, in case of cubic systems, the anisotropy energy can be expressed as a function of the power of direction cosines α_x, α_y and α_z of the direction of magnetization with the cube edges. The expression of energy density for cubic systems can be written as

$$E_{ani} = K_0 + K_1\left(\alpha_x^2\alpha_y^2 + \alpha_y^2\alpha_z^2 + \alpha_x^2\alpha_z^2\right) + K_2\alpha_x^2\alpha_z^2\alpha_y^2) \quad (2.14)$$

*K*i's are the i^{th} order magnetocrystalline anisotropy constants.

On the other hand, for crystals having uniaxial anisotropy, the energy density can be written as

$$E_{ani} = K_u\alpha_x^2 \quad (2.15)$$

where K_u is the uniaxial anisotropy constant.

2.1.4.2 Magnetic Dipolar (Shape) Anisotropy and Demagnetizing Energy:

The second common example is size of the magnetic element that gives rise to the shape anisotropy in the system when element size is reduced to micrometer and nanometer range [187]. It is one of the anisotropic dipolar interactions of unsaturated magnetic surface charges (stray and demagnetization fields) entering into the picture because of inability to preserve the symmetry of the geometry of magnetic elements. Here the energy corresponding to the stray field can be written as:

$$E_{dem} = -\frac{\mu_0}{2}\int_v M \cdot H_{dem}\, d\tau \qquad (2.16)$$

The value of E_{dem} for an irregularly shaped magnetic element is strongly influenced by its structure and geometry and can become a complicated function of position. The magnetization direction of the element will align with the direction of minimum E_{dem}.

2.1.4.3 Volume, Surface, and Perpendicular Magnetic Anisotropy:

Broken inversion symmetry in the lower dimensional thin films and multilayers, give rise to an additional effective anisotropy term that contains both contributions i.e., surface anisotropy (K^S) and volume anisotropy (K^V). The expression of effective anisotropy of a system having thickness *t* can be written as:

$$K^{eff} = K^V + \frac{2K^S}{t} \qquad (2.17)$$

The second term plays a major due to the reduction of film thickness because of its "twice" multiplication factors and inverse dependency on thickness. Below a critical thickness ($t_c = -\frac{2K^S}{K^V}$), the film magnetization prefers perpendicular orientation, giving rise to perpendicular magnetic anisotropy (PMA) [188-190]. PMA can be originated from the reduced spatial symmetry, localized epitaxial strain at the interface, and electronic band structure. The PMA in magnetic material is very crucial to enhance the thermal stability in nanomagnets at room temperature which makes it desirable for information storage. When this FM layer is in contact with a non-magnetic layer, the energies and wave functions of OOP states get modulated due to interfacial hybridization. These hybridizations are sensitive to the local interface structure and affects the SOC perturbation, which in turn, changes the anisotropy energy. Hence, the PMA increases with the strength of the hybridization [51].

2.1.4.4 Configurational Anisotropy:

The competition between exchange and dipolar interaction becomes very crucial in case of nanostructures. Here we can artificially configure magnetic structures in various non-ellipsoidal

elements. In a non-ellipsoidal element, the changes of magnetization from a uniform to a non-uniform state cost huge energy which is known as configurational anisotropy [191,192]. This anisotropy depends on the shape and lattice symmetry of the nanoelements and this can be further classified as below [193,194]:

A. Intrinsic Configurational Anisotropy:

Here the anisotropy [113,191] arises because of the deviation from a single domain state to different magnetic spin texture, e.g., leaf, flower, C- or S-state in a single magnetic element in the micro- or nanoscale when it is kept under the various orientation of bias magnetic field.

B. Extrinsic Configurational Anisotropy:

Magnetostatically unsaturated regions located near the edges of an element vary with the azimuthal (in-plane) direction of the bias magnetic field (φ). As a result, the magnetostatic interaction between the elements also changes significantly and that influences the magnetic stray field (or demagnetizing field) distributions as well as the configurational magnetic anisotropy [194,195] depending upon the configuration of the magnetic elements.

2.2 Timescale of Magnetization Dynamics:

Magnetization dynamics cover a wide range of temporal regimes, starting from femtosecond (fs) to microsecond (μs) timescales to describe different phenomena [196]. This timescale (τ) can also signify different interaction energies (E) according to Heisenberg relation: $\tau = h/E$. The fastest dynamics occurring process usually in femtosecond (fs) timescale that includes Heisenberg interaction (~ 10 fs), pulsed laser-induced ultrafast demagnetization (few hundreds of fs) and SOC and STT (~10 fs – 1 picosecond (ps)). The timescale of magnetization reversal process is around a few ps to a few hundreds of ps. The timescale of the vortex core switching is a few tens of ps to several nanoseconds (ns) timescale [197]. Again, the timescale of precessional magnetization dynamics is few ps to a few hundreds of ps and the magnetization damping related to precessional motions is in sub ns to tens of ns timescale. In a ferromagnetic material, the SW propagates in a few hundred ps to tens of ns before getting damped. Finally, the slowest one is the domain wall dynamics which typically takes place between a few ns to a few μs. In this thesis, the studies are primarily based on ultrafast demagnetization and SW dynamics. A discussion of these phenomena is given below.

2.3 Ultrafast Demagnetization:

Before the 1995s, data writing applications were done on ferromagnetic films through Curie-point writing [198]. The recovery time of magnetization in ferromagnetic materials after excitation by a very short (fs) high-energy laser pulse sets the limitation in data processing speed. Here, the electrons are excited above the Fermi level because of electron-electron scattering and these are called hot electrons. The loss of phase memory (incoherent process) of the electronic wave function with respect to excitation during charge and spin thermalization can lead to demagnetization of a ferromagnetic material. This observation was first reported in 1996 by Beaurepaire *et al.* by shining a femtosecond laser on a thin foil of Ni [87]. They describe this observation of ultrafast demagnetization by a simple theoretical argument based on a phenomenological three-temperature model (3T-model) which is one of the most acceptable phenomenological models for demagnetization. With time, several stand-alone theories were proposed to explain different experimental observations on ultrafast demagnetization [88,89,199,200]. Despite having all those proposed models and mechanisms, the exact underlying microscopic processes involved in this ultrafast loss of magnetization have remained debatable.

2.3.1 Three-temperature Model and Modification:

The first observation of this ultrafast quench in magnetization was phenomenologically explained based on the 3T-model where electron, spin and lattice are the three different coupled temperature baths with their respective temperature T_e, T_s and T_l inside an FM system [94]. During this process, the photon energy of the high-energy laser is absorbed by the electronic temperature bath and creates hot electrons. As a result, the temperature of this bath rises very rapidly as shown in Fig. 2.3 and the spin angular momentum remains conserved under dipole approximation. Afterwards, the tendency of redistribution of majority and minority spins via scattering gives rise to an increase in spin temperature with a certain time delay, leading to a rapid loss in magnetization in the system. Later, the energy from both electron and spin baths is distributed to the lattice bath which causes another rapid rise in the lattice temperature and leads to a fast remagnetization. After a certain time-delay of the order of a few ps, all three reservoirs come into equilibrium. Figure 2.3 portray the sequence of events after laser excitation as proposed by the 3T-model. According to this model, the temperature evolutions of the electron, spin and lattice heat baths can be written by three coupled differential equations [87] given as:

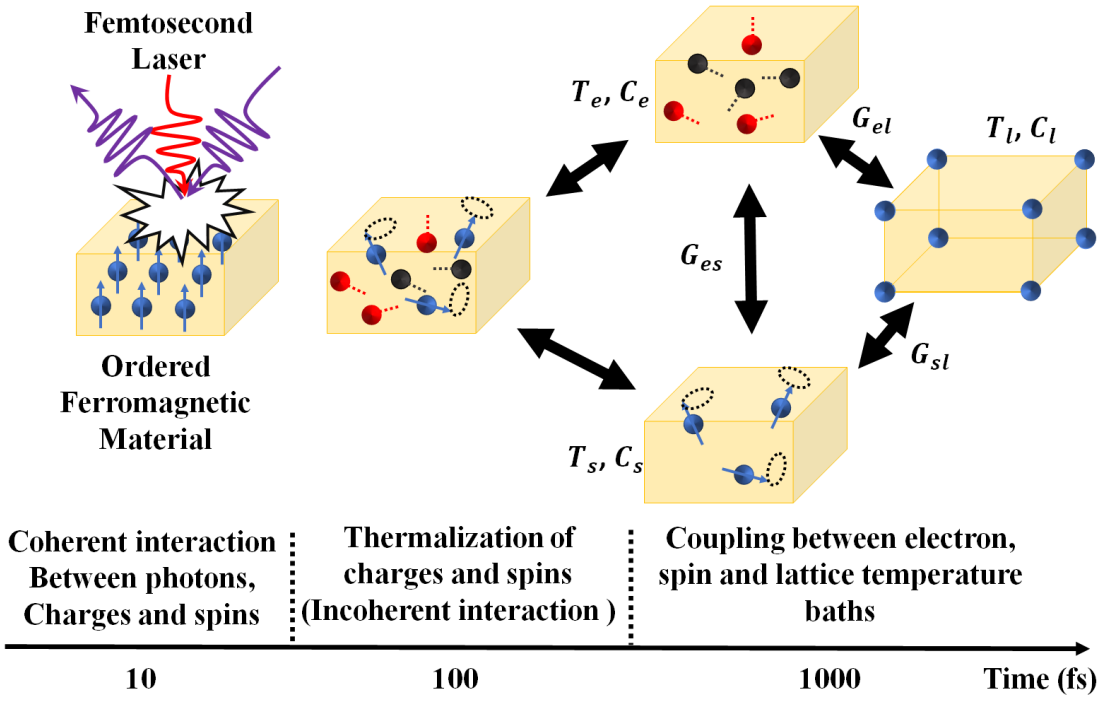

Figure 2.3: Ultrafast demagnetization and relaxation mechanisms according to the 3T-model.

$$C_e(T_e)\frac{dT_e}{dt} = -G_{el}(T_e - T_l) - G_{es}(T_e - T_s) + P(t)$$

$$C_s(T_s)\frac{dT_s}{dt} = -G_{es}(T_s - T_e) - G_{sl}(T_s - T_l)$$

$$C_l(T_l)\frac{dT_l}{dt} = -G_{el}(T_l - T_e) - G_{sl}(T_l - T_s) \qquad (2.18)$$

Here, C_e, C_s and C_l are the respective specific heat capacity of the electron, spin, and lattice baths and G_{el}, G_{es} and G_{sl} are the respective electron-lattice, electron-spin and spin-lattice coupling parameters. $P(t)$ is the form of Gaussian laser excitation and C_e is proportional to the T_e, i.e., $C_e = \gamma T_e$, where γ is determined by the density of states of electron around the Fermi level. In recent years, a modified 3T-model is proposed by Jiang *et al.* to understand the effect of superdiffusive spin transport (SST) present

in a system consisting of a highly conducting FM layer and low conducting NM layer. The modified 3T-model can also be written by three coupled differential equations given as [84]:

$$C_e(T_e)\frac{dT_e}{dt} = -G_{el}(T_e - T_l) - G_{es}(T_e - T_s) + P(t) + S(t)$$

$$C_s(T_s)\frac{dT_s}{dt} = -G_{es}(T_s - T_e) - G_{sl}(T_s - T_l) - P_{dsp}.S(t)$$

$$C_l(T_l)\frac{dT_l}{dt} = -G_{el}(T_l - T_e) - G_{sl}(T_l - T_s)$$

$$S(t) = S_d(P(t) \otimes e^{-\frac{t}{\tau_{sst}}})$$

$$\frac{\Delta M(t)}{M_0} = -\frac{(T_s(t)/T_c)^{\frac{3}{2}} - (T_0/T_c)^{\frac{3}{2}}}{1-(T_0/T_c)^{\frac{3}{2}}} \quad (2.19)$$

T_0 and T_c are the initial spin temperature and Curie temperature of FM respectively. *S(t)* denotes the energy injected into ($S(t) > 0$) or ejected from ($S(t) < 0$) electron subsystem by superdiffusive electron transport. P_{dsp} is the degree of spin polarization of superdiffusive electron flow with respect to spin-

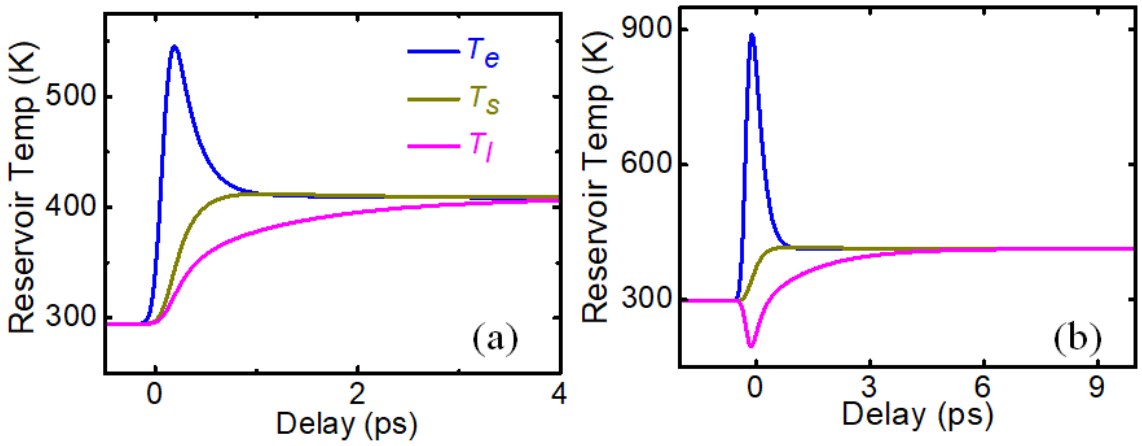

Figure 2.4: Temperature evolution of electron (E), spin (S) and lattice (L) heat baths after laser excitation according to 3T-model (a) and modified 3T-model (b).

majority states of FM layer, and varies between -1 and 1. As a result, $P_{dsp}.S(t)$ indicates the energy injected into or ejected from a spin subsystem via SST and only $P_{dsp}.S(t) > 0$ produces transient magnetization enhancement (TME) in the system. The ratio of amplitude of the superdiffusive energy

to transient absorbed energy is described by S_d in the FM layer. Finally, the transient magnetization change, $\frac{\Delta M(t)}{M_0}$, is calculated using Bloch's $\frac{3}{2}$-law: $M \propto [1-(T_s/T_c)^{\frac{3}{2}}]$, where M_0 is the initial saturation magnetization. The variation of all three temperatures according to the 3T-model and modified 3T-model are shown in Fig. 2.4.

2.3.2 Mechanisms Involved Behind Ultrafast Demagnetization:

Although the phenomenological 3T-model could explain the ultrafast drop of magnetization and fast recovery process, this model also has a few drawbacks as listed below.

1. The actual underlying microscopic mechanisms involved in the ultrafast demagnetization process such as the energy transfer process from laser photons to ordered ferromagnetic system, momentum transfer mechanisms between different temperature baths etc. are not considered properly.
2. This model is also not able to explain the origin of the type-II demagnetization (a sub-ps demagnetization with a successive slow few ps drop of magnetization) process reported in rare-earth ferrimagnets.

Several microscopic mechanisms such as spin-orbit coupling [199,201], phonon-mediated spin-flip scattering [93,96], electron-magnon interaction [202], phonon-phonon interaction [203], optical inter-site spin transfer [82,204], superdiffusive spin current transport [89], Coulomb interaction for electron-electron scattering [91] were proposed over time to solve these discrepancies in the 3T-model. We will discuss a brief overview of superdiffusive spin current transport which have motivated this doctoral thesis work.

2.3.2.1 Superdiffusive spin current transport:

The microscopic mechanisms for the transfer of angular momentum are debatable based on the above theories because most of these are based on a common assumption that the laser pulse must interact directly with the ordered spin system and dissipate an ultrafast angular momentum through different channels [89]. In 2008 Malinowski *et al.* first time observed that the spin transport of hot electrons accelerates the demagnetization process for a synthetic antiferromagnetic (SAF) structure [88]. Later, in 2010, Battiato *et al*. proposed a semiclassical model to understand the ultrafast drop of magnetization with the help of superdiffusive spin transport where the electrons with majority spin diffuse faster into the substrate as opposed to the minority spin [89]. No spin-flip channel is included in this model and the phenomena of ultrafast demagnetization is explained by considering the spin-dependent transport

of photon-excited electrons. The electrons in the quasi-localized d band absorb the photon energy and go above the Fermi level into the more delocalized s bands or p bands. As the velocity in s bands or p bands is much higher (1 nm/fs) than in the d band, thus electrons become extremely mobile. Therefore, those hot electrons can travel in any random direction and experience various spin-conserving scattering events which create a cascade of electrons. The final transport equation after completing the second cascading can be written as:

$$\frac{\partial \eta^{tot}}{\partial t} + \frac{\eta^{tot}}{\tau} = (-\frac{\partial}{\partial z}\hat{\phi} + \hat{I})(\hat{S}\eta^{tot} + S^{ext}) \quad (2.20)$$

Here, η^{tot}, τ and S^{ext} are the density of electron, spin lifetime and electron source term, respectively. $\hat{\phi}$ and $\hat{I}$ represent flux and identity operators. $\hat{S}$ can be defined as $\hat{S}\eta^{[1]}=S^{[2]}$ where $\eta^{[1]}$ and $S^{[2]}$ are the density of first-generation electrons and second-generation excitation term. As the lifetime of majority and minority spins electrons are not equal which helps to the gradual decrease in the majority spins in the magnetic layer. This loss of majority spin carriers reduces the net magnetization of the system leading to ultrafast demagnetization. The general diffusive motion of particles can be described by the variance of the displacement (σ^2) with $\sigma^2(t) \propto t^b$, b = 1, while for the ballistic transport b = 2. For superdiffusive spin transport, b is time-dependent and neither diffusive nor ballistic (b = 2 for a shorter lifetime and b = 1 for a longer lifetime).

2.4 Precessional Magnetization Dynamics:

In presence of an external magnetic field and any kind of external perturbation, the magnetic moments of a magnetic material experience a torque, which induces precession in magnetization around an effective magnetic field consisting of an external field (H_0), exchange field (H_{ex}), dipolar field (H_{dip}), anisotropic field (H_{ani}) and $h(t)$, a time-varying magnetic field in the system. Since the damping is always present in any FM system, the precessional motion executes a damped spiral motion about the effective field direction. This precessional magnetization dynamics is well described phenomenologically in the LLG equation [205] as shown in Fig. 2.5(b). In 1935, Lev Landau and Evgeny Lifshitz first introduced a torque equation name as Landau-Lifshitz (LL) equation always present in any FM system. This precessional torque in any physical system can eventually be damped out after some time. Landau and Lifshitz (LL) accounted for this by modifying the torque equation to include a damping term along with the precessional torque term, which is given by:

$$\frac{d\boldsymbol{M}}{dt} = -\gamma\left(\boldsymbol{M} \times H_{eff}\right) + \frac{\lambda}{M_S^2}\boldsymbol{M} \times \left(\boldsymbol{M} \times H_{eff}\right) \tag{2.21}$$

where M_S is saturation magnetization and λ is LL damping term with a dimension of sec^{-1}. In 1955, the phenomenological dimensionless damping term (α = damping constant) was added by Gilbert [206]. The final form of LLG equation can be written as:

$$\frac{d\boldsymbol{M}}{dt} = -\gamma\left(\boldsymbol{M} \times H_{eff}\right) + \frac{\alpha}{M_s}\boldsymbol{M} \times \frac{d\boldsymbol{M}}{dt} \tag{2.22}$$

The Gilbert damping parameter is related to LL parameter by the relation, $\alpha = \frac{\lambda}{\gamma M_S}$ and the effective field can be expressed as:

$$H_{eff} = H_0 + H_{ex} + H_{dip} + H_{ani} + h(t) \tag{2.23}$$

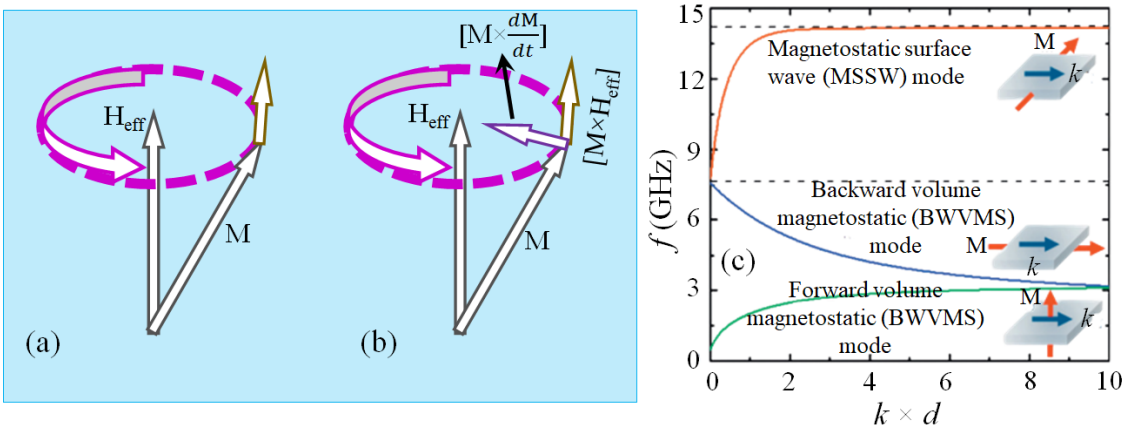

Figure 2.5: (a)-(b) Precessional motion of magnetization (M) around effective magnetic field (H_{eff}) without and with damping. (c) The dispersion relation for different types of magnetostatic SW modes.

2.4.1 Magnetic Damping:

The control and tunability of magnetic damping [53,207-209] in an FM can speed up the relaxation process and accelerate the spiral motion of magnetization to equilibrium which can create opportunities for the importance of magnetic recording technology. In general, memory pixels in MRAM should have a comparatively large damping and the fastest magnetization reversal is achieved when the required time is only about a single period of precession. On the contrary, low-damping materials are desirable candidates for long-distance SW propagation-based devices and to reduce the write current in STT-MRAM devices.

There are two types of magnetic damping: (i) intrinsic damping and (ii) extrinsic damping.

(i) Intrinsic Damping:

Intrinsic damping is inevitable in a magnetic material with a perfect crystal structure, which mainly originates from the itinerant conducting electrons and strength of SOC. The few most common model to understand intrinsic damping in the magnetic system is the s-d exchange interaction model, breathing Fermi surface model etc. In 1976, Kambersky suggested a new torque correlation model by considering intra-band and inter-band transitions where damping is proportional to ξ^2 (correlated SOC strength: ξ) at low temperatures and ξ^3 at high temperatures [210]. In addition, phonon-mediated spin-flip scattering [211-213], and ordinary scattering [214,215] are few processes which can modulate intrinsic damping.

(ii) Extrinsic Damping:

Extrinsic damping of an FM is avoidable, which could also initiate dissipation of energy during the spin precession. A few processes which mainly contribute to extrinsic damping are inhomogeneous magnetic anisotropy [216], two-magnon scattering [217], impurities, phonon drag [208], injection of spin current [218], spin current-induced torque [219], spin pumping [220], eddy current [221], doping or capping with another material [36], and controlling the temperature of the system [53]. Inversion symmetry breaking at the interface can also modulate the Gilbert damping parameter [218]. Additionally, in FMR measurements, global excitation plays a role in the effect of superposition of local resonance for long wavelength (small *k*) variation in magnetic properties. This arises mainly due to defects in the large area averaging. Magnetostatic contribution also plays an important role in affecting the magnon-energy dispersion due to damping. In this thesis, we have only discussed spin pumping contribution as below:

(A) Spin Pumping:

Spin pumping is a method of generating a spin current, and it is a spintronic analogue of a battery in conventional electronics [19]. In NM/FM heterostructure, accumulated spins at the interface due to spin precession in FM layer are directed from the FM layer to the NM layer in the form of pure spin current [222]. This effect in NM/FM layered systems was first proposed in 1988 by Hurdequint *et al.* to interpret the results of a spin resonance experiment [223]. Later in 2002, Y. Tserkovnyak and A. Brataas theoretically demonstrated this damping enhancement in NM/FM heterostructures by employing the time-dependent adiabatic scattering theory [36,224]. The expression for effective damping of the FM layer is given by the spin pumping theory

$$\alpha_{eff} = \alpha_0 + \alpha_{SP} \tag{2.24}$$

Here, α_0 is the intrinsic Gilbert damping parameter and the additional damping term, α_{SP} is attributed to the spin pumping mechanism, which is given by [54]:

$$\alpha_{SP} = \frac{\gamma h g_{\uparrow\downarrow}}{4\pi M_s t_{CoFeB}} \tag{2.25}$$

Here, $g_{\uparrow\downarrow}$ is the intrinsic spin-mixing conductance. The enhancement of the Gilbert damping is higher for NM layers with a higher spin-flip relaxation rate (r). This r can be roughly expressed as:

$$r \propto Z^4 \tag{2.26}$$

Here, Z is the atomic number.

2.4.2 Spin Wave:

The decrement of saturation magnetization with increasing temperature was explained by F. Bloch in

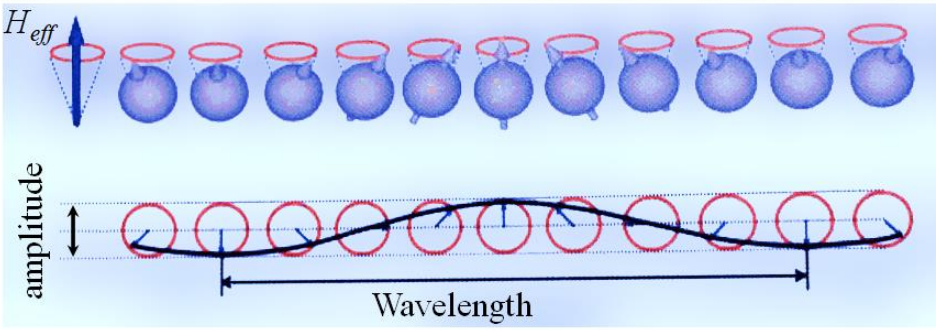

Figure 2.6: Cartoon of spin wave propagation.

1930 through the introduction of the concept of SWs [41]. All the spin magnetic moments are parallel to each other in a minimum energy state of any FM. Now the presence of any tiny external stimuli, a phase lag between two neighbouring spins is propagating throughout the system in the form of a wave known as a SW (see Fig. 2.6). The quanta of SW are called magnon. In presence of an external magnetic field, all ferromagnetic spins precess uniformly in phase about the direction of the magnetic field. The frequency of this uniform precession (well known as ferromagnetic resonance or FMR frequency) can be obtained by solving the LLG equation (Eqn. (2.16)) with the condition of $\frac{dm}{dt}$ = 0. In 1948, C. Kittel derived the resonance condition near wavevector (k) $k \approx 0$ after solving LLG equation by considering the demagnetizing field which is expressed as [225]:

$$f_{FMR} = \frac{\gamma}{2\pi}[\{H_0 + (N_y - N_z)M_s\}\{H_0 + (N_x - N_z)M_s\}]^{1/2} \tag{2.27}$$

In the case of non-uniform precession, phase shift associated with finite *k* of the spin system along with the interaction between magnetic moments play a significant role in characterizing SW frequency and associated SW dispersion. The SW energy is primarily dominated by dipolar energy in long wavelength regime due to the negligible role of phase difference and hence the SW is manifested as dipolar-dominated or magnetostatic SWs in 1961 by Damon and Eshbach (DE). These dipolar dominating modes as anisotropic and characterized into three classes [226,227] as shown in Fig. 2.5(c):

(I) Magnetostatic Surface SW or DE mode:

When M_s and *k* lie in the film plane and are perpendicular to each other, then the SW mode frequency can be written as [226,227]:

$$f_{DE} = \frac{\gamma}{2\pi}[H_0(H_0 + M_s) + (2\pi M_s)^2(1 - e^{-2k_{\parallel}d})]^{1/2} \quad (2.28)$$

(II) Magnetostatic Backward Volume Mode (MSBVM):

When M_s and *k* lie in the film plane and are parallel to each other, then the SW mode frequency can be written as [228]:

$$f_{MSBVM} = \frac{\gamma}{2\pi}[H_0(H_0 + 4\pi M_s \frac{1-e^{-2k_{\parallel}d}}{k_{\parallel}d})]^{1/2} \quad (2.29)$$

(III) Magnetostatic Forward Volume Mode (MSFVM):

When M_s is in out-of-plane direction and *k* is in the film plane, then the SW mode frequency can be written as [174]:

$$f_{MSFVM} = \frac{\gamma}{2\pi}[(H_0 - 4\pi M_s)(H_0 - 4\pi M_s \frac{1-e^{-k_{\parallel}d}}{k_{\parallel}d})]^{1/2} \quad (2.30)$$

The frequency of dipole-exchange modes in presence of the subsistent amount of exchange constant (A) becomes larger than the dipolar modes. The contribution from exchange interaction plays a dominating role for higher wave vectors as the exchange has a quadratic contribution to the dispersion relation.

When the SW energy is primarily dominated by exchange energy in short wavelength as opposed to dipolar energy, it is known as exchange SWs. These modes are isotropic in nature and can be expressed as [174]:

$$f = \frac{4Js}{h}(1 - cos\, ka) \tag{2.31}$$

Here, J is the exchange integral, k is the wavevector and a is interspinal separation.

The exchange length can be written as:

$$l_{ex}(r) = \sqrt{\frac{2A}{\mu_0 M_S^2}} \tag{2.32}$$

Further, it is also possible to excite exchange SWs in a direction perpendicular to the film surface in the form of standing SWs known as perpendicular standing SW (PSSW). For a given thickness of d, the wavevector for PSSW can be expressed as:

$$k_\perp = \frac{n\pi}{d} \tag{2.33}$$

Again, the characteristic dispersion relation by taking dipole-exchange interaction into account is given by [229]:

$$f_{dip\_exc} = \frac{\gamma}{2\pi}\left[(H + 4\pi M_s k_\parallel d\, sin^2\Phi_{k_\parallel} + \frac{2A}{M_s}k_\parallel^2)(H + 4\pi M_s - 2\pi M_s k_\parallel d + \frac{2A}{M_s}k_\parallel^2)\right]^{1/2} \tag{2.34}$$

where $\Phi_{k_\parallel}$ is the angle between the applied field H and $k_\parallel$.

2.5 Ferromagnetic Resonance (FMR):

When a steady magnetic field is applied to an FM material, its magnetization starts to precess around the effective magnetic field (H_{eff}) present in the system. The associated angular frequency (ω) is governed by the Larmor precession for electron spin:

$$\omega = \gamma H_{eff} \tag{2.35}$$

If an alternating magnetic field (H_{rf}) with an angular frequency (ω) is applied in the perpendicular direction to the bias field, then resonance will occur under the following condition:

$$\omega = \gamma\sqrt{BH_{eff}} \tag{2.36}$$

Here B is the magnetic induction. Consequently, the magnetization will start to precess with resonant frequency by absorbing power from the alternating magnetic field. This phenomenon is called ferromagnetic resonance (FMR) [225,229].

2.5.1 Microwave Excitation and Detection:

FMR spectroscopy is a method to study the magnetization dynamics of a ferromagnetic system to investigate the SWs and spin dynamics. Currently, various methods are available for FMR measurements such as stripline-based FMR (SL-FMR) [230], pulsed inductive microwave magnetometry-based FMR (PIMM-FMR) [231] and vector network analyzer-based FMR (VNA-FMR). The SL-FMR technique is comparatively simpler but its sensitivity is poor. The PIMM-FMR technique relies upon the inductive detection of magnetization and uses a dc magnetic field. The main advantage of a VNA-FMR setup is it can extract both phase and amplitude information of the signal.

In the following paragraphs, the VNA-FMR technique is discussed comprehensively.

2.5.2 Vector Network Analyzer Incorporated Broadband FMR:

Here magnetization dynamics of a sample is studied directly in the frequency domain. The microwave input signal with a broad frequency window starting from 10 MHz to 50 GHz is launched into the sample by a VNA and SW output absorption spectra at a fixed static magnetic field are recorded in terms of scattering (S) parameters [232]. The excitation power of the input signal can be varied by the VNA, which is useful for the study of linear as well as nonlinear spin dynamics.

2.5.2.1 Vector Network Analyzer (VNA):

Network analyzers [233] are typically used to measure components, devices, circuits, and sub-assemblies. At lower frequency regime, one can measure those quantities of a device by using simpler tools. Whereas for higher frequency regimes, like radio and microwave frequencies, it is almost impossible to measure those quantities using a simpler tool and therefore, the VNA-FMR spectrometer is used. The VNA can measure both amplitude and phase simultaneously of an incident signal as well as transmitted and/or reflected signal from a device. A systematic calibration method is needed to eliminate systematic errors before starting the experiment. Finally, the S parameters are calculated by computing of appropriate ratios of the signals, which are similar to our familiar results. The main advantage of a broadband FMR (or VNA-FMR) spectrometer, over a conventional FMR spectrometer, are the following:

a) A resonance cavity is used in conventional FMR spectrometers to study a specific resonance frequency with a high-quality factor [234]. On the contrary, a non-resonant cavity is used in broadband FMR spectrometer to investigate a broad frequency range from a few MHz to tens of GHz with flat

quality factor. It makes broadband FMR spectrometer more convenient for the study of multi-modal systems like magnetic nanostructures.

b) The low-frequency regime (MHz to 1 GHz) is extremely important to study domain wall motion-driven dynamics, vortex core dynamics etc., where the broadband FMR spectrometer is more suitable than the conventional FMR.

The VNA system consists of several components such as compositions (including signal generator, signal separation blocks (test set), signal receiver, processor and display), transmission line (coplanar waveguide), high frequency device characterization (reflection parameters, transmission parameters, group delay) and scattering (S-) parameters. A few of important components are briefly discussed in the following paragraphs.

A. Coplanar Waveguide:

The coplanar waveguide (CPW) [235] was first invented in 1969 by Chang P. Wen. The main advantage of CPW is it is easily mountable on any active devices like the integrated circuit (like

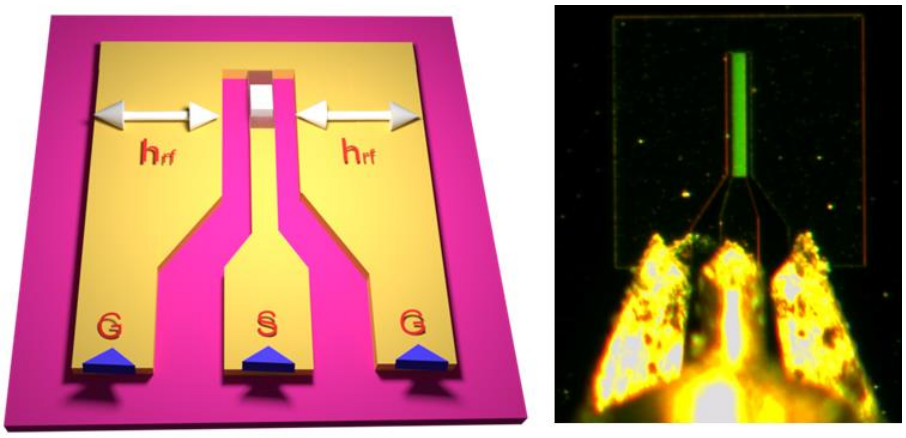

Figure 2.7: Schematic of the experimental geometry. The directions of the rf field (h_{rf}) are shown in the schematic.

microstrip). A CPW can be fabricated by using optical lithography technique and it is generally used for the propagation of microwave signals [234]. The CPW is generally designed with three terminals i.e., a single conductor (signal line) in between a pair of return conductors (ground lines). These three lines are typically fabricated in the plane of a dielectric medium and hence, it is called coplanar waveguide. In coplanar waveguide, electromagnetic energy is concentrated within the dielectric. The presence of the ground plane on each side of a signal trace provides natural shielding for the signal

against interference from other signals. The width (w) of the signal line, the separation gap (s) between signal line to ground line, relative dielectric constant, and thickness of dielectric medium play crucial roles to the determinate effective dielectric constant and impedance of the whole system (website: https://chemandy.com/calculators/coplanar-waveguide-with-ground-calculator.htm). These three lines are shorted at one end in the reflection geometry and, they are always separated by a small gap in the transmission geometry. In this thesis, we have used only reflection geometry as shown in Fig. 2.7. An insulating layer is used to separate the FM samples and the signal line to avoid damaging/shorting the samples from direct RF current. The magnetic field lines generated from rf current (I_{rf}) get flattened close to the surface of signal line due to its rectangular shape. This in-plane RF magnetic field (h_{rf}) perturbs the spin system from its equilibrium state as illustrated in Fig. 2.7.

B. Reflection Parameters:

The most general reflection parameter is reflection coefficient (Γ) and is defined by the ratio of the reflected signal (V_{ref}) and the incident signal (V_{inc}) i.e., $\Gamma = \frac{V_{ref}}{V_{inc}}$. Γ is a complex number and its magnitude is called rho (ρ). According to the maximum power transfer theorem, there is no reflection ($V_{ref} = 0$) in the VNA if the load impedance (Z_L) is equal to the characteristic impedance (Z_0) or else $V_{ref} \neq 0$. For both short and open circuit cases, $|V_{ref}|=|V_{inc}|$, and $\rho=1$. Now, one important parameter in the transmission line i.e., return loss, which can be expressed as $-20\log_{10}\rho$. It signifies that the amount of the reflected signal is lower than the incident signal in decibel unit. The return loss becomes infinity when $Z_L=Z_0$ and 0 dBm for open or short conditions. The voltage standing wave ratio (VSWR) is another very common parameter used to quantify the reflection. The relation between VSWR and ρ is, VSWR = $\frac{(1-\rho)}{(1+\rho)}$. The VSWR is 1 for no reflection and infinity for full reflection.

C. Transmission Parameters:

The most general reflection parameter is transmission coefficient (T) and is defined by the ratio of the transmitted signal (V_{tra}) to the incident signal (V_{inc}) i.e., $T = \frac{V_{tra}}{V_{inc}}$. If $|V_{tra}|<|V_{inc}|$, this is called insertion loss and the phase part of T is called the insertion phase. It is typically expressed in dBm unit.

D. Scattering (S-) Parameters:

S-parameters are the components of scattering (S-) matrix to describe the electrical behaviour of a circuit in frequency domain. They are useful to study the electrical behaviour of a circuit working at RF or microwave (MW) frequencies. These parameters depend on the measurement frequency and port impedance. An electrical circuit is usually treated as a black box and it can interact with surrounding

circuits through connecting ports. The network (interconnection of different electrical elements) is characterized with the help of S-matrix. To characterize a network having N number of ports an N-dimensional S-matrix is required, which has N2 complex components. At very high frequencies, direct measurement of impedance (*Z*) or admittance (*Y*) or hybrid (*h*) parameters of a network becomes hard due to the underneath reasons:

1. It is difficult to measure total current and voltage of a network in that high-frequency regime.

2. It is challenging to achieve perfect open/short conditions.

3. The device under test (DUT) may not stay stable under such high-frequency regime or in open/short conditions.

However, to avoid the above-mentioned difficulties, S-parameters offer the following advantages:

1. It is easier to measure S-parameters in such high-frequency regime.

2. S-parameters can relate to various familiar measurements, such as return loss, insertion loss, and VSWR of a network.

3. These parameters can also be used to calculate *Y*, *Z*, or *h*- parameters.

D.1 Calculations for the Scattering (S-) Parameters:

According to the numbering convention of S-parameters, the first number signifies the port associated with output signal and second number signifies the port associated with input signal. If it represents a measurement then the output signal connects with port 2 and incident signal enters into port 1. Whereas if both the numbers are same (e.g., S_{11}), this corresponds to reflection measurement geometry. Figure 2.8 shows schematically the measurement conditions for (a) two-port and (b) one-port measurement geometries, respectively. Here Z_S and Z_L respectively correspond to the source and load impedances and both are terminated at Z_0. V_S represents input signal voltage level. On the other hand, V_1, V_2 and I_1, I_2 represent corresponding potential differences and currents across the respective loads. If the incident signals (a_1, a_2) and acquired signals (b_1, b_2) represent corresponding voltage travelling waves from the two-port device then both the b_1, and b_2 wave can be described as a linear combination of a_1, and a_2 wave. These relationships can be expressed as follows:

$$b_1 = S_{11}a_1 + S_{12}a_2$$

$$b_2 = S_{21}a_1 + S_{22}a_2 \tag{2.37}$$

The above two equations can be written in the matrix notation as,

$$\begin{bmatrix} b_1 \\ b_2 \end{bmatrix} = \begin{bmatrix} S_{11} & S_{12} \\ S_{21} & S_{22} \end{bmatrix} \begin{bmatrix} a_1 \\ a_2 \end{bmatrix} \tag{2.38}$$

Now, the four S-parameters can be written as:

1. Forward reflection coef., $S_{11} = \frac{b_1}{a_1}\Big|_{a_2=0}$ & Reverse reflection coef., $S_{22} = \frac{b_2}{a_2}\Big|_{a_1=0}$
2. Forward transmission coef., $S_{21} = \frac{b_2}{a_1}\Big|_{a_2=0}$ & Reverse transmission coef., $S_{12} = \frac{b_1}{a_2}\Big|_{a_1=0}$ (2.39)

These S_{ij} parameters are also shown in Fig. 2.8. In this thesis, we have only used S_{11} parameter and one-port measurement in reflection geometry to collect the SW spectra from ferromagnetic nanostructure sample.

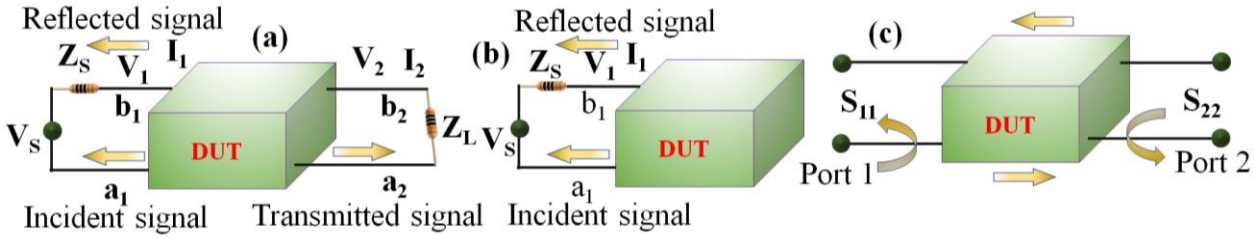

Figure 2.8: Schematic representation of (a) two- and (b) one-port microwave excitation and detection systems. (c) A graphical representation of the scattering (S) parameters.

2.6 Magneto-optical Kerr Effect (MOKE):

The interaction of the light beam with magnetic material can give rise to a modification in polarization, intensity, phase and spectrum of the output beam. This effect was first proposed by Michael Faraday in 1845 when the linearly polarized light transmitting through a glass plate in presence of a magnetic field, becomes elliptically polarized light. In 1877, John Kerr has observed a similar type of effect for reflected light. This phenomenon is known as the magneto-optical Kerr effect (MOKE) [236-238] and the corresponding angle of rotation of the plane of polarization (i.e., the major axis of the ellipse) and ellipticity are called the Kerr rotation (θ_k) and Kerr ellipticity (ϵ_k). These two quantities are directly proportional to the magnetization of the system and related to the expression:

$$\theta_k + i\epsilon_k = \frac{k}{r};\ \text{where } k \ll r \tag{2.40}$$

where *r* and *k* denote the parallel and perpendicular electric vector components of the reflected light.

2.6.1 Origin of MOKE:

There are mainly two theories to explain the origin of MOKE: (i) macroscopic and (ii) microscopic

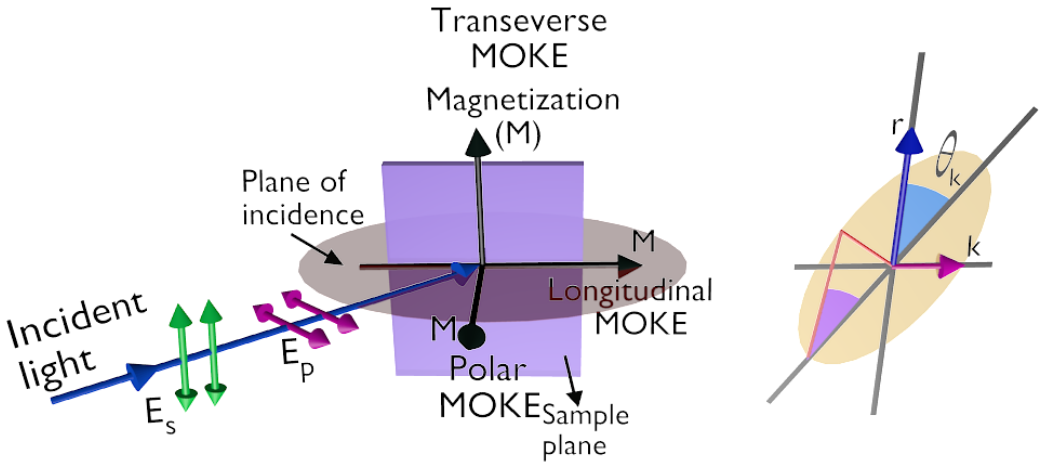

Figure 2.9: (a) Schematics of polar, longitudinal, and transverse MOKE geometries are shown. (b) The geometry of the Kerr rotation (θ_k) and Kerr ellipticity (ε_k).

[238,239]. When light travels through a medium, macroscopically the electrons inside that medium follow the motion of the electric vector of light beams. As a result, the left (right)-circular motion of the electrons is guided by the left (right) circularly polarized (LCP (RCP)) light and the radii of LCP and RCP are equal in the absence of a magnetic field. As linear polarized light is the combination of LCP and RCP with equal amplitude then the dielectric tensor will be equal for both cases. Now due to the presence of a magnetic field, an additional Lorentz force will be exerted by electrons. Therefore, the radii of the LCP and RCP are not equal. Hence, the amplitude and phase of the reflected beam are converted from linear polarized light to elliptically polarized light. Microscopically, MOKE can be considered to be originated from the spin-orbit interaction. Here, the motion of the electrons under the influence of the electric field of light creates a magnetic vector potential and affects the SOC of the system. This generated SOC can be written as: $S \times \nabla V$, where, S and ∇V are the spin angular momentum and the electric field in the system respectively. This effect will be present in both FM and NM materials [53]. It is most dominating in FM due to the unbalanced population of electron up-spin and down-spin in FM materials and which is cancelled out in the case of NM materials. Now depending

upon the orientation of the magnetization direction (M) of an FM and the plane of the incidence, the Kerr effect can be classified into three different geometries (shown in Fig. 2.9), namely, longitudinal, transverse and polar. When M is parallel to the plane of incidence and lies in the sample plane, it is referred to as longitudinal Kerr effect. When M lies in the sample plane and is perpendicular to the plane of incidence, it is called the transverse Kerr effect. When M is perpendicular to the sample plane and parallel to the plane of incidence, it is known as the polar Kerr effect.

Chapter 3

3. Fabrication and Characterization Techniques

Modern nanochip technology fully relies on how precise and good-quality chips can be made [240]. There are many techniques to design and fabricate those nanochips. . This chapter presents a summary of the methods used for fabrication, experimental characterization, and numerical analysis in the present thesis. The successful implementation of miniaturization of nano-magnetic systems in the future technology demands the fabrication of good quality thin films and confined structures with minimum structural and compositional defects. In this length scale, the intrinsic magnetic properties of a material strongly depend upon the surface and interface quality of two dissimilar materials, and chemical order [241]. So, it is extremely important to optimize the steps of the fabrication procedure and detailed static and dynamic characterization are also necessary to examine and optimize the respective magnetic parameters.

In this thesis, the thin films or multilayers have been deposited by a dc/rf magnetron sputtering unit and different nanodots have been fabricated with the help of electron beam (e-beam) evaporation and e-beam lithography technique. The surface morphology and elemental quality have been characterized by atomic force microscopy (AFM) [242], scanning electron microscope (SEM) [243], energy dispersive x-ray spectroscopy (EDX) [244] and X-ray diffraction (XRD) [245]. The magnetic spin texture and magnetization reversal mechanisms have been experimentally examined using magnetic force microscopy (MFM) [246], and vibrating sample magnetometry (VSM) [247] as well as magneto-optical Kerr effect (MOKE) magnetometry [248], respectively. The objective of this thesis can be broadly described as exploring the different fundamental as well as technological aspects of the spin and/or spin wave dynamics in three different possible domains, i.e., wave vector domain, time domain and frequency domain in patterned magnetic nanostructures and thin film heterostructures. For that, we have employed a custom-built Brillouin Light Scattering (BLS) spectroscopy in wave vector domain, time-resolved magneto-optical Kerr effect microscope (TR-MOKE) in time domain and broadband vector network analyzer-based FMR (VNA-FMR) in frequency domain.

The magnetization dynamics of uniform FM can be determined under the macrospin formalism. Under the small angle approximation, the non-linear differential LLG equation is linearized and solved to calculate the SW frequency and other parameters. However, the demagnetizing field arising from the unsaturated magnetic dipoles in confined magnetic patterned structures at the finite boundaries affects

the static spin texture as well as the magnetization dynamics. Hence, the calculations are not straightforward and the situation becomes more complex for the samples having non-ellipsoidal geometries where analytical solution becomes more complicated. Again, various fabrication limitations and measurement restrictions are imposed on the real system and the theory faces serious challenges to reproduce the real situation due to the lack of appropriate approximations and boundary conditions for nanoscale magnetic systems. Hence, the development of various micromagnetic modelling and computer-based numerical techniques have emerged to address these issues. Micromagnetism is a continuum theory where the magnetic parameters vary continuously in space. In the micromagnetic simulation, the sample is divided into several unit cells each of which consists of a magnetic moment (macrospin) which interacts with the neighbouring cell's moment by short-range exchange and long-range dipolar interactions, under the influence of anisotropy fields, and in presence of external magnetic fields, where additional field terms can also be introduced. In this thesis, we have used the finite difference method-based OOMMF, LLG micromagnetic simulator and MuMax3 along with analytical and numerical techniques such as the plane-wave method investigate the properties of the dynamic magnetization of confined systems.

3.1 Fabrication Techniques:

3.1.1 Sputtering:

Sputtering deposition is a physical vapour deposition (PVD) technique to deposit high quality continuous films and multilayers at a high-vacuum environment of about 10^{-7} Torr or better as schematically shown in Fig. 3.1 [249]. The primary requirement of a sputtering unit is an anode: a substrate with substrate holder, a high vacuum chamber, and a cathode: the target material. A high-voltage power supply is used to create and stabilize a neutral gas plasma within a vacuum chamber, where atoms, ions, electrons, and photons coexist in a nearly balanced state. The process begins when the power supply is turned on, causing free electrons in the plasma to quickly accelerate away from the negatively charged cathode. These accelerated electrons then collide with the neutral gas atoms they encounter, resulting in the creation of positively charged ions (i.e., Ar +) [250]. Those positive charge cations of inert gas in the plasma attract towards the negatively charged target and bombard with this negatively charged target material or source material (desired to be deposited). This collision dislodges and ejects neutral atoms into space and those ejected atoms traverse towards the anode (substrate) and start to condense into a substrate.

The traditional sputtering technique is plagued by two significant issues, namely slow deposition rates and target overheating caused by excessive electron bombardment. One solution to these problems is

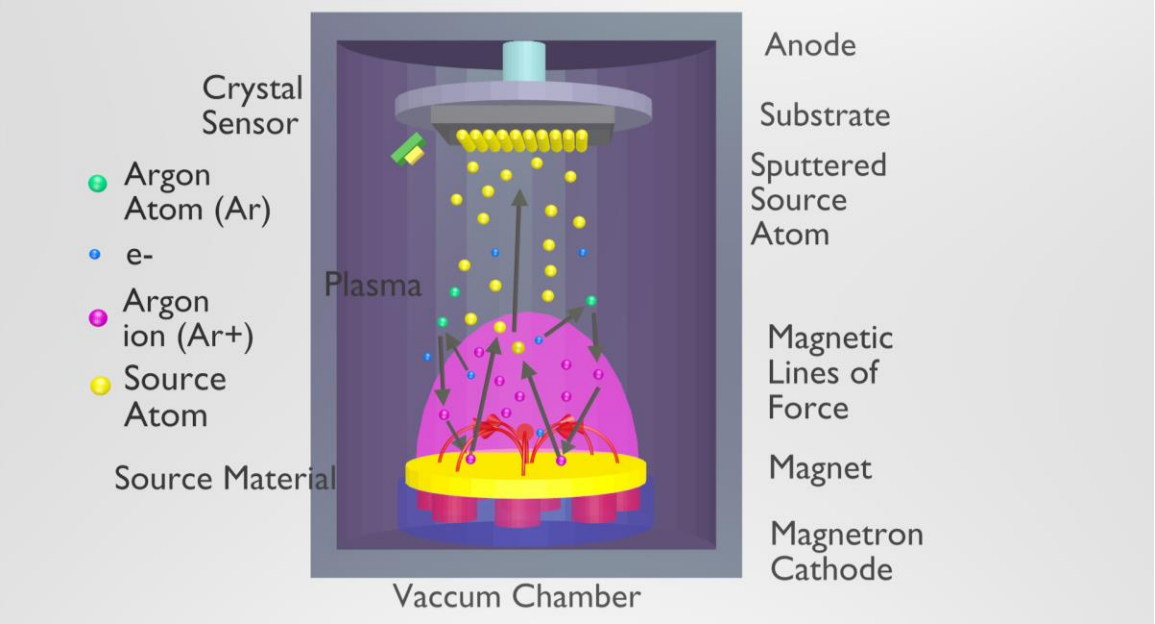

Figure 3.1: Schematic of RF-DC magnetron sputtering unit.

to use magnetron sputtering. In this case, the presence of a strong magnetic field near the target area causes travelling electrons to spiral along magnetic flux lines near the target instead of being attracted toward the substrate. It will increase the probability of a greater number of ionizing Ar atoms inside the chamber which cause more ejected atoms from the target. This process increases the efficiency of the sputtering process and minimizes impurities to form in the thin film.

3.1.2 E-beam Evaporation (EBE):

This is another physical vapour deposition (PVD) technique, where an intense beam of electrons generated from a hot tungsten filament by thermionic emission is directed towards the source material by electric and magnetic fields [251]. The collision of those electron beams with source materials causes heating in the source material and helps to reach its boiling point. Now, the vapour of the material steers towards the substrate which is loaded on a sample holder (The sample holder is mounted on a rotation motor, which rotates during the deposition) and gets condensed uniformly all over its surface (see Fig. 3.2). Since thermal energy is very low, the pressure in the chamber is maintained in a way so that the mean free path remains lesser than the distance between the electron beam source and

the substrate [252]. One of the major advantages of e-beam evaporation is the ability to rotate several source materials into the path of the electron and deposit sequentially multiple thin films without breaking the vacuum.

3.2.3 E-beam Lithography (EBL):

The electron beam lithography technique (EBL) [253] is widely used to draw a custom pattern such as

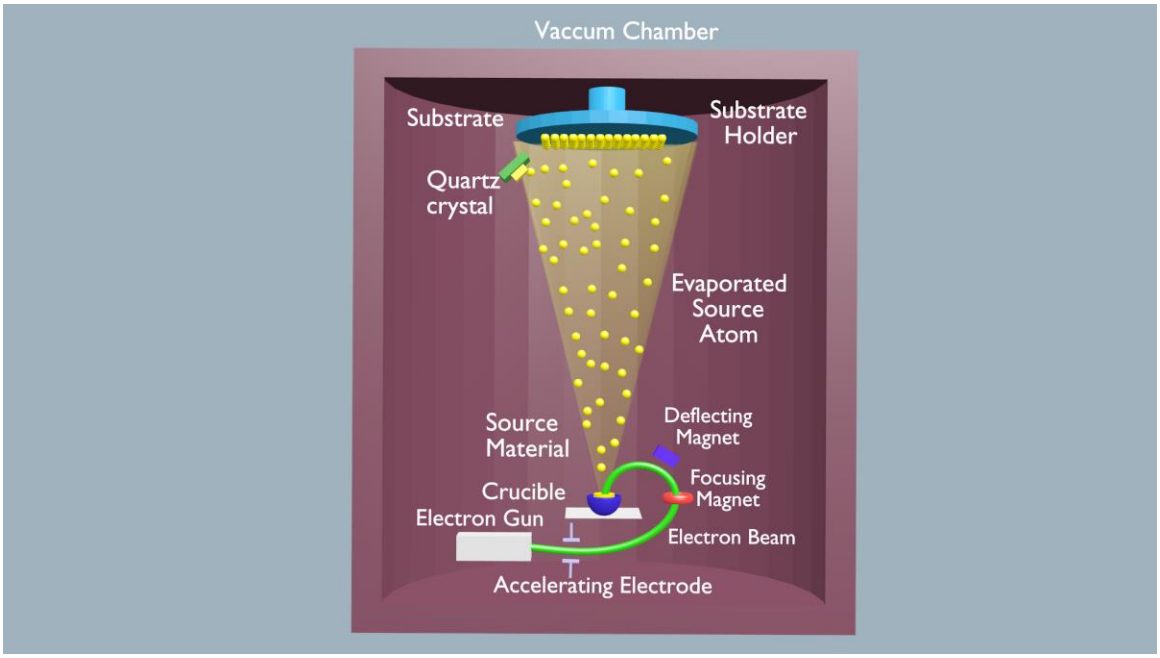

Figure 3.2: Schematic of electron-beam evaporation.

1D, 2D pattern onto the surface of a material coated with a layer of resist by a tightly focused and precisely controlled electron beam (exposure). The advantage of e-beam lithography is that the high-energy electron beam possesses a much shorter wavelength than the wavelength of ultraviolet (UV) light used in photolithography. So, this technique is capable of fabricating nanostructures with very high resolution down to the nanometer (nm) scale. This technique is composed of the following fundamental steps (See Fig. 3.2):

i) To begin the process, a clean substrate is first spin-coated with a bilayer of polymethyl methacrylate (PMMA 495K and 950K), a positive-tone electron beam resist. The use of two layers aids in achieving an undercut edge profile of the resist following pattern development.

ii) Next, the resist is exposed to focused electron beams within a scanning electron microscope connected to a computer. A commercially available design software, such as Auto CAD, is

used to draw the desired structure, which is then printed onto the resist layers by an accelerated electron beam, controlled by the computer.

iii) Following the writing step, the resist is developed using a solution of methyl isobutyl ketone (MIBK) and isopropyl alcohol (IPA) in a 1:3 ratio, followed by rinsing in water.

iv) Next, the desired material is then deposited onto the developed resist.

v) Finally, the lift-off process is carried out in acetone with ultrasonic agitation, removing the unexposed resist and the deposited film on top of it.

3.2 Static Characterization Techniques:

3.3.1. Scanning Electron Microscopy (SEM):

A scanning electron microscope (SEM) [243,244] is a type of microscope which uses a focused beam of electrons to characterize the surface topography and morphology of samples with very high resolution down to the nm scale. The electrons in the beam interact with the sample, producing a variety of signals which contain the information about the surface texture and composition. The emission of that signal from the specimen increases as the energy of the primary electron beam increases until a certain limit is reached. When an electron beam is used to scan a sample surface, several signals are generated, including secondary electrons (used for SEM imaging), auger electrons, transmitted electrons, backscattered electrons (a result of elastic scattering), visible light (cathodoluminescence - CL), photons (including characteristic X-rays for elemental analysis and continuum X-rays), and heat. Variations in the intensity of secondary electrons relative to the incident electrons produce two-dimensional and quasi-three-dimensional views of the sample surface. Modern SEMs can reach a resolving power better than one nm. In this thesis, FEI Quanta 200 (at SNBNCBS) was used to image 2D nanostructures (see Fig. 3.3).

3.3.2 Energy Dispersive X-ray:

Energy dispersive X-Ray analysis (EDX) [244], referred to as EDS or EDAX, is an important x-ray technique used to identify the elemental composition and chemical characterization of materials (see Fig. 3.3). Generally, it has been typically used in conjunction with scanning electron microscopes or x-ray spectrometers. A specialized type of Si or Li detector, equipped with spectrum analyzer software, is used to determine the energy and quantity of emitted X-rays. Since each element has a distinctive atomic structure and emission spectrum, and this information can be used to identify the elements in a

sample. At the ground state, an atom has electrons orbiting the nucleus in specific orbits. When a high-energy beam of charged particles, like protons, electrons, or X-rays, strikes the sample, it creates an electron hole in the inner shell by exciting and ejecting electrons. Now the electrons from higher energy shells then jump to fill the inner shell electron deficiency. To stabilize the atom, the energy difference between these two energy shells is emitted as an X-ray. The individual elements are recognized from

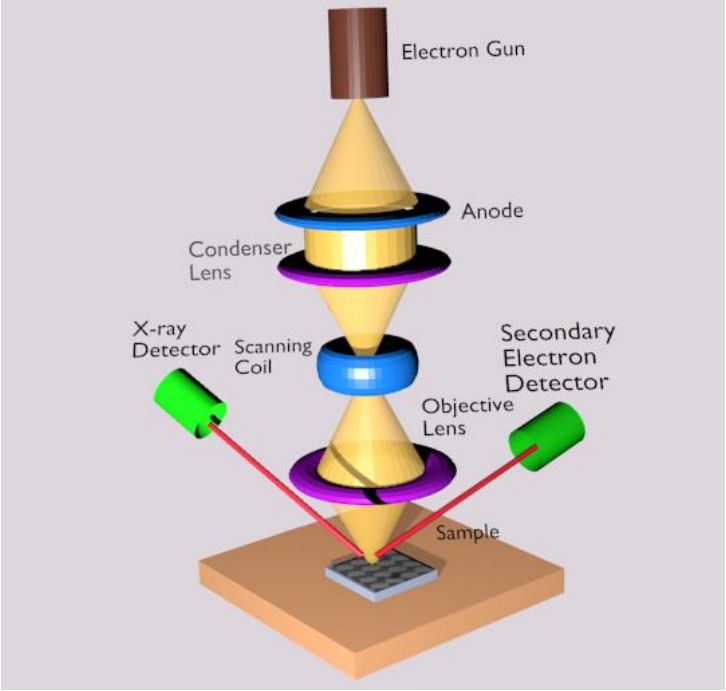

Figure 3.3: Schematic of scanning electron microscope (SEM) and energy dispersive X-ray (EDX).

the peak energy values of the X-rays and the relative intensities of the peaks give the atomic percentage of the elements in the specimen.

3.3.3 X-ray Diffraction:

X-ray diffraction (XRD) [245,254] is a widely used technique to investigate the crystallinity, imperfections, and structure of solid samples. To measure the lattice constant of an element, the measuring tool should be of the order of lattice constant, an X-ray is only the suitable choice for this measurement. When X-rays having wavelength λ, is scattered from a regular crystal lattice with interatomic separation d, the scattered beams form secondary waves. These secondary beams can interfere constructively in certain directions according to Bragg's condition:

$$2d \sin\theta = n\lambda \qquad (3.1)$$

Here, θ is the incident angle which varied between a range of angles in small steps and n is an integer. In practice, reflected intensities are measured as a function of the reflected beam with respect to the direction of the incident beam i.e., the angle 2θ (see Fig. 3.4). The diffraction peaks are converted to *d*-spacings to identify the elements present in the sample. The peak positions give direct information about the crystal plane. Typically, this is done by matching the data with standard reference patterns

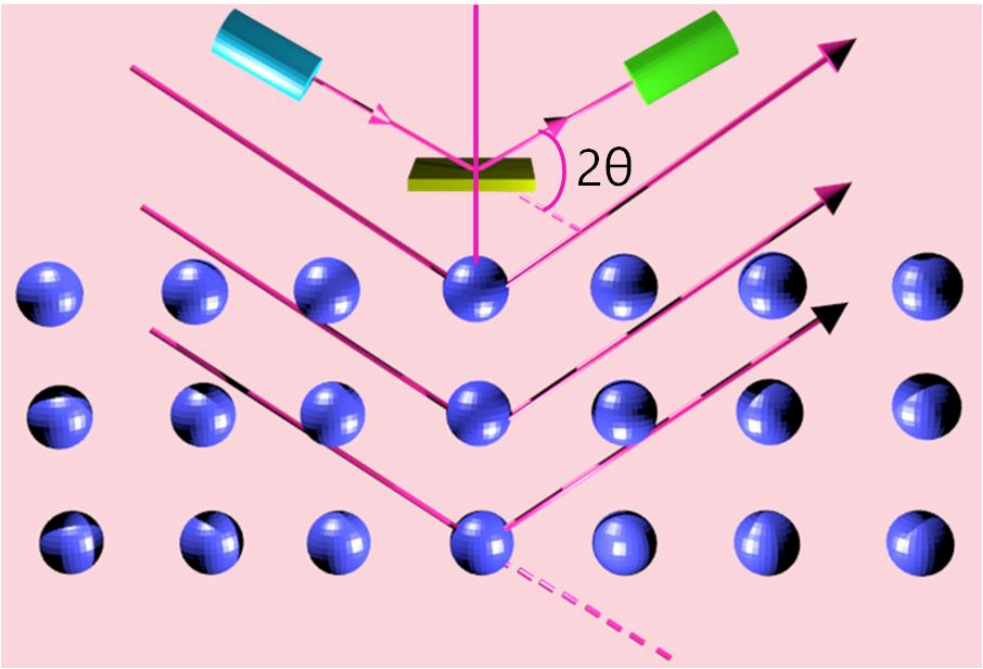

Figure 3.4: Schematic of X-ray diffractometer and diffraction of X-ray from the atomic planes.

(i.e., Inorganic Crystal Structure Database (ICSD) or International Centre for Diffraction Data (ICDD)).

3.3.4 Vibrating Sample Magnetometer (VSM):

The vibrating sample magnetometer (VSM) [247] (or Foner magnetometer) is a scientific instrument that measures magnetic properties as a function of applied magnetic field (*H*) and temperature (*T*). Its working principle is based on Faraday's law of induction states that an electric field is generated in a coil when there is a changing magnetic flux passing through it. Mathematically electromotive force (*E*) is induced in the coil having turns *N*:

$$E = -NA\frac{dB}{dt} \qquad (3.2)$$

A is the area of the sample and B is magnetic induction. As we know $B = \mu_0(M + H)$ then the above equation become:

$$E = -NA\frac{dM}{dt} \qquad (3.3)$$

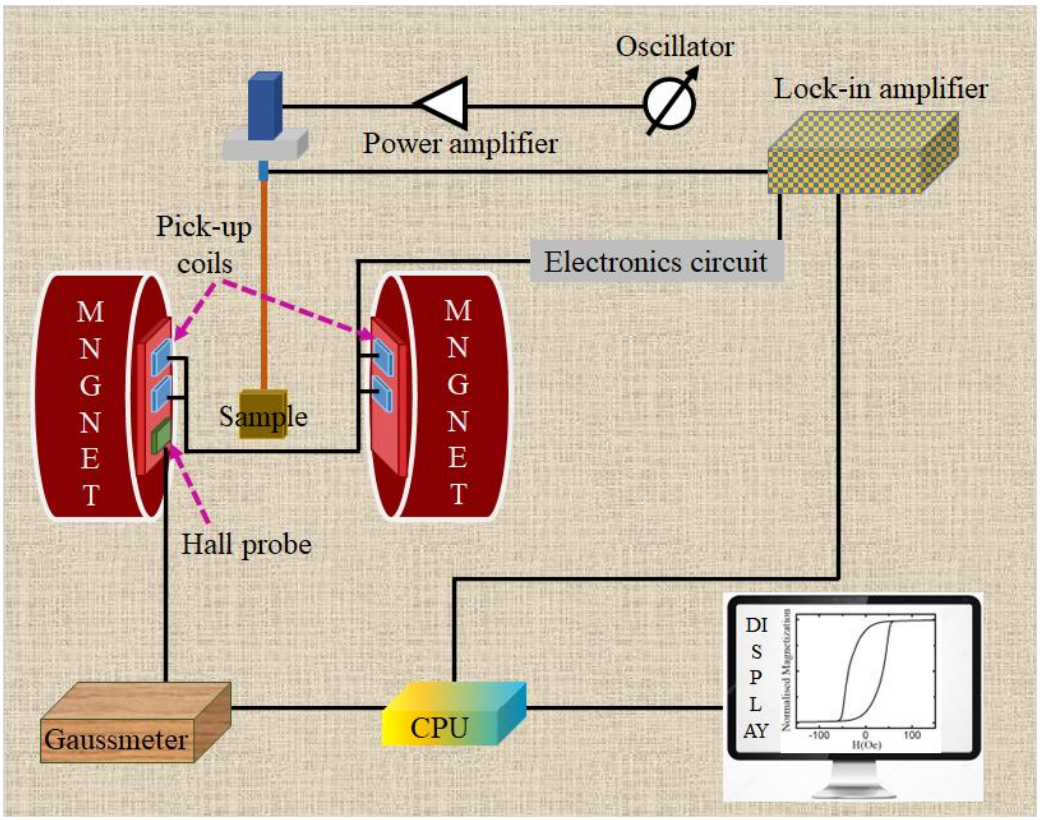

Figure 3.5: Schematic of vibrating sample magnetometer.

Since the magnetization M depends on the total magnetic moment (m) and G is the geometric factor of the sample, Eq. 3.3 finally reduces to:

$$E \propto -m\omega z G y_0 n_c n_\omega \cos \omega t \qquad (3.4)$$

where ω and z are the frequency and amplitude of vibration respectively, y_0 is the distance to pick-up coils, n_c the number of turns of pick-up coils.

This electric field is basically used to examine the magnetic moment of a sample. The schematic diagram of the setup is shown in Fig. 3.5. Here, the sample is mounted to a piezoelectric transducer and placed in a constant magnetic field. As a result, the magnetic dipole moment of the sample creates a stray magnetic field around the sample. Here, a piezoelectric transducer transforms a sinusoidal electrical signal (created by an oscillator/amplifier) into a vertical vibration of the sample rod that generates an oscillation of the sample's magnetic moment. As a result, a voltage is induced in the pick-up coil, situated near the sample, that is independent of the applied field. The VSM technique utilizes this phenomenon to convert the sample's dipole field into an AC electrical signal, which can be amplified and measured with a lock-in amplifier using the piezoelectric signal as a reference signal. General measurement of magnetic moment as small as ~ 10^{-5} emu is possible. When there is a variation in the applied magnetic field or temperature, the magnetic dipole moment of the sample is modified, and this modification can be used to examine the M-H or M-T curves of a FM.

3.3.5 Atomic Force Microscopy (AFM) and Magnetic Force Microscopy (MFM):

The atomic force microscope (AFM) [242] is widely used in materials science including soft biological materials to investigate local properties of specimens, such as morphology, roughness, dynamics etc. Normally, the AFM probe consists of a cantilever with a sharp tip at its end. This sharp tip is used to scan over a surface with a resolution better than 100 times the optical diffraction limit. The information on the specimen is obtained by measuring the force between a tip and the specimen. The sample is placed on a piezo-electric (PZ) controller which helps in performing the raster scan. When the tip is coming into the vicinity of the sample surface, it experiences lateral as well as vertical deflections due to several forces such as van der Waals forces, capillary forces, chemical bonding, electrostatic forces, and magnetic forces. A laser beam is pointed on top of the tip to sense the deflection of the tip after being reflected and captured in a four-quadrant photodiode (see Fig. 3.6). A two-dimensional image of the local properties can then be acquired by performing a raster scan over a small area of the sample. Mainly three possible AFM operating modes are present in our system and describes below:

i) Contact mode: The contact mode is also known as static mode AFM, where the tip is moved across the sample's surface while maintaining constant repulsive force between the tip and the surface. This force is maintained by using a feedback amplifier that applies feedback voltage to the piezo. To prevent damage to the sample during measurement, low stiffness cantilevers are used to achieve a large enough deflection signal while keeping the interaction force low. The feedback amplifier adjusts the height of

the sample surface during scanning based on the signal obtained, and this ensures that a constant force is maintained throughout the scan.

ii) Non-Contact Mode: In non-contact mode, also known as dynamic mode AFM, the tip oscillates close to the sample surface with small amplitude, and the forces between the tip and the sample are much weaker compared to the contact mode. These forces include Van der Waals force. The cantilever

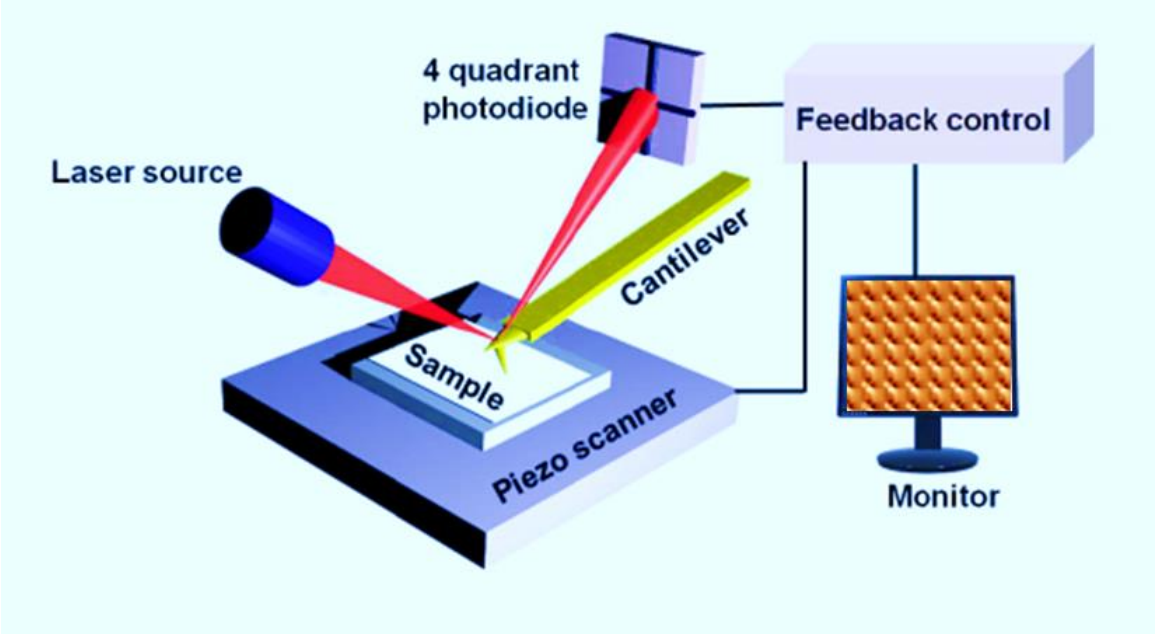

Figure 3.6: Schematic of magnetic force microscopy (MFM).

is made to oscillate at or near its resonant frequency, and any changes in amplitude, phase, or frequency of the oscillation caused by the interaction between the tip and the sample are measured to obtain the topographic image of the sample surface.

iii) Tapping Mode: The AFM tapping mode, in which a vertically oscillating cantilever interacts with a sample at or near its resonant frequency using a piezoelectric crystal, is the most used AFM mode in ambient conditions. In this mode, lateral force interactions between the tip of the cantilever and sample are reduced because of the intermittent tip-sample contact. The resulting change in oscillation amplitude is used to identify and measure surface features.

As referred above, AFM can detect various forces, and one of the widely used variations is magnetic force microscopy (MFM) [246], which can reveal the magnetic configuration of a sample's surface. The MFM utilizes a cantilever tip coated with a thin magnetic layer with high coercivity (such as Co)

that preserves its magnetization state during imaging. As the tip approaches the sample, it detects not only the atomic and electrostatic forces but also the magnetic forces between the sample and the tip. However, a dual scan is required where after taking an AFM image, the tip is scanned again over the sample at an elevated height to extract the contrast of magnetic signal. Depending on the strength of the stray field from the sample, MFM can operate in static and dynamic mode.

3.3.6 Static Magneto-optical Kerr Effect (S-MOKE) Magnetometer:

The S-MOKE technique is the local and non-invasive magneto-optical tool to measure magnetization reversal in terms of Kerr rotation or ellipticity of confined and continuous thin film [53,196]. It can

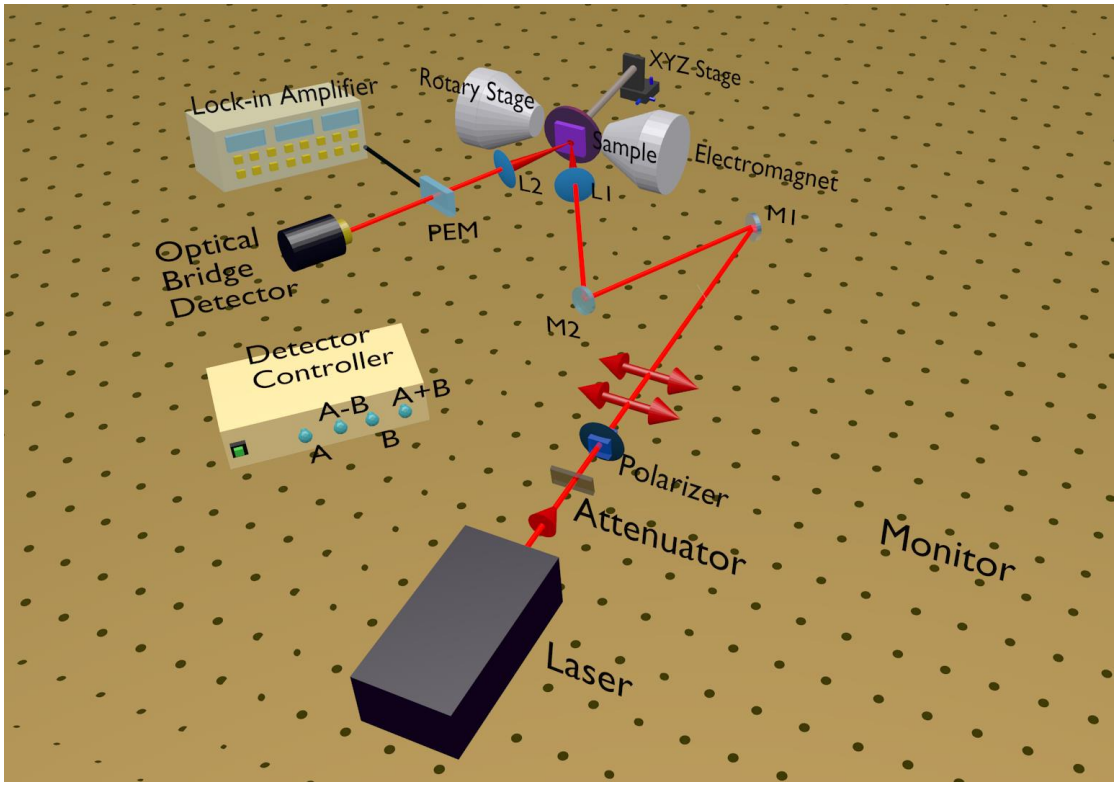

Figure 3.7: Schematic of the static-MOKE system presents in our laboratory at S.N. Bose national centre for Basic Sciences

sense localized surface-sensitive magnetic properties in a nonuniformly distributed system (like wedge shape film). In our thesis, we have primarily used the longitudinal MOKE geometry (magnetization parallel to both the plane of incidence and the sample surface) in our laboratory at the S. N. Bose National Centre for Basic Sciences although static-MOKE can measure magnetization reversal in all three geometries (see Fig. 3.7). A continuous-wave He-Ne laser having wavelength of 632.8 nm and an electromagnet are used in our setup for the detection of the in-plane magnetic field-controlled Kerr

signal. A polarizer is used to create the incident beam fully linearly polarized. The reflected beam from the sample surface is guided towards an optical bridge detector (OBD) through a photoelastic modulator (PEM; 1 kHz frequency modulation) to detect the rotation in the plane of the polarization. The frequency of the PEM provides the reference signal to the lock-in amplifier. A LabVIEW-based software is used to monitor the Kerr signal during magnetization reversal measurement.

3.3 Spin Dynamics and Spin-wave Dynamics Measurements:

3.3.1 Brillouin Light Scattering (BLS) Technique:

The light scattering technique is one of most powerful techniques to study various physical properties in gases, liquids, and solids. In this technique, the incident light interacts with a sample and the scattered light from the sample carries information about many important physical properties. In the so-called Raman scattering [255], incident photons interact with the rotational or vibrational degree of freedom of the system. Brillouin light scattering (BLS) is a technique that involves the scattering of photons from low-frequency excitations, such as phonons, magnons, and plasmons. BLS is non-contact and non-invasive, allowing for the measurement of elastic properties in various materials, including water [256,257], solids [258], and organic materials like the eye lens [259]. In this thesis, we will investigate only magnon contribution in continuous and confined ferromagnetic thin films using BLS.

In 1922, L. Brillouin [260] and in 1926, Mandelstam [261] independently predicted the phenomenon of light scattering from acoustic waves. A few years later, in 1930, Gross experimentally confirmed this observation of light scattering in liquids [262]. The development of the laser in the 1960s brought about a revolution in this field of study. However, it was only after Sandercock developed a sophisticated spectrometer in 1971 that researchers were able to investigate acoustic waves and spin waves in optically opaque materials [260]. The key development of this spectrometer is to pass the scattered light multiple times through two Fabry-Perot interferometers for dramatic enhancement of the sensitivity of a Fabry-Perot interferometer [261]. Sandercock and Wettling were able to detect both surface and bulk spin waves in polycrystalline films of Fe and Ni by utilizing two interferometers in tandem [262,263]. Since then, BLS has become a valuable tool in magnetism research due to its flexibility in samples, as well as its high frequency, phase, and time resolution, and its ability to provide localized spatial resolution. The other advantages include:

(i) The ability to measure the thermal excitations at ambient conditions.

(ii) Investigation of SW response over a broad frequency range up from 2 GHz to 500 GHz with down to 30 MHz digital resolution.

(iii) Further, the magnetic properties of a FM, such as saturation magnetization, isotropic exchange constant, magnetic anisotropy, iDMI, effective damping, spin-mixing conductance, and interfacial parameters between two different magnetic materials can be obtained using BLS.

(iv) Investigation of SW dispersions with various absolute values and orientations of the corresponding wavevectors in all three possible applied magnetic field geometry.

3.3.1.1 Working principle:

In BLS spectroscopy, a highly monochromatic laser beam is incident on the sample surface. Most of the part of incident light undergoes either absorption or reflection. and only a small part of it scatters elastically as well as inelastically from the thermally excited SWs in the sample. In the case of elastic scattering (like Rayleigh scattering), the energy or frequency of the scattered photons remains unchanged while in inelastic scattering, the energy or frequency of the scattered beam is increased or decreased. This change in the frequency is attributed to the SWs frequency present in the sample. The backscattered light (180° from the incident light) is collected by the same lens which is used to focus the incident beam on the sample surface, within a solid angle. This geometry is well known as 180° backscattered geometry. It has a few advantages. (i) It can maximize the magnitude of SW wave vector involved in the 180° backscattered process and (ii) it can minimize the phonon contribution after isolation of scattered beam from the reflected beam. In addition, one 90° analyzer in the scattered beam path have used to block the rest of the phonon part and only magnon part is passed through it. The scattered light is frequency analyzed using a high resolution (3+3)-pass tandem Fabry-Perot interferometer (TFPI) to extract the nature of the surface and bulk magnons.

The process of inelastic scattering can be explained as a collision between a photon and a magnon from a quantum mechanical perspective. The mechanism is depicted in Fig. 3.8(a)-(b). The conservation laws of energy (frequency) and momentum (wave vector) are followed during the interaction between the magnon and the incident (i) and scattered (s) photons. The following equations represent the conservation laws:

$$\omega_S = \omega_i \pm \omega$$

$$k_s = k_i \pm k \tag{3.5}$$

where '+' ('-') sign represents for the anti-Stokes (Stokes) shift and ω_i, ω_s and k_i, k_s are the respective angular frequencies and wave vectors of the incident and scattered light. Here, the perpendicular

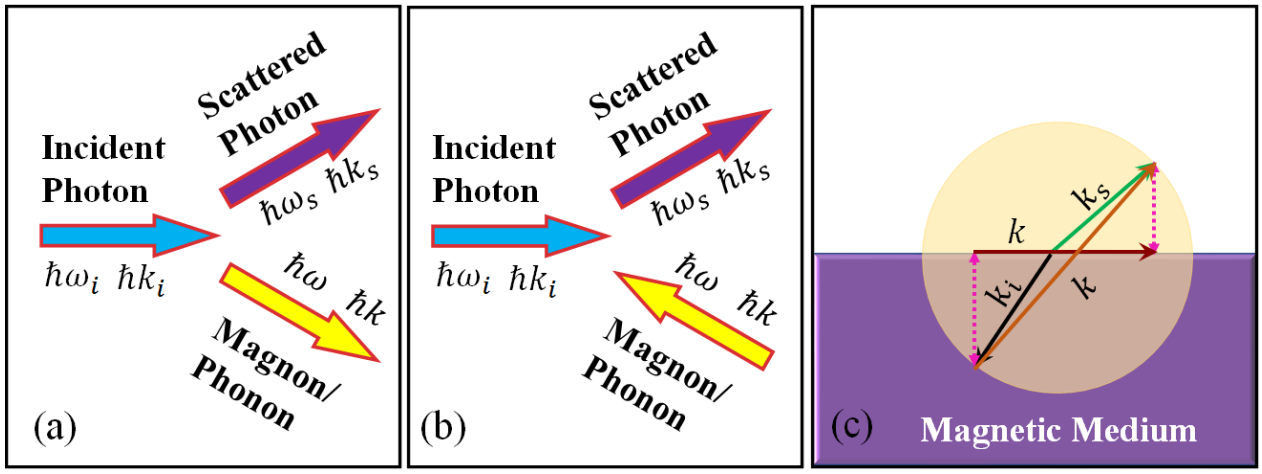

Figure 3.8: Schematic of the (a) creation (stokes) and (b) annihilation (anti Stokes) scattering processes. (c) Schematic of the scattering of incident laser beam by surface and bulk magnons.

component of the wave is not conserved for light scattering from thin films due to translational symmetry breaking. The equations mentioned above are applicable only to the wave vector component k that is parallel to the plane of the film. In the case of BLS, the energy of a magnon is ~ 10^{-4} eV, which is much smaller than the energy of a visible photon (a few eV). Thus, the amount of energy exchanged between the system and the incident light during the scattering (i.e., the magnon energy) is very small compared to the incident photon energy. Therefore, the scattered photon's wave vector (k_s) should be very similar to the wave vector k_i of the incident photon. In Fig. 3.8(c), the scattering pattern of a bulk magnon by a photon is depicted, where the magnon has a component perpendicular to the surface. The scattered photon's wave vector (k_s) is constrained to lie on a dashed circle of radius equal to the incident photon's wave vector (k_i). The cone represents the scattered beam's collection angle in the BLS experiment, with its central axis aligned with the incident photon's wave vector. For the backscattered geometry (k_s = - k_i), the wave vector magnitude of the emitted or absorbed bulk magnon |k| is always twice the magnitude of the incident photon wave vector (2|k_i|).

On the other hand, in the case of the scattering of a photon by a surface magnon, the direction of *k* lies only on the sample surface and the momentum will be conserved only on the plane of the sample surface as shown in Fig. 3.8(c). Therefore, the wave vector of the magnon being probed in the experiment can be written as:

$$\left|\vec{k}\right| = \left|\left(\overrightarrow{k_i} - \overrightarrow{k_s}\right) sin\,\theta\right| = 2\left|\overrightarrow{k_i}\right| sin\,\theta \tag{3.6}$$

Bragg's condition, which is expressed in Eq. 3.6, is a useful approximation for many light scattering experiments. By adjusting either the wavelength λ or the angle θ, the magnitude of *k* can be changed accordingly.

3.3.1.2 Calculation of the uncertainty to select the SW wave vector:

The SW wave vector selection is subject to uncertainty due to the finite aperture angle of the objective lens used for both focusing and collecting light from the sample. For a finite value of θ, the spread in *k* can be written as:

$$\Delta k = 2k_i\, cos\,\theta\, sin\frac{\phi}{2} = 4\frac{\pi}{\lambda} NA \cos\theta \tag{3.7}$$

where ϕ is the collecting angle of lens and NA is the numerical aperture defined by $sin\frac{\phi}{2}$. To minimize the uncertainty caused by the focusing of the incident beam, a narrow beam with a width of approximately 50 μm is used in our experiment, which increases the size of the focused spot.

3.3.1.3 Polarization of scattered beam:

To understand the scattering of light from the SWs, we have to understand the magneto-optic interaction between incident photon and magnon. The presence of precessing magnetization or SW in a medium can cause a spatially periodic fluctuation in the polarizability, due to the Lorentz force experienced by oscillating electric dipoles. This results in the emission of the scattered electromagnetic wave, whose electric field vector is perpendicular to that of incident wave. In the linear response regime, a magnetic material responds to the presence of an external optical electric field by developing an electric polarization, ***P***, which is proportional to the electric field, ***E***. The relation between ***P*** and ***E*** in this linear response regime [264] can be written as

$$4\pi\vec{\boldsymbol{P}} = (\epsilon_{11} - 1)\vec{\boldsymbol{E}} + \frac{K}{M_s}\left(\vec{\boldsymbol{E}} \times \vec{\boldsymbol{m}}\right) \tag{3.8}$$

with the frequency-dependent complex coefficients ϵ_{11} (dielectric constant) and K (magneto-optic coefficient), which depends on the actual details of the band structure. This process is illustrated in Fig. 3.9(a) for p-polarized incident light (polarization parallel to the plane of incidence) in DE geometry (the propagation of SW is perpendicular to the magnetization direction). When a monochromatic laser

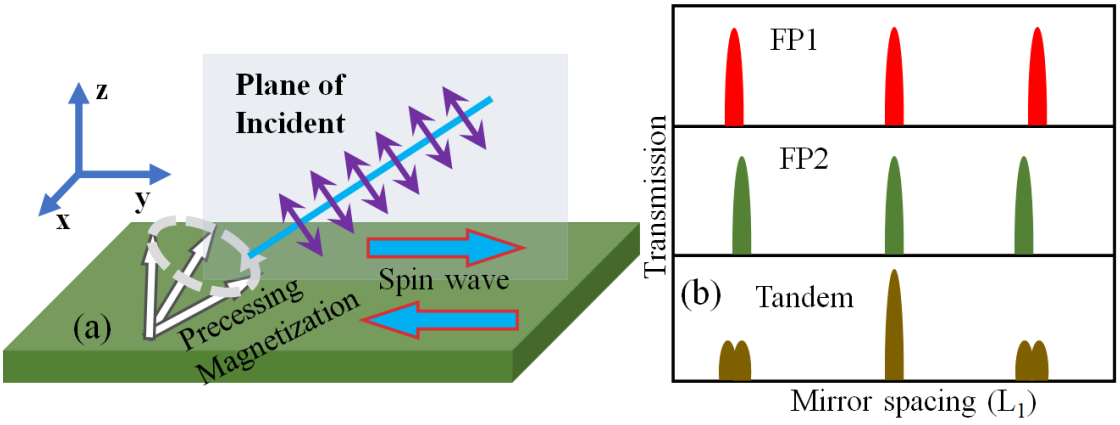

Figure 3.9: (a) Schematic illustration of the interaction between p-polarized incident beam and precessing magnetization. (b) Transmission Spectra of FP1 and FP2 and in tandem operation.

beam is incident on the ferromagnetic sample, its electric dipoles start to oscillate mainly due to its oscillatory electric field given as $\vec{\boldsymbol{E}} = E_x\hat{\imath} + E_y\hat{\jmath}$. Considering the dynamic component of $\boldsymbol{M}$ i.e., $\boldsymbol{m}$, $\boldsymbol{M}$ can be expressed as $\boldsymbol{M}$=$\boldsymbol{M_0}$+$\boldsymbol{m}$, where $\boldsymbol{m} = m_x\hat{\imath} + m_y\hat{\jmath}$. Now from eq. 3.8, the $\boldsymbol{m}$ exerts a Lorentz force (proportional to $(\vec{\boldsymbol{E}} \times \vec{\boldsymbol{m}})$) on the electric dipoles. As a result, the direction of polarization of scattered beam for p-polarized incident beam is pointing in the $\hat{k}$ i.e., s-polarized scattered beam. The same reasoning applies to the incident light with s-polarization, indicating that the scattered light will be p-polarized. Therefore, the scattered light by a magnon is always polarized perpendicular to the polarization of the incident light. Whereas when light is scattered by acoustic phonons, no change in polarizations of the incident and scattered beam is observed. Therefore, by choosing an appropriate orientation of the analyzing polarizer, we have eliminated the phonons part of backscattered ray in the experiment [264].

3.3.1.4 Experimental setup:

In general, BLS measurement is performed in two different geometries:

(i) Forward scattering geometry: Here the scattered light is collected after transmission of the probing beam through a transparent sample.

(ii) Back scattering geometry: Here the 180° backscattered light is collected from the surface of opaque sample. To the extension of this geometry, the concept of BLS microscopy (micro-BLS) can also be employed to map the profile of SW in a space-, time- and phase-resolved manner. However, this thesis will only focus to discuss the details of the conventional backscattered geometry.

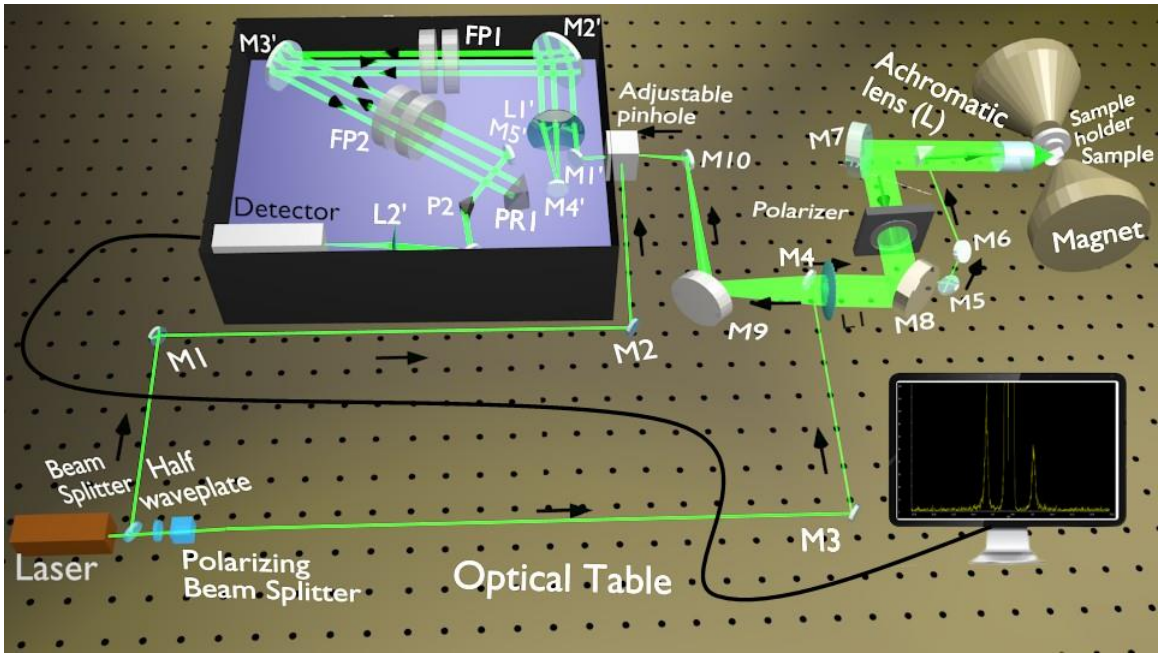

Figure 3.10: Schematic diagram of the BLS system present in our laboratory at S.N. Bose national centre for Basic Sciences.

The schematic of the conventional BLS set-up is shown in Fig. 3.10. The experimental assembly of BLS consists of many important components such as single mode continuous solid-state laser (green laser, $\lambda = 532$ nm), beam splitter (BS), half-wave plate (HWP), polarizing beam splitter (PBS), mirrors (M), achromatic doublet (Ach), electromagnet, polarizer (P), focusing lens (L), tandem Fabry-Pérot interferometer (TFPI) together with single photon detector (D), and a computer equipped with multi-channel analyzer software (GHOST or TFPDAS4.2).

A laser beam of power 230 mW and wavelength 532 nm is split into two parts (1:9) using a beam splitter (BS). The 10% is used as a reference beam that goes directly towards the TFPI using mirrors M1 and M2. The purpose of this reference beam is manifold:

(i) it helps to stabilize the mirror spacing of the FP etalons;

(ii) it forms the central elastic peak in a BLS spectrum to measure the frequency shift of the scattered beam w.r.t. the incident one.

(iii) for estimation of the transmission order of the (FP) etalon which is required to find out the frequencies of SW present in scattered beam.

In order to eliminate any small in-plane polarized component from the other part (90%) of partially polarized beam of the laser, the beam is first sent through HWP and PBS. Now the beam is perpendicularly polarized to the optical table and is then guided by the mirrors M3, M4, M5, M6 and Pr towards the sample. The sample is lying between the poles of an electromagnet at the focal length of the achromatic doublet (Ach) lens. To minimize the obstruction of the backscattered beam, a tiny prism mirror is used as the mirror Pr. The sample is mounted on a rotation stage that allows it to be rotated in the vertical plane to adjust the angle of incidence and select different transferred SW wave vectors according to Eq. 3.6. The measurements are conducted under a perpendicular magnetic field to *k*, in the DE geometry. The scattered beam is then collected by the same Achromatic lens (Ach) and directed through crossed analyzer (P), which filters out the elastically scattered beam and the signal from phonons. Next, the magnon signal is focused by a lens (L1) and directed towards the entrance pinhole of a (3+3)-pass tandem FPI for frequency analysis. Inside the tandem FPI, the beam encounters mirror M1' and is directed towards FP1 via lens L1' and mirror M2'. Once the beam passes through FP1, it undergoes the first pass (beam 1) until it gets reflected by the mirror M3' (beam 2) and eventually passes through FP2. The beam is then reflected from PR1 and retraces its path via FP2 (beam 3) and FP1 (beam 4) before reaching mirror M4'. The beam is again reflected at M4' and passes through FP1 and FP2 for the third time (beam 5 and beam 6 respectively) before arriving at the single-photon counter (D) for detection. The reason for the multi-pass arrangement is to increase the contrast of the inelastically scattered light. Finally, the beam enters into the detector which is a single photon counter and the data is stored in the computer for further analysis.

3.3.1.5. Instrumentation:

Here, we will present some details of the important components of the conventional BLS system.

3.3.1.5.1 Solid state laser:

A very narrow bandwidth and very precise single-mode solid state continuous wave (CW) laser is used in our BLS setup. The output power of the ‘Excelsior’ laser is 230 mW (300 mW during installation) and the wavelength is 532 nm (green laser). The laser system consists of the laser head, and a separate controller unit, which directly plugs into the electrical power. Here a diode laser is used to pump the

Nd^{3+} ions doped in the crystal of yttrium vanadate (Nd: YVO_4). The 1064 nm wavelength emitted photons of Nd:YVO_4 is further sent through a nonlinear crystal of lithium triborate (LBO) for frequency doubling (wavelength 532 nm) and this visible light is the finally emitted beam from the laser head. The laser beam that is emitted has a diameter of approximately 670 μm and a beam divergence of around 1.03 mrad. Overall, the laser system is extremely steady and reliable at room temperature in terms of output power and beam pointing.

3.3.1.5.2 Tandem Fabry-Pérot interferometer:

The basic working principle of BLS is similar to that of the Raman scattering. Frequency shift in case Raman scattering effect is in the THz region whereas BLS frequency shift is around GHz region. In BLS, achieving high spectral resolution for frequency analysis of SWs is a crucial challenge, as the inelastic scattering of photons has a small cross-section compared to the elastic scattering. To ensure efficient detection of the fractional amount of incident laser power with a high signal-to-noise ratio, high contrast is necessary. To address these issues, a (3+3) pass Tandem Fabry-Pérot Interferometer (TPFI) is utilized in the BLS setup. The TPFI consists of two single FPIs connected in series, where the light passes through each FPI three times, as illustrated in Fig. 3.10. Initially, we will provide a brief overview of the transmission characteristics of a single FPI. After that, we will describe the realization and operation of the tandem mode.

Fabry-Pérot interferometer:

The FPI uses the phenomenon of multiple beam interference that arises when light hits through a cavity (length: L) mounded with two partially reflective parallel mirrors. Each time the light encounters one of the surfaces, a portion of it is transmitted out, and the remaining part is reflected back. The net effect is to break a single beam into multiple beams which interfere with each other. The condition for constructive interference under normal incidence is given by:

$$L = \frac{n\lambda}{2} \qquad (3.9)$$

where n = 1, 2, 3, 4, … refers to the transmission order and λ is the wavelength of the light. The free spectral range (FSR) Δf (difference between the frequencies of the consecutive orders) can be written as:

$$\Delta f = \frac{c}{2L} = \frac{150}{L}\ \text{GHz.mm}^{-1} \qquad (3.10)$$

Here c is the velocity of light. The 'finesse' of the cavity is related to FSR, as given by:

$$F = \frac{\Delta f}{\Delta f_{FWHM}} \tag{3.11}$$

where Δf_{FWHM} denotes the full-width half maximum of the transmission curve. The resultant transmitted intensity (I_t) is:

$$I_t = \frac{I_0}{1+\left(\frac{2F}{\pi}\right)^2 sin^2\frac{2\pi L}{\lambda}} \tag{3.12}$$

where I_0 represents the intensity of the incident light. The equation mentioned above is referred to as the Airy function, which establishes a connection between the frequency, mirror spacing, and periodicity of the transmitted intensity. The coefficient of finesse (F) is a quantitative parameter which measures the sharpness of interferences and instrument quality. The relationship between F and reflectivity R of the Fabry-Pérot etalons is given by:

$$F = \frac{\pi\sqrt{R}}{(1-R)} \tag{3.13}$$

According to Eq. 3.13, increasing the reflectivity of a Fabry-Pérot interferometer (FPI) can improve its finesse, resulting in higher frequency resolution as Δf_{FWHM} decreases. Conversely, increasing the length of the FPI while keeping the R constant can reduce the free spectral range (FSR) and also improve frequency resolution by maintaining the finesse at a constant value. The contrast of an FPI is defined as

$$C = 1 + \frac{4R}{(1-R)^2} \tag{3.14}$$

The contrast indicates that more is the number of reflections inside the cavity, the sharper is the interference maximum. The degree of contrast in an interferometer with n passes is equal to the contrast of a single-pass interferometer raised to the power of n.

Tandem operation:

Since the transmitted intensity is a function of the mirror spacing it is periodic for multiple passes. This should create periodic FSR and becomes a major concern for the FPI. For instance, if we consider a fixed mirror spacing L and the presence of two wavelengths say λ_1 and λ_2 then

$$2L = m_1\lambda_1 = m_2\lambda_2 \tag{3.15}$$

When two wavelengths are transmitted through a FPI, they can be in different orders. However, since the order of the second wavelength cannot be determined from the reference beam, it remains unidentifiable. Now it can be challenging to determine whether a peak signal corresponds to the Stokes side of a particular transmission order or the anti-Stokes signal of the preceding order. Therefore, it becomes a challenge to accurately distinguish between the signals. In order to solve the issues with identifying the peak signals and accessing the transmission order of wavelengths, a tandem principle is employed. This involves passing the light through two interferometers consecutively, which are mounted at an angle α. This arrangement was developed by Dr. J. R. Sandercock in 1971 and is depicted in Fig. 3.10. The both FPIs each consist of two mirrors, one of which is mounted on a translation stage and the other on an angular orientation device. The translation stage allows for movement of the right mirror of each pair along the optical axis of FP1. A displacement *d* of the translation stage leads to a change of the mirror distance in FP1 by $\Delta L_1 = d$, while the change for FP2 is given by:

$$\Delta L_2 = \Delta L_1 cos(\alpha) \tag{3.16}$$

and corresponding synchronization condition is given as:

$$\frac{\delta L_2}{\delta L_1} = \frac{\Delta L_2}{\Delta L_1} \tag{3.17}$$

Now it can suppress the intermixing of different orders and the process is to adjust the transmission of each FPI separately before the scanning of the linear stage. Despite of having different transmission orders of these two FPIs, they together provide a central transmission order, which can be adjusted by changing the mirror spacing of FP2 (See Fig. 3. 9(b)). At the same time, the other orders are suppressed because of different FSR of the two FPIs. In this operation, we can also increase FSR of final spectrum without affecting the resolution. Now when we move the stage of TFPI, the mirror spacing of FP1 and FP2 are also changed by

$$l_1 = (L_{10} + d) \tag{3.18}$$

$$l_2 = (L_{10} + d)\cos\alpha \tag{3.19}$$

respectively, where L_{10} is the initial mirror spacings of FP1, at d = 0. The (3+3) passes through the FPIs in the tandem arrangement eliminate the ambiguities in the transmission order and enhance contrast by passing the light three times. The light is then directed to a photomultiplier to count

transmitted photons as a function of mirror spacing and frequency shift. The scanning stage sweeps the distance corresponding to the desired frequency window, and the data is recorded for a long time to obtain sufficient statistics. The resulting BLS intensity is proportional to the spin wave intensity at a particular frequency. The TFP alignment steps are described in detail in its manual [265,266].

3.3.2 Time-resolved Magneto-optical Kerr Effect (TR-MOKE) Magnetometry:

This set-up is based on an optical pump-probe measurement, where the s-polarized fundamental output having λ = 800 nm, pulse-width = 35 fs, and repetition rate = 1 kHz from an amplified femtosecond laser (LIBRA, Coherent) is used as the probe beam and its second harmonic having λ = 400 nm, pulse-width of > 35 fs and repetition rate = 1 kHz is used as the pump beam. A mechanical chopper of frequency 373 Hz is used to modulate the pump laser while the Kerr rotation and total reflectivity of the reflected probe beam from the sample is measured using lock-in amplifiers at the reference frequency (373 Hz) in a phase-sensitive manner. The probe path is continuously varied using a motorized delay stage fitted with a retro-reflector to introduce a variable time delay between the pump and the probe beam. The temporal resolution of the measurement is limited by the cross-correlation between the pump and probe pulses (~ 100 fs). The probe beam is focused to a spot size of ~100 μm and normally incident on the sample, whereas pump beam has a larger spot size of ~300 μm, which is obliquely (approximate angle of incidence = 25°) incident on the sample maintaining a spatial overlap with the probe spot under a bias magnetic field (H) whose strength and orientation can be varied during the measurement. The Kerr rotation and the reflectivity are measured separately and simultaneously using a polarized beam splitter and two silicon photodiodes. This setup is used to study the ultrafast demagnetization, relaxation and damped precessional dynamics of magnetic samples. The method to generate an amplified femtosecond laser pulse is extremely sophisticated and complicated. The entire amplifier (Libra) system from Coherent consists of the following units: ultrafast oscillator (Vitesse), diode-pumped solid-state pump laser (DPSS, Evolution), stretcher and compressor grating arrangements, regenerative cavity, synchronized delay generator etc. In the following subsections, we will discuss those units briefly.

3.3.2.1 Working principle of libra:

The physical phenomena that are associated with the regenerative amplification of femtosecond laser within Libra [267] are described briefly in the following section:

(i) Chirped pulse amplification (CPA): It is a technique for amplifying the ultrashort laser pulse to extremely high pulse energy with the laser pulse being stretched out temporally and spectrally before amplification. CPA can minimize the unwanted self-focusing loss within a very short path length of this highly intense laser beam. Before this amplification, a weak and short-duration pulse is generated and the peak power is reduced significantly after stretching. Next, the pulse is amplified without any self-focusing. Finally, the amplified pulse is compressed to its original pulse duration. Libra employs CPA to stretch a weak pulse by 10,000 times with the help of a grating and amplifies by a factor of 10^6 by using Ti:sapphire crystal.

(ii) Pulse stretching and compressing – Pulse stretchers and compressors are devices that can delay certain frequencies relative to others by sending different frequencies in different directions. These devices are mainly diffraction gratings that can elongate a short laser pulse into a longer one and vice versa. Inside the stretcher optical components, the higher frequency blue light travels a longer maximum optical path and introduces longest time delay whereas the lower frequency red light travels a longer minimum optical path and introduces shortest time delay. As a result, the optical pulse gets stretched due to positive group velocity dispersion (GVD) and the output pulse is known as a positively chirped pulse. Pulse compression follows the reverse mechanism of pulse stretching. Here, the bluer frequencies tend to travel a shorter optical path in comparison to the redder frequencies resulting in a negative GVD. In this case, the output pulse is called a negatively chirped pulse. Although after passing through the stretcher the laser pulse gets stretched temporally, after compression, it returns to its initial temporal width again.

(iii) Regenerative amplification (RGA) – For a Ti:sapphire crystal absorption spectra locate around 400-450 and 268 nm depend on the square of the Ti3+ doping level, suggesting an origin from pairs of Ti^{3+} ions. However, most of this range covers the short wavelength side of the fluorescence spectrum. Thus, the actual range of lasing becomes limited to only the IR range. This crystal has large gain bandwidth, which is exploited for pulse amplification. In the RGA cavity of Libra, Ti:sapphire crystal rod is used to amplify a single nJ pulse (selected from the mode-locked train of seed laser emitted from Vitesse) to mJ pulse. However, the amount of amplification for a single pass within the crystal is very small. Here, RGA cavity offers a multi-pass movement inside the seed laser so that sufficiently high overall gain can be achieved.

3.3.2.2 Optimization of the amplified pulse:

Efficient amplification depends mainly on three factors i.e., precise coordination of timing of seed source, amplifier pump source and amplifier PCs. The synchronization and delay generator (SDG Elite) [268] supplies digital control of the timing signal and essential voltages to operate the RGA cavity. The seed laser and pump laser are the input to operate SDG Elite, and it supplies a trigger signal for each PC at an adjustable delay. Additional delay signals can also be adjustable for other experiments as per user's requirement. All delays can operate at the pump laser frequency or an integral divisor. The system includes a Gate input which is addressable to each channel individually. Except the timing between the stimuli, bandwidth of the seed laser is an extremely important parameter to monitor. Seeding the RGA cavity and the beam having insufficient bandwidth may cause permanent optical damage. A pair of photodiodes located in the stretcher compartment is used as indicators of the range of bandwidth of the seed laser. SDG monitors these parameters and shows an error message once any fault occurs. After efficient generation of amplified pulse, the pulse width of the beam can be optimized by the user externally. A fine-tuning of the compressor delay stage, containing mirrors (CM2-3), can also be performed by remote control. The pulse width can also be tuned manually by the angle of both gratings.

3.3.2.3 Second harmonic generator:

The second harmonic generator (SHG) is a nonlinear optical medium where two laser pulses of same frequency interact with a nonlinear material and generate a new combined laser pulse of frequency twice that of the initial frequency. In our experimental setup, SHG (Model: Harmonic, HGS-T) is used to generate the pump beam of wavelength 400 nm [269]. This model can also generate the third harmonic with wavelength in deep UV regime, from the fundamental beam. The basic operational principle of SHG depends on the second-order susceptibility tensor of a dielectric material. Since the refractive index and polarization are also function of susceptibility of dielectric materials, so, they can also have both linear and higher-order nonlinear electric field terms. When dipoles of a non-centrosymmetric crystal are placed under an oscillating electric field of frequency ω, then its output radiation contains both fundamental frequency ω and its second-harmonic frequency 2ω. The second-harmonic output power can be expressed as:

$$P \propto \frac{l^2 P_\omega^2 \eta^2 \phi}{A} \tag{3.20}$$

Where, l is the length of the non-linear crystal, P_ω is the input power, η is the non-linear coefficient, ϕ is the phase-matching coefficient and A is the beam spot-size. To increase the output power of the second-harmonic beam, the beam spot size is decreased and collimated by using pair of lenses. The collimated beam is then tightly focused on the non-linear SHG crystal (which is Barium Beta-borate (BBO) in our case) which generates a horizontally-polarized frequency-doubled beam and a vertically-polarized residual of the fundamental beam. These two beams are isolated by a prism which diffracts the second-harmonic beam onto another pair of prisms. This type of optical arrangement has three purposes: (i) the second-harmonic beam becomes parallel to the fundamental beam, (ii) the output beam maintains a fixed direction independent of the crystal orientation, and (iii) the ellipticity induced in the second-harmonic beam is compensated. In the end, both the fundamental and second-harmonic beams exit parallelly through two different output ports. To minimize the temporal broadening due to GVD, a very thin BBO crystal is used.

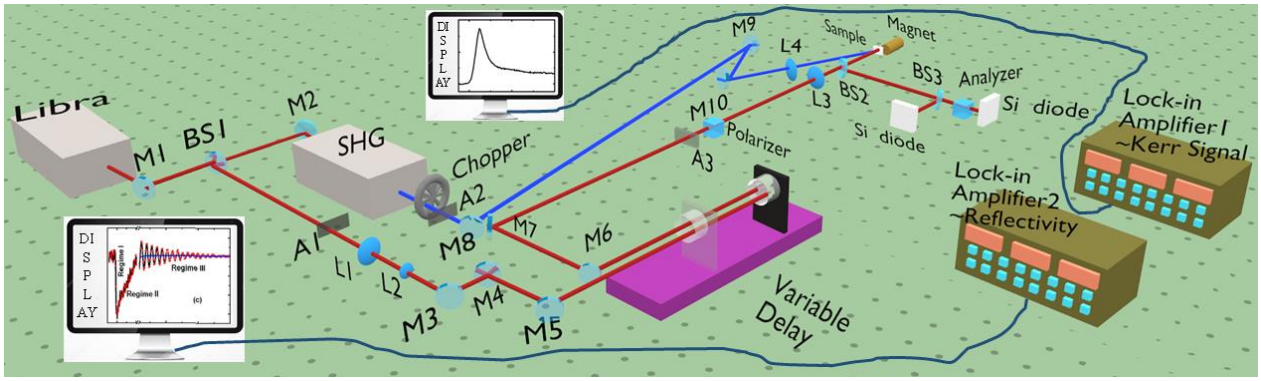

Figure 3.11: Schematic diagram of the non-collinear TR-MOKE system present in our laboratory at the S. N. Bose National Centre for Basic Sciences, Kolkata.

3.3.2.4 Description of the TR-MOKE set-up in noncollinear geometry:

The vertically-polarized (s-polarized) output beam from the Libra amplifier laser having wavelength of 800 nm is split into two parts using a beam splitter. One part of this fundamental beam is transmitted through the SHG for frequency doubling and the 400 nm (frequency-doubled output beam) output beam from SHG is used as the pump beam and incident obliquely onto the sample plane. The other fundamental part is attenuated to a very low power beam and is used as the probe beam. This beam is collimated by using a pair of plano-convex lenses of 10 and 15 cm focal length to also reduce diameter of the beam. This collimated beam is transmitted through a motorized variable delay stage (from

Newport, Model: ESP301-1N) with a retro-reflector (Model: M-IMS500PP) for the introduction of a variable time delay up to maximum of 2 ns. The output beam from the retro-reflector is guided by different optics toward the sample and incident normally onto the sample surface after passing through a plano-convex lens. A Glan-Thompson polarizer (Thorlabs, Model: GTH5M) with a 100000:1 extinction ratio, is used in the probe beam path for the high degree of polarization. A few variable attenuators are placed in the pump and probe paths for power adjustment. The sample is placed on a holder which is connected to an x-y-z translational stage. The spot size of the pump and probe beam is about 300 and 150 μm, respectively. The probe beam is placed at the centre of the pump beam to avoid probing any non-uniform exciting part of the sample. Both pump and probe beams are kept slightly defocused on the sample to avoid any damage to the samples. The reflected pump beam is blocked while the back reflected probe beam is split into two parts by using a beam splitter. One part is directly sent to a silicon photodetector to measure the total reflectivity of the sample. The other part passes through a Glan-Thompson polarizer (used as an analyzer) and is sent to another silicon photodetector to measure the Kerr rotation. The analyzer is kept near the extinction angle so that it mainly passes the Kerr rotated probe beam with a minimal reflectivity background. The output of both silicon photodetectors is measured by two different lock-in amplifiers (Stanford Research System, Model: SR830). The external magnetic field is applied by using a permanent bar magnet. The pump beam is periodically chopped (chopper frequency = 373 Hz) by an optical chopper (Thorlabs, Model: MC2000B with 10 slots chopper blade). This chopper also provides the reference to the lock-in amplifiers for phase-sensitive detection of both time-resolved reflectivity and Kerr rotation. The time-dependent dynamic data is collected by using a home-built LabView software. The humidity and temperature of the laboratory are maintained at around 30% and 22°C, respectively. A photograph and schematic diagram of the TR-MOKE set-up is shown in Fig. 3.11.

3.3.3 Broadband Ferromagnetic Resonance (FMR) Spectrometer:

The SW is excited by an RF current launched from the VNA. The dynamics of the magnetization can be studied as a function of the bias magnetic field strength and orientation as well as power of the microwave input signal. A coplanar waveguide (CPW) shorted at one end is employed to measure the real part of forward reflection coefficient (S_{11}) in reflection geometry. This technique provides a straightforward measurement of FMR over a broad frequency window [270]. The complete broadband VNA-FMR setup is shown in Fig. 3.12.

3.3.3.1 Experimental setup:

The broadband FMR experiments are performed using a home-built probe station and a VNA (Agilent, PNA-L N5230C) as schematically shown in Fig. 3.12 to study magnetization dynamics in FM samples. We have used an electromagnet which is powered by a high-voltage bipolar power supply (KEPCO, BOP 36-6D) to apply in-plane bias magnetic field to the samples. This power supply can deliver DC current of up to 6A and DC voltage of up to 36V. We have designed probe station in such a way that the azimuthal angle of the in-plane bias magnetic field can be rotated by up to 360° with 1° angular resolution. A CCD camera-based microscope (Shodensha Inc.) supported with illumination setup is used to view the top side sample surface. A multi-axis micro positioner (NPS, 800MRF-L) is used to make contact between microscale picoprobes and the CPW. A radio-frequency (rf) excitation is swept

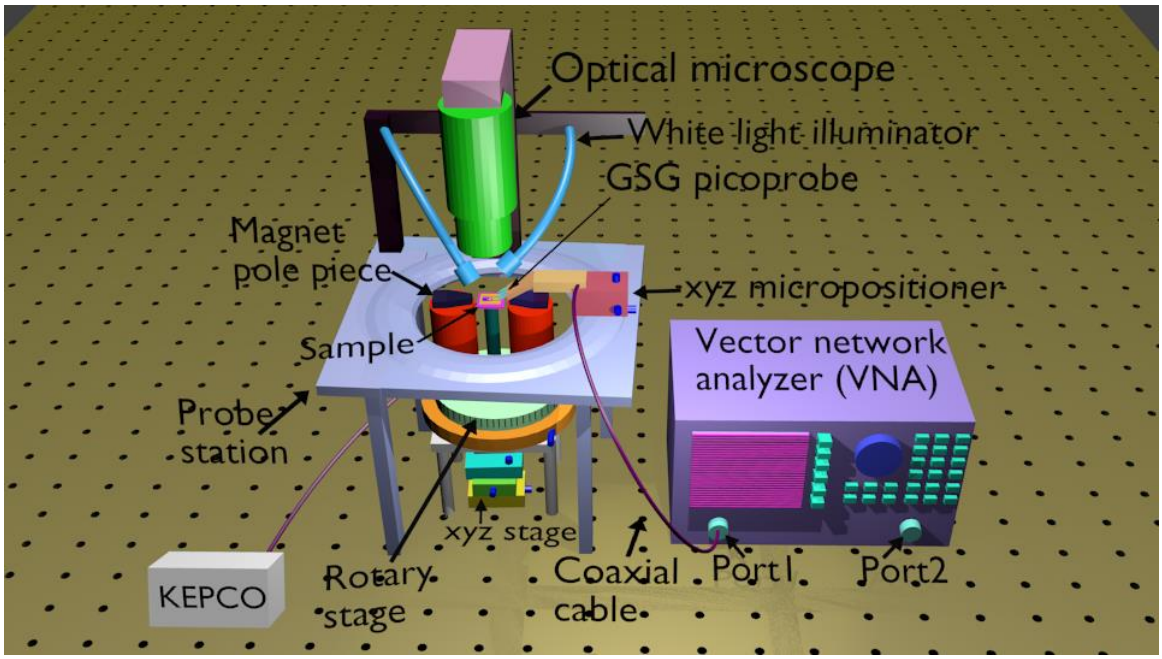

Figure 3.12: Schematic diagram of the broadband VNA-FMR system present in our laboratory at S.N. Bose national centre for Basic Sciences.

in the form of a microwave current (I_{rf}) in a broad frequency range (10 MHz to 50 GHz) with power varying between −15 dBm and +6 dBm by using a vector network analyzer (VNA), which is fed into a shorted CPW microstructure using a nonmagnetic ground-signal-ground (G-S-G) type probe (GGB industries, Bandwidth of 40 GHz, Model No. 40A-GSG-150-EDP) via an RF coaxial cable (Model No. N1501A-203). This microwave current generates a microwave magnetic field (h_{rf}) along the signal line. We have only used reflection geometry in this thesis as discussed in chapter 2. In reflection geometry, the short-circuited CPW is used to measure forward reflection coefficient (S_{11}) using a single

picoprobe. The power is absorbed by the magnetic specimen at various sweeping frequencies over the onward and return journey of the microwave signal flowing through the CPW. This generates the characteristic FMR spectrum of that ferromagnetic sample in reflection geometry. Again, to minimize the nonlinear background present in the spectrum, the characteristic FMR spectrum is subtracted from a reference signal measured at the highest bias magnetic field. However, sometimes nonmagnetic humps still appear in the FMR spectrum that does not show any bias magnetic field dependence. Finally, the real part of S_{11} parameters as a function of microwave power, bias field strength or orientation are extracted to study the FMR resonance spectra of ferromagnetic samples.

3.3.3.2 Calibration Procedure:

The fundamental reason behind the need for a systematic calibration of VNA is to extract more refined and accurate results free from unwanted and erroneous signals originating from any internal or external spurious noises [271,272]. In the VNA-FMR setup, the CS-5 calibration substrate from GGB industries has been employed as a standard kit. The typical components required to calibrate a microwave measurement system include open, short, load and through. The successive contacts are made between the probe and a set of gold pads patterned on the calibration substrate to perform the short-open-load (SOL) method of calibration in reflection measurements [273,274]. The electrical 'short' is executed by making contact between the picoprobe and shorting bar or offset 'short'. The electrical characteristics in short condition includes a very small inductance which is thought of as an equivalent electrical path in series connection with the perfect 'short' and that depends on the pitch (tip spacing) of the probe. The 'open' circuit helps to avoid the pick-up of fringing electric fields at the tip of the probe. The 'load' pad comprises of two 100 thin-film resistors in parallel to make well-defined 50 terminations to execute maximum transfer of power. Particularly in high-frequency regime, the 'load' can manifest as either a low shunt capacitance or a low series inductance depending upon the pitch value of the probe. Since the resistor pads and open pads are almost identical thus, load capacitance value is nearly same as the open capacitance. Similarly, the current path length in the 'load' condition and 'short' condition are almost identical. Since the inductance causes current to lag behind the voltage whereas current leads the voltage due to the effect of capacitance. These two opposing consequences tend to compensate each other, which makes 'load' almost purely resistive for some intermediary probe pitch. In very good calibration conditions, almost noiseless with six orders of amplitude signal is observed from the standard sample. The accuracy of this calibration process is solely limited by the standard kit and expert hand of calibration.

3.3.3.2.1 Spurious modes:

Spurious modes are unwanted extra modes in addition to the intended signals that can originate from harmonics, intermodulation, electromagnetic interference, or frequency conversion in an electrical system. Those modes can cause interference and degradation of the intended signals. During calibration, the calibration pads i.e., 'load' or 'open' or 'short' can absorb significant fraction of the signals from the adjacent pad to another and generate an anomaly in the output spectrum [275]. The through-lines are designed to propagate the balanced coplanar mode where the electric and magnetic fields are confined near the gap between the centre line and the ground planes. When the substrate is situated on a metallic holder, a small fraction of the signal can be dissipated through the metallic holder and can act as the ground plane. It can also create certain deviations in the calibration. An electrically insulated holder as a replacement for the metallic holder is required to avoid this situation. Some additional spurious modes may also be generated due to the nonlinear response of the DUT at very high frequencies.

3.3.3.3 Device measurement:

Another source of the spurious signal is the mismatch of the probing environments due to the difference between the device (sample) and standard calibration substrate. Generally, the base material for the device and the standard calibration substrate is different and more importantly, the dissimilarities of line width and spacing between them lead to a difference in the output signal. A post-measurement technique named "de-embedding" is usually used to remove the above-mentioned deviation and to extract information about the device under test after minimization of the errors. The basic idea is to make exactly similar structures on top of the calibration substrate as in the device to be tested (DTBT).

3.4 Numerical Techniques:

3.4.1 OOMMF:

This software was developed by M. J. Donahue and D. G. Porter at the National Institute of Standards and Technology (NIST) in 1999 [276]. Initially, it was an open-source CPU-based micromagnetic simulator. In 2016, a modified version of GPU-based OOMMF is introduced by Sidi Fu and Vitaliy Lomakin, UC San Diego. The core OOMMF code is written in C++ and Tcl/Tk and is used for portable user interfaces across a wide range of Unix, Windows, and Mac OS X platforms. It utilizes an ordinary differential equation solver to relax spins on a quasi-two-dimensional mesh of square cells. At the beginning of the simulation, all the required parameters such as anisotropy, applied field, saturation

magnetization, exchange stiffness constant, damping, gyromagnetic ratio, sample structure and dimensions are provided through an input file called 'MIF' file. The convergence criterion in the simulation is created by setting the stopping value of dm/dt or time, which is set in such a way that the maximum torque, m × H (where m = M/MS) goes well below 10^{-6} A/m at T = 0 K. One can also use periodic boundary condition in this package. A very small external perturbation in terms of the additional field is provided to simulate the magnetization dynamics in any system. The time-dependent components of magnetization, demagnetizing field and energies can be extracted in the output file with '.omf', '.ohf' or '.ovf' formats.

3.4.2 MuMax3:

Mumax3 is open-source software written in Go and CUDA, which requires high-performance graphics card [277]. It is available free of cost under the GPLv3 license on http://mumax.github.io. This nVIDIA GPU package was developed by the DyNaMat group of Prof. Van Waeyenberge at Ghent University for a Linux, Windows or Mac platform. The output is stored in form of '.ovf' data format and this file is also compatible with the postprocessing and viewing tools for OOMMF. The code is written in a text file in '.mx3' or '.go' format. To solve the LLG equation, MuMax3 uses Runge-Kutta methods (RK45, RK23, RK12 RK1) with different convergence criteria and error estimation. MuMax3 provides a relax function that attempts to find the systems' energy minimum. MuMax3 can also perform finite temperature employing a fluctuating thermal field $\vec{B}_{them}$ according to Brown:

$$\vec{B}_{them} = \vec{\eta}_{step}\sqrt{\frac{2\mu_0 k_B T\alpha}{B_{sat}\gamma_{LL}\Delta V\Delta t}} \qquad (3.21)$$

Where $\vec{\eta}_{step}$ is a random vector from a standard normal distribution whose value is changed after every time step. In this case, only Euler and Heun solvers are used in Mumax3 as they do not require torque continuity between steps.

3.4.3 LLG Micromagnetic Simulator:

M. R. Scheinfein is the designer and licensor of this commercial simulator [278]. In this simulator, the LLG equation is solved by FDM like in OOMMF. However, the LLG simulator has some extra features, which are not available in OOMMF. The temperature effect can be introduced here by providing an equivalent random magnetic field. Additionally, there is provision to trigger the

magnetization dynamics by spin-polarized current, which is an essential requirement for spin valve-like structures. Another important feature is that the magnetostatic interaction among magnetic nanoelements can be visualized better by coloured contour plots. Finally, in the LLG simulator, it is easier to control the input magnetic parameters in a multilayered nanostructure, as compared to that in OOMMF.

3.4.4 Plane Wave Method (PWM):

The PWM is a vastly used and simple method to calculate the band structure and excitation spectra in

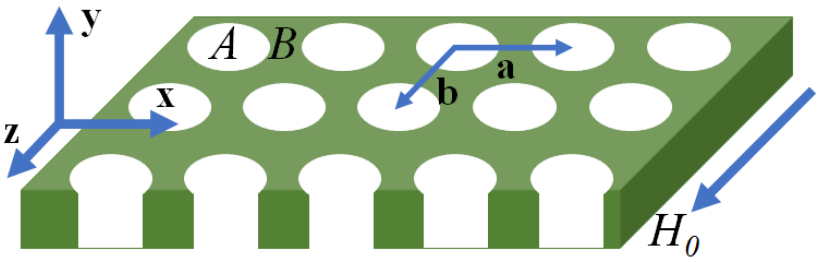

Figure 3.13: A rectangular MC formed by circular ferromagnetic elements A embedded in matrix B.

any shape of scattering centres and for various dimensions of the periodicity for any periodical lattice e.g., in electronic, phononic, photonic, or magnonic crystals [113,279-282]. In magnonic crystals (MCs), the inhomogeneity of the internal magnetic field is taken into consideration in the form of the superposition of plane waves, which eventually converts the LLG equation to an eigenvalue equation. The eigenvalues (SW frequencies) and eigenvectors (amplitude of the dynamical component of the magnetization vector) are obtained subsequently using standard numerical routines.

The MC structure under consideration comprises a periodic array of scattering centers made of ferromagnetic material A with finite thickness, embedded in an infinite matrix of ferromagnetic material B. The scattering centers are arranged in a square array with square cross-sections, as shown in Fig. 3.13. The coordinate system used has the x-axis perpendicular to the surface plane, and an external bias field H is applied in the sample plane along the z-axis. We solve the Landau–Lifshitz (LL) equation, i.e., the equation of motion of the magnetization vector $\boldsymbol{M}(r, t)$ in space and time, given by:

$$\frac{\partial \boldsymbol{M}(\boldsymbol{r},t)}{\partial t} = -\gamma\mu_0 \boldsymbol{M}(\boldsymbol{r},t) \times \boldsymbol{H}_{eff}(\boldsymbol{r},t) \quad (3.22)$$

Here, effective magnetic field ($\boldsymbol{H}_{eff}(\boldsymbol{r},t)$) is given by:

$$\boldsymbol{H}_{eff}(\boldsymbol{r},t) = \boldsymbol{H} + \boldsymbol{H}_{dem} + \boldsymbol{H}_{ex}, \quad (3.23)$$

where the total demagnetizing field ($\boldsymbol{H}_{dem}$) can be written as:

$$\boldsymbol{H}_{dem} = \boldsymbol{H}_d(\boldsymbol{r}) + \boldsymbol{h}_d(r)e^{i2\pi\nu t} \quad (3.24)$$

The quantities, namely the static and the dynamic components of the dipolar field are denoted as $\boldsymbol{H}_d(\boldsymbol{r})$ and $\boldsymbol{h}_d$ respectively, which satisfy the condition of magnetostatic Maxwell's equations. The exchange field ($\boldsymbol{H}_{ex}$) is given by $\boldsymbol{H}_{ex} = (\boldsymbol{\nabla}.\, l_{ex}^2(\boldsymbol{r})\boldsymbol{\nabla})m(\boldsymbol{r},t)$ [283]; where exchange length ($l_{ex}(\boldsymbol{r})$) = $\sqrt{\frac{2A(\boldsymbol{r})}{\mu_0 M_S^2(\boldsymbol{r})}}$. For simplicity, we neglect any contribution from the anisotropy field. In the linear approximation, the component of the magnetization vector parallel to H_0 is constant in time t, with larger amplitude than the dynamic perpendicular components i.e.,

$$\boldsymbol{M}(\boldsymbol{r},\, t) = M_s(\boldsymbol{r})\hat{\boldsymbol{z}} + \boldsymbol{m}(\boldsymbol{r},\, t) \quad (3.25)$$

with $|\boldsymbol{m}(\boldsymbol{r},t)| << M_z(\boldsymbol{r})$ and $M_z \sim M_s$.

So, the final form of H_{eff} can be written as:

$$\boldsymbol{H}_{eff}(\boldsymbol{r},t) = \boldsymbol{H} + \boldsymbol{H}_d(\boldsymbol{r}) + \boldsymbol{h}_d(\boldsymbol{r})e^{i2\pi\nu t} + (\boldsymbol{\nabla}.\, l_{ex}^2(\boldsymbol{r})\boldsymbol{\nabla})m(\boldsymbol{r},t) \quad (3.26)$$

The respective components of $\boldsymbol{M}(\boldsymbol{r},\, t)$ and $\boldsymbol{H}_{eff}(\boldsymbol{r},t)$ in different coordinate axes can be used to calculate the vector product on the right-hand side of Eq. 3.22, equating which with corresponding left-hand side renders the expressions for the dynamic magnetization components $m_x(r)$ and $m_y(r)$ as follows:

$$m_x(r) = \frac{\gamma\mu_0}{i\omega}\left(m_y(r)(H + H_{ms}) - \boldsymbol{M_s h_{d,y}} - \boldsymbol{M_s}\nabla.\, l_{ex}^2(\boldsymbol{r})\nabla m_y(r)\right) \quad (3.27)$$

$$m_y(r) = \frac{\gamma\mu_0}{i\omega}\left(-m_x(r)(H + H_{ms}) + \boldsymbol{M_s h_{d,x}} + \boldsymbol{M_s}\nabla.\, l_{ex}^2(\boldsymbol{r})\nabla m_y(r)\right) \quad (3.28)$$

In the next step, we use Bloch's theorem with lattice constant "a" to find the solution of the LL equation so that: $\boldsymbol{m}(\boldsymbol{r}) = \sum_G m_{\boldsymbol{k}}(\boldsymbol{G})e^{i(\boldsymbol{k}+\boldsymbol{G}).\boldsymbol{r}}$, where $\boldsymbol{G} = (G_x, G_z) = \frac{2\pi}{a}(n_x, n_z)$ and $\boldsymbol{k} = (k_x, k_z)$ are denoted the reciprocal lattice vector of the periodic structure and the wavevector in the first Brillouin zone (BZ)

respectively. The material parameters M_s, A and consequently l_{ex}^2 have the periodicity of the lattice constant, i.e.,

$M_s(\vec{r}+\vec{a})= M_s(\vec{r})$, $A(\vec{r}+\vec{a})=A(\vec{r})$ and $l_{ex}^2(\vec{r}+\vec{a})=l_{ex}^2(\vec{r})$ (3.29)

Next, the Fourier transformation of $\boldsymbol{M}_s(\boldsymbol{r})$ and $l_{ex}^2(\boldsymbol{r})$ to obtain the relevant quantities in reciprocal space using:

$$M_s(\boldsymbol{r}) = \sum_G M_s(\boldsymbol{G})\, e^{i\boldsymbol{G}.\boldsymbol{r}} \quad (3.30)$$

$$l_{ex}^2(\boldsymbol{r}) = \sum_G l_{ex}^2(\boldsymbol{G})\, e^{i\boldsymbol{G}.\boldsymbol{r}} \quad (3.31)$$

Here $$M_s(G) = \begin{cases} M_{S,A}t + M_{S,B}(1-n) & G = 0 \\ (M_{S,A} - M_{S,B})I(G) & G \neq 0 \end{cases} \quad (3.32)$$

where n is the filling fraction of magnetic material and $M_{S,A}$ and $M_{S,B}$ are saturation magnetization of two magnetic materials A and B, respectively. Finally, $I(G)$ is a function that is specific to the nanodot structure used in the calculation.

In general, the reciprocal lattice vector G can be calculated using the expression $\vec{G} = (m\vec{a}^* + n\vec{b}^*)$, where

$$\vec{a}^* = 2\pi \frac{\vec{b}\times\hat{n}}{|\vec{a}\times\vec{b}|} \quad (3.33)$$

$$\vec{b}^* = 2\pi \frac{\hat{n}\times\vec{a}}{|\vec{a}\times\vec{b}|} \quad (3.34)$$

m, n are integers, $\vec{a}\ (\vec{a}^*)\ and\ \vec{b}\ (\vec{b}^*)$ are the lattice vectors of real (reciprocal) lattice.

According to Ref. [284], for the considered structure, the magnetostatic fields can be expressed as:

$$H_{ms,z}(r_\parallel, x) = -\sum_G \frac{M_S(G)}{G^2} G_z^2 \times \left(1 - \cosh(|G|x)\, e^{-\frac{|G|d}{2}}\right) e^{iG.r_\parallel} \quad (3.35)$$

$$h_{ms,y}(r_\parallel, x) == -\sum_G \frac{m_x(G)}{|q+G|^2} (q_y + G_y)^2 \times \left(1 - \cosh(|(q+G)|x)\, e^{-\frac{|q+G|d}{2}}\right) e^{i(q+G).r_\parallel} \quad (3.36)$$

$$h_{ms,x}(r_{\parallel},x) == -\sum_G m_x(G)\times\cosh(|(q+G)|x)\,e^{-\frac{|q+G|d}{2}}e^{i(q+G).r_{\parallel}} \quad (3.37)$$

where d is the thickness of the slab. In the works presented in this thesis, the above expressions are calculated at $x=d/2$, i.e., at the surface of the film.

Eqs. 3.29 - 3.37 can be substituted into Eqs. 3.27 and 3.28 to obtain the dynamic magnetization components in the form of infinite system of equations in Fourier space:

$$\frac{i\omega}{\gamma\mu_0}m_{x,q}(\vec{G}) = Hm_{y,q}(\vec{G}) + \sum_{\vec{G}'}\frac{m_{y,q}(\vec{G})}{|q+\vec{G}'|^2}(q_y+\vec{G}'_y)^2\times\left(1-\cosh(|q+\vec{G}'|x)\,e^{-\frac{|q+\vec{G}'|d}{2}}\right)M_S(\vec{G}-\vec{G}') - \sum_{\vec{G}'}\frac{m_{y,q}(\vec{G})}{|\vec{G}-\vec{G}'|^2}(\vec{G}_z-\vec{G}'_z)^2\times\left(1-\cosh(|\vec{G}-\vec{G}'|x)\,e^{-\frac{|\vec{G}-\vec{G}'|d}{2}}\right)M_S(\vec{G}-\vec{G}') + \sum_{\vec{G}'}\sum_{\vec{G}''}(q+G').(q+G'')\,l_{ex}^2(G''-G')M_S(G-G'')m_{y,q}(\vec{G}) \quad (3.38)$$

$$\frac{i\omega}{\gamma\mu_0}m_{y,q}(\vec{G}) = -Hm_{x,q}(\vec{G}) - \sum_{\vec{G}'}m_{x,q}(\vec{G})\cosh(|q+\vec{G}'|x)\,M_S(\vec{G}-\vec{G}') - \sum_{\vec{G}'}\frac{m_{x,q}(\vec{G})}{|\vec{G}-\vec{G}'|^2}(\vec{G}_z-\vec{G}'_z)^2\times\left(1-\cosh(|\vec{G}-\vec{G}'|x)\,e^{-\frac{|\vec{G}-\vec{G}'|d}{2}}\right)M_S(\vec{G}-\vec{G}') + \sum_{\vec{G}'}\sum_{\vec{G}''}(q+G').(q+G'')\,l_{ex}^2(G''-G')M_S(G-G'')m_{x,q}(\vec{G}) \quad (3.39)$$

When a finite number N of reciprocal lattice vectors is considered, the above system of equations becomes finite. The problem then reduces to an eigenvalue problem with eigenvalues $\frac{i2\pi f}{\gamma\mu_0 H}$ and eigenvectors $m_{x,q}(\vec{G})$ and $m_{y,q}(\vec{G})$, which can be structured in a matrix form as follows:

$$\widehat{M}m_q = \frac{i2\pi f}{\gamma\mu_0 H}m_q \quad (3.40)$$

with the eigenvector defined as $m_q^T = [m_{x,q}(G_1)\ldots\ldots m_{x,q}(G_N), m_{y,q}(G_1)\ldots\ldots m_{y,q}(G_N)]$. The matrix $\widehat{M}$ is the following Block matrix

$$\widehat{M} = \begin{pmatrix}\widehat{M}^{xx} & \widehat{M}^{xy}\\ \widehat{M}^{yx} & \widehat{M}^{yy}\end{pmatrix} \quad (3.41)$$

The sub-matrices of $\widehat{M}$ are given by

$$\widehat{M}^{xx} = \widehat{M}^{yy} = 0 \tag{3.42}$$

$$\widehat{M}_{ij}^{xy} = \delta_{ij} + \sum_l \frac{(q+G_j).(q+G_l)}{H} l_{ex}^2 \left(G_l - G_j\right) M_S(G_i - G_l) + \frac{\left(q_y+G_{y,j}\right)^2}{H\left|q+G_j\right|^2}\Big(1 - C\big(q + G_{j,x}\big)\Big) M_S\big(G_i - G_j\big) - \frac{\left(G_{z,i}-G_{z,j}\right)^2}{H\left|G_i-G_j\right|^2} M_S\big(G_i - G_j\big)\Big(1 - C\big(G_i - G_j, x\big)\Big) \tag{3.43}$$

$$\widehat{M}_{ij}^{yx} = -\delta_{ij} - \sum_l \frac{(q+G_j).(q+G_l)}{H} l_{ex}^2 \left(G_l - G_j\right) M_S(G_i - G_l) + \frac{1}{H} C\big(q + G_{j,x}\big) M_S\big(G_i - G_j\big) - \frac{\left(G_{z,i}-G_{z,j}\right)^2}{H\left|G_i-G_j\right|^2} M_S\big(G_i - G_j\big)\Big(1 - C\big(G_i - G_j, x\big)\Big) \tag{3.44}$$

where reciprocal lattice vector indices i, j, and l are integers in the range <1, N>. The system of equations described above can be solved using numerical methods for various values of SW wavevector q to obtain the corresponding eigenvalues that give the SW frequency (f) and eigenvectors (m_q). In order to compare the calculated dispersion with the experimentally obtained band structure using BLS, the square of the modulus of the fundamental harmonics of magnetization needs to be determined, i.e.,

$$I_{BLS} = I_0\left|m_q(G=0)\right|^2 \tag{3.45}$$

Once the q and f have been determined, the spatial mode profiles can be calculated by determining the modulus of the dynamic magnetization ($\boldsymbol{m}_x(\boldsymbol{r})$ or $\boldsymbol{m}_y(\boldsymbol{r})$) at each spatial point. It is important to note that the PWM calculations assume that both the scattering centres and the matrix are composed of FMs. However, when dot or antidot arrays are being considered, where either the scattering centres or the matrix are made up of a NMs, a very small value should be assigned to the material parameters to prevent any unphysical solutions.

Chapter 4

4. Defect Density and Rashba Shift Induced Interfacial Dzyaloshinskii-Moriya Interaction and Spin Pumping in Single Layer Graphene/$Co_{20}Fe_{60}B_{20}$ Heterostructures: Implications for New Generation Spintronics

I. Introduction:

Spin-orbitronics aims to utilize the coupling between spin and orbital angular momentum and takes advantage of spin degree of freedom of electrons involving a wide range of interfacial phenomena[58]. These include interfacial perpendicular magnetic anisotropy (iPMA)[285], Rashba effect[286], spin pumping[36], spin Hall effect (SHE)[35] and interfacial Dzyaloshinskii-Moriya interaction (iDMI)[15,17] to name a few. However, most interfacial phenomena are associated with large spin-orbit coupling (SOC) and because SOC is proportional to Z^4 (Z: atomic number), heavy metals (HMs) are the natural choices for nonmagnetic (NM) layer[17,53,54,64]. Recently, two-materials such as graphene, MoS_2 and topological insulators have shown promises in engineering interface magnetism[18,20,54-57] . Graphene, a monolayer of carbon atoms, shows prolonged spin relaxation time (~ μs)[71] and long spin diffusion length (~ μm)[59,69,70] which lead to long-distance propagation of spin angular momentum through this material. In addition, graphene has many other interesting properties such as high electron mobility[287], massless linear electronic dispersion[59], low resistivity[288], gate controllable spin transport in spin-valve device[289], weak hyperfine interaction[290] etc., that promote graphene as an attractive material for new generation nanoscale and energy-efficient spintronics. Graphene has low intrinsic SOC but its SOC is sensitive to defects, which can be controlled through processes like proximity to ferromagnet (FM)[72,289,291], absorption[74,292], intercalation[75,79,293], fluorination[76,294], hybridization[73,295,296] etc. The SOC of graphene gives rise to non-zero effective mass of electrons and induces a bandgap in its electronic dispersion[297,298]. A major modification of the band structure of graphene occurs when placed in proximity with a metallic layer because of the strong hybridization between the out-of-plane $2p_z$ orbital of the carbon atoms and the d_{z^2} states of a metallic layer and the ensuing sublattice-symmetry breaking[59]. This proximity effect leads to the observation of an anomalous Hall effect[72], enhancement of the Rashba SOC[18], defect induced iDMI[54], spin pumping[218], perpendicular magnetic anisotropy[57,79] etc. in graphene/metallic heterostructures.

The iDMI is an important interfacial phenomenon originated from broken inversion symmetry at the HM/FM interface and strong SOC of the HM. Several direct and indirect measurement techniques such as Brillouin light scattering (BLS)[17,54,55,63,64], magnetic domain wall velocity[16], asymmetric hysteresis loop method[299] etc. have been used to measure iDMI. Recently, graphene-induced enhancement of the iPMA and unusual iDMI have been reported at graphene/cobalt interface, which was explained in terms of a conduction electron mediated Rashba-DMI mechanism[20]. Additionally, they reported that graphene on top of cobalt can be used as an efficient protection from oxidation by air exposure[20]. Yang *et al.* reported a significantly large iDMI value in graphene/FM interface which is equivalent to many commonly used HM/FM interfaces, and Rashba SOC present at the graphene/FM interface was found to be responsible for this significant iDMI. However, iPMA and iDMI increased almost linearly with the number of graphene/FM junctions present in that system[18]. More recently, defect induced iDMI have been reported in 2D material/FM heterostructures, e.g. graphene/$Ni_{80}Fe_{20}$ (Py), MoS_2/Py systems, where the iDMI values have been found to vary significantly with Ar pressure during FM layer deposition[54,55], which actively controlled the defect and the ensuing extrinsic SOC at the interface. Despite of some theoretical and experimental works that attempted to explain the iDMI in terms of Rashba shift and defects present in such systems, a systematic experimental study to correlate iDMI with Rashba shift and defect density is missing in the literature.

Here, we have investigated iDMI in single layer graphene (SLG)/CoFeB(t_{CoFeB}) heterostructures using BLS spectroscopy which is a well-used and direct method of extracting iDMI[17,54,55,64]. CoFeB is an important ferromagnetic material for spintronics application because of its high spin polarization, low Gilbert damping parameter and low coercivity. We used four different CoFeB thicknesses in our experiment. An asymmetric SW dispersion was observed in the Damon-Eshbach (DE) geometry for all four SLG/CoFeB samples. The frequency shift between two propagation directions, i.e., along the $+k$ and $-k$ directions (k = wave-vector) increased linearly with k at an identical magnetic field. The extracted value of iDMI from this frequency shift is found to be independent of magnetic field and inversely proportional to t_{CoFeB}. We also observed an exponential growth of iDMI with defect density (n_D) and established an inverse relationship between Rashba shift and t_{CoFeB}. Furthermore, we extracted effective damping which increases linearly with t_{CoFeB} and exponentially with n_D in this system. We compared this variation with reference CoFeB thin films without SLG underlayer and found negligible damping modulation with t_{CoFeB} in the reference films. Our study leads to a comprehensive understanding of the SOC at the SLG/FM interface and the ensuing iDMI property, opening new

avenues for controlling nanoscale chiral spin-textures like skyrmions and application in graphene-based nanoscale spin-orbitronic devices.

II. Experimental and Theoretical Methods:

Sample Preparation: We used commercially obtained high-quality SLG (from *Graphenea inc.*), which was grown by chemical vapour deposition (CVD) onto a thermally oxidized silicon (001)/300-nm-thick silicon dioxide (Si/SiO_2) substrate. On top of it was deposited a $Co_{20}Fe_{60}B_{20}$ (CoFeB hereafter) layer with varying thickness (t_{CoFeB}) of 1.5, 3, 4 and 6 nm using dc magnetron sputtering at room temperature and 1.2 mTorr Ar pressure as shown schematically in Fig. 4.1(a). The average base pressure of the deposition chamber before deposition was 0.3 μTorr. A dc voltage of 375 V was used for the deposition and a deposition rate of 0.2 Å/s was maintained. A 2-nm-thick SiO_2 protective layer was subsequently deposited on top of the CoFeB layer using rf sputtering (base pressure = 0.3 μTorr, Ar pressure = 1.4 mTorr, deposition rate = 0.3 Å/S, rf power = 60 W) to protect the sample from degradation (Fig. 4.3(a)). The deposition parameters were thoroughly optimized and retained nearly identical for all the samples. The nominal thicknesses of the CoFeB and SiO_2 layers were monitored by using a quartz crystal microbalance.

Characterization Methods: The surface topography of SLG/CoFeB and CoFeB thin films were determined by atomic force microscopy (AFM). The SLG and SLG/CoFeB thin films were characterized by micro-Raman experiment with an excitation laser frequency of 532 nm. The magnetic hysteresis loops were measured using vibrating sample magnetometer (VSM) at room temperature. The spin-wave (SW) dispersion relation (frequency vs. wavevector) of the samples were measured in the Damon-Eshbach (DE) geometry using BLS spectroscopy in the conventional back-scattered geometry[113]. The output of a single-mode continuous wave (CW) solid-state laser of wavelength λ = 532 nm and power of about 60 mW was made incident on the sample. The wavevector associated with the SW was calculated using the relation $k = 2k_{in}\sin\theta_{in} = \frac{4\pi}{\lambda}\sin\theta_{in}$, where θ_{in} is the incidence angle in the back-scattered geometry and k_{in} is the wavevector of the incident laser beam. We have varied k in the range $0 \leq k \leq 20.45$ rad/μm in our experiment to extract the asymmetry in the SW frequency (f) dispersion, i.e., f vs. k due to iDMI. The back-scattered light was collected by an achromatic lens and sent to a (3+3)-pass tandem Fabry-Pérot interferometer for detection of the Stokes and anti-Stokes inelastic spectra corresponding to the SW frequencies. In the DE geometry, the sample

magnetization (M) and *k* are mutually orthogonal and lie in the sample plane[227]. More details of the BLS measurements can be found elsewhere[53].

III. Results and Discussions:

Figure. 4.1(a) shows a schematic structure of graphene/CoFeB which the arrows schematically indicate clockwise and anticlockwise spin spiral chirality. The AFM images in Figs. 4.1(b)-(c) reveal the surface topography of SLG/CoFeB(t_{CoFeB}) bilayers with t_{CoFeB} = 1.5 and 6 nm. Figure 4.1(d) presents the

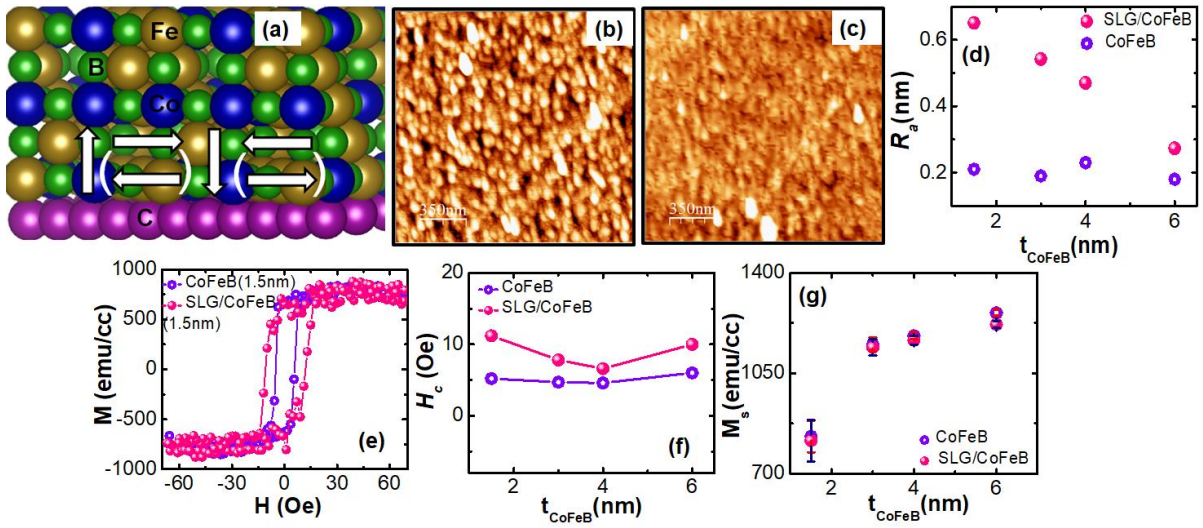

Figure 4.1: (a) Cartoon of SLG/CoFeB bilayer showing the magnetic vector chirality due to DMI from the SLG interface. (b)-(c) AFM image of the SLG/CoFeB (1.5 nm)/SiO_2 and SLG/CoFeB (6 nm)/SiO_2 samples. (d) Variation of average roughness (R_a) extracted from the AFM images as a function of CoFeB thickness. (e) Magnetic hysteresis loops for SLG/CoFeB (1.5 nm)/SiO_2 and CoFeB (1.5 nm)/SiO_2 samples. (f) Variation of coercive field (H_C) as a function of CoFeB thickness. (g) Variation of saturation magnetization (M_S) as a function of CoFeB thickness.

variation of average topographical roughness (R_a) of the samples with t_{CoFeB} in SLG/CoFeB in comparison to the reference CoFeB films with identical thicknesses but without SLG underlayer. The roughness remains nearly constant at around 0.2 nm with t_{CoFeB} in the reference CoFeB layers. However, the roughnesses of SLG/CoFeB bilayers are significantly larger than those of the reference CoFeB layers at lower values of t_{CoFeB} (e.g., R_a = 0.65 nm at t_{CoFeB} = 1.5 nm) but they decrease rapidly with the increase in t_{CoFeB} and reached a value of ~ 0.27 nm, i.e. very close to the reference CoFeB layer at t_{CoFeB} = 6 nm. The magnetic hysteresis loops at room temperature for SLG/CoFeB (1.5 nm) and reference CoFeB (1.5 nm) are shown in Fig. 4.1(e). Figure 4.1(f) plots the variation of coercive field (H_C) for these two sets of samples which reveals lower values of H_C for the reference CoFeB films

than the SLG/CoFeB heterostructures, besides a small nonmonotonic variation with t_{CoFeB}. The increment of coercivity of this system indicates that the initial growth of the CoFeB layer on the SLG results in partial pinning of interface spins[300]. This also indicates that SOC may play an important role in SLG/CoFeB system[301,302]. The variation in saturation magnetization (M_S) as a function of t_{CoFeB} for both sets of samples is shown in Fig. 4.1(g). The M_S is almost same for both SLG/CoFeB and the reference CoFeB films. Besides, both sample sets follow the same trend of variation with t_{CoFeB}, i.e., a sharp increase from 1.5 to 3 nm followed by a gradual increase with t_{CoFeB}.

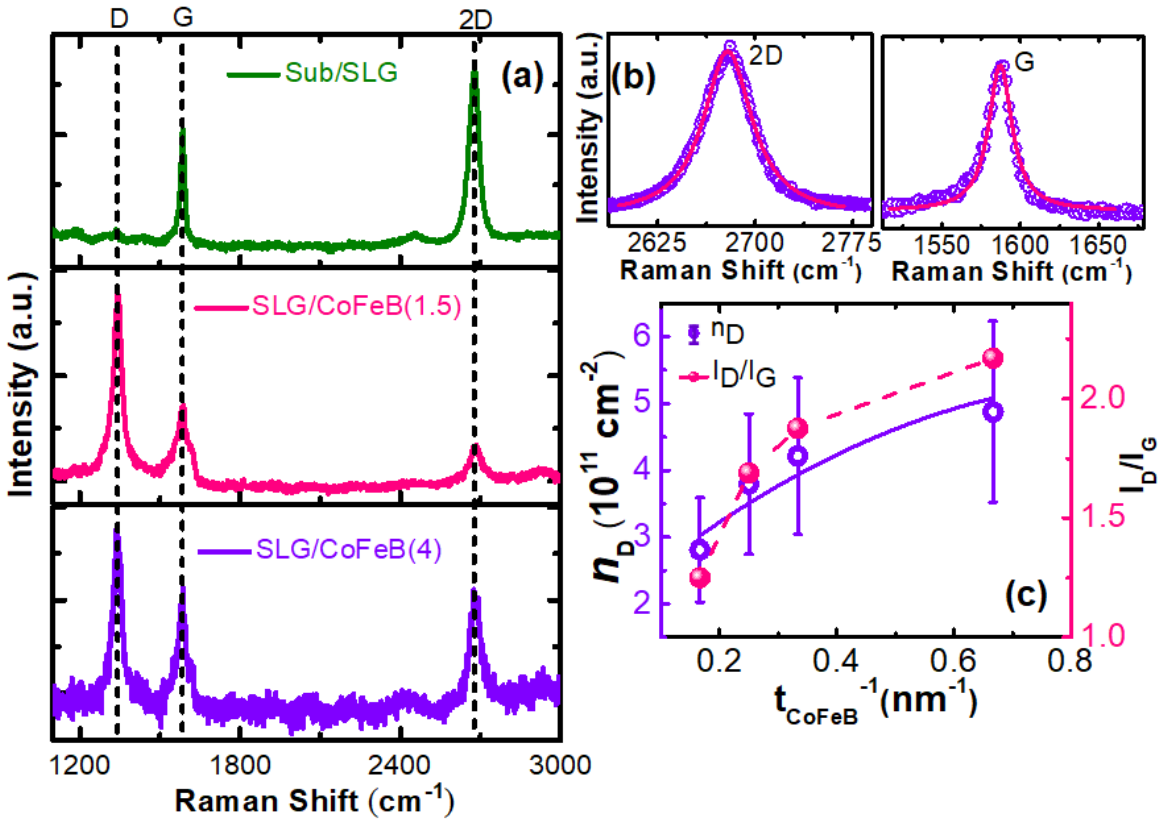

Figure 4.2: (a) Raman spectra of CVD-grown SLG on Si/SiO_2 substrate (top panel), SLG/CoFeB (1.5 nm)/SiO_2 (middle panel) and SLG/CoFeB (4 nm)/SiO_2 (bottom panel). (b) Intensity profile of 2D and G peak of SLG. (c) Variation of defect density (n_D) and I_D/I_G as a function of inverse of CoFeB thickness. The error bars in n_D is calculated from the n_D expression. Symbols represent experimental data points and solid lines are the corresponding theoretical fits for (b)-(c).

The Raman Spectra of SLG and SLG/CoFeB films are shown in Fig. 4.2(a) (top panel). The two most prominent signatures of graphene are the G peak at ~1581.8 cm^{-1} and the 2D peak (or G') at ~2678.9 cm^{-1}. Here, the G peak is a doubly degenerate zone-centre E_{2g} mode and the 2D peak is a second order

of zone-boundary phonons. The perfect Lorentzian shape of the intensity profile and height of 2D and G peaks in Fig. 4.2(b) are confirm the single-layer nature of graphene. An additional D peak at ~1339 cm^{-1} appears in the Raman spectra (Fig. 4.2(a)) when CoFeB is deposited over SLG. This D peak is a signature of the disorder arrangement of atoms at the interface[303] and appears mainly in the presence of defects in the system. Figure 4.2(c) represents the variation in spectral weight ratio (I_D/I_G) which shows that 'I_D/I_G' ratio increases with the inverse of t_{CoFeB}. We have subsequently calculated the defect density (n_D) using the relation, n_D (cm^{-2}) = $\frac{(1.8 \pm 0.5) \times 10^{22}}{\lambda(nm)_R^4}\left(\frac{I_D}{I_G}\right)$ where λ_R= 532 nm is the excitation wavelength of laser used in our Raman measurement[304]. Here, $\frac{1.8\times10^{22}}{\lambda(nm)_R^4}\left(\frac{I_D}{I_G}\right)$ and $\frac{(\pm0.5\times10^{22})}{\lambda(nm)_R^4}\left(\frac{I_D}{I_G}\right)$ represent the defect density and the error in defect density. Since n_D is proportional to I_D/I_G, a similar variation of n_D with the inverse of CoFeB thickness is observed in Fig. 4.2(c). Again, we fitted our result with a second order polynomial equation: $y= A+Bx+Cx^2$ where $y = n_D$ and $x = 1/t_{CoFeB}$. The best fit shows an increasing trend of n_D with the inverse of CoFeB thickness with fitting parameters, A = 1.89×10^{11} cm^{-2}, B = 7.75×10^{4} cm^{-1} and C = -4×10^{-3}. We have also calculated the average crystallite size[305] (L_a), i.e. the average distance between two consecutive defects using the expression, L_a = $\frac{(2.4 \times10^{-10})}{\lambda(nm)_R^{-4}}\left(\frac{I_G}{I_D}\right)$ as tabulated in Table-I. The nature of L_a follows an opposite trend to that of n_D, which indicates that the defect density decreases with an increase of t_{CoFeB} in SLG/CoFeB.

Table-I. Average crystallite size variation for single layer Graphene/$Co_{20}Fe_{60}B_{20}$(t)/SiO_2 samples with different CoFeB thicknesses.

CoFeB Thickness (nm)	***L_a* (nm)**
1.5	8.86
3	10.25
4	11.38
6	15.38

To investigate the iDMI in SLG/CoFeB samples, we measured SW dispersion by applying an in-plane bias magnetic field in the BLS setup. Figure 4.3(a) shows the schematic of the BLS measurement geometry where ***B*** and ***k*** represent two mutually perpendicular quantities, namely, the in-plane bias

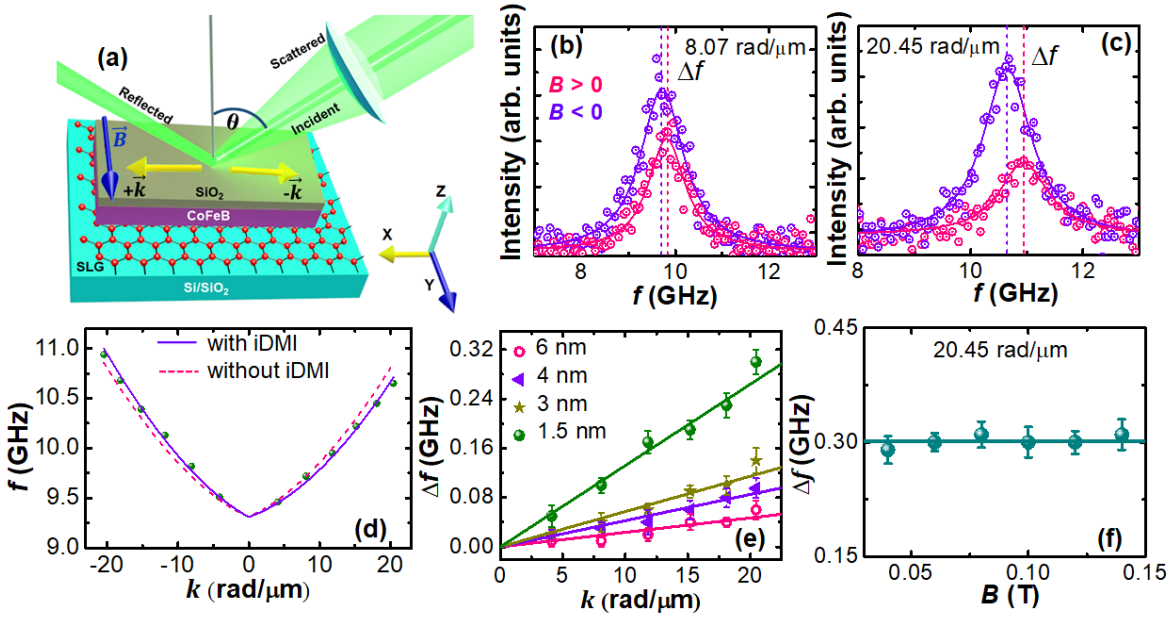

Figure 4.3: (a) Schematic of the sample stack along with the BLS measurement geometry where the incident and scattered light beams lie in the z-x plane and are at an angle θ to the z-axis. Representative BLS spectra at (b) k = 8.07 rad/μm and (c) k = 20.45 rad/μm under oppositely oriented external magnetic fields B = 0.1 T. (d) Spin-wave dispersion for SLG/CoFeB (1.5 nm) sample at B = 0.1 T. Symbols represent the experimental data points, the solid curve shows the fit to the data points using Eq. (1) and the dotted curve shows the theoretical spin-wave dispersion in absence of DMI. (e) Representation of Δf vs. k for all four SLG/CoFeB/SiO_2 samples. Symbols represent the experimental data points and solid lines are the fit using Eq. (2). (f) Plot of Δf as a function of B for SLG/CoFeB (1.5 nm)/SiO_2.

magnetic field and wave-vector, respectively. The SW dispersion under oppositely oriented ***B*** along *y*-axis is detected simultaneously as Stokes and anti-Stokes peaks in the spectra. The experimental BLS spectra for SLG/CoFeB (1.5 nm) sample for two different wave-vectors, namely, k = 8.07 rad/μm and 20.45 rad/μm, are shown in Figs. 4.3(b)-3(c). The BLS spectra are well fitted with a single Lorentzian function (fitted curve is shown by solid line) to extract the SW frequency for each wavevector. Here, magenda and violet symbols indicate BLS spectra for B = 0.1 T applied in two opposite directions of y-axis. The frequency difference (Δf) between these two peak positions in counterpropagating SWs ($\pm k$; along $\pm x$) is related to the strength of iDMI. The SW dispersion at B = 0.1 T is shown in Fig. 4.3(d), which is modelled using a modified SW dispersion relation after the DMI effect is included in the DE geometry[64]:

$$\omega = \omega_o + \omega_{DM} = \mu_0\gamma\sqrt{[H + Jk^2 + \xi(kL)M_S][H - H_U + Jk^2 + M_S - \xi(kL)M_S]} - \frac{2\gamma}{Ms}Dk \quad (4.1)$$

Here, $\gamma = \frac{g\mu_B}{h}$, g is the Lande g factor, while L and μ_0 are the thickness of CoFeB layer and vacuum permeability, respectively; $J = 2A/\mu_0 M_S$ is the SW stiffness, A *is* the exchange constant; D is the DMI constant, $H_U = 2K_U/\mu_0 M_S$ is the uniaxial anisotropy field (K_U = uniaxial anisotropy constant) and $\xi(kL) = 1 - (1 - \exp|-kL|)/|kL|$. For SLG/CoFeB (1.5 nm) sample, using g = 2.00, M_S = 0.812 MA/m, and A = 19.5 pJ/m, the fitted experimental data yielded the following values: H_U = 16.4 ± 2 kA/m and D = 102 ± 3 μJ/m^2.

The DMI-induced frequency shift of counterpropagating SWs is given by[64]

$$\Delta f = \left\{\frac{[[f(-k, M_z) - f(k, M_z)] - [f(-k, -M_z) - f(k, -M_z)]]}{2}\right\}$$

$$\Delta f = [\omega(-k) - \omega(+k)]/2\pi = \frac{2\gamma}{\pi Ms}Dk \quad (4.2)$$

is linear with D and k. The frequency shift for SLG/CoFeB (1.5 nm) sample can also be experimentally observed in Fig. 4.3(f) for a range of external magnetic field from B = 0.04 T to 0.16 T which is independent of B. Equation (4.2) also supports our result quantitatively. An average frequency shift of 0.31 GHz is observed for SLG/CoFeB (1.5 nm) sample, whereas no frequency asymmetry is found in the reference CoFeB (1.5 nm) thin film. The same is observed for all reference samples, i.e., Sub/CoFeB (t_{CoFeB})/SiO_2. Figure 4.3(e) shows a linear variation of Δf with k for all four SLG/CoFeB (t_{CoFeB})/SiO_2 samples. The slope of Δf vs k is maximum for SLG/CoFeB (1.5 nm) and minimum for SLG/CoFeB (6 nm). We have used respective M_S values from Fig. 4.1(f), and g = 2.00 ± 0.02 for all SLG/CoFeB (t_{CoFeB}) samples to obtain the values of D at different CoFeB thicknesses. The linear dependence of D with the inverse of t_{CoFeB} is shown in Fig. 4.4(a). The values of D obtained from fitting of the experimental data with Eqs 4.1 and 4.2 are found to be consistent. The linear dependence of D with the inverse of CoFeB thickness indicates pure interfacial origin of the DMI present in the SLG/CoFeB heterostructures[63].

Only a few reports exist on the iDMI in graphene/FM heterostructures, e.g. in graphene/$Ni_{80}Fe_{20}$/Ta[54], graphene/Co/Pt[20] and graphene/$[Co/Ni/graphene]_n^2$. However, in those reports, layers of relatively heavier element such as Ta, Pt, Ni are present on the other side of the FM forming a second interface. This may raise a question on the true contribution of the graphene/FM interface to the iDMI, because substantial iDMI has also been reported in Ta/FM[306], Pt/FM[64] and

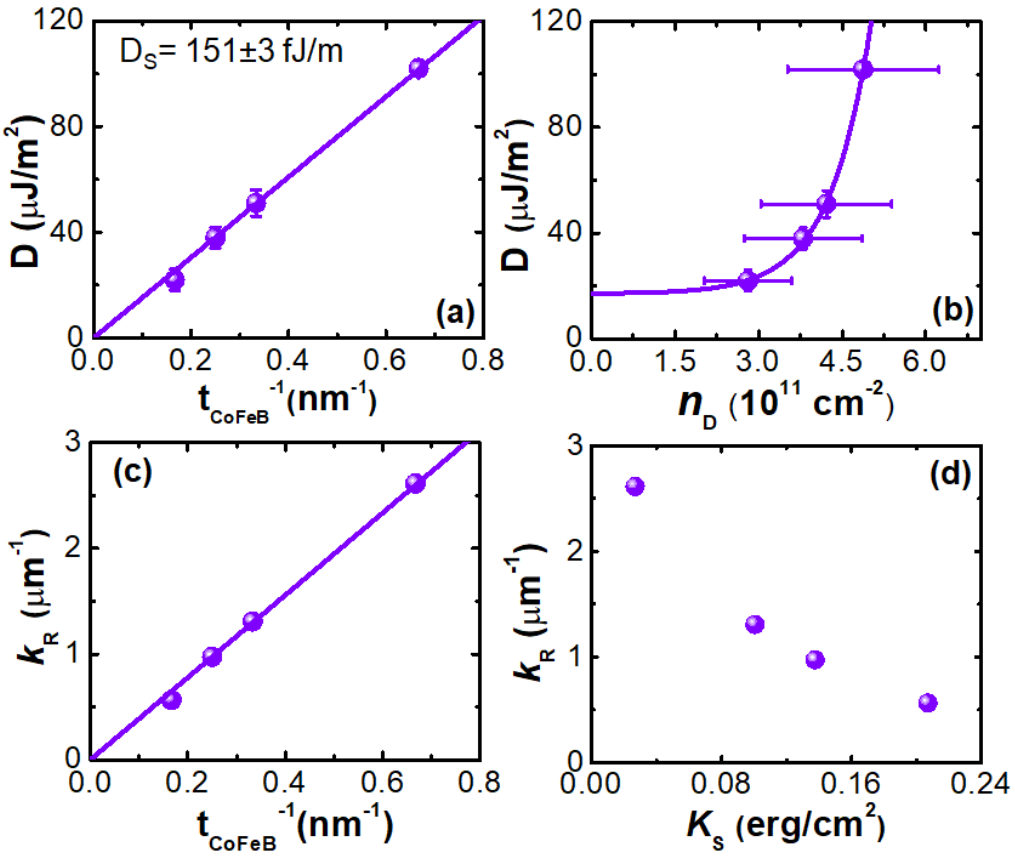

Figure 4.4: (a) Extracted DMI constant (D) vs inverse of CoFeB thickness for all four SLG/CoFeB/SiO_2 samples. (b) Variation of D as a function of defect density (n_D). (c) Plot of Rashba shift (k_R) vs inverse of CoFeB thickness for all SLG/CoFeB/SiO_2 samples. (d) Variation of k_R as a function of K_S for all four SLG/CoFeB/SiO_2. Symbols represent experimental data points and solid lines are the corresponding theoretical fits.

FM/Ni[64] heterostructures. Therefore, we have used a SiO_2 overlayer on the CoFeB layer to underpin the true contribution of the graphene/FM interface to the iDMI and observed a substantial D value from the SLG/CoFeB interface. The solid lines in Fig. 4.4(a) show a linear fit to the data using the following expression[63]:

$$D = \frac{D_S}{t_{CoFeB}} \tag{4.3}$$

where D_S is the surface DMI, a material interface parameter that is independent of FM thickness for fixed temperature and deposition pressure. Equation 4.3 is valid for purely interfacial DMI only. Subsequently, we obtained D_S = 151 ± 3 fJ/m at 1.2 mTorr of Ar pressure (P_{Ar}) during sputter deposition, which is 1.5 times larger than that reported for graphene/Py/Ta heterostructures at P_{Ar} = 2 mTorr[54] indicating a more favourable interface for graphene/CoFeB as opposed to graphene/Py/Ta[54]. The maximum D value of 102 μJ/m^2 in SLG/CoFeB (1.5 nm) is found to be independent of B ($= \mu_0 H$).

The observation of significantly high and stable D value in graphene-based heterostructure in our study can be considered to originate due to point-defect induced extrinsic SOC in SLG/CoFeB heterostructures [293,304]. To underpin this further, we have correlated D with n_D in Fig. 4.4(b). The solid line shows an exponential growth of D with n_D following an empirical relation: $D(n_D) = D(0)\exp(\frac{n_D}{\nu}) + D_0$. From there, we extracted the inverse of growth coefficient, ν = 7.38 × 10^{10} cm^{-2} and amount of iDMI at n_D = 0, i.e., $D(n_D = 0)$ as 17.13 μJ/m^2 [$D(0)$ = 0.11 μJ/m^2 and D_0 = 17.02 μJ/m^2] from the fit. Initially, D remains almost constant with n_D, but a drasctic increase in D was observed above a threshold value $n_D \approx 3.5\times10^{10}$ cm^{-2}. We also calculated the Rashba shift (k_R) using the relation: $D = 2Ak_R$[307] and observed a very small defect-induced k_R. Figure 4.4(c) shows a linear dependence of k_R with inverse of CoFeB thickness. The maximum value of k_R is found to be 2.5 μm^{-1} which is much smaller than that reported in the works on Rashba-shift-induced iDMI in graphene-based heterostructures [18,20]. Furthermore, we calculated the surface anisotropy constant (K_S) using the following expression: $K_S = 2\pi M_S t_{CoFeB}(M_S - M_{eff})$. The calculated K_S shows a monotonic decrease with k_R in Fig. 4.4(d).

Figure 4.5(a) displays the variation of spectral linewidth, i.e. magnon lifetime with k at B = 0.12 T. Experimental results reveal that the lifetime of SW propagating in $+k$ direction is relatively smaller than that in $-k$ direction, showing a minimum. We have fitted the experimental variation of linewidth (Δf_{res}) with k using the equation[64]:

$$\Delta f_{res} = 2\alpha_a \gamma \mu_0 (H_0 + Jk^2 - H_u/2 + M_s/2)\left[1 + \frac{\omega_{DM}(k)}{\omega_o(k)}\right] \tag{4.4}$$

By using the same magnetic parameters as those discussed previously in this paper, the average damping parameter α_a was found to be $(17.2 \pm 1.7) \times 10^{-3}$ for SLG/CoFeB (1.5 nm) sample. The local minima of damping shifts to non-zero k in presence of Rashba SOC[308]. From the fit, we also obtained a minimum of Δf_{res} at $k \approx +2.7$ μm^{-1} corresponding to the Rashba shift, which is very close to that

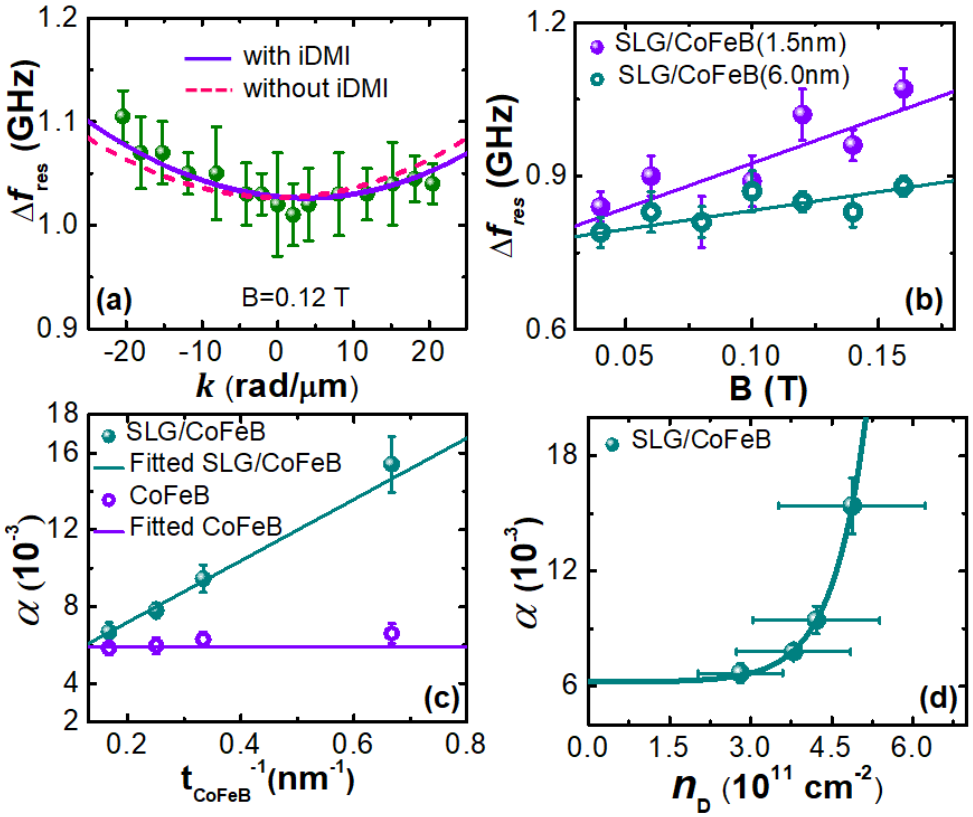

Figure 4.5: (a) Linewidth (FWHM: Δf_{res}) of BLS spectra in the SLG/CoFeB (1.5 nm)/SiO_2 sample as a function of wave-vector. (b) Variation of Δf_{res} as a function of B for SLG/CoFeB (1.5 nm)/SiO_2 and SLG/CoFeB(6 nm)/SiO_2 samples. (c) Extracted effective damping (α) as a function of inverse CoFeB thickness for SLG/CoFeB/SiO_2 and CoFeB/SiO_2 samples. (d) Plot of α vs. defect density (n_D) for all SLG/CoFeB/SiO_2 samples. Symbols represent experimental data points and solid lines are the corresponding theoretical fits.

extracted analytically in SLG/CoFeB (1.5 nm) sample. The nature of Δf_{res} curve is symmetric very near to $k_R = -\frac{8\pi^2 m_e \alpha^R}{h^2} = 2.5$ μm^{-1} and asymmetric with respect to $k = 0$. The Δf_{res} value at wave vector $+k$ differs from that at $-k$, indicating the presence of a chiral damping in the Rashba model[308].

To further explore of the effect of defect induced extrinsic SOC, we have investigated the spin pumping effect from the CoFeB layer into the SLG from the BLS linewidth analysis at $k \approx 0$ using the equation[219]:

$$\Delta f_{res} = \Delta f_{res}^{extrinsic} + \frac{2\mu_0 \alpha_{eff} \gamma}{\pi} H \quad (4.5)$$

where the BLS linewidth and the extrinsic linewidth at $k \approx 0$ are expressed as Δf_{res} and $\Delta f_{res}^{extrinsic}$, respectively and α_{eff} is the effective damping. The expression for effective damping of the FM layer is given by the spin pumping theory:

$$\alpha_{eff} = \alpha_0 + \alpha_{SP} \quad (4.6)$$

Here, α_0 is the intrinsic Gilbert damping parameter and α_{SP} is the damping due to spin pumping effect, which is given by[36]:

$$\alpha_{SP} = \frac{\gamma h g_{\uparrow\downarrow}}{4\pi M_S t_{CoFeB}} \quad (4.7)$$

Here, $g_{\uparrow\downarrow}$ is the intrinsic spin-mixing conductance, and the other parameters carry the usual meaning as discussed earlier in this paper. Figure 4.5(b) shows the variation of Δf_{res} and B for two samples, namely SLG/CoFeB (1.5 nm) and SLG/CoFeB (6 nm), and we observed relatively higher slope in SLG/CoFeB (1.5 nm) than the other one. We extracted α_{eff} from the linear variation of Δf_{res} and B. The α_{eff} in the reference CoFeB films is almost independent of CoFeB thickness shown in Fig. 4.5(c). However, it shows a linear variation with the CoFeB thickness in SLG/CoFeB samples. This additional linear enhancement of damping can be attributed to spin pumping mechanism. During spin pumping, spin accumulation occurs at the SLG/CoFeB interface due to precession spins in the ferromagnetic CoFeB layer. These accumulated spins resulted in a flow of pure spin current in the adjacent SLG layer. The extracted value of $g_{\uparrow\downarrow}$ at P_{Ar} = 1.2 mTorr is (1.67 ± 0.05) × 10^{19} m^{-2}. Furthermore, an exponential growth of α_{eff} with defect density (n_D) in SLG/CoFeB samples is also shown in Fig. 4.5(d) which further confirms the defect induced extrinsic SOC at the SLG/CoFeB interface. Finally, the correlation of D and α_{eff} with n_D shows the role of enhancement SOC at SLG/CoFeB interface on the iDMI and spin-pumping in this system.

IV. Conclusions:

In summary, we have systematically measured a sizable iDMI and spin pumping for SLG/CoFeB heterostructures using BLS spectroscopy. The iDMI and effective damping show a linear variation with CoFeB thickness in SLG/CoFeB stacks and both of these physical quantities have values significantly larger than those of the graphene/Py/Ta system reported previously[54]. We found a small Rashba shift[18] present in these stacks. However, iDMI and spin pumping were found to be correlated with the defect density present at the surface of SLG. Interestingly, both of these quantities show exponential increment with defect density. This corroborates that defect-induced extrinsic SOC plays a major role in the observed iDMI, spin pumping and spin-mixing conductance in these samples. The observation of surface DMI constant of 151 fJ/m at a moderate Ar pressure of 1.2 mTorr is already similar to that observed for W and Ta-based heterostructures and can potentially be further enhanced by optimizing the Ar pressure during sputter deposition of the FM layer. It, therefore, promises the possibilities of stabilizing chiral spin textures like nanoscale skyrmions and their manipulation using defect-induced extrinsic SOC at the SLG/FM interface for development of new-generation energy-efficient memory and logic devices devices.

Chapter 5

5. Femtosecond Laser-induced Transient Magnetization Enhancement and Ultrafast Demagnetization Mediated by Domain wall Origami

I. Introduction:

The achievement of ultrahigh processing speeds in next-generation magnetic memory and logic devices demands the manipulation of magnetic order at ultrashort timescales. However, conventional schemes for magnetization switching, involving the application of picosecond magnetic field pulses [309] or via spin transfer torque [27,222,310] or spin-orbit torque [311,312], can offer switching times of several hundred picoseconds to nanoseconds at best [313,314]. Realizing ultrafast optical switching by the application of femtosecond laser pulses thus poses an exceptionally exciting alternative. A pioneering step in this direction was the demonstration of subpicosecond ultrafast demagnetization of a nickel thin film by the application of a 60-fs laser pulse [87], making it the fastest known means for the manipulation of magnetization [87,315]. Already, a large degree of tunability of the demagnetization time has been achieved experimentally, varying from the femtosecond time scale to 100s of picoseconds [53,83,88,90,316,317] by tuning material parameters such as the degree of spin polarization [318] and chemical ordering [319] or experimental parameters such as the laser pulse width and excitation fluence [96,201]. On the other hand, excitation with ultrafast laser pulses can not only trigger demagnetization, but has also been demonstrated to transiently enhance magnetic ordering in transition metal alloys [320], manganites [321], and ferromagnetic semiconductors [85].

Over the two decades since the advent of ultrafast demagnetization, different mechanisms have been proposed to explain the associated ultrafast dissipation of energy and angular momentum [96,201,322]. Spin-flip processes were originally considered to be the primary channel for angular momentum transfer at ultrafast timescales, but often cannot be straightforwardly applied to explain the varied physics that may arise in magnetically heterogeneous systems such as magnetic alloys, compounds, and multilayers. A theory of super-diffusive spin transport (SST)[89] was later developed to understand ultrafast demagnetization in layered ferromagnet (FM)/metal, FM/semiconductor (SC)[84] and FM/metal/FM[86] heterostructures. Alongside intrinsic spin-flip processes, interlayer spin currents were proposed to play a significant role to control optically driven ultrafast magnetization dynamics, depending critically on the composition of the multilayer system [92], as well as FM layer thickness and repeat numbers [197]. In 2008, Malinowski *et al.* reported that the demagnetization proceeds faster for a mutually antiparallel orientation of the magnetization in antiferromagnetically coupled $[Co/Pt]_n$

multilayer stacks [88], indicating more efficient spin transport across the conductive spacer. In a 2012 study on a Ni/Ru/Fe trilayer system, an ultrafast transient enhancement of magnetization of the buried Fe layer occurring after femtosecond laser excitation of the oppositely magnetized Ni layer was attributed to SST [86]. Such multilayered systems represent transversely structured magnetization profiles with the spacer layers serving as junctions separating regions of opposite magnetization. On the other hand, the presence of a magnetic domain structure represents a heterogeneous magnetization profile along the sample plane with the domain walls representing the junctions. Only a few works have characterized ultrafast demagnetization in presence of a nanoscale domain network and mostly explain their result with the help of spin-dependent transport across the domain walls [86,90,97]. Faster demagnetization was observed in these systems as compared to that in systems without a domain structure, attributed to the direct transfer of spin angular momentum between neighbouring domains [90]. However, to the best of our knowledge, an experimental demonstration correlating magnetic field-free ultrafast demagnetization and anomalous transient magnetization enhancement with the details of the underlying magnetic domain configuration is still missing in the literature.

In this work, time-resolved magneto-optical Kerr effect (TR-MOKE) magnetometry was used to investigate the ultrafast laser-induced magnetization dynamics for various underlying magnetic domain configurations of a ferromagnetic multilayer sample in the absence of an external magnetic field. Remarkably, not only could the expected ultrafast demagnetization be observed, but also an anomalous transient magnetization enhancement (TME) for certain domain configurations. The observed magnetization dynamics is strongly dependent on the magnetic state of the samples and shows a phase transition from typical ultrafast demagnetization to a purely TME-dominated spin dynamics through a state where both TME and demagnetization are observed in the system. The two phenomena and the dominance of one versus the other is found to be controlled by the effective surface area of domain wall in different domain configurations which can either promote or hamper the transfer of majority and minority spin through the domain wall via SST mechanism. Thus, a typical nature of the laser induced spin dynamics could be observed in our system by inducing changes in the underlying domain landscape which is additionally found to be greatly tunable by means of an external magnetic field. Thereby, our results pave the way to control magnetic field-free ultrafast demagnetization and TME for the development of ultrafast spintronics devices driven by magnetic spin-texture.

II. Experimental and Theoretical Methods:

Sample Fabrication: The multilayer stacks for this study were deposited on Si(001)/SiO_2(100 nm) substrates with a confocal DC magnetron sputter system, ATC-2200, from AJA International at room temperature at a base pressure of $\approx 3 \times 10^{-7}$ Torr. The Ar sputtering gas pressure was set to 3 mTorr. The sample holder was rotated at about 1 Hz frequency and slow deposition rates of ~ 0.1 nm/s were chosen to ensure homogeneous deposition of different layers on the substrate. A seed-layer composed of 1.5 nm Ta and 20 nm Pt was used, with the Ta providing adhesion and the Pt providing a strong (111) texture for optimal Co/Pt growth with high PMA. Additionally, a capping layer of 2.4 nm Pt was placed on top of the multilayer to prevent oxidation.

Domain Reconfiguration: The domain states for which magnetization dynamics were measured are depicted in Figs. 5.1(a)-(e). A given domain state was reconfigured following a systematic process via changing different minor hysteresis loops. Following out-of-plane (OOP)AC demagnetization of two identical copies of the multilayer stack, two nearly parallel stripe domain states were observed with the presence of some junctions (Figure 5.1(b)), which we designated domain configuration [S1].Subsequently, the relative number of junctions in the remanence state were reduced in one of the samples by applying a 2kOe in-plane (InP) magnetic field as shown in Fig. 5.1(a) (configuration [S2]).The pure OOP AC demagnetized sample was then placed in a 14kOe OOP magnetic field and a bubble domain-like state was realized in remanence as shown in Fig. 5.1(e) (configuration [S3]). This bubble domain sample was placed in a 6kOe OOP magnetic field and another mixed domain state was observed comprising bubble-like domains along with a relatively smaller number of stripe domains (Fig. 5.1(d)) (configuration [S4]). Finally, this mixed bubble domain sample was placed in a -3kOe OOP magnetic field and a labyrinth domain state was observed as shown in Fig. 5.1(c) (configuration [S5]).

TR-MOKE Measurements: Measurement of magnetization dynamics were carried out using a two-color time-resolved magneto-optical Kerr effect (TR-MOKE) technique in a noncollinear geometry

using a 400 nm pump beam and 800 nm probe beam having a pump-probe cross-correlation width of ~100 fs. The s-polarized fundamental output of an amplified femtosecond laser (LIBRA, Coherent) having λ = 800 nm, pulse-width = 35 fs, and repetition rate = 1 kHz was used as the probe beam while its second harmonic having λ = 400 nm, pulse-width of > 35 fs and repetition rate = 1 kHz was used as the pump. A mechanical chopper of frequency 373 Hz was used to modulate the laser pump while the

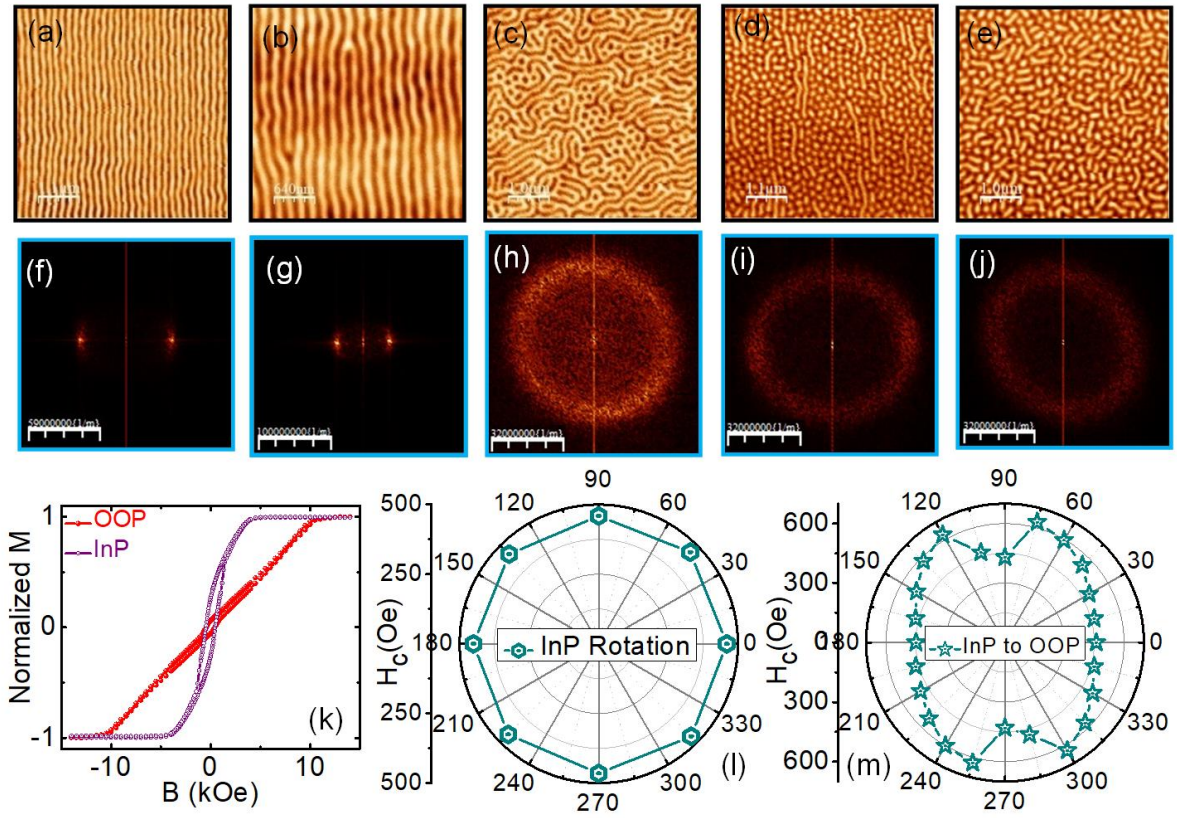

Figure 5.1: (a)-(e) The magnetic force micrographs (MFMs) of five different domain configurations [S2], [S1], [S5], [S4], and [S3]. (f)-(j) Modulus of 2D Fourier transforms of images in (a)–(e), respectively. (k) Magnetic hysteresis loops when magnetic field is applied in-plane and out plane direction of sample plane. Coercive field as a function of azimuthal angle (l) and polar angle (m) of applied magnetic field.

Kerr rotation and total reflectivity of the reflected probe beam from the sample were measured using lock-in amplifiers at a reference frequency of 373 Hz in a phase-sensitive manner. The probe beam was focused to a spot size of ~100 μm and normally incident on the sample, whereas the pump beam having a larger spot size of ~300 μm, was incident obliquely (approximate angle of incident = 25°) on the sample maintaining a spatial overlap with the probe spot. The time-varying Kerr rotation data ($\Delta\theta_k$) was normalized with θ_k, where $2\theta_k$ corresponds to the change in Kerr rotation for the complete reversal

of magnetization. A fixed probe fluence of 1.50 $mJcm^{-2}$ and varying pump fluences from 5.20 to 12.99 $mJcm^{-2}$ were used for all the measurements. All experiments were carried out in ambient conditions.

III. Results and Discussions:

Magnetic force micrographs (MFMs) of different domain states ([S1]-[S5]; see the Methods section) observed in the ferromagnetic multilayer stack Ta(1.5nm)/Pt(20nm)/$[Co(3nm)/Pt(0.6nm)]_{22}$/Pt(2.4nm) are shown in Fig. 5.1. Two nearly pure stripe domain states, a labyrinth domain state and two mixed states consisting of bubble-like domains interspersed with stripe domains are presented in Figs. 5.1(a)-(e) respectively. Figure 5.1(f)-(j) depict the modulus of 2D fast Fourier transforms [323] of the different domain states presented in Figs. 5.1(a)-(e) respectively. The modulus of FFTs for the vertical stripe domains aligned on the x-axis show single peaks on the x-axis as shown in Figs. 5.1(f)-(g) corresponding to the configurations of Fig 5.1(a) and 5.1(b), whereas the rest of the domain states are arranged in both x- and y-axis and the modulus of FFTs of these are radially averaged as shown in Figs. 5.1(h)-(j). Figs. 5.1S(a)-(e) (Appendix A) show the power spectral density (PSD) of 2D FFTs of domain configuration of Figs. 5.1(a)-(e) respectively. The PSD profiles are fitted using an asymmetric Lorentzian function to extract the average wavenumber k and the linewidth Δk. One half of k^{-1} corresponds to the average domain width w whereas Δk represents the broadening of the PSD profile due to the presence of nonuniformities in the domain structure. The values of k, Δk and average domain width are tabulated in Table I.

The room temperature InP and OOP magnetic hysteresis loops of the multilayer samples measured using vibrating-sample magnetometry (VSM) are shown in Fig. 5.1(k). The saturation magnetization M_s is found to be 1450 emu/cc while the OOP and InP saturation magnetic fields are 11.5 kOe and 4.4kOe respectively. Further, room temperature hysteresis loops were measured at different azimuthal angles (φ) of the in-plane magnetic field. The plot of extracted coercive field vs. φ is shown in Fig. 5.1(l), which reveals negligible in-plane magneto-crystalline anisotropy in the sample. The hysteresis loops were also recorded at different polar angles θ going from InP to OOP as shown in Fig. 5.1(m).

Table I: Important parameters associated with different domain configurations

Domain Configuration	k (10^6 m^{-1})	Δk (10^6 m^{-1})	w (nm)
Pure ACD State [S1]	5.69 (k_x)	1.55 ± 0.06	175 ± 10
Remanence after InP +2kOe [S2]	5.90(k_x)	1.00 ± 0.06	169 ± 10
Remanence after OOP +14kOe [S3]	4.90 ($k_{x,y}$)	2.50 ± 0.09	204 ± 8
Remanence after OOP +6kOe [S4]	5.13 ($k_{x,y}$)	1.87± 0.09	194 ± 8
Remanence after OOP -3kOe [S5]	5.31 ($k_{x,y}$)	1.80 ± 0.07	188 ± 8

The laser induced magnetization dynamics are measured using TR-MOKE magnetometry [53,319] by recording the transient change in Kerr rotation as a function of pump-probe delay as shown in Fig. 5.2(a). To validate our result in different domain configurations, we also performed TR-MOKE measurement in the presence of a saturating InP magnetic field where we only observed ultrafast demagnetization. Fig. 5.2(b) shows a representative TR-MOKE trace obtained in the saturation region at a pump fluence10.40mJcm^{-2} under an in-plane bias magnetic field of 5.0kOe. The Kerr rotation signal comprises three distinct temporal regimes: (i) ultrafast demagnetization regime, (ii) fast magnetization recovery regime and (iii) precessional regime. The time-resolved data spanning the first two temporal regimes are fitted with a phenomenological expression obtained by solving the equations of the three-temperature model (3TM) to extract the ultrafast demagnetization time τ_m and fast relaxation time τ_r. The analytical expression is [88,200]:

$$-\frac{\Delta\theta_k}{\theta_k} = \left[\left\{\frac{A_1}{\left(\frac{t}{\tau_0}+1\right)^{\frac{1}{2}}} - \frac{(A_2\tau_r - A_1\tau_m)e^{-\frac{t}{\tau_m}}}{\tau_r-\tau_m} - \frac{\tau_r(A_1-A_2)e^{-\frac{t}{\tau_r}}}{\tau_r-\tau_m}\right\}\Theta(t) + A_3\delta(t)\right] \otimes \mathrm{G}(t) \quad (1)$$

where A_1, A_2, and A_3 are constants that are respectively related to the amplitude of magnetization after

equilibrium, the maximum rise of electronic temperature due to the laser excitation and state-filling effects occurring during pump-probe temporal overlap described by a Dirac delta function $\delta(t)$. $G(t)$ denotes the Gaussian function representing the temporal profile of the laser pulse, and $\Theta(t)$ is a step function. The electron and spin temperatures rise during the ultrafast demagnetization and eventually undergo a fast relaxation by dissipation of energy to the lattice manifesting as the magnetization

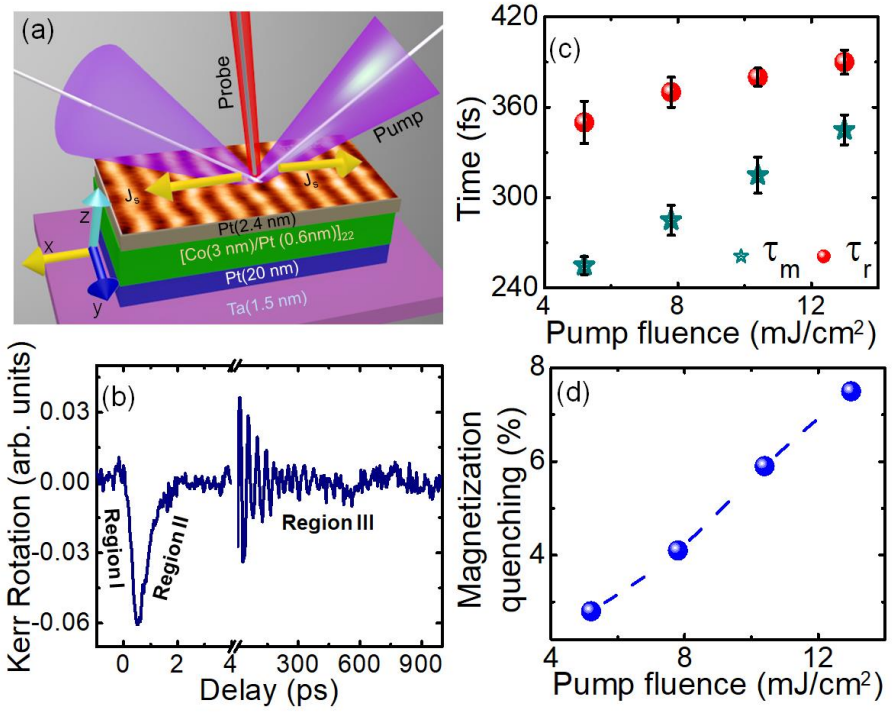

Figure 5.2: (a) Schematic of the film stack along with TR-MOKE geometry. (b) Representative TR-MOKE trace where different temporal regions are marked. (c)-(d) The variation of ultrafast demagnetization time (τ_m) and magnetization quenching with laser fluence respectively.

recovery. A monotonic increment in τ_m and τ_r is observed with the pump fluence (Fig. 5.2(c)). The increase in τ_m with pump fluence arises due to enhanced spin fluctuations due to increased temperature of the spin system resulting in a corresponding increase of the dynamic longitudinal susceptibility and a decrease of the exchange interaction strength[324]. Figure 5.2(d) shows the variation of the maximum magnetization quenching obtained for different pump fluence values in the InP saturation regime.

Figure 5.3(a) shows a representative TR-MOKE signal for [S2], [S5] and [S4] domain configurations at remanence for an exciting pump fluence of 12.99 mJcm^{-2}. In case of stripe domain configuration and

labyrinth domain configuration, TR-MOKE signal consists of three-part (i) ultrafast demagnetization (ii) magnetization recovery along with TME, and (iii) final magnetization recovery regimes. The complete representation of TR-MOKE trace for [S2] is shown in Fig. 5.2S(a) (Appendix A). Figures 5.3(b)-(d) respectively show the variation of TR-MOKE signal with different pump fluences for [S2], [S5] and [S4] domain configurations at remanence. When femtosecond gaussian laser hits the stripe

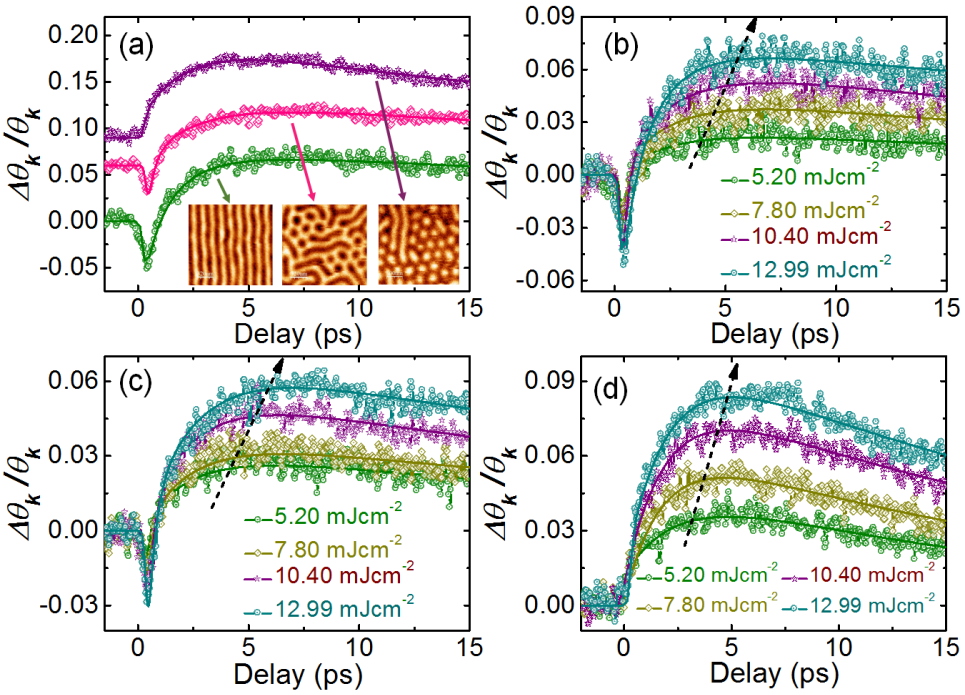

Figure 5.3: (a) Representative TR-MOKE for [S2], [S5] and [S4] domain configurations for a fixed pump fluence 12.99 mJ cm^{-2}. (b)-(d) Representative TR-MOKE trace for [S2], [S5] and [S4] with laser fluences respectively.

domain configuration (schematic is shown in Fig. 5.4(a)), the direct transfer of unequal spin angular momentum between neighbouring domains occurs [90]. Since the mobility of majority spin carriers is much larger than minority spin carriers, a fact that forms the basis of the SST model [89], the majority spin transport through the domain wall gives rise to demagnetization and parallelly leads to an increase in the density of minority carriers in the neighbouring domains as shown in Fig. 5.4(b). After the demagnetization, these majority spins diffuse back to their equilibrium domain state through the

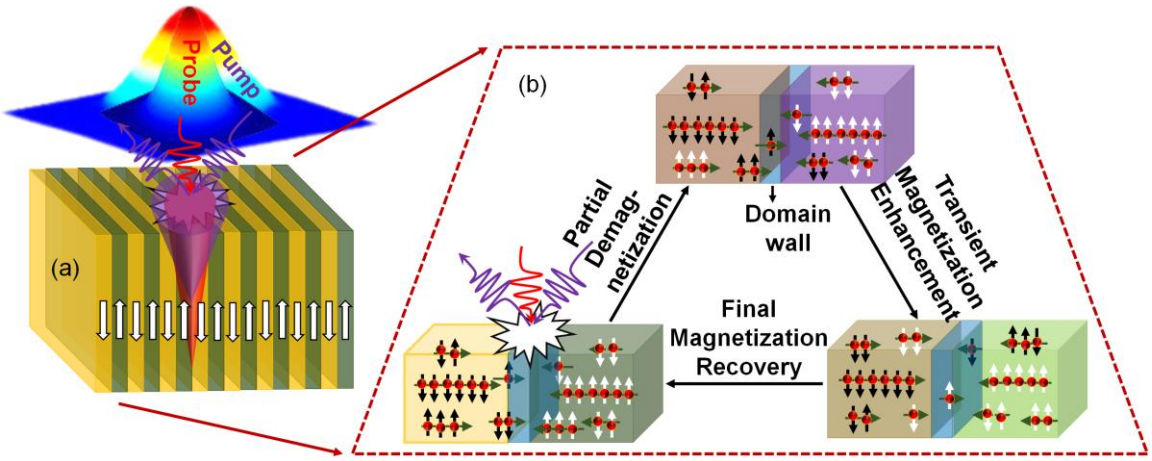

Figure 5.4: (a)-(b) A schematic showing the processes involved in ultrafast demagnetization, transient magnetization enhancement (TME) and final magnetization recovery after laser bombardment onto the stripe domain configuration.

domain wall. During this process, a greater number of minority spin carriers i.e., demagnetizing majority spin along with additional less mobile excited spins (mainly, minority spin carriers of neighbouring domains) are reverted back from the neighbouring domains through the domain wall over a relatively larger time scale (~ps). In case of stripe domain configurations, this spin angular momentum transfer occurs only in x-direction. This situation creates another imbalance state due to the enhancement of majority carriers and hence of the effective magnetization in the system. Earlier reports have also shown similar transient increases in magnetization in GaMnAs occurring by photoexcited hole-mediated enhancement of ferromagnetic ordering [85]. However, a recent report demonstrated TME before demagnetization [84], which is not observed in our case due to the highly mobile majority spin carriers traversing much faster than minority spins[89]. In the end, these extra excited spins tend to get reinstated to their original domain configuration. As expected, the final magnetization relaxation occurs over a much larger time scale (~ tens of ps). The complete mechanism is illustrated schematically in Fig. 5.4(b). MFM images recorded after pump-probe measurements are presented in Fig. 5.2S(b)-(c) of the Appendix A which confirm that a given domain state retains its configuration post laser excitation. It is to be noted that Elliot-Yafet type of SFS may still occur during the laser-induced demagnetization on both sides of any domain wall [93]. However, this process cannot account for the TME and final magnetization recovery process observed in our system. The

experimental time-resolved traces in Fig. 5.3 are fitted with a modified phenomenological expression to extract the time constants characterizing the ultrafast magnetic response, i.e., the ultrafast demagnetization time (τ_m), fast magnetization recovery time along with TME (τ_{tme}), and the final magnetization relaxation time (τ_r).The analytical expression is[85]:

$$\frac{\Delta M_z}{M_z} = G(t) \otimes \left\{ \Theta(t) . \left\{ A_1 \exp\left(-\frac{t}{\tau_m} \right) + A_2 \left[1 - \exp\left(-\frac{t}{\tau_{tme}} \right) \right] \cdot \exp\left(-\frac{t}{\tau_r} \right) \right\} \right\} \quad (2)$$

Figures 5.5(a), 5.5(c) and 5.5(e) reveal a monotonous variation of all three-time constants (τ_m, τ_{tme}, and τ_r) for [S2], [S5] and [S4] domain configurations at remanence with an increment of pump fluence. The variation of maximum magnetization quenching and the amplitude of magnetization enhancement with pump fluence for [S2], [S5] and [S4] domain configurations at remanence are shown in Figs. 5.5(b), 5.5(d) and 5.5(f) respectively. A slightly faster demagnetization is observed in stripe domain configuration in comparison with InP saturated state. The time scale τ_m follows the trend of previously reported observations of faster demagnetization in an antiparallel state [86,88,317].The maximum magnetization quenching in the stripe domain configuration is also much smaller than the saturated state (Figure 5.3(a)).

The MFM images shown in Figs. 5.1(a)-(e) demonstrate that the number of junctions (domain wall) and the effective junction area are progressively increased across the transition from 1D to 2D domain state which can destroy the ferromagnetic ordering in the system and reduce the effective magnetization. The amplitude of demagnetization can also be reduced due to the loss of ferromagnetic ordering in the initial state prior to laser exposure. On the other hand, the number of junctions and effective junction area are drastically increased in the bubble-like domain state. Here, spin-angular momentum transfer can occur in any direction due to drastic enhancement of disorder in the system. Consequently, demagnetization is irrelevant for this state, and the transfer of spin angular momentum from one domain to the neighbouring domain can only create an imbalance state by introducing some ferromagnetic ordering to the system and enhancing the effective transient magnetization of the system as shown in Fig. 5.3(d) for different pump fluences. The variation of τ_{tme}, and τ_r with pump fluence are shown in Fig. 5.5(e) while the variation of the degree of observed magnetization enhancement is shown in Fig. 5.5(f). TR-MOKE measurements performed in the [S1] and [S3] domain configurations yielded a similar result (Figs. 5.3S(a)-(f), Appendix A).

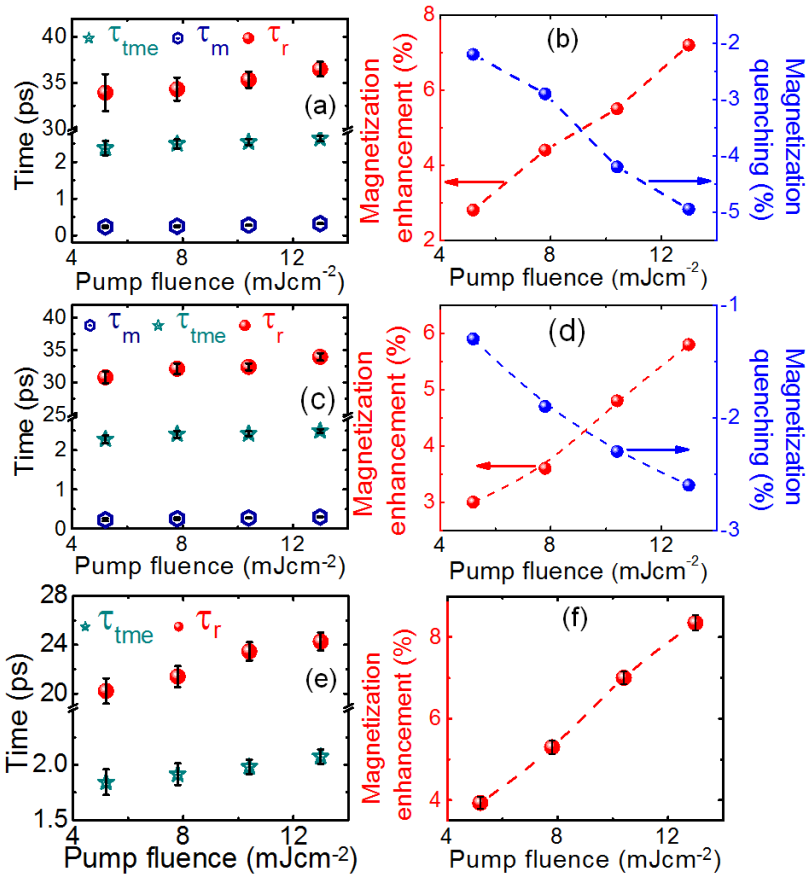

Figure 5.5: (a)-(b) The variation of different time constants and amplitudes with pump fluence for [S2]. (c)-(d) The variation of different time constants and amplitudes with pump fluence for [S5]. (e)-(f) The variation of different time constants and amplitude with pump fluence for [S4].

In addition to influencing the maximum magnetization quenching and leading to faster demagnetization, transfer of spin angular momentum can also influence the amplitude and time for TME. Faster TME and magnetization recovery are also observed due to an increase in number of junctions and junction areas due to the transformation from 1D to 2D domain configuration. Figures 5.6(a)-(b) show the variation of demagnetization amplitude and time with the parameter $\frac{k_y}{k_x}$ which characterizes this phase transition. We observe a small monotonic decrement and faster demagnetization due to this 1D to quasi-1D transition and ending up with zero magnetization loss due

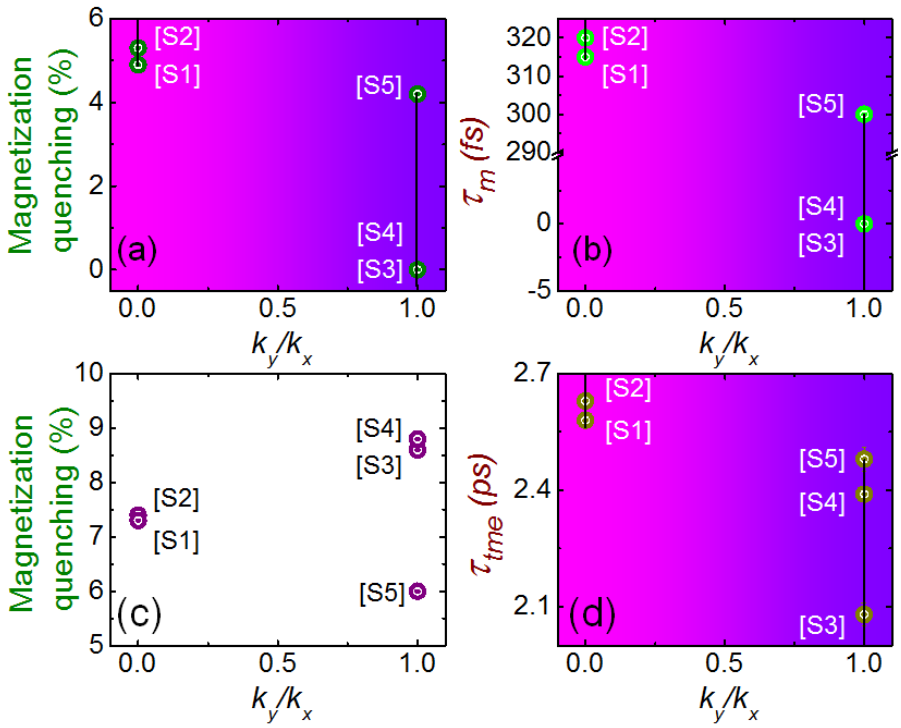

Figure 5.6: (a)-(b) The variation of maximum magnetization quenching and demagnetization time (τ_m) with k_y/k_x. (c)-(d) The variation of transient magnetization enhancement amplitude and time (τ_{tme}) with k_y/k_x.

to very drastic reduction of ferromagnetic ordering in 2D domain configurations. Furthermore, the TME amplitude and τ_{tme} also follow a similar variation with $\frac{k_y}{k_x}$ (Figs. 5.6(c)-6(d)).Our results clearly demonstrate that the demagnetization amplitude, time as well as the timescale and amplitude of magnetization enhancement can be tuned in different domain states by controlling the transfer of spin angular momentum depending on the details of the underlying domain configuration. Moreover, we were able to achieve a significant variation of the laser-induced magnetization response during the phase transition from 1D to 2D domain configurations at remanence, demonstrating a transformation from a two-step to a single-step-like character, which may be exploited for two-step switching operations in ultrahigh speed spintronic devices.

IV. Conclusions:

In this work, different magnetic domain configurations were achieved in a Ta(1.5nm)/Pt(20nm)/$[Co(3nm)/Pt(0.6nm)]_{22}$/Pt(2.4nm) multilayer sample, identified as two nearly pure stripe domain states, labyrinth domain and two bubble-like domain states. The sample shows an

in-plane easy axis with negligible in-plane magneto-crystalline anisotropy. To study the variation of laser-induced magnetization response with the details of the underlying domain structure, time-resolved experiments were performed using a two-color magneto-optical Kerr effect technique. Sub-picosecond ultrafast demagnetization is observed in the stripe domain and labyrinth domain states whereas a transient enhancement of magnetization (TME) follows the fast demagnetization in all the domain configurations studied. A faster demagnetization is observed in the stripe domain states in comparison with in-plane saturation state. The amplitude and time constants of demagnetization and TME are found to be sensitive to the laser pump fluence. A drastic change to zero magnetization quenching is observed in two disordered bubble domain-like configurations which can be attributed to a loss of the initial magnetization of the system. While the initial demagnetization occurs due to the transfer of spin majority carriers from one domain to another, transfer of minority carriers between two neighbouring domains in any direction can transiently enhance the ferromagnetic ordering and resultant magnetization in the system. After a long-time delay (~ few tens of ps for final magnetization relaxation), the enhanced-magnetized state reverts back to its initial domain configuration. Thus, spin-transport-dependent ultrafast demagnetization as well as ultrafast magnetization enhancement is observed in our system which is moreover well controlled by the microscopic domain landscape. This two-step-like behaviour of the laser-induced magnetization dynamics viz. ultrafast demagnetization closely followed by TME opens a new route for further tunability of the magnetization response parameters by exploring different more complex domain configurations in various other ferromagnetic multilayers which will be vital for the development of magnetic spin-texture-driven ultrafast spintronics devices.

Chapter 6

6. Bias Field Orientation Driven Reconfigurable Magnonics and Magnon-Magnon Coupling in Triangular Shaped $Ni_{80}Fe_{20}$ Nanodot Arrays

I. Introduction:

Hybrid systems[119-124] allow us to accelerate the fundamental development in nanotechnology using different carriers such as superconducting qubits, phonons, photons and magnons. The field of magnonics[39,40] uses the carrier magnon (quanta of spin waves) to transfer quantum information coherently from one quantum state to another quantum state in an artificially patterned periodic nanostructure, popularly known as magnonic crystals (MCs)[100,325]. Recent developments in this field have successfully triggered research interest in integrating various fundamental effects such as spin pumping [36,220], interfacial Dzyaloshinskii-Moriya interaction (DMI) [15,17,19], spin-orbit coupling (SOC) [53,326], non-linearity [327,328], topological effects [329,330], spin-textures [113,116] etc. with magnonics. Thereby, it strengthens the fundamentals as well as promoting new-generation magnonic devices with superior functionalities. In this context, the interaction of magnon with different quantum particles such as magnon, microwave phonons, and photons is important for the possibility of energy harvesting and quantum transduction[119,123,328,331-335]. The strength of magnon photon coupling in a cavity resonator is proportional to square root of the number of spins (N) present in the magnetic material. This helps to overcome the weaker coupling strength (g_0) between individual spins and the microwave field, i.e., $g = g_0\sqrt{N}$ [124,331]. It is nontrivial to achieve significant amount of coupling strength from the $\sqrt{N}$ dependence in modern integrated magnetic systems with magnetic elements having nanoscale dimensions. Consequently, magnon-magnon coupling have been demonstrated in an array of works involving primarily magnetic bilayers, multilayers and large microscale elements having very large value of N [332,335-337]. However, it has recently been demonstrated that the magnon–magnon coupling strength in patterned nanostructures can be drastically enhanced by nourishing the inter-element dipolar coupling[328,338] . This opens the possibility of tailoring the coupling strength by various geometric parameters of nanomagnet arrays. This includes element size, shape, and periodicity of the array as well as external factor such as bias magnetic field and microwave power [121,328,331-333]. Recently magnon magnon coupling has also been reported in voltage controlled magnonic nanochannels [51]. Avoided crossing with very large value of

cooperativity of about 60 has been observed numerically in a single nanodot forming a magnonic cavity where the coupling strength depends on geometric parameters of the cavity[333]. Moreover, magnon-magnon coupling has also been demonstrated in the antiferromagnetic resonance modes of a layered antiferromagnet, $CrCl_3$[334] as well as ferromagnetic resonance modes of YIG/Co[332] and YIG/Py[337] heterostructures. However, a huge scope of investigating and optimizing these phenomena lies in patterned ferromagnetic nanostructures.

The fundamental understanding of spin waves (SWs) in myriads of MCs have been explored and number of SW-based miniaturized microwave components and devices have been introduced during last one decade. These include filters[339], transistor[108], multiplexer[107], splitter[103], interferometer[40], grating[46], waveguides[340], phase shifters[341], nanograting couplers[105], directional coupler[104] nanomagnetic antenna[342,343] and neuromorphic computing[344]. In nanodot arrays, inhomogeneous internal field and interdot interaction[345,346] can efficiently control their magnetic properties, leading towards complex spin configurations and spin waves within the nanomagnet array[113,347-349]. In this context the shape of the nanodots have been extensively studied[193,350,351] , providing a testbed for exploring diverse spin textures and variation in nature of SW modes and their anisotropic behaviour. In the above studies the triangular shaped nanomagnets showed most complex SW dynamics with a large number of standing SWs. These cover a wide range of frequencies as well as occurrence of both even and odd modes due to broken mirror symmetry about a certain axis. Engineering of shape distortion in coupled arrays of ferromagnetic nanodots have also been investigated in detail[113,352-354] to control those magnetic interactions. A linear chain of deformed nanodot array each containing magnetic vortex state has been reported to efficiently transfer excitation energy of vortex core gyration via SWs[352,353]. Deliberate introduction of controlled asymmetric egglike shape distortion to an ideal elliptical structure has been shown to lift the degeneracy of end modes[354].

In view of the above knowledge, we have investigated the spin-wave dynamics of triangular shaped $Ni_{80}Fe_{20}$ (permalloy; Py hereafter) nanodot arrays having vertex deformation. While vertices 1 and 3 have rounded corners, vertex 2 is flattened. Our objective is to study the stability of the complex SW modes in such structure with deformation as well possibility of creation or annihilation of existing modes of a triangular shaped nanodot. We have measured the spin-wave dynamics in two different samples of varying lattice constants using broadband ferromagnetic resonance (FMR) spectroscopy

and analyzed the results using micromagnetic simulations. In this system we have observed an energy transfer between two lower frequency modes by varying the strength of in-plane bias magnetic field, i.e., a mode repulsion (avoided crossing) indicating their mutual coherence. The magnetic stray-field interaction changes drastically in the mode repulsion regime due to the anisotropic dipolar interactions between the triangular nanodots. Additionally, we have observed a relatively large and stable frequency gap due to mode repulsion for specific in-plane bias field angles. This frequency gap remains invariant with the rf excitation power (P) over a long range, i.e., -15 dBm $\leq P \leq$ +5 dBm. However, the strength of avoided crossing, SW frequency and the frequency gap can be tuned by varying the nanodots dimensions. Furthermore, using micromagnetic simulations, we have demonstrated that the coupled SW modes propagate longer as opposed to uncoupled modes present in the same system. This observation will aid the design energy-efficient and hybrid systems-based new generation nanoscale magnonic devices.

II. Experimental and Numerical Methods:

Sample Preparation: A continuous Py film of 20 nm thickness and two 20-nm-thick Py triangular shaped dot arrays arranged in square lattice with side length (lattice constant) of 325 nm (395 nm) [S1] and 235 nm (305 nm) [S2], respectively, were fabricated by a combination of electron beam lithography (EBL) and electron beam evaporation (EBE). First, a 20-nm-thick Py film with a 60-nm-thick protective Al_2O_3 layer was deposited using EBE on top of a self-oxidized Silicon (Si) (100) substrate in an ultrahigh vacuum chamber at a base pressure of 2×10^{-8} Torr. For EBL, a bilayer polymethyl methacrylate/methyl methacrylate PMMA/MMA bilayer resist pattern was used on the Si substrate for a dose time of 1.0 μs and at a beam current of 500 pA. A coplanar waveguide (CPW) made of Au with 150 nm thickness, 25 μm central conductor width (w), 300 μm length, and 50 Ω nominal characteristic impedance (Z_0), was integrated on top of the triangular dot array as well as the continuous Py film, at a base pressure of 6×10^{-7} Torr for the broadband FMR measurement. Subsequently, a 5-nm-thick protective Al_2O_3 layer was deposited on top of the Au layer at the same base pressure. The waveguide was patterned using maskless photolithography.

Measurement Technique: The surface topography of the samples was imaged by scanning electron microscope (SEM) and was further supported by atomic force microscope (AFM) images. The broadband FMR experiments were performed using a vector network analyzer (VNA, Agilent, PNA-L, N5230C; 10 MHz to 50 GHz) and a homebuilt high-frequency probe station with a nonmagnetic G-S-G type probe (GGB Industries, Model No. 40A-GSG-150-EDP) [193,328]. The excitation power of

the microwave input signal was varied in the range of −15 to +5 dBm by the VNA and fed into a CPW structure shorted at one end, generating a microwave magnetic field h_{rf} along the y-axis of the nanodot array (Figure 6.1(a)). The in-plane bias magnetic field (H) was rotated in the x-y plane in a range $0^o \leq \varphi \leq 20^o$ and $160^o \leq \varphi \leq 200^o$ with respect to x-axis and the output signal was collected from the same end of the CPW in the reflection geometry.

Micromagnetic Simulation: We performed micromagnetic simulations to underpin the nature and origin of the SW modes of the deformed triangular nanodot arrays using the Mumax3 software[277]. We also used LLG-Micro[278] software to calculate the stray field and internal field distributions, respectively. The samples were discretized into rectangular prism-like cells with dimensions 4 × 4 × 20 nm^3. The material parameters, i.e., Gilbert damping constant (α) = 0.008 [328,351], exchange stiffness constant (A) = 1.3 × 10^{-6} erg/cm [328,347], saturation magnetization (M_s) = 720 emu/cm^3, gyromagnetic ratio (γ) = 17.95 MHz/Oe and magneto-crystalline anisotropy constant (K) = 0 were used in the simulation. To understand the spatial maps of power and phase of each SW mode, we used our home-built MATLAB-based code DOTMAG[355]. Here, the fast Fourier transformation (FFT) of time-domain magnetization was obtained along any surface of sample by keeping one of the coordinates fixed (either x or y or z). If we fix y = y_1 then the FFT is taken along the x-z plane is given by: $\widetilde{M}^{z_1}(f,x,z) = FFT\left(M^{y_1}(t,x,z)\right)$. Then the power and phase can be calculated for a specific resonant mode of frequency $f = f_1$ which can be written as:

Power: $$P^{y_1 f_1}(x,z) = 20log_{10}\left|\widetilde{M}^{y_1}(f_1,x,z)\right| \quad \text{and}$$

Phase: $$\phi^{y_1 f_1}(x,z) = \text{atan2}\left(Im\left(\widetilde{M}^{y_1}(f_1,x,z)\right), Re\left(\widetilde{M}^{y_1}(f_1,x,z)\right)\right)$$

$$= 2\arctan\frac{Im\left(\widetilde{M}^{y_1}(f_1,x,z)\right)}{\sqrt{\left(Re\left(\widetilde{M}^{y_1}(f_1,x,z)\right)\right)^2+\left(Im\left(\widetilde{M}^{y_1}(f_1,x,z)\right)\right)^2}+Re\left(\widetilde{M}^{y_1}(f_1,x,z)\right)} \quad (1)$$

III. Results and Discussions:

A schematic of the experimental setup is shown in Fig. 6.1(a). Figures 6.1(b)–1(c) show SEM images of two deformed equilateral triangular nanodot arrays with base length (l) and lattice constant (a) of (l = 325 nm and a = 395 nm; S1) and (l = 235 nm, and a = 305 nm; S2) with about ±10 nm deviation in

lateral dimensions over the whole array. The coordinate system along with H and φ are represented at

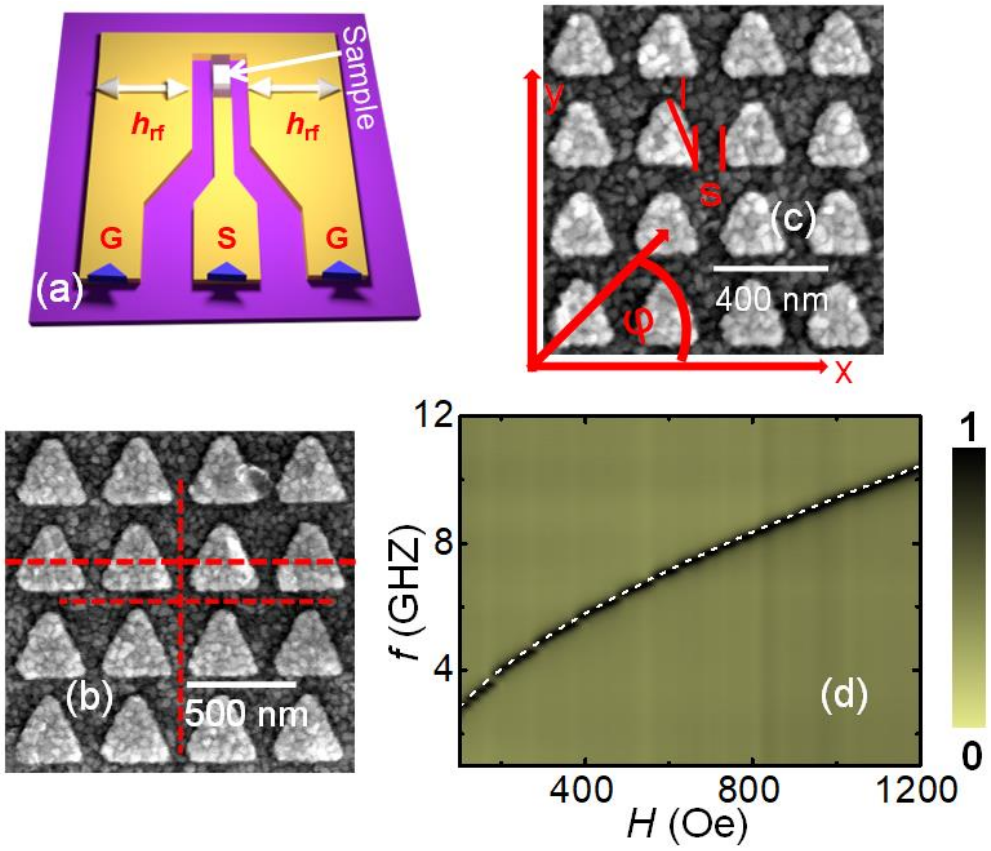

Figure 6.1: (a) Schematic of the experimental geometry. The directions of the rf field (h_{rf}) are shown in the schematic. (b)–(c) Scanning electron micrographs of $Ni_{80}Fe_{20}$ triangular nanodot arrays S1 and S2. The bias field orientation (φ), base length (l), and separation (s) are shown in (c). (d) Surface plot of bias-field-dependent SW mode frequencies for Py thin film of 20-nm thickness at excitation power of $P = -15$ dBm. The Kittel fit is shown by white line.

the bottom left corner of Fig. 6.1(c). Figure 6.1(d) shows the experimental H-dependent FMR frequency (f) of the Py thin film as a surface plot, which is fitted with the Kittel formula [225], given by:

$$f = \frac{\mu_0 \gamma}{2\pi}\sqrt{(H + H_K)(H + H_K + 4\pi M_S)} \qquad (2)$$

to extract various magnetic parameters as used in the micromagnetic simulations stated above. Here, $\gamma = \frac{g\mu_B}{h}$, g is the Lande g-factor and μ_0 is the vacuum permeability. The magnetic parameters extracted from the fit are g = 2.04 ± 0.02, M_S = 725 ± 10 emu/cc and the anisotropy field (H_K) = 0. The spatial maps of magnetization at angles φ = 0º, 15º, and 165º at H = 850 Oe are shown in Fig. 6.1S (Appendix

B). To explore the effects of the defects and deformation on the SW modes on triangular shaped nanodot, we compared the simulated SWs for perfect shaped and deformed single triangular nanodot

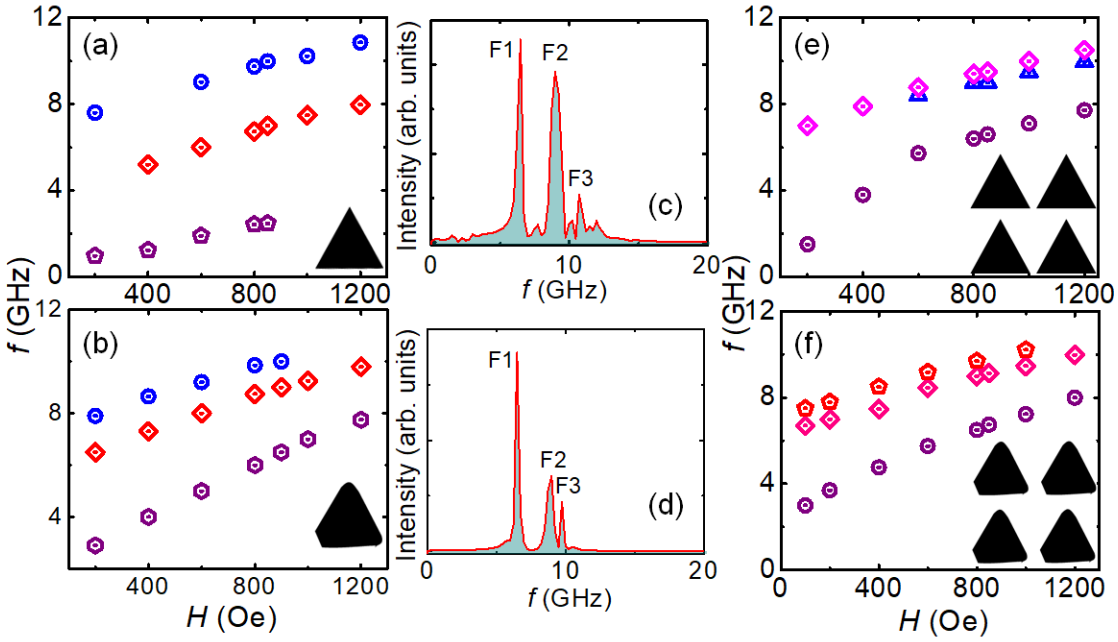

Figure 6.2: Simulated SW frequencies as a function of bias magnetic field at an orientation (φ) of 0º and P = -15 dBm for single regular triangle (a) and deformed triangle (b). Inset shows the representation of single triangle. Simulated SW spectra for regular triangular dot array (c) and deformed triangular dot array (d). Simulated SW frequency as a function of bias field at φ of 0º and P = -15 dBm for regular triangle dot array (e) and deformed triangle dot array (f). Inset shows representative magnified view of triangular dot array.

at φ = 0º as shown in Figs. 6.2(a)-(b). While for the perfectly shaped single triangular nanodot the two higher frequency modes (F2 and F3) show regular magnetic field variation of frequency, the lowest frequency mode (F1) ceases to exist for $H \geq 850$ Oe. In contrast, for the deformed single nanodot two low frequency modes (F1 and F2) again display regular field dispersion with slight differences in frequencies and the highest frequency mode (F3) ceases to exist for $H \geq 900$ Oe. On other hand, the SW spectra for arrays of perfectly shaped and deformed triangular nanodots are shown in Figs. 6.2(c)-(d) and the corresponding bias field dependence of SW frequencies are shown in Figs. 6.2(e)-(f). In case of the perfect shaped triangular nanodot array, the two higher frequency modes (F2 and F3) are very close in frequency, whose separation decreases and eventually they merge at around 600 Oe. On the other hand, the lowest frequency mode shows the usual magnetic field variation of its frequency. In case of deformed nanomagnets, F2 and F3 are again close together but their spacing remains nearly invariant with bias magnetic field, while F1 shows similar behaviour as for the perfect shaped triangular

nanodot array. It is therefore clear that the role of defect on the distribution of dipolar interaction between the nanomagnets in our real sample is not same as perfect shaped triangular nanodot array.

Figure 6.3(a) represents three representative experimental SW spectra with three different values of H of 1200 Oe, 800 Oe and 400 Oe for the sample S1 at $\varphi = 0^{o}$ and P = -15 dBm. Figures 6.3(b)-(e) display four representative bias-field-dependent SW frequencies (Re(S_{11}) parameter) for S1 at $\varphi = 0^{o}$, 15^{o}, 165^{o} and 195^{o}, respectively, at P = -15 dBm. Here, the experimental results are shown by 3D surface plot

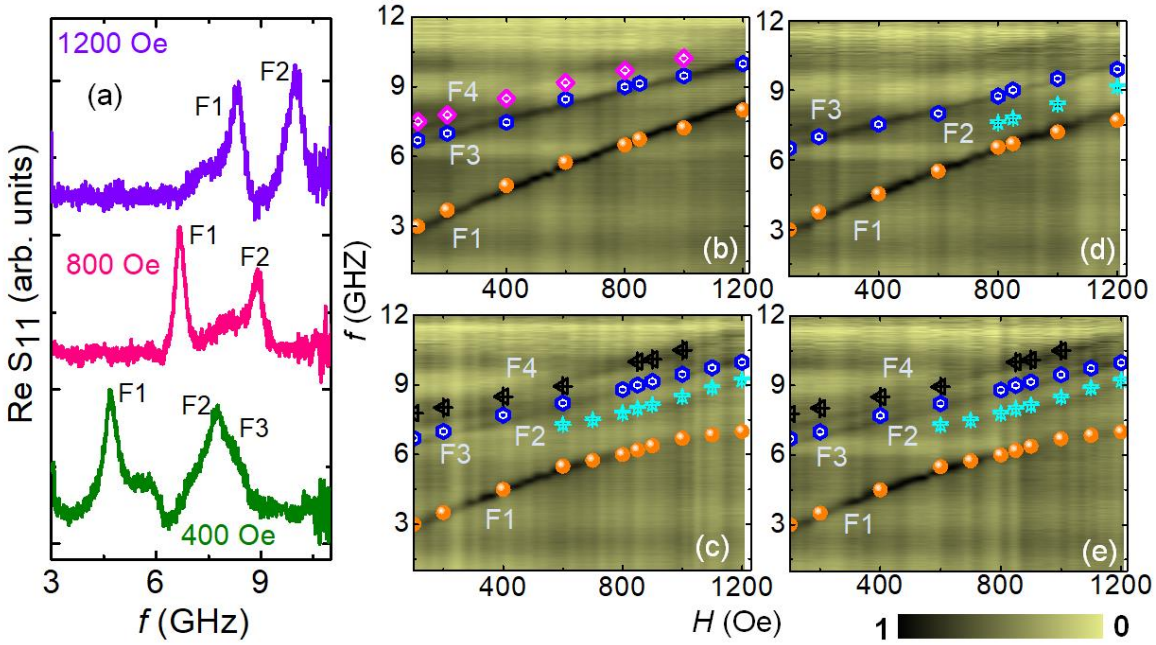

Figure 6.3: (a) Re(S_{11}) parameter as a function of bias magnetic field at $\varphi = 0^{o}$ and P = -15 dBm for sample S1. (b)-(e) Surface plots of bias-field-dependent SW mode frequencies for φ = (b) 0°, (c) 15°, (d) 165° and (e) 195°, respectively, at P = -15 dBm. Simulated SW frequencies are shown by symbols. The color map of experimental surface plot is shown at the bottom of the figure.

and simulated SW frequencies are shown by symbols. Micromagnetic simulations have qualitatively reproduced all the observed experimental modes using near experimental parameters as discussed in the micromagnetic simulation section. At $\varphi = 0^{o}$ and 180^{o}, identical field dispersion of SW modes is observed as shown in Fig. 6.3(b). Here three monotonic and noninteracting modes are observed. The nature of F1 and F3 modes and their H-dependence at $\varphi = 165^{o}$ is similar to that for $\varphi = 0^{o}$ as shown in Fig. 6.3(d). However, one additional monotonic and noninteracting mode (F2) appears in the simulated

SW spectra for $H > 800$ Oe at $\varphi = 165^{\circ}$ (Fig. 6.3(d)). At $\varphi = 15^{\circ}$ and 195°, we have four SW modes in experimental as well as simulated SW spectra (Fig. 6.3(c) and Fig. 6.3(e)). Here, an avoided crossing is observed between two modes F1 and F2 at $H \approx 900$ Oe, and we will characterize the nature of all SW modes later in this article. Furthermore, SW dispersion for deformed single triangular nanodot at $\varphi = 15^{\circ}$ is shown in Fig. 6.2S (Appendix B) where two SW modes (F2 and F3) cross each other at $H =$ 700 Oe and avoided crossing between F1, and F2 or F3 mode also occurs at around the same field value. Figure 6.4(a) is a magnified version of F1 and F2 modes for three different φ values of 10°, 15° and 20° for the sample S2 at frequencies where avoided crossing occurs as discussed later. Here, the intensity and the linewidth of F1 and F2 modes are exchanged as we increase φ from 10° to 20°. These phenomena correspond to a mode crossover with φ[356]. The weightage of intensity and linewidth for both modes at 15° is almost identical. The lifetime of F1 and F2 also interchanges with increasing φ from 10° to 20° through a state at around 15° where both of those two modes have an equal probability of lifetime. This observation indicates a route to control lifetime of a SW mode. The separation between these two modes at avoided crossing point is defined by the quantity $\delta_{FR} = F2_R\text{-}F1_R$ and the complete variation of δ_{FR} and the behaviour of F1 and F2 will be discussed later. The bias-field-dependent SW frequencies are shown in Figs. 6.4(b)-(e) for S2 for $\varphi = 0^{\circ}$, 15°, 165° and 195°, respectively, at $P = -15$ dBm, which also reveals rich anisotropic SW properties. At $\varphi = 0^{\circ}$ and 180°, two monotonic and noninteracting modes with identical bias field variation are observed in the experiment as shown by the 3D surface plot in Fig. 6.4(b). On that other hand, we observe three similar modes in the simulation as shown by the symbols. At $\varphi = 165^{\circ}$, we observe two modes (F1 and F3) whose frequencies are monotonically varying with bias field over the entire field region, along with one additional mode (F2) appearing for $H \geq 760$ Oe between F1 and F3 (Fig. 6.4(d)). The F2 mode also varies monotonically for rest of the increasing bias field both in the experiment as well as the simulation. For $\varphi = 15^{\circ}$ and 195°, we observe a drastically different behaviour as shown in Fig. 6.4(c) and 6.4(e). Here, the lowest frequency mode F1 shows a downward curvature, while two higher frequency modes F2 and F4 show upward curvature with a clear signature of mode repulsion or avoided crossing at $H \approx 845$ Oe. Moreover, modes F1 and F2 show a crossover where mode F2 sacrifices its power to F1 for $H \leq 600$ Oe, while they coexist in the region: $600 \text{ Oe} \leq H \leq 1200$ Oe. The highest frequency mode F4, on the other hand, shows a monotonic variation with H in the entire field region (Fig. 6.4(c) and 6.4(e)). The

SW mode frequencies are slightly lower for S1 than that for S2. Table 1 shows different parameters associated with the avoided crossing for S1 and S2, which will be discussed later in this article.

Figure 6.5 displays the nature of each SW mode at avoided crossing point (H = 900 Oe for S1 and 850

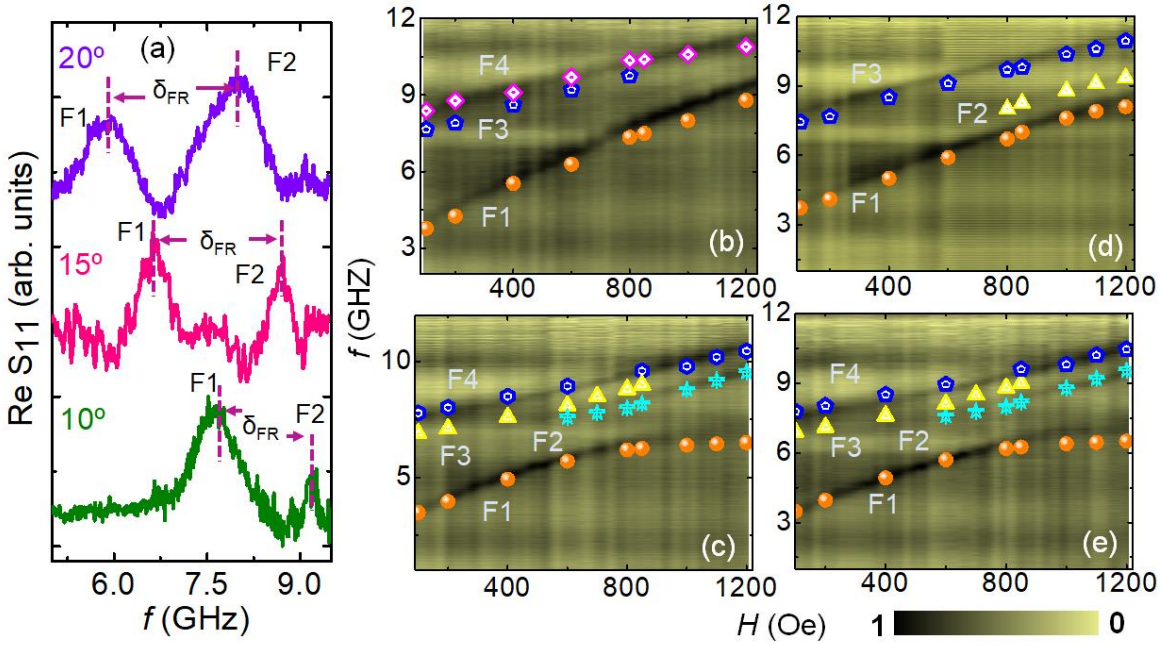

Figure 6.4: (a) Close in representation of Re(S_{11}) parameter at different values of φ = 10º, 15º and 20º at P = -15 dBm for sample S2. (b)-(e) Surface plots of bias-field-dependent SW mode frequencies for φ = (b) 0°, (c) 15°, (d) 165° and (e) 195°, respectively, at P = -15 dBm. Simulated SW frequencies are shown by symbols. The color map of experimental surface plot is shown at the bottom of the figure.

Oe for S2) using the spatial distribution of simulated power and phase profiles. The images reveal primarily three types of modes; a) purely backward volume (BV)-like mode with mode number representing as (m, 1), b) purely Damon-Eshbach (DE)-like mode with mode number (1, n) and c) mixed BV-DE-like mode with mode number (m, n). The mode F1 for both S1 and S2 shows mode number of (4,1) at φ = 0º and 15º. However, the quantization number of F1 changes to (3,1) for both S1 and S2 at φ = 165º. Interestingly the flattened edge of the triangle holds one localized mode for φ = 0º and 15º, which disappears at 165º. On the other hand, F2 shows identical behaviour with mode number of (4,1) at φ = 15º and 165º but it ceases to exist at φ = 0º for both S1 and S2. For F3 the mode

quantization number continuously changed as (7,2), (5,1), (6,1) for φ = 0º, 15º, 165º in S1 and (4,2), (4,3), (3,3) for φ = 0º, 15º, 165º in S2. Interestingly, F4 retains its mode character at both φ = 0º and

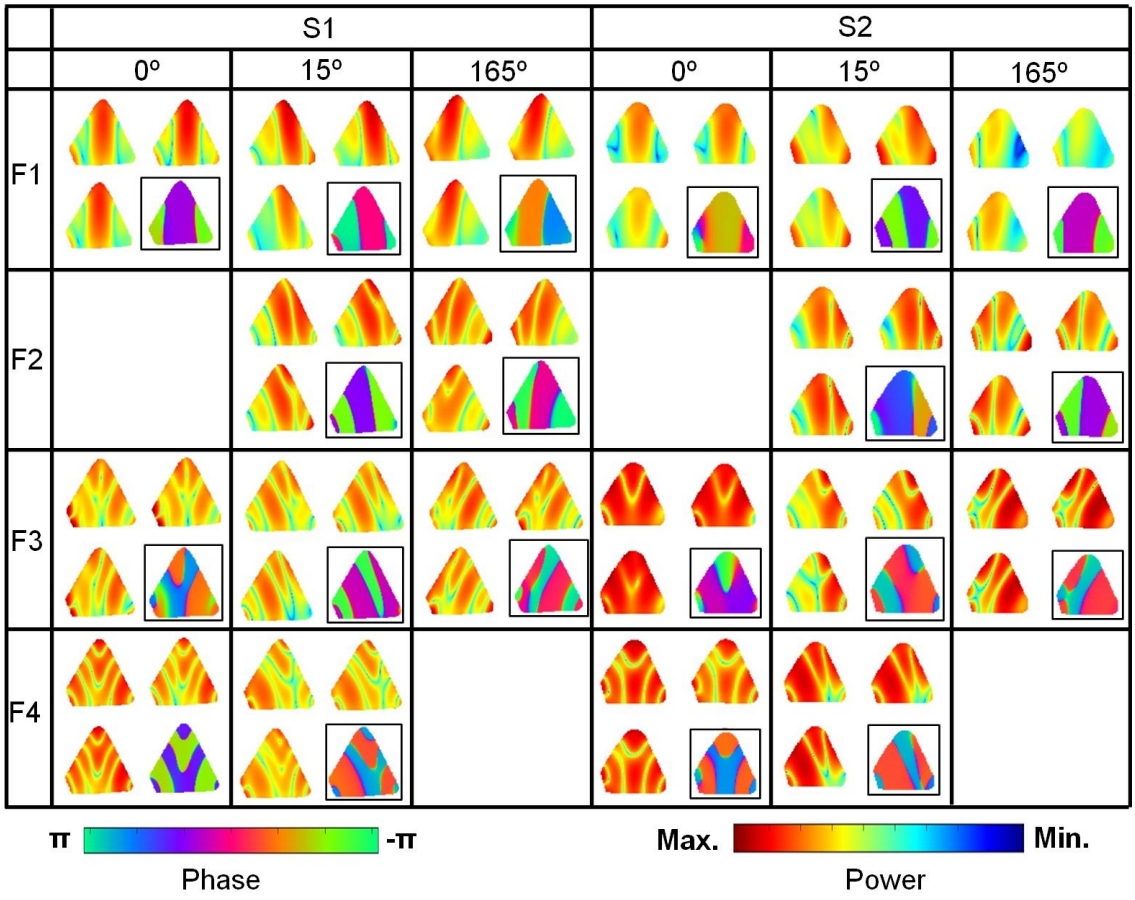

Figure 6.5: Simulated spatial distribution of power and phase of the SW modes during the avoided crossing (*H* = 900 Oe for S1 and 850 Oe for S2) at φ = 0°, 15°, and 165°.

15º (5,3) in S1 and (5,2) in S2 before disappearing at 165º. However, despite having the same quantization number, the spatial distribution of power and phases are not identical due to slightly different spin configuration with angle and dimensions. Nevertheless, the most remarkable aspect is that at φ = 15º, the mode quantization number (4,1) and spatial distribution of phase match exactly for F1 and F2 modes having a constant phase difference (of ~ 90º). Such a phase difference of ~ 90º between two interacting modes due to strong magnon-magnon coupling have already been reported in synthetic antiferromagnetic systems[357]. Therefore, here too we anticipate the presence of magnon-magnon coupling between modes F1 and F2 presumably via the dynamic dipolar interaction as observed in other nanomagnetic systems before[328,338]. Such similarities in phase profiles between

modes F1 and F2 have also been observed for sample S2. We have further calculated the magnon-magnon cooperativity, C = $\frac{\delta FR^2}{k_1 k_2}$,where k_1 and k_2 are full width at half maximum of the linewidth and δ_{FR} is the separation between the peaks of F1 and F2 at the avoided crossing point. The extracted C-values are shown in Table 1 for both S1 and S2. At φ = 15º and 20º for S2, and φ = 15º for S1, $\delta_{FR} > k_1$ and k_2, i.e., the interaction between F1 and F2 can be considered to fall in the strong coupling regime[358]. We have observed highest C-value at φ = 15º for both the samples (C = 3.62 for S1 and C = 21.11 for S2). However, at φ = 10º, $\delta_{FR} < k_1$ and $> k_2$, indicates that the coupling strength is intermediate for both S1 and S2. Here, we observe relatively large C-value for S2 due to $\delta_{FR} < k_1$ and $>> k_2$.

Table 1: Important parameters associated with avoided crossing for both S1 and S2.

Sample	**Angle (φ) (°)**	**Magnetic Field (*H*) (Oe)**	**Experimental δ_{FR} (GHz)**	**Simulated δ_{FR} (GHz)**	**Cooperativity C**
D-325-S-70	10	1080	1.08	0.8	0.65
(S1)	15	900	1.71	1.4	3.62
D-235-S-70	10	1020	1.57	1.3	13.5
(S2)	15	850	1.91	1.75	21.11
	20	795	2.23	2.0	2.75

For further insights into this observation, we simulated magnetic stray field distributions for both S1 and S2. Figures 6.6(a)-(c) display the simulated stray field distribution for sample S2 for φ = 0º, 15º, and 165º at *H* = 850 Oe (i.e., at the avoided crossing point). A significant variation in the stray field interaction is observed at φ = 15º, where each nanodot is found to be coupled with its neighbouring nanodots via stray magnetic fields. The stray-field interaction for S1 also has similar distribution with φ and is shown in Figs. 6.3S(a)-(c) of the Appendix B. Here, the uncompensated spins[328,349] at the edges of the dots are modified significantly at the avoided crossing point within a specific range of φ and that boosts the dynamic dipolar interaction between the neighbouring nanodots. Next, we investigate the transformation of simulated magnetostatic field distribution at different φ values for S1

and S2. The linescans of stary field distribution (B_x, B_y) in nonmagnetic region are shown in Fig. 6.6(d) for S2. Figure 6.6(e) shows the variation of (B_x, B_y) with φ for S2. The maximum value of B_x and B_y

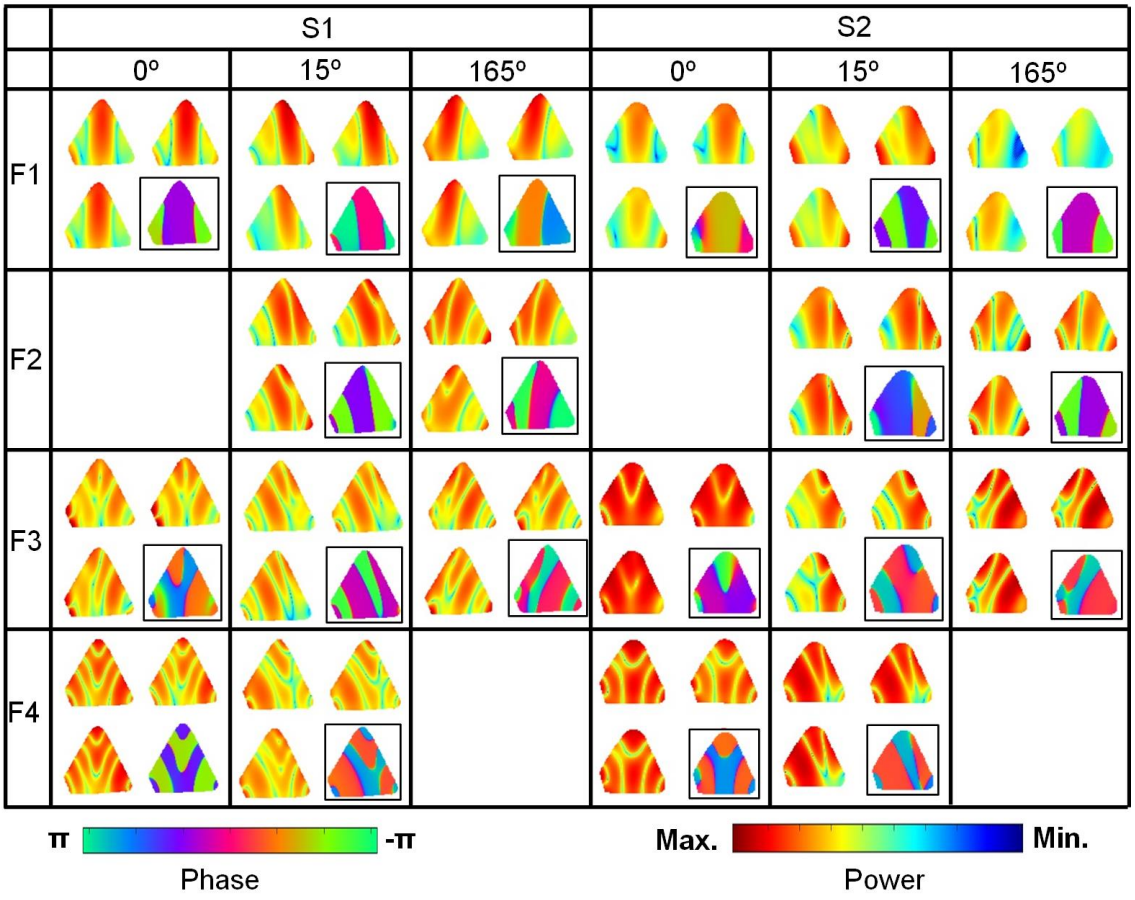

Figure 6.6: Simulated spatial distribution of power and phase of the SW modes during the avoided crossing (H = 900 Oe for S1 and 850 Oe for S2) at φ = 0°, 15°, and 165°.

are close to each other at 10° ≤ φ ≤ 20° whereas they are well separated at other angles. We also calculated the internal field inside the triangles for S2 and presented it in Fig. 6.6(f). The stray-field distribution for S1 also has similar variation with φ and is shown in Figs. 6.3S(d)-(f) of the Appendix B. The (B_x, B_y) and internal field values are slightly larger for S1 than for S2 and the variation of B_x-value with φ follows the same trend as the variation of the C-value with φ (Table 1).

Figures 6.7(a)- 6.7(b) shows the bias-field dependent SW frequencies for P = +5 and 0 dBm, which can be compared to Fig. 6.4(c) which shows the same for P = -15 dBm at φ = 15° for S2. The characteristic features of all SW modes are almost identical in all three cases. Figure 6.7(c) presents the variation of δ_{FR} with P for -15 dBm ≤ P ≤ +5 dBm, which shows invariance within this power

range. Moreover, the cooperativity factor *C* is also invariant within this power range. The spatial distribution of magnetization is found to be nearly identical for this power range as presented in the inset of *P* = -15 dBm (left) and +5 dBm (right) plots. To validate this result, we also calculated variation of stray field distribution and that is also found to be invariant within this power range as shown in Fig. 6.7(d). We have observed similar results for S1 too due to the reasons as discussed above.

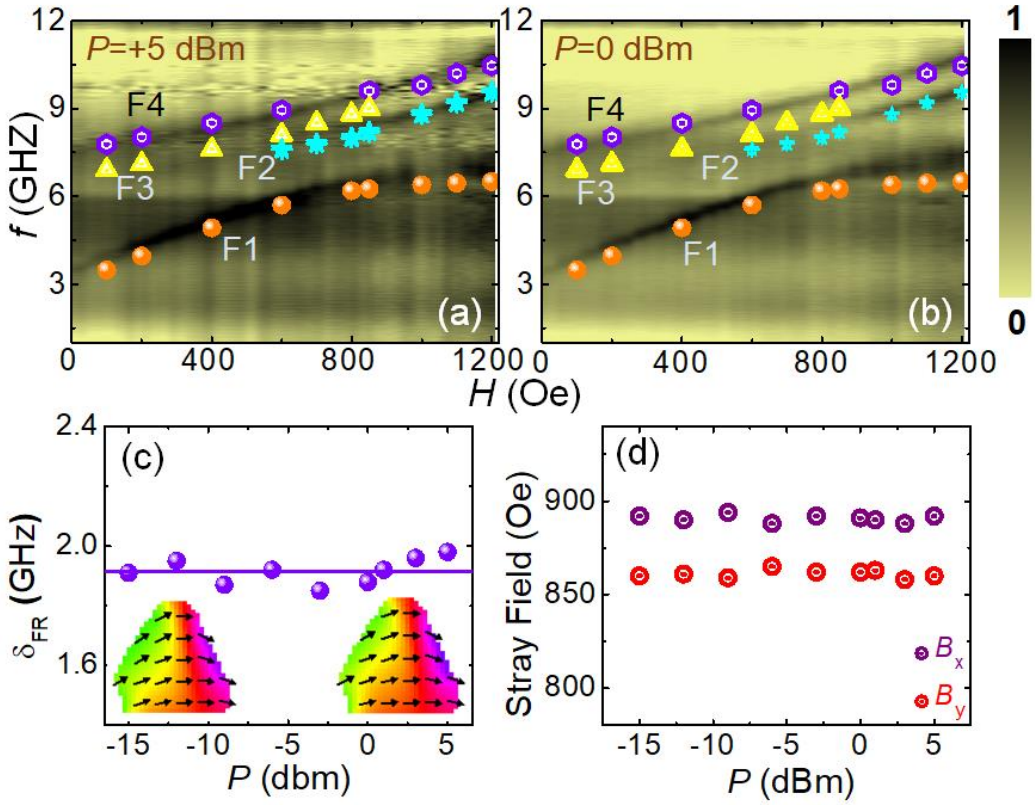

Figure 6.7: (a)-(b) Surface plots of bias-field-dependent SW mode frequencies for *P* = +5 dBm and 0 dBm, respectively, for φ = 15°. Simulated SW frequencies are shown by symbols. The color map of experimental surface plot is shown at the right side of the figure. (c) Variation of avoided crossing gap (δ_{FR}) as a function of *P* for sample S2. Inset shows representative magnetization at *P* = -15 dBm (left), and *P* = +5 dBm (right). (d) Variation of simulated stray magnetic field distribution with *P* for φ = 15°.

Figure 6.8 provides an exemplary demonstration of manipulation of SW propagation with external bias field angles at *H* = 850 Oe and *P* = -15 dBm. Using Mumax3 software, we launched a time-varying field of 'sinc' profile with frequency cut-off of 20 GHz over a small square region (as indicated by black square) within the dot at the centre of a 9 × 9 array of nanomagnets. Figures 6.8(a)-(c) shows the spatial distribution of power corresponding to the different SW modes obtained for S2 at φ = 0º, 15º (195º), and 165º, respectively. Figure 6.8(a) (φ = 0º) shows that mode F1 is mostly dispersive along

the y-direction (> 1.2 μm) but shows a rapid dissipation along the x-direction (about 0.7 μm). For φ = 15º (195º), both F1 and F2 propagate nearly isotropically in all directions, i.e., both modes are

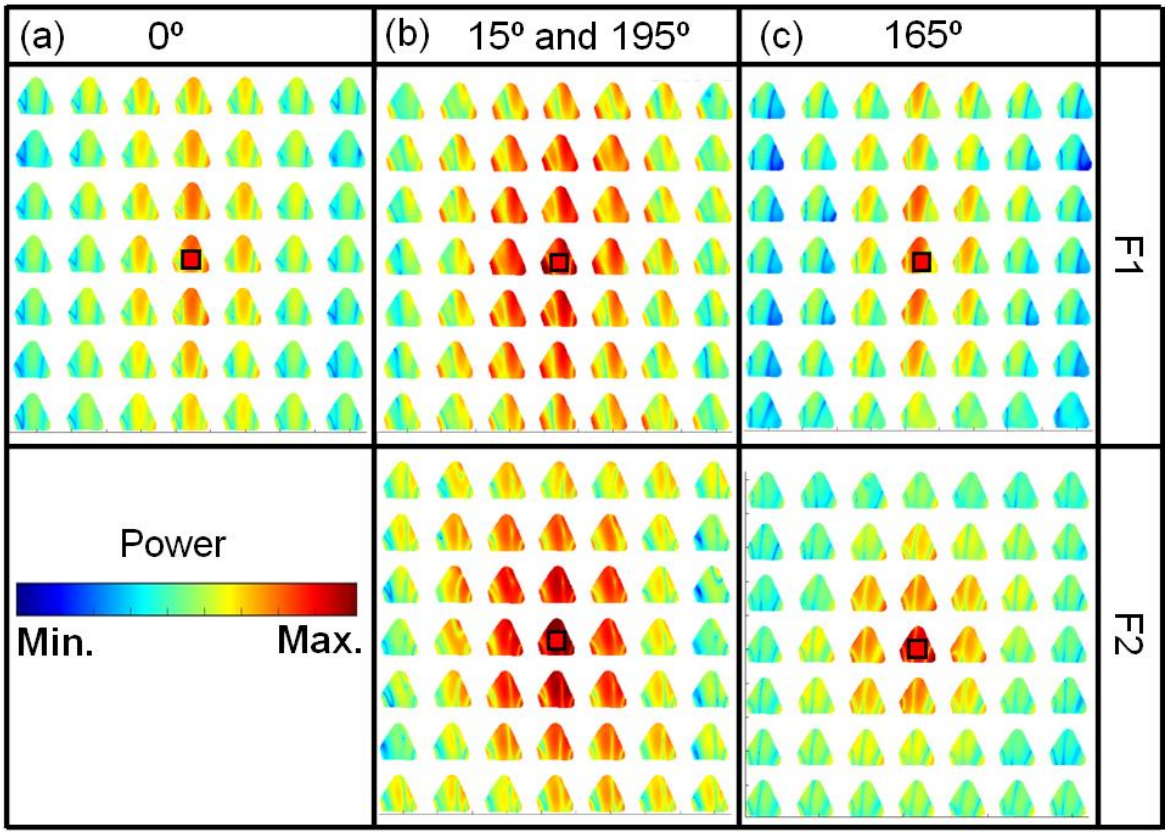

Figure 6.8: Simulated spatial distribution of power corresponding to two lowest frequency SW branches for sample S2 for φ = (a) 0°, (b) 15° (195°) and (c) 165°.

dispersive in both x and y directions with propagation length of greater than 1.2 μm in the y-direction and about 1.0 μm in the x-direction, as shown in Fig. 6.8(b). These two modes have also shown a dispersion along the corner of figures. Figure 6.8(c) (φ = 165º) again shows no coherence between F1 and F2 leading to their faster decay upon local excitation. The mode F1 decays within about 0.6 μm length from the excitation centre along the x-direction and 1.2 μm length along the y-direction, whereas mode F2 disappears within about 0.6 μm length from the excitation centre along both x- and y-direction. Overall, these simulation results reveal an interesting feature for the coupled modes F1 and F2. Due to their mutual magnon-magnon coupling these hybrid modes coherently propagate much longer through the array in a nearly isotropic manner at φ = 15º (195º) as opposed to φ = 0º and 165º. The other uncoupled modes also do not show such coherent propagation characteristics. This also asserts the magnon-magnon coupling between F1 and F2 at φ = 15º (195º). Such selective and

anisotropic magnon-magnon coupling and the ensuing coherent propagation of SW modes will be important for the development of improved classical or quantum magnonic devices based on such nanodots array.

IV. Conclusions:

In summary, we have performed a combined experimental and simulation study revealing anisotropic SW mode anticrossing in 20-nm-thick Py triangular shaped nanodot arrays. By varying the azimuthal angle of bias magnetic field in the range $0^o \leq \varphi \leq 20^o$ and $160^o \leq \varphi \leq 200^o$, we have investigated the bias-field strength dependent SW frequencies for two samples, S1 and S2. We have observed avoided crossing between two SW branches in a range of $10^o \leq \varphi \leq 15^o$ as well as $190^o \leq \varphi \leq 195^o$ for S1, and $10^o \leq \varphi \leq 20^o$ and $190^o \leq \varphi \leq 200^o$ for S2. This is found to be originated from the anisotropic behaviour of dynamic dipolar interaction between the nanodot with φ. The avoided crossing occurs between F1 and F2 modes when significant variation in stray magnetic field is also observed in the system. In addition, the spatial distribution of phase of these two modes are found to be identical with a 90^o phase offset. These two modes show spatial coherence over the entire array during the occurrence of avoided crossing due to their mutual coherence. This interesting feature of SW can be used to design directional coupler or splitter. We have also observed that the strength of mode avoided crossing is also invariant of the rf excitation power over a wide range of -15 dBm $\leq P \leq$ 5 dBm. However, it is possible to reconfigure the strength of the mode coupling and the anticrossing field by varying the azimuthal angle of bias field for both the samples. Furthermore, we have demonstrated by simulation that the coupled SW modes propagate over longer distances through the array as opposed to other modes in these samples. Finally, the observation of anisotropic behavior of the magnon–magnon coupling and the longer SW propagation length for the coupled SW modes in such ferromagnetic nanodot arrays are promising candidates for designing energy-efficient and hybrid system-based new generation nanoscale magnonics.

Chapter 7

7. Spin Texture Driven Reconfigurable Magnonics

I. Introduction:

Modern charge-based circuits consist of a large number of transistors fabricated as integrated chips with metallic interconnectors. With ever-increasing density of storage, memory and processor units the technology faces huge challenges of thermal runaway [6] and the thermal management is proposed to be done more efficiently by spin-based devices. Consequently, research fields like spintronics [10,359], magnonics [39,100], spin-orbitronics [312] and magnon spintronics [360] have emerged rapidly during last few decades. In these fields, the charge current is replaced by various alternatives such as spin polarized current, pure spin current, magnon current to name a few. Magnonics use spin waves (SWs) as information carrier through a periodically patterned magnetic media, popularly known as magnonic crystal (MC). It deals with the excitation, propagation and detection of magnons and its properties such as magnonic band structures, band gap, spatial mode profiles, etc. SWs have much smaller propagation velocity than that of the electromagnetic (EM) waves at the same frequency and hence, several order shorter wavelength (micro to nanometer scale) than its EM-wave counterpart. Thus, magnonics fit perfectly with nanotechnology, leading towards on-chip data transfer and processing. The SW properties of MCs can be efficiently tailored by its geometric parameters such as shape [351], size [361], lattice constant [362], lattice symmetry [118], material [363] and external magnetic field, and reconfigurable magnonic band structure [114] can be obtained.

During the last one decade coupled arrays of ferromagnetic nanodots have been studied in great detail [352,353,364-367]. Among them coupled chains of nanodots have attracted significant interest due to their inherently large shape anisotropy aiding efficient transfer of energy, while retaining its large tunability as opposed to a plain nanowire or nanostripe structure. Consequently, linear arrays of nanomagnets have been used to design magnetic logic architecture [366,367]. Furthermore, linear arrays of magnetic nanodisks containing vortex states have been shown to transfer excitation energy in terms of vortex core gyration aided by SW [352,353] and its experimental demonstration [364,368] leading towards magnetic vortex-based logic operation [368] and proposed transistor operation [109]. Tunability of magnetic configurational anisotropy in differently ordered chains of elliptical nanomagnets have been demonstrated [369]. Recently, linear arrays of shaped nanomagnets have been used for reconfigurable waveguide design to transmit and locally manipulate SWs without the need for any external bias field after initialization [340]. More recently, strongly overlapped nanomagnets

forming pusedo-one dimensional magnonic crystals have shown reconfigurable magnonic band structure by slight variation of the bias field orientation [114]. However, the role of magnetic history dependent tunable spin texture on the SW propagation in a chain of nanomagnets has not been explored in the literature.

Here, we have investigated the SW dispersion by Brillouin light scattering (BLS) in chains of connected nanomagnets, where each nanomagnet with 30 nm thickness has a rounded rectangular shape with 780 nm × 540 nm lateral dimensions having a 230 nm radius of curvature of the rounded ends and they are all tilted at about 29° from the chain axis. By changing the magnetic-field history the spin texture is interchanged between magnetic leaf, 'S' and vortex state and the ensuing magnonic band structure, including band gap is reconfigured. A bifurcation [370-372] of magnetic state at an identical magnetic field is observed leading towards a remarkable change in the magnon dispersion, including the band gap and group velocity. The observations are important for designing nanomagnet-based bias-field reconfigurable and energy efficient magnon waveguides.

II. Experimental and Theoretical Methods:

72 × 72 μm^2 array of 30-nm-thick polycrystalline $Ni_{80}Fe_{20}$ (permalloy: Py hereafter) dots with geometry as described above has been fabricated in a square lattice symmetry onto a thermally oxidized silicon (001)/ silicon oxide (Si/SiO_2) substrate using a combination of electron-beam lithography and electron-beam evaporation. The substrate is spin coated with bilayer polymethyl methacrylate (495 and 950 K) positive-tone e-beam resist. The beam current used during electron-beam lithography is 5.4 pA for line dose of 1.5 nC/cm. The connected dot pattern is defined after development of the electron-beam exposed resist in methyl isobutyl ketone (MIBK) and isopropyl alcohol (IPA) (MIBK : IPA, 1:3) solution. Thereafter, 30-nm-thick Py is deposited at a deposition rate of 0.2 Å/S using electron-beam evaporation at a base pressure of 30 nTorr. A 2-nm-thick SiO_2 protective layer has been deposited on top of Py using rf sputtering (base pressure = 0.2 μTorr, Ar pressure = 5 mTorr, deposition rate = 0.3 Å/S, rf power = 60 W) to protect the sample from degradation. Subsequently, lift-off is done in acetone using ultrasonic agitation to obtain the connected dots. The surface topography of the sample is determined by scanning electron microscopy (SEM) and atomic force microscopy (AFM). The static magnetic configuration of the sample is imaged by magnetic force microscopy (MFM). The SW dispersion relation of the sample is measured by BLS spectroscopy in the conventional back-scattering geometry. The output of a single mode CW solid state laser of wavelength (λ) of 532 nm with power

of about 60 mW is made incident on the sample. The wavevector (k) associated with the SW has been calculated using the relation $\boldsymbol{k} = 2\boldsymbol{k}_{in}\sin\theta = \frac{4\pi}{\lambda}\sin\theta$, where θ is the angle of incidence in the backscattered geometry and k_{in} represents the wavevector of the incident laser beam. In our experiment, we have probed k up to 8.2 rad/μm along Γ-Y symmetry axis, i.e., up to the second Brillouin zone (BZ). We have theoretically calculated SW dispersion (i.e. frequency (f) versus wavevector (k) diagram) and spatial profile of the SW modes using plane wave method (PWM) [279]. In PWM, we consider elliptical-shaped dots with material parameters corresponding to Py as, saturation magnetization, M_s = 800 kA.m^{-1}, exchange constant $A = 1.3 \times 10^{-11}$ J.m^{-1}, and $g = 2$, while very small values of M_s and A are assigned to the air gaps to avoid any non-physical frequency values. A total number of 450 plane waves have been considered to ensure a satisfactory convergence of the eigenvalue problem.

Here $$M_s(G) = \begin{cases} M_{S,A}t + M_{S,B}(1-t) & G = 0 \\ (M_{S,A} - M_{S,B})P(G) & G \neq 0 \end{cases} \qquad [7.1]$$

where, t is the filling fraction of Py in the lattice defined as $t = \frac{\pi cd}{a^2}$; c and d denote the semi-major and semi-minor axis of the Py nanodots. $M_{S,A}$ and $M_{S,B}$ ($<< M_{S,A}$) are saturation magnetizations of Py and the air gap, respectively. Finally, $P(G)$ is a function specific to the elliptical structure of the nanodots used in this calculation.

We have also used Object Orientated Micromagnetic Framework (OOMMF) software [276] for calculation of magnetic ground state of the dots under certain field configurations and LLG micromagnetic simulator [278] for simulation of MFM image by discretizing the samples into cuboidal cells of dimensions 4 × 4 × 32 nm^3 (we consider thickness of Py to be 32 nm for MFM simulation) and material parameters for Py are considered same as that described above for PWM calculation.

III. Results and Discussions:

The scanning electron micrograph (SEM) of the sample is shown in Fig. 7.1(a), which reveals that the sample has a high quality. The dimensions of the rounded rectangles are 780 nm × 540 nm with about ±1.5% deviation in various dots in the array. The dots are tilted at an angle of 29 ± 1° from the x-axis as shows in Fig. 7.1(a). The spacing between consecutive chains of dots along z-axis varies periodically between about 670 and 230 nm when moved along x-axis. The AFM image in Fig. 7.1(b) further reveals the topography and height of the sample. Figure 7.1(c) confirms that the height of the dots

obtained from AFM is around 30 nm. The average roughness of the dots obtained from AFM measurement (Fig. 7.1(d)) is about 0.86 nm.

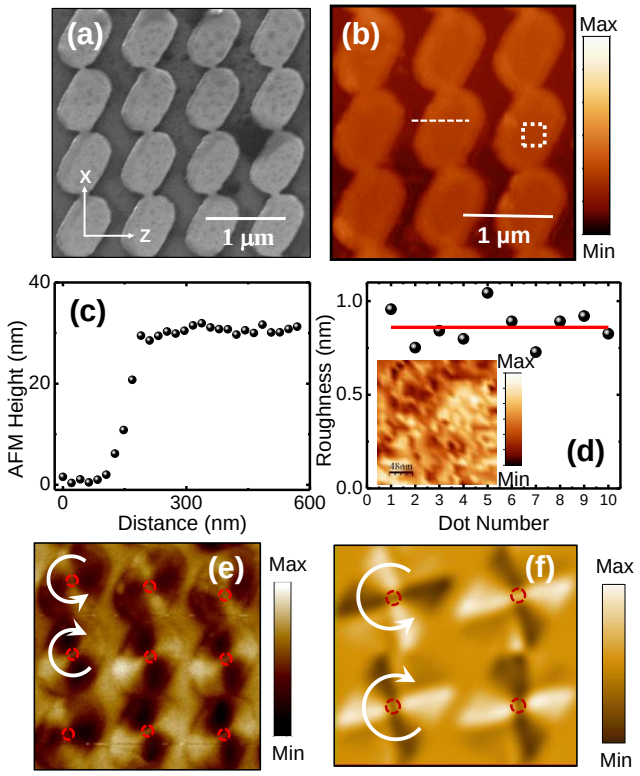

Figure 7.1: Scanning electron microscope (SEM) and (b) atomic force microscope (AFM) image of the sample. (c) Height of nanodot obtained from the AFM image along the dotted line in (b). (d) Roughness of various dots in the sample along with a high-resolution image taken from the dotted box in (b) is shown in the inset. (e) Experimental and (f) simulated magnetic force microscope (MFM) image of the sample in the AC demagnetized state. The arc arrows represent chirality of vortex found from the simulation.

Figure 7.1(e) presents the experimental MFM image of the sample in the AC demagnetized state, which reveals magnetic vortex state in the dots. In Fig. 7.1(f), we present the simulated MFM image in the AC demagnetized state, which clearly reproduces the magnetic vortex states in the dots in agreement with the experimental image. The experimental and simulated MFM images in the remanent state show quasiuniform magnetic state, while the simulated image at H_3 = 330 Oe, obtained by raising the magnetic field from the AC demagnetized state, shows a shifted core vortex states with the cores shifting in opposite directions for opposite spin chiralities [373]. We have simulated the static magnetic configurations of the sample at different bias magnetic field (H) values starting from the AC demagnetized state to saturated state, i.e., $0 \leq H \leq 500$ Oe at an interval of 5 Oe and collected the snapshots of the M_y component of magnetization to form a movie, **M1** (Appendix C) [373]. In this movie, we have shown a well controlled the movement of the vortex core with the variation in H.

Motion of vortex cores with opposite chiralities is reconfirmed in this movie, M1. This result corresponds to a first-order phase transition from vortex to leaf state at H = 465 Oe as will be described later.

Figures 7.2(a)-(g) show experimental BLS spectra, while the schematic of the BLS measurement geometry is shown in Fig. 7.2(h). In Figs. 7.2(a)-2(c), we present three representative BLS spectra for three different magnetic states, namely leaf state (H_1 = 850 Oe), 'S' state (H_2 = 330 Oe obtained by

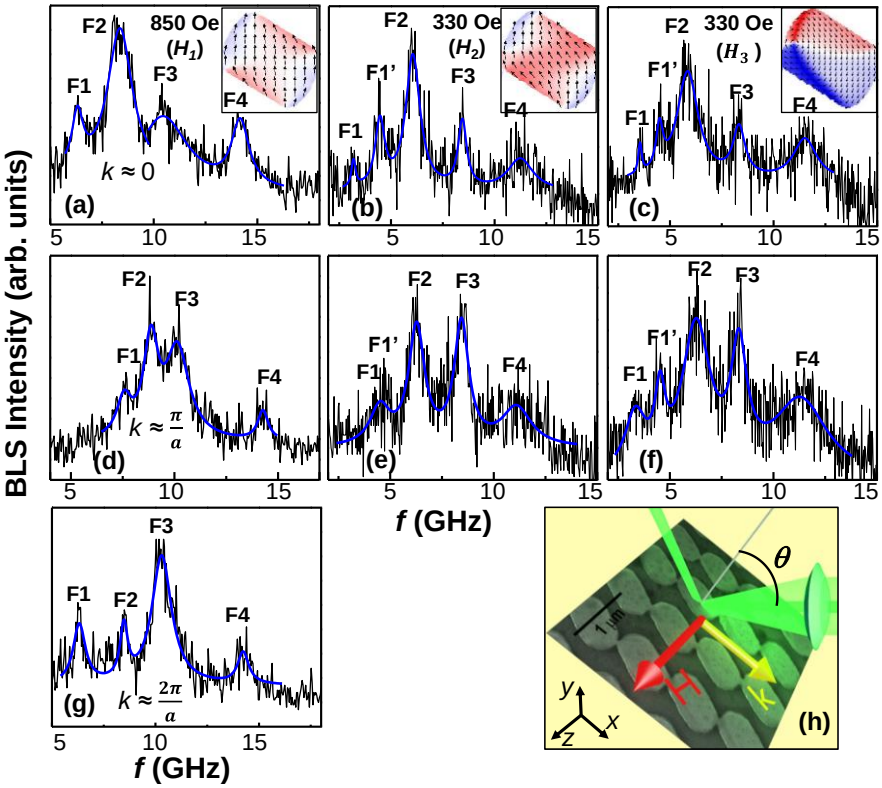

Figure 7.2: (a)-(c) The Stokes side of BLS spectra taken at three different magnetic history, i.e. leaf state (H_1 = 850 Oe), 'S' state (H_2 = 330 Oe, when decreased from saturation field) and shifted-core vortex state (H_3 = 330 Oe, when increased from AC demagnetized state) at k ≈ 0. The simulated magnetic states are shown in the insets. (d)-(f) The Stokes side of BLS spectra taken for leaf, 'S' and shifted-core vortex state, respectively at the first BZ boundary (k ≈ π/a). (g) The Stokes side of BLS spectra taken for the leaf state at the second BZ boundary (k ≈ 2π/a). The solid lines represent the Lorentzian fits to identify the peaks. (h) Schematic of BLS measurement in the Damon-Eshbach (DE) geometry.

reducing the field from saturated state) and shifted core vortex state (H_3 = 330 Oe obtained by increasing the field from AC demagnetized state) at near the center of the Brillouin zone ($k \approx 0$). In Figs. 7.2(d)-(f), we present three representative BLS spectra at k = 4.1 rad/μm (1st BZ boundary, $k \approx \pi/a$) for three above different magnetization states. We aim to study the possibility of tuning the

magnonic band structure due to the interaction between the propagating SW and different spin textures as mentioned above. This is even more interesting as we could achieve two contrasting spin textures at the same bias-field magnitude of 330 Oe but having two different magnetic history [372], namely a 'field-bifurcation'. We observe four clear peaks for H_1 = 850 Oe, while for H_2, H_3 = 330 Oe, five modes are observed for $k \approx 0$ (Figs. 7.2(a)-(c)). On the contrary, at $k \approx \pi/a$, four peaks are well resolved for H_1 = 850 Oe and H_2 = 330 Oe, while for H_3 = 330 Oe, five well resolved peaks are observed (Figs. 7.2(d)-(f)). Interestingly, we also observe that the intensities of F2 and F3 modes have been interchanged beyond the first BZ as shown in Figs. 7.2(a), 7.2(d) and 7.2(g) while at the boundary of the first BZ, intensities of those two modes are nearly equal. These results correspond to a mode cross-over in the wave-vector domain.

The experimental SW dispersion relations for these three different bias fields are plotted in Figs. 7.3(a)-(c) as symbols. While for H_1 = 850 Oe three clear band gaps (BGs) of 0.53 GHz, 1.00 GHz, and 3.5

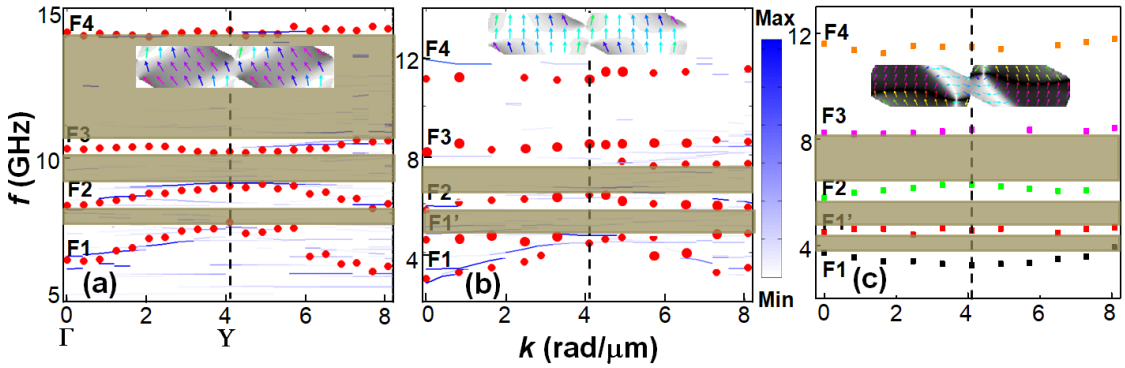

Figure 7.3: (a)-(c) Magnonic band structure corresponding to three different magnetic states, i.e. leaf, 'S' and shifted core vortex state, respectively. Here, filled symbols represent BLS peak frequencies for different k values, the dashed vertical line is the boundary of the first BZ, while the band gap is shown by the shaded areas. The three-dimensional surface plots of the plane wave method calculated spin-wave dispersion is superposed on the experimental data in (a) and (b). The corresponding color map for (a)-(b) is shown at the right side of the figure. The simulated magnetization configuration in the spin-wave propagation channels for the three magnetic states are shown in the insets.

GHz are observed, H_2, H_3 = 330 Oe show starkly different behavior. For H_2 = 330 Oe, the two lowest frequency bands merge at the first BZ boundary leaving only two BGs between F1, F1' and F2 (1.05 GHz), F2 and F3 (1.12 GHz). On the contrary for H_3 = 330, three BGs of 0.8 GHz (F1 and F1'), 1.26 GHz (F1' and F2) and 2.02 GHz (F2 and F3) are observed. The calculated magnonic band structures using PWM are shown in Figs. 7.3(a) and (b) as the three-dimensional surface plots superposed on the

experimental dispersions. The color map (white to blue) of the intensity of SW modes ($I \propto |m_y(k)|^2$) is shown next to the dispersion. The color scale of the surface plot is adjusted such that only the high-intensity SWs are visible as blue regions, which clearly reveals that the high-intensity experimental and calculated modes are in general agreement. We have also observed reconfigurability in SW dispersion for Py-made diatomic dots in two different spin textures coupling regimes: leaf state-leaf state coupling and leaf state-C state coupling (shown in Appendix C).

It is clear that the internal spin texture modulates the SW propagation significantly, which has also been shown in different systems before [374,375]. However, the observation of different spin textures and the ensuing difference in magnon dispersion and magnon BG at an identical magnetic field, the 'field-bifurcation' phenomenon [372] in dynamic system may open up new applications in spintronics

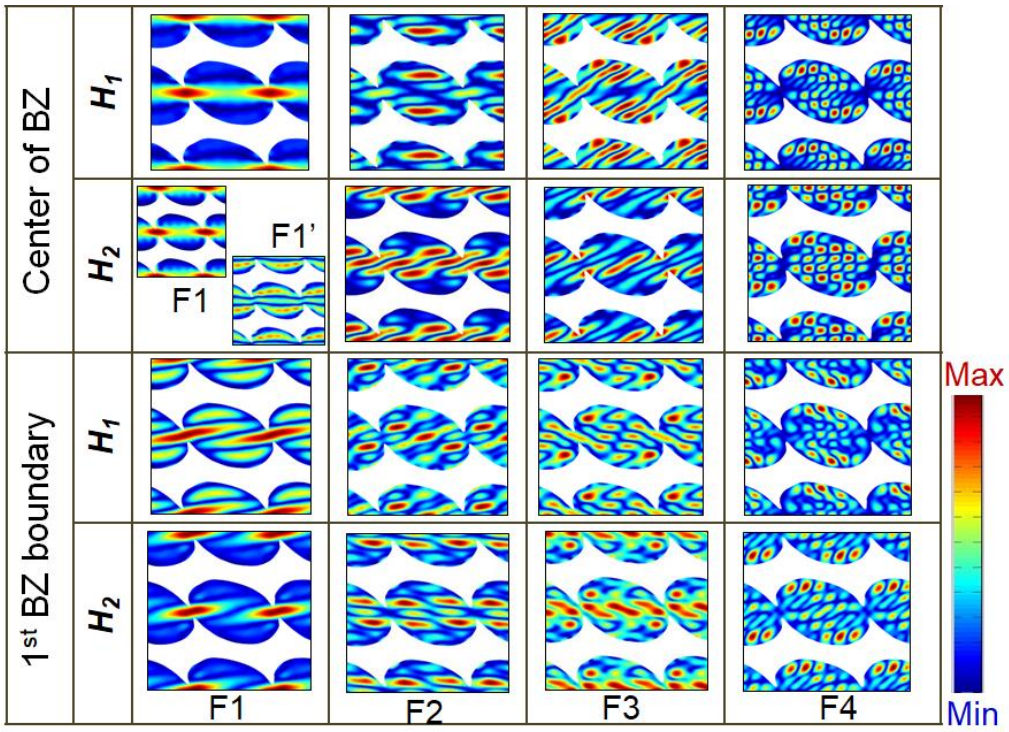

Figure 7.4: Spatial profiles of selected spin-wave modes (F1, F1', F2, F3, and F4) for two different magnetic states, namely the leaf and 'S' state at $k \approx 0$ and $k \approx \pi/a$.

and magnonics. In order to understand the spin-texture-dependent magnon dispersion, we first calculate the SW mode profiles for H_1 = 850 Oe (ground state shows leaf state) and H_2 = 330 Oe (ground state shows 'S' state), as shown in Fig. 7.4.

In the following, we will use SW mode quantization numbers as (m,n), which describe the quantization along the major and the minor axes of the dots. Figure 7.4 reveals that at the centre of the BZ, F1 is a propagating SW mode extending through a channel joining the dots in both 'leaf' and 'S' states leading towards almost identical dispersion in both states. However, an additional mode F1' appears in the 'S' state, which also propagates through the same channel but having additional quantization (3,1) and a weakly dispersive nature. At the boundary of the 1st BZ, F1 ceases to propagate through the channel, showing a pseudo-extended nature between two successive dots with quantization numbers (4,1). Mode F2 shows qualitatively similar dispersion for both leaf and 'S' states, while the dispersion is steeper in the 'leaf' state indicating greater group velocity. Interestingly, the mode profiles vary significantly as the mode quantization axis rotates by 24° in the 'S' state with (m,n) as (4,2) and (6,1) in the leaf and 'S' state. At the 1st BZ, both the quantization numbers and axes change to (7,1), 19° in the leaf and (5,2), 0° in the 'S' state. The mode F3 shows a negative dispersion in the leaf state, while it is almost dispersionless in the 'S' state. This is evident from the mode profile at the centre of the BZ, which shows pseudo-extended character in the leaf state with mode quantization numbers (8,2), allowing transfer of energy through the chain of dots. However, the mode is fully localized within the individual dots in the 'S' state with quantization numbers (7,2) leading towards no or negligible transfer of energy. At the edge of the 1st BZ, the mode quantization number becomes (2,4) and (3,4) and quantization axes change by 160° in the leaf and 'S' state, respectively. Mode F4 is dispersionless in both states, showing fully localized behavior with quantization numbers (10,8) and (9,5) in the leaf and 'S' states at the centre of the BZ. These modes transform into (9,6) and (11,6) at the boundary of the 1st BZ.

Next, we inspect the detailed spin textures within the channels of propagation through the chains of dots for all three magnetization states, namely, leaf, 'S' and vortex state as shown in the insets of Fig. 7.3(a)-(c). In the leaf state the spins are almost parallel with slight periodic canting within the channel of SW propagation and hence the SW dispersion is affected primarily by the periodicity of the structure. In the 'S' state the SW interacts with a spin texture with sharp contrast posing additional periodicity in the magnetic potential. The ensuing scattering of the SWs from these additional scattering centres probably leads to the new SW mode F1'. On the contrary the spin texture in the shifted-core vortex state shows the formation of 90° domains near the connected regions and this is the origin of the drastically different magnonic band structure in this case. The weakly negative dispersion of F1 is probably associated with this spin texture. Due to the technical difficulties, PWM calculations could not be performed in the shifted-core vortex state. However, to extract the information about the SW

mode profiles in this magnetic state, we have used OOMMF micromagnetic simulation when the connected dots are uniformly excited at k = 0 and a home-built code [355]. The results are shown in

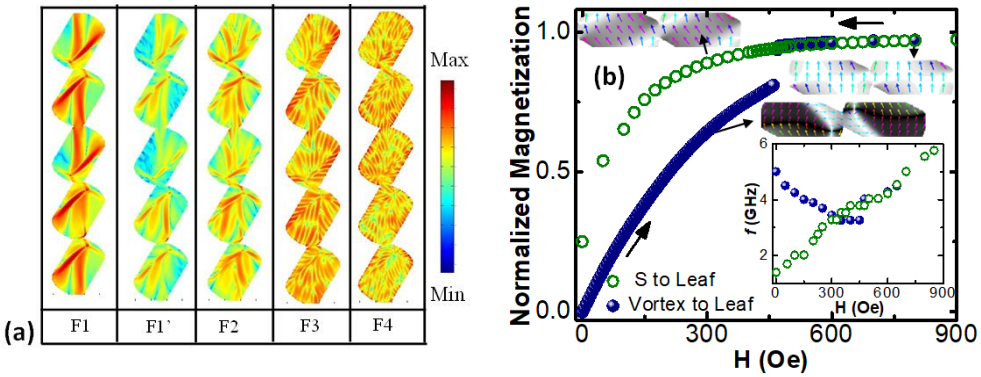

Figure 7.5: (a) Simulated power maps showing spin-wave modes (F1, F1', F2, F3, and F4) profile for the shifted-core vortex state at k = 0. The corresponding color map is shown at the right side of the figure. (b) Simulated variation of normalized magnetization with applied magnetic field. Arrows represent the path of variation from one spin texture to another spin texture. Inset represents simulated spin-wave frequency vs. bias magnetic field along two different paths of magnetic field history.

Fig. 7.5(a). All the modes show nonuniform character with F1 showing a somewhat extended nature with its power flowing through the nanochannels connecting the dots. Consequently, this mode shows a dispersive nature. F1' shows almost nonexistent power in the nanochannels and consequently this mode does not extend throughout the sample showing a nondispersive character. F2 again shows a weakly extended nature and hence a weak dispersion in the magnonic band structure. F3 and F4 are fully quantized modes localized in the individual dots with negligible power in the propagation channel and they are fully dispersionless. This causes the nature of dispersion of the SWs observed in this case. We now look into the transformation between the above three magnetic states. The calculated M-H curves in Fig. 7.5(b) clearly show that the transformation from the leaf to the 'S' state occurs continuously as we reduce the magnetic field from the saturation state to lower value. On the contrary, when the magnetic field is increased from the AC demagnetized state, the magnetization shows a sudden jump due a first order phase transition at around 465 Oe (vortex annihilation field) as the vortex state is transformed into the leaf state. This is also reflected into the calculated SW frequency as shown in the inset of Fig. 7.5(b). The SW frequency decreases monotonically as the field is reduced from the saturation and the magnetization state transforms from the leaf to 'S' state. On the contrary, the frequency shows a clear jump at a magnetic field of about 465 Oe, followed by a minimum and an increase as the field is further reduced. Such a minimum in frequency vs. magnetic field, indicates a SW mode softening as observed before [328,376]. The observed variation in the spin texture and its

ensuing magnetic properties leads to only a quantitative change in the SW dispersion in the leaf and the ‘S’ state but a major qualitative variation in the dispersion of the mode F1 where a negative dispersion in the shifted-core vortex state is observed as opposed to a positive dispersion in both the leaf and the ‘S’ states.

IV. Conclusions:

In summary, we have performed a combined experimental and numerical study of magnonic band structure in coupled rectangular-shaped ferromagnetic dots with rounded edges. By varying the magnetic field strength and history, we were able to obtain three different spin textures, namely ‘S’ state, leaf state and shifted-core vortex state. The magnonic band structure exhibited a remarkable variation due to the interaction of SW with different spin textures, viz. the variation in number of modes and their dispersion behavior. This is particularly prominent when the spin textures provide abrupt variation in the propagation channel of the SWs, namely by ‘S’ state and shifted-core vortex state, where an additional mode appears. The results are numerically reproduced by plane wave method-based numerical calculations. The calculated SW mode profiles show a remarkable variation of power in the propagation channel, quantization number of the modes and their quantization axes originating from different spin-textures in the ground state. Further calculation shows a first order phase transition in the magnetization as well as frequency with bias field strength for the transformation from vortex to leaf state, while a continuous change from ‘S’ to leaf state. In addition, magnon dispersion can also be tuned by leaf state – leaf state coupling and leaf state – C state coupling present in di-atomic dots system. Such a rich variation in the static and dynamic magnetic characteristics lead to the ensuing variation in magnonic band structures. Observation of such reconfigurable band structure with external bias magnetic field and ensuing spin texture would pave way for the advancement of a new research field called topological magnonics.

Chapter 8

8. Bias Field Orientation Driven Magnetic Microstates and Spin Wave Dynamics in Nanoscale Artificial Spin Ice System

I. Introduction:

Frustration is a form of instability that arises in a system due to competing interactions that cannot all be satisfied simultaneously. Artificial spin ice (ASI) is a type of metamaterial composed of an array of lithographically fabricated two-dimensional or three-dimensional nanomagnets [160,377-380]. The frustration in these arrays creates topologically disordered ground states with macroscopic degeneracy, even in ferromagnetic systems. In these systems, special magnetic textures, such as pairs of magnetic monopoles and anti-monopoles connected via 'Dirac strings' [154,155] can be formed. The studies of ASI with different spatial symmetry such as kagome [156], triangular [164], square [158] and brickwork [161] arrangements have mainly focused on the observation of magnetic monopoles, residual entropy at low temperatures, the degeneracy of magnetic ground states, and the dynamics of magnetic charge on the emission, propagation, and absorption of domain walls [154,164,381].

The fundamental understanding of microstate-dependent reconfigurability in spin-wave (SW) dynamics in ASI systems have attracted interest for the last one decade due to their potential application in terms of miniaturization, speed, and energy consumption in spin texture driven reconfigurable magnonics [40,53,113,116]. In the context of an in-depth understanding of the different types of ASI microstates on field-swept spin dynamics, ferromagnetic resonance (FMR) has mostly been used for global excitation in a large area ASI array [129,168,382-384]. Through a combination of experimental studies using global FMR and local Brillouin light scattering (BLS) spectroscopy on a kagome ASI, it was shown that the generation of microstates can trigger different microwave-assisted switching of strings and SW dynamics [129,168]. The study of angular-dependent magnetization dynamics on a honeycomb ASI revealed localized spin dynamics which differ from clusters of ferromagnetic nano-ellipses [382,385]. Further, the effect of spin texture at the vertex in a connected square ASI sample due to the variation of the orientation of the bias magnetic field was found to have a strong effect on spin transport and high-frequency dynamics [386]. Wang *et al.* hypothesized the possible interactions of SWs with different microstates present in a square ASI sample and explored the effect of correlations between different pairs of islands with lattice constants [158]. Subsequently, the manipulation of magnetization dynamics with those different possible magnetic defects in ASI lattices was theoretically

demonstrated to create new localized modes in the system [387], where the spectral amplitude of that mode is proportional to the density of defects [129]. In the above studies, the propagation of Dirac strings through the lattice can also introduce an additional tunability of the magnonic band structure with novel functions such as reconfigurability and nonreciprocity in SW dynamics [167,388]. Li *et al.* experimentally demonstrated a flat magnonic band structure for both Damon-Eshbach (DE) and backward volume (BV) geometry in the saturation region in a large vertex-separated square ASI sample [389]. Very recently, macrospin–vortex bistable system has revealed the number of hysteresis loops with controllable SW spectra, leading to the gradual increase of vortex mode amplitudes and a decrease of the macrospin modes [390]. This presents the potential for a reconfigurable magnonic device (RMD) based on the observation of microstate-dependent mode-hybridization and anticrossings [391,392], which could be used to control and manipulate the transmission and reflection of SWs. The dipolar interaction responsible for coupling in nanopatterned RMDs provides relative freedom and reconfigurability to control mode-hybridization phenomena. Such a device could have a wide range of applications, including the development of new types of memory and neuromorphic computing systems [390,392-395].

Here, we present magnetic microstate driven SW dynamics using both Brillouin light scattering (BLS) and micromagnetic simulation in a disconnected square ASI sample made of $Ni_{80}Fe_{20}$ (permalloy, Py hereafter). We observe a stable 2-in-2-out spin configurations at remanence for $0° \leq \varphi \leq 45°$ (φ is in-plane bias magnetic field orientation). Rich SW spectra are observed in the system and a detailed SW dispersion with both φ and bias field strength (H) have been studied experimentally and by numerical simulations. We observe a transition from a W-shaped mode softening to monotonous dispersion of low-frequency SW mode as φ is tuned from 0° to 45°, due to the reconfiguration of localized SW modes profile. Further, we introduce type-III and type-I ASI defects, and topological defects (magnetic vortices) into a type-II ASI system in five different ways. These five microstates provide rich magnonic spectra with precise control over mode frequency shift, microstate-specific anti-crossing gap opening and tuning, and the number of dominating SW modes. We have been able to identify SW modes which act as markers for type-I, type-II and type-III ASI microstates as well as magnetic vortices in such system using BLS spectroscopy.

II. Experimental and Theoretical Methods:

A 23-nm-thick polycrystalline Py elongated nanodots array covering 90 × 90 μm^2 area was fabricated in a square ASI arrangement on a thermally oxidized silicon (001)/silicon oxide (Si/SiO_2) substrate via a combination of electron-beam lithography, thermal evaporation and lift-off process. The substrate is spin coated with single-layer polymethyl methacrylate (950 K) positive-tone e-beam resist. After development of the resist pattern using MIBK developer at 950 K, a 23-nm-thick Py film was thermally evaporated at a base pressure of 9.0×10^{-7} Torr. The samples were then capped with 3.7 nm of Al_2O_3 at a base pressure of 2.6×10^{-6} Torr to protect them from oxidation. The surface topography of the sample was determined using scanning electron microscopy (SEM) and atomic force microscopy (AFM). Its static magnetic configuration at remanence and AC demagnetized (ACD) states were captured by magnetic force microscopy (MFM). Its experimental hysteresis loops were measured using static magneto-optical Kerr effect (S-MOKE) at ambient conditions. The bias field-dependent SW dispersion of the sample was measured by BLS spectroscopy in the conventional back-scattering geometry [261]. In this BLS measurement, a single mode CW solid-state laser of wavelength (λ) of 532 nm with the power of about 100 mW is made incident on the sample, with the wavevector (k) associated with the SW kept at $k \approx 0$ for this measurement in the DE geometry. A free spectral range (FSR) of 30 GHz and a 1024 multichannel analyzer were used to collect the data as the in-plane (InP) field strength (H) was varied from +1400 Oe to -1400 Oe, tracing the upper branch of the magnetic hysteresis. Further details of this BLS setup can be found elsewhere [19]. High-field-resolution (interval = 10 Oe) BLS measurements were also carried out in the same experimental condition from -50 to 50 Oe, where the microstate-dependent spin texture remained intact.

We have used Mumax3 software [277] where 4 × 4 girds of square ASI system with 2D periodic boundary conditions (2, 2, 0) are considered to simulate the ground spin texture, and magnetization dynamics . The sample was discretized into cuboidal cells of 4 × 4 × 22.5 nm^3, with the Py layer thickness being 22.5 nm. The material parameters used in the simulation were: Gilbert damping constant (α) = 0.008, exchange stiffness constant (A) = 1.3×10^{-6} erg/cm, saturation magnetization (Ms) = 780 emu/cm^3, gyromagnetic ratio γ = 17.95 MHz/Oe and magneto-crystalline anisotropy constant (K) = 0 [113]. The simulated time-varying magnetization was run for 4.05 ns at 10 ps steps. To understand the spatial maps of power and phase of each spin-wave mode, we have used our home-built MATLAB-based code DOTMAG [355].

III. Results and Discussions:

The scanning electron micrograph of the sample is shown in Fig. 8.1(a). The length, width and lattice constant of nanobars (NBs) are found to be around 480 nm, 180 nm, and 660 nm respectively. The deviation in the measured dimensions is ±10 nm in length, and ±5 nm in width while the heights of the

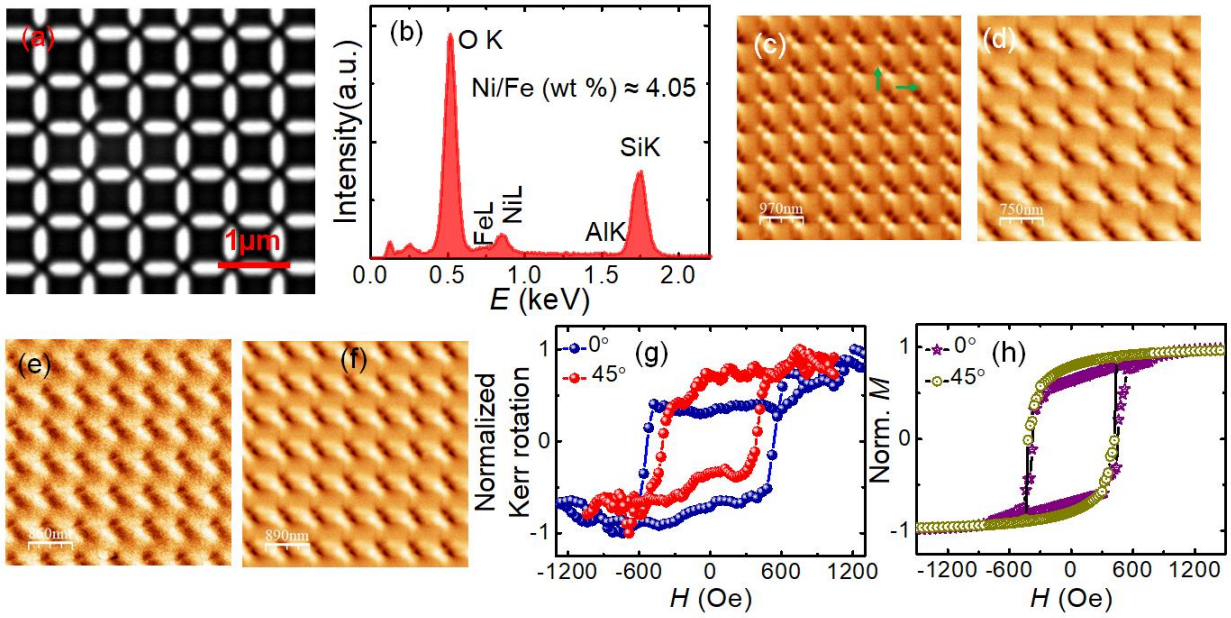

Figure 8.1: (a)-(b) Scanning electron micrographs and energy dispersive X-Ray of $Ni_{80}Fe_{20}$ ASI nanobar array. (c)-(f) MFM images at remanence states for φ = 0°, 15°, 30° and 45°, respectively. (g)-(h) Experimental and simulated hysteresis loops.

NBs are found to vary by ±0.75 nm measured via an atomic force microscope (AFM). The energy dispersive x-ray (EDX) spectrum of the sample in Fig. 8.1(b) shows a weight ratio between Ni and Fe of around 4.05. Figures 8.1(c)-(f) show the MFM images at remanence state at angles φ = 0°, 15°, 30° and 45°, respectively, all showing 2-in-2-out type-II ASI spin configurations. Figures 8.1(e)-(f) represent experimental and simulated hysteresis loops at φ = 0° and 45°. The coercive field is found to be ~ 450 Oe for φ = 0° and ~ 320 Oe for φ = 45° which are much higher than the Py thin film.

In-plane Bias Field Orientation Dependent SW Dynamics of Square ASI:

Figures 8.2(a)-(d) show the representative BLS spectra for φ = 0°, 15°, 30° and 45° at $k \approx 0$ in the DE geometry at different H values, while the schematic of the BLS measurement geometry is shown in Fig. 8.3(f). We have used the multipeak Lorentzian function fit to extract SW modes frequencies (f) as represented by the coloured solid lines in Fig 8.2. Figures 8.3(a)-(e) are the five representative 3D

surface plots of SW field dispersion (f vs H dispersion) over a range -1400 Oe ≤ H ≤ +1400 Oe at φ = 0°, 15°, 30°, 45° and 90°, respectively, where the solid symbols represent the simulated SW mode frequencies. Here, we have observed an anisotropic nature and number of SW modes with varying φ.

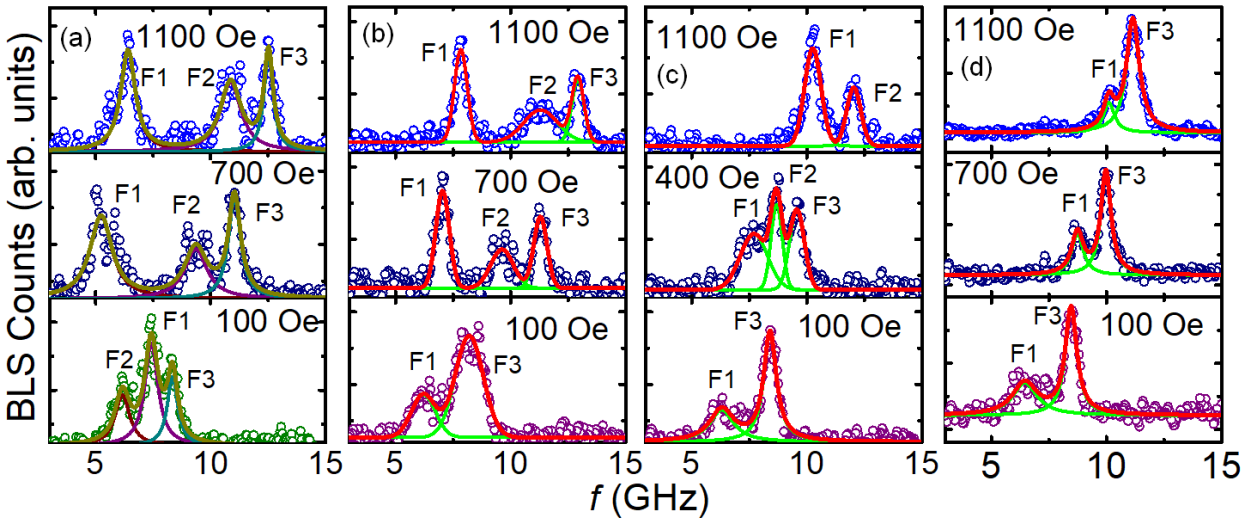

Figure 8.2: Representative BLS spectra measured at wave vector $k \approx 0$ for different magnetic field strengths at φ = 0°, 15°, 30° and 45°, respectively.

At φ = 0° and φ = 15°, the number of dominating SW modes is three, except for -450 ≤ H ≤ +100 Oe (Figures 8.3(a)-(b)). At φ = 30°, there are two dominating SW modes, except for +200 Oe ≤ H ≤ +600 Oe and -500 Oe ≥ H ≥ -700 Oe (Figure 8.3(c)). For φ = 45°, only two dominating SW modes are observed (Figure 8.3(d)). As the magnetic field is reduced, the low-frequency SW mode (F1) at φ = 0° (and 15°) changes its slope i.e., $\partial f/\partial H$ changes from +ve to -ve (-ve to +ve) on the positive (negative) side of H ("W" shaped field dispersion). Figs. 8.3(a)-(b) represent this "W" shaped SW field dispersion with a clear minimum at $|H| = |H_S| \approx 750$ Oe, indicating mode softening phenomena. The depth of the "W" shaped well (d), as shown in Figs. 8.3(a)-(b), is 1.9 GHz and 1 GHz, respectively, for φ = 0° and 15°. Further, the slope ($\partial f/\partial H$) of F2 and F3 is +ve when 1400 Oe ≥ H ≥ -450 Oe (and 1400 ≥ H ≥ -400 Oe), -ve for the rest of the negative H at φ = 0° (and 15°). Notably, a sudden jump in frequencies of ~3.9 GHz for F2 and ~4.2 GHz for F3 mode is observed at H (= H_T : transition point) = -450 Oe for φ = 0° and H_T = -400 Oe for φ = 15°. This jump is associated with a change in the magnetic microstate, which is confirmed by the magnetization reversal field in the static-MOKE loop [166,391]. In addition, the first two modes F1 and F2 cross each other on the positive side of f *vs* H dispersion at around H = 300 Oe. In simulation, this crossing is observed at $H \approx 450$ Oe. The overall variation of simulated field

dispersion is in good qualitative agreement with the experiment result. Further, the mode-to-mode separation i.e., frequency gap between (F1, F2) and (F2, F3) are constant at φ = 0° and 15° for $|H| \geq$ 800 Oe. This frequency gap increases for φ = 30° and becomes closer for φ = 45° as represented in Figs. 8.3(a)-(d). The intensity of F1 mode is transferred to F3 through F2 for φ = 15°. The slope of F1

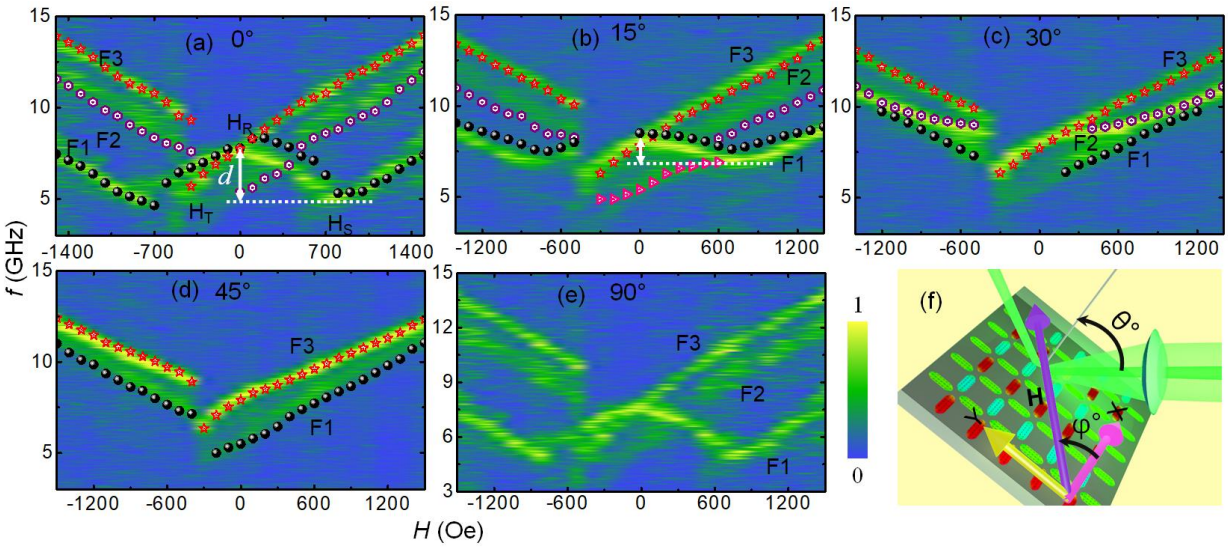

Figure 8.3: Surface plots of bias-field-dependent SW mode frequencies for φ = 0° (a), 15° (b), 30° (c), 45° (d) and 90° (e). Simulated SW frequencies are shown by symbols. The color map of experimental result is shown at the side of the surface plots. (f) Schematic of the BLS measurement geometry.

and F3 is +ve for $H \geq -300$ Oe and -ve for $H \leq -400$ Oe at φ = 30°. The F2 mode maintains a correlation between F1 and F3, which vanishes when F2 is not present in the field dispersion at φ = 45° (Figure 8.3(d)). As a result, F1 and F3 modes become well separated with decreasing *H*. Additionally, a sudden jump of ~3.7 GHz and 2.8 GHz in the frequencies of F1 and F3 modes is observed at H_T = -350 Oe for both φ = 30° and 45°. Figure 8.4(e) shows the surface plot of SW field dispersion at φ = 90° which is identical to that for φ = 0°. This result confirms the homogeneous growth of the square ASI sample, satisfying symmetry considerations which were not fully achieved by Lendinez *et al.* in the angular-dependent study of field dispersion [396]. This may be due to the quality and uniformity of the sample [158].

To understand the spin-wave mode profiles, the power phase distribution at mode softening point (H_S = 750 Oe) and higher (*H* = 1000 Oe) and lower (*H* = 400 Oe) sides of the mode softening point have been calculated using a home-built MATLAB-based post-processing code [355]. To replicate a square ASI sample, an array of 4 × 4 grids of square ASI with 2D periodic boundary conditions was considered

in the Mumax3 software [277]. Figures 8.4(a)-(b) shows representative spatial distributions of power and phase at φ = 0° and φ = 45°, respectively. The phase profiles reveal three classes of modes: a) purely backward volume (BV)-like modes with quantization numbers along the direction of *H*, represented as (m, 1); b) purely Damon-Eshbach (DE)-like modes with quantization numbers

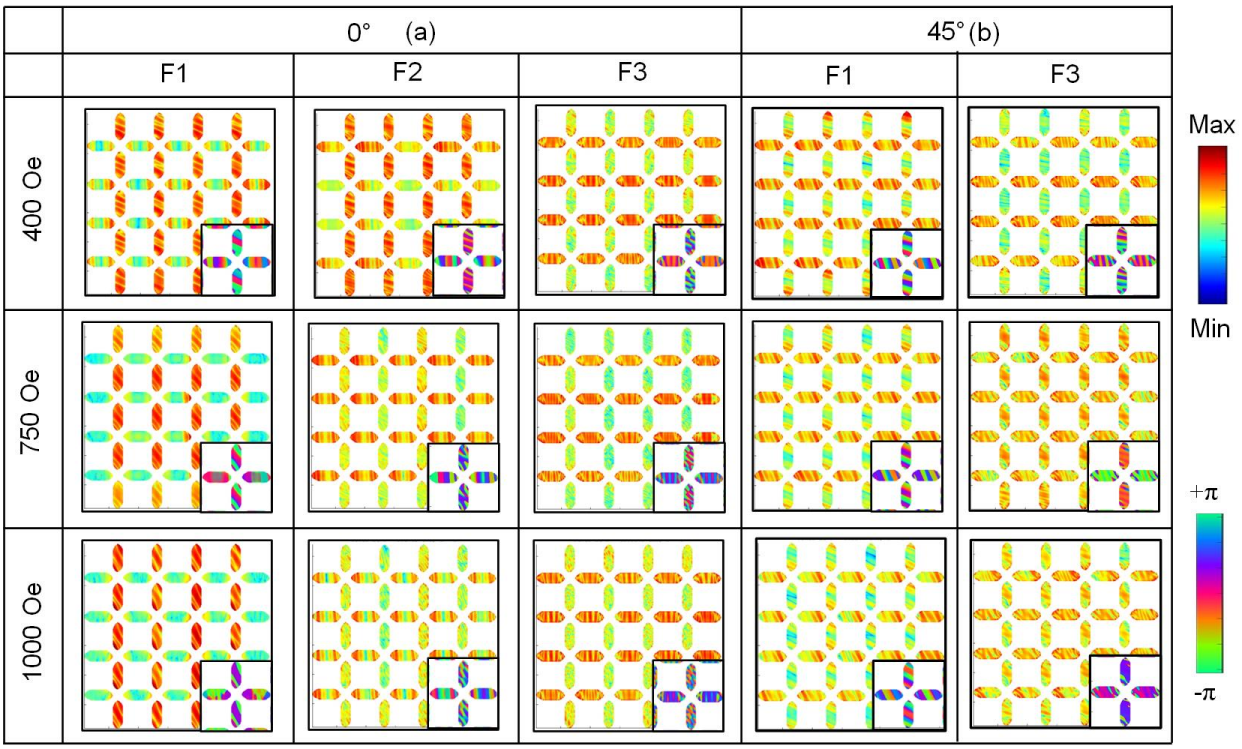

Figure 8.4: (a)-(b) Simulated spatial distribution of power and phase of the SW modes for different magnetic fields at φ = 0° (a) and 45° (b), respectively.

perpendicular to the direction of *H*, represented as (1, n); and c) mixed BV-DE-like modes with mode numbers (m, n). At φ = 0°, the power distribution of the low-frequency F1 mode remains unchanged with *H*, and most of the power is localized at the vertical nanobars (VNBs) (Figure 8.4(a)). The quantization number of the F1 mode at *H* = 1000 Oe is (5,1) in the horizontal nanobars (HNBs) and (1,4) in the VNBs, but due to the low power in the HNBs, it is difficult to identify the correct quantization numbers. The quantization number of the F1 mode changes to (4,1) and (1,5) in the HNBs and VNBs, respectively, at the mode softening point (H_S = 750 Oe). Further, the quantization number of the F1 mode becomes (6,1) and (1,4) for the HNBs and VNBs respectively at *H* = 400 Oe. So, the phase profiles of VNBs undergo a transition from odd-even quantization to even-even quantization due to mode softening. The F2 mode is a uniform mode (UM) on both arms before crossing (between F1 and F2 modes: *H* = 450 Oe), and becomes UM in VNBs and edge mode (EM) in HNBs after crossing

($H \leq 450$ Oe). The quantization numbers of F2 mode in HNBs are (8,1), (6,1), and (6,1) and in VNBs are (2,9), (2,9), and (1,9) for H = 1000 Oe, 750 Oe, and 400 Oe, respectively. Meanwhile, the power of F3 mode is localized only on HNBs of ASI, with the quantization numbers (12,2), (12,1), and (11,1) in HNBs, and (2,11), (2,9), and (2,9) in VNBs for H = 1000 Oe, 750 Oe, and 400 Oe, respectively. Figure 8.4(b) shows the power and phase distribution at φ = 45°. Here F1 shows nearly UM in HNBs and EM in HNBs. Interestingly, the quantization number of F1 mode changes as (5,1), (5,1), (8,1) in HNBs and (1,6), (1,8), (1,8) in VNBs for H = 1000 Oe, 750 Oe and 400 Oe, respectively. Further, F3 is another UM in both NBs with power distributed on both NBs at high field (H > 500 Oe) and only on HNBs in low field ($H \leq 500$ Oe). The quantization numbers of F2 mode are (7,1), (9,1), (11,1) in HNBs and (1,5), (1,7), (1,11) in VNBs for H = 1000 Oe, 750 Oe and 400 Oe, respectively.

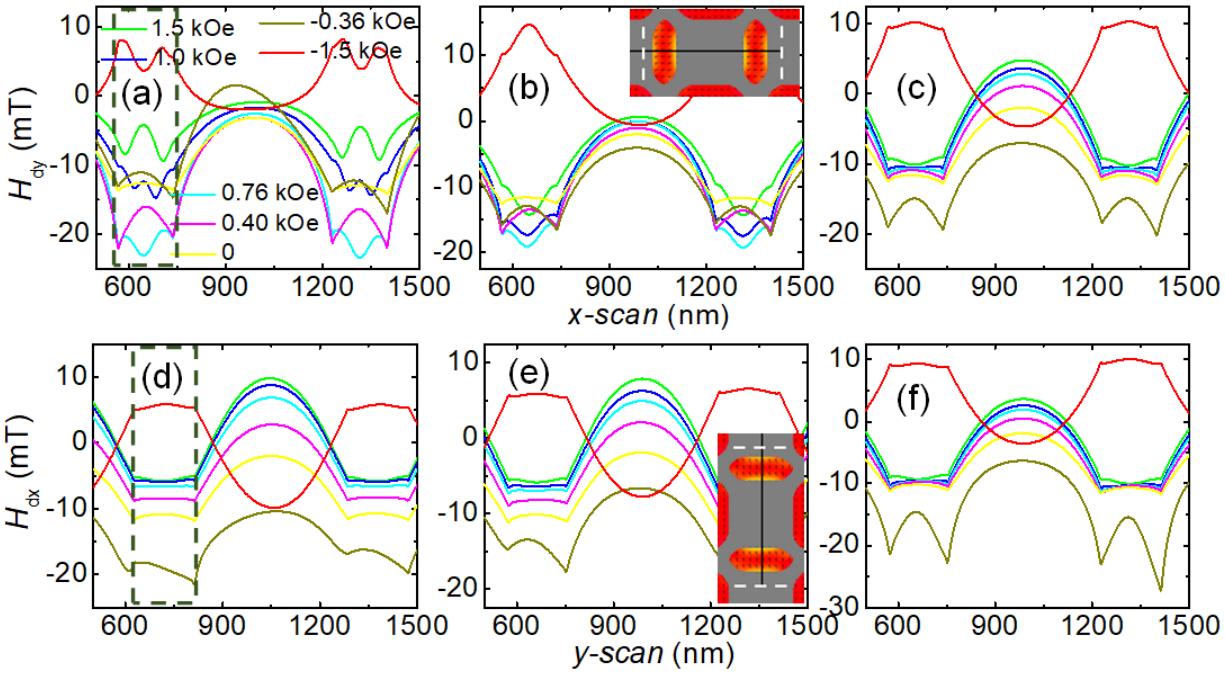

Figure 8.5: (a)-(c) Linescans of the simulated demagnetization field component H_{dy} at φ = 0°, 15° and 45°, respectively. The linescans direction is shown in the inset of (b). (d)-(f) Linescans of the simulated demagnetization field component H_{dx} at φ = 0°, 15° and 45°, respectively. The linescans direction is shown in the inset of (e). The green rectangular dashed box indicates the inner region of the nanobars.

For further insights into this observation, we have simulated demagnetization field distributions for all φ values. Figures 8.5(a)-(f) displays the simulated demagnetization field distribution for φ = 0°, 15°, and 45° at different H. A significant variation in the y-component demagnetization field profile (H_{dy}) inside the VNBs is observed for φ = 0° and 15° at $H \leq H_S$ which corresponds to the mode softening in

F1 mode. Further, a stark jump in the x-component demagnetization field profile (H_{dx}) inside the HNBs is observed for all φ at $H \leq H_T$, which corresponds to the frequency jump in F3 mode. This indicates that the uncompensated spins at the respective NBs are modified significantly at H_S and H_T points, boosting the dynamic dipolar interaction between the neighbouring NBs.

Microstate-dependent SW Dynamics of Square ASI:

Microstate and vortex Reconfiguration: Figures 8.6(a)-(e) depicts the microstates and vortex states for which corresponding SW dynamics were measured, while Figures 8.6(f)-(j) provides magnified views

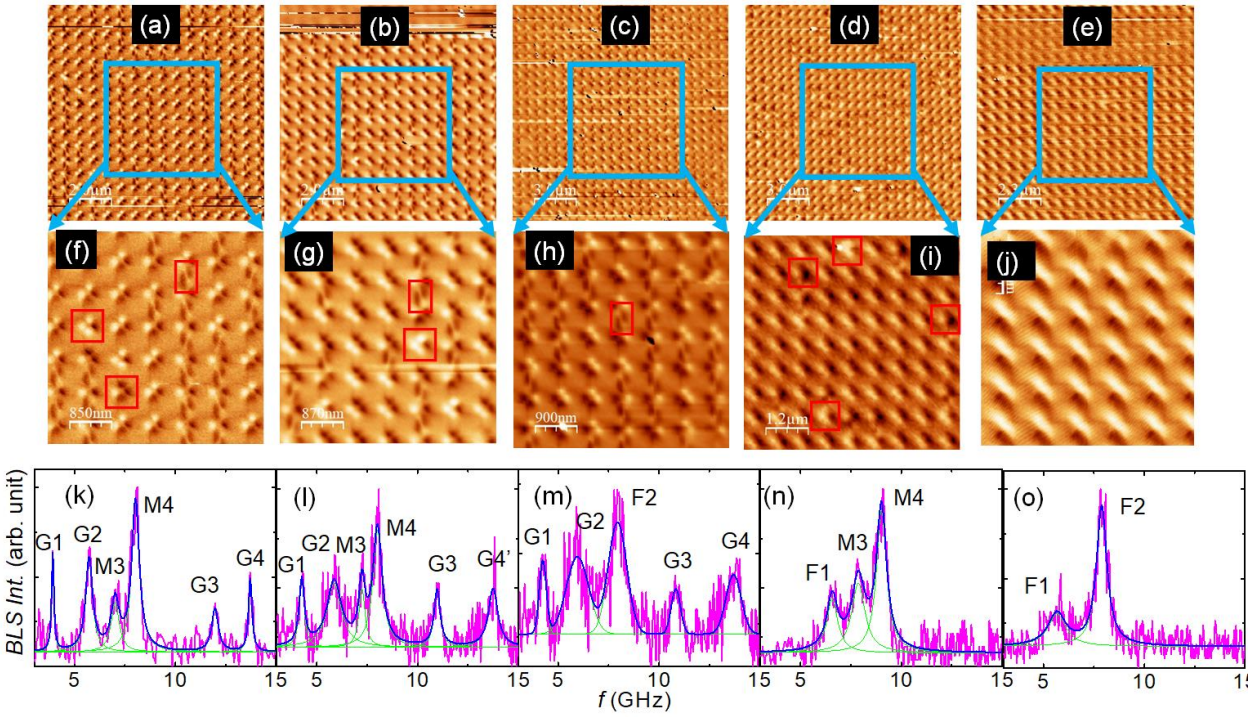

Figure 8.6: (a)-(e) MFM images for different ACD state such as [S1]-[S5] state, respectively. (f)-(j) Magnified views of those MFM images. (d)-(f) Representative BLS spectra measured at wave vector k ≈ 0 for [S1]-[S5] states, respectively.

of the same. A systematic process of changing different InP angular AC demagnetized (ACD) loops were used to reconfigure each state. Following the InP ACD state by 40 cycles to reach 0 Oe from 1400 Oe at φ = 0°, a vortex-[type-III] (V-T3) was observed with the presence of [type-II] (T2), which were designated microstate configurations [S1] (Figure 8.6(f): (V-T3-T2)). The relative number of vortices in the ACD state at φ = 15° was reduced by performing 40 cycles of ACD state, resulting in the configuration [S2]: (V-T3-T2) as shown in Fig. 8.6(g). Further, 55 cycles of ACD state to reach 0 Oe at φ = 15° resulted in the configuration [S3]: (V-T2) where the T3 microstate was missing, as shown

in Fig. 8.6(h). Moreover, the vortex state is absent in the 40 cycles ACD microstate at φ = 30° (Fig. 8.6(i) configuration [S4]: (T2-T3)). Finally, at φ = 45°, the pure T2 microstate is observed in the 40 cycles ACD state (Fig. 8.6(j) configuration [S5]: (T2)).

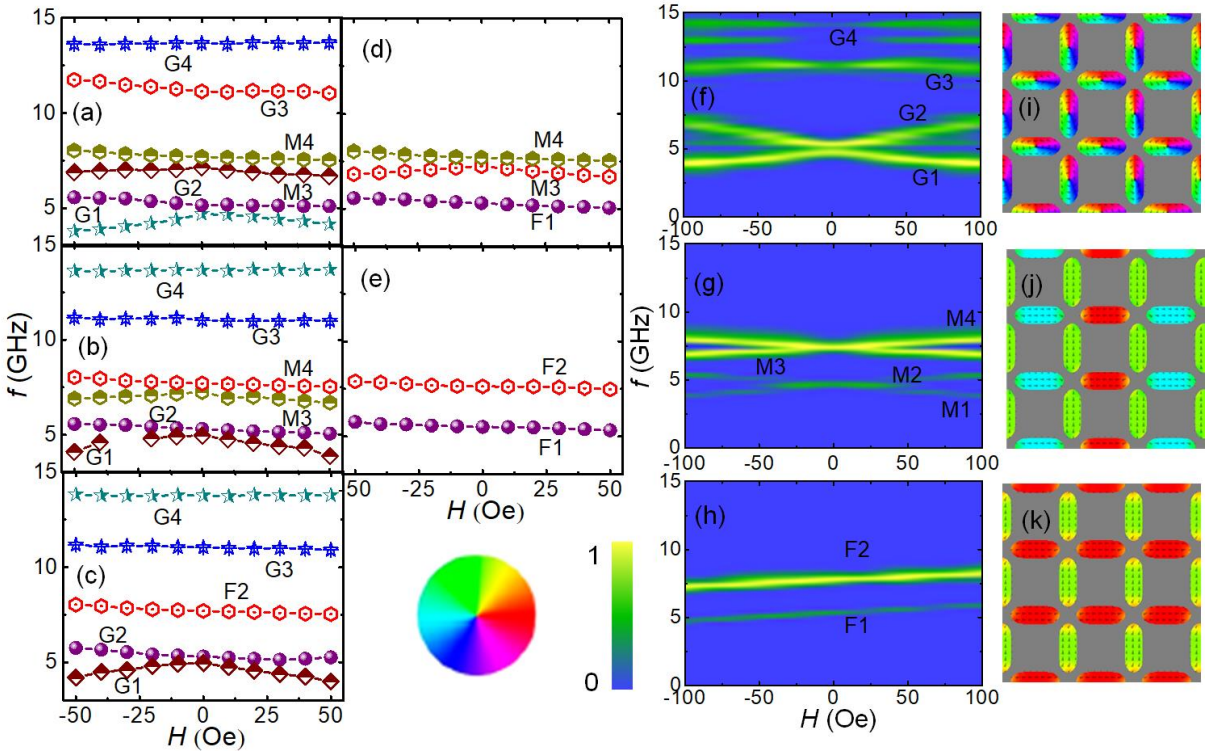

Figure 8.7: (a)-(e) Bias-field-dependent SW mode frequencies for [S1]-[S5] states. (f)-(h) Simulated SW field dispersion for pure vortex state, T3 and T2 ASI microstate. (i)-(k) Representative vortex, T3 and T2 microstate.

SW Dynamics: The representative BLS spectra for [S1]-[S5] at k ≈ 0 in the DE geometry at H = -100 Oe are shown in Figs. 8.6(k)-(o). Figures 8.7(a)-(e) are the five representative 3D surface plots of SW field dispersion over a range -50 ≤ H ≤ +50 Oe for [S1]-[S5] states. We have observed a significant change in the number of modes for different states. To identify the origin of those modes, we have performed micromagnetic simulation in pure vortex state, T3 and T2 microstate as represented in Figs. 8.7(i)-(k). The vortex state, T3 and T2 microstate dependent simulated SW dispersion are represented in Figs. 8.7(f)-(h). Four dominating modes (G1, G2, G3, and G4) are observed for pure vortex states, with an avoided crossing at H = 0 Oe and f ≈ 5 GHz between G1 and G2. Similarly, four dominating SW modes (M1, M2, M3, and M4) are observed for the pure T3 microstate, along with two avoided crossings at H = 0 Oe; one at f ≈ 4.9 GHz between M1 and M2, and another at f ≈ 7.5 GHz between M3 and M4. The slope ($\partial f/\partial H$) of modes G1 and G2 is higher than that of M1 and M2, as well as M3

and M4. Finally, only two SW modes with positive slopes, labelled as F1 and F2, are observed for pure T2 microstates, as shown in Fig. 8.7(h). These results illustrate the unique nature and type of SW spectra in the vortex, T3 and T2 microstates. Further extension of those outputs in our [S1]-[S5] microstates led to the observation of six modes (G1, G2, G3, G4, M3 and M4) for [S1] and [S2], five modes (G1, G2, G3, G4 and F2) for [S3], three modes (F1, M3 and M4) for [S4], and two modes (F1 and F2) for [S5] microstate. Here, the slopes of G1 and G2 modes for [S3] is also higher than M3 and M4 modes for [S4].

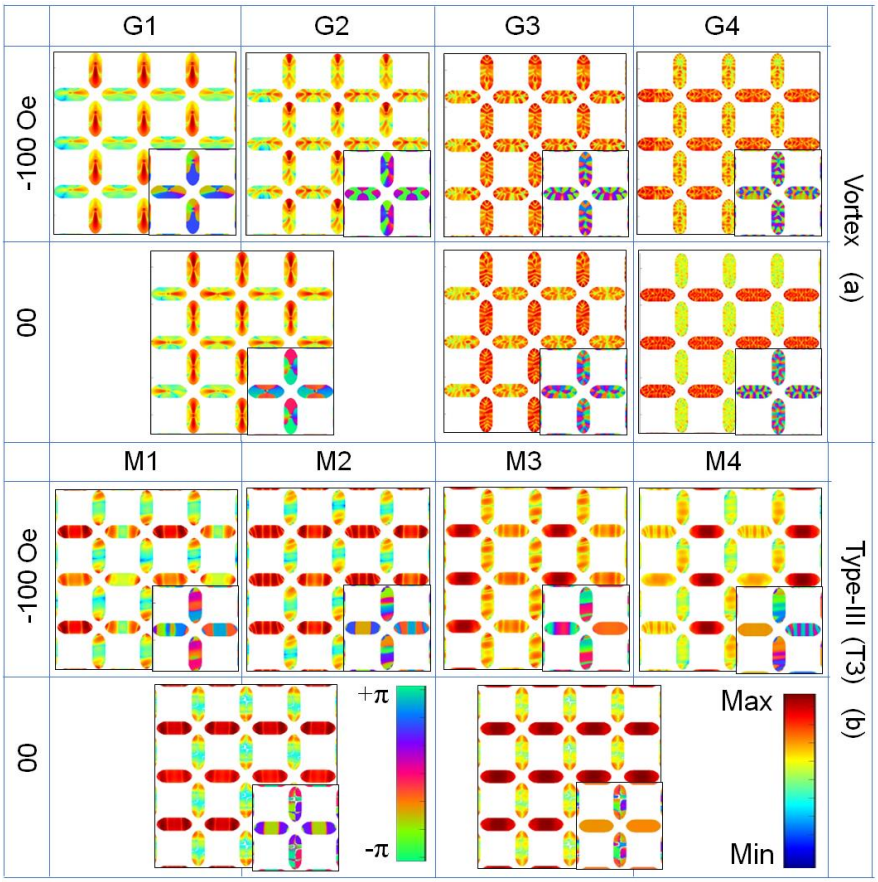

Figure 8.8: (a)-(b) Simulated spatial distribution of power and phase of the SW modes for vortex (a) and T3 ASI state (b) at H = -100 Oe and 0 Oe respectively.

Figures 8.8(a)–(b) shows the spatial profiles of the pure vortex and T3 microstate magnon modes at *H* = 0 and -100 Oe. At *H* = -100 Oe, the G1 and G2 modes are bulk butterfly-like modes localized mostly at VNBs, below and above the vortex core, respectively. The quantization numbers of G1 and G2 are (2,4), (2,4) in VNBs and (2,2), (5,2) in HNBs for *H* = -100 Oe. The G3 and G4 are whispering gallery-like vortex modes, with quantization numbers of (3,10), (3,12) in VNBs and (10,3) and (14,3) in HNBs

for both H (0 and -100 Oe). When H = 0 Oe, the power of G1 and G2 modes is symmetrically distributed in each of the NBs with quantization numbers of (2,4) in VNBs and (2,2) in HNBs. The M1 and M2 are the UM with most of their power localized in the left arm of the HNB of a unit grid for M1 and in both arms of HNBs for M2, respectively, at H = -100 Oe. The quantization number of M1 and M2 modes are (1,5), and (1,5) in VNBs, respectively, while their quantization numbers in the left and right HNB of a unit grid are (6,1) and (3,1) for M1 and (3,1) and (6,1) for M2. At H = 0, they become another UM with quantization numbers (2,4) in VNBs and (3,1) in HNBs. Meanwhile, the M3 and M4 are also UMs with most of their power localized in the left arm of the HNB of a unit grid for M3 and the right arm of the HNB of a unit grid for M4 at H = -100 Oe. The quantization number of those M3 and M4 modes are (1,4), and (1,5) in VNBs, respectively, while the left and right arms of the HNBs of a unit grid have quantization numbers of (5,1) and (1,1) for M3 and (1,1), (11,1) for M4. When H = 0, these modes become localized UM in HNBs with quantization numbers (2,4) in VNBs. The localization of M3 and M4, specifically at the left and right arms of the HNBs, leads to the design of "0" and "1" in the binary digits in magnonics. This phenomenon is also useful for the design of frequency-selective magnonic sensors and filters, enabling the development of new-generation magnonic devices.

IV. Conclusions:

In conclusion, we have investigated the magnetization dynamics of square artificial spin ice (ASI) nanostructure composed of Py using a combination of BLS spectroscopy and micromagnetic simulations. The experiment MFM images revealed 2-in-2-out type-II ASI states at various remanences for $0° \leq \varphi \leq 45°$ and $\varphi = 90°$ (in-plane bias field orientation: φ). The magnetic hysteresis loop was also measured by S-MOKE for $0° \leq \varphi \leq 45°$ which showed a single-step reversal and a good agreement was found using micromagnetic simulation. Field-dependent SW dispersion have revealed rich anisotropic behaviour in the number of SW modes, SW frequency (f), and BLS intensity. A ‘W’ shaped SW field dispersion is observed for low-frequency SW mode at $\varphi = 0°$ and 15°, which transferred to a monotonic field dispersion at $\varphi = 45°$ due to the transition of the y-component of the demagnetizing field (H_{dy}) inside NBs. Furthermore, a sharp jump in frequencies of the rest of SW modes is observed at H_T where a similar jump is observed in the distribution of the demagnetization field for all φ. The calculated SW mode profiles also show a striking difference in power and phase profile due to a change in φ. Most of the power is localized either in HNBs or VNBs for $\varphi = 0°$ whereas the power is distributed on both NBs for $\varphi = 45°$. In addition, five different microstates are reconfigured in the same ASI sample. The

presence of these five microstates offers a wide range of magnonic spectra, allowing precise control over mode frequency shifting, the opening and tuning of microstate-specific anti-crossing gaps, and the number of dominating SW modes. The versatility of microstate-dependent SW modes and anti-crossing gap control demonstrated in this study opens up a range of potential applications, including binary digits, filters and sensors. This can be used to further characterize the SW band structure of ASI-based nanomagnetic systems for application in magnonic logic [397] and neuromorphic devices [390,393,394]. Besides, this study provides characteristic BLS peaks for specific magnetic microstates in ASI more like molecular spectra or x-ray diffraction study where the configuration of the magnetic microstates can be predicted in the ASI system only by measuring the BLS spectra and without doing extensive MFM imaging. This leads to a step forward to the ASI physics.

Chapter 9

9. Summary and Future Perspective

9.1 Summary:

In summary, we have investigated the spin dynamics and spin-wave dynamics in different spintronic and magnonic systems in three different possible experimental domains, i.e., wave vector domain (Brillouin light scattering (BLS) spectroscopy), frequency domain (broadband vector network analyzer based ferromagnetic resonance (VNA-FMR)) and time domain (time-resolved magneto-optical Kerr effect (TR-MOKE) microscopy) in systems ranging from patterned magnetic nanostructures to thin film heterostructures. We have studied different phenomena like ultrafast demagnetization, fast relaxation, magnetization precession, spin-wave (SW) dispersion and damping in ferromagnetic (FM) thin films, nonmagnetic (NM)/FM heterostructures and single layer graphene (SLG)/FM heterostructures. Further, we have performed SW dispersion and magnetization dynamics in FM nanostructures. All the samples used in this thesis were prepared by different techniques including thin film heterostructures by DC and RF magnetron sputtering under ultrahigh vacuum and nanostructure using a combination of electron beam lithography (EBL), electron beam evaporation and ion milling. The topographical and elemental properties have been characterized by scanning electron microscopy (SEM), atomic force microscopy (AFM), energy dispersive X-ray (EDX), micro-Raman spectroscopy analysis techniques, and X-ray diffraction (XRD). The static magnetic properties have been studied by the vibrating sample magnetometry (VSM), magnetic force microscopy (MFM) and static magneto-optical Kerr effect (S-MOKE) magnetometry. Further, micromagnetic simulations such as OOMMF, MuMax3, and LLG micromagnetic simulator and numerical plane wave method have been explored to reproduce our experimental observations.

First, we have investigated both qualitatively and quantitatively the pure iDMI and pure spin current in SLG/CoFeB/SiO_2 heterostructure using BLS technique. Both qualities i.e., iDMI and effective damping have shown a linear variation with inverse of CoFeB thickness (t_{CoFeB}) in SLG/CoFeB stacks. The micro-Raman spectra of SLG and SLG/CoFeB films represent the variation in spectral weight ratio (I_D/I_G) which shows that 'I_D/I_G' ratio increases with the inverse of t_{CoFeB}. We have subsequently calculated the defect density (n_D) from this spectral weight ratio. Finally, the correlation between D and α_{eff} with n_D shows the role of enhancement of extrinsic spin-orbit coupling (SOC) at SLG/CoFeB interface leading to the sufficiently high iDMI and effective damping in this system even at moderately

low Ar sputtering pressure. Interestingly, both of these quantities show exponential increments with defect density. This corroborates that the defect-induced extrinsic SOC plays a major role over Rashba SOC in the observed iDMI, spin pumping and spin-mixing conductance in these samples. Our study promises the possibilities of stabilizing chiral spin textures like nanoscale skyrmions and their manipulation using defect-induced extrinsic SOC at SLG/FM interface for developing new-generation energy-efficient memory and logic devices.

After exploring a reasonable amount of iDMI and pure spin current flow during spin pumping from CoFeB to SLG, we have explored another type of spin transport (ST) in our study on Co/Pt multilayer system. Here, we have systematically varied different domain configurations at the ac demagnetized state, and a few different remanence states and saturated state. We have investigated the ultrafast demagnetization process along with transient magnetic enhancement (TME) using TR-MOKE magnetometry in Co/Pt multilayer system for those different magnetic domains in absence of any bias magnetic field. We have proposed a new mechanism of transfer of spin angular momentum between two neighbouring domains to enhance effective magnetization in the system. These ST-driven ultrafast magnetization dynamics show a phase transition from pure ultrafast demagnetization state to pure TME state through a state where both TME and demagnetization co-exists in the system. Further, the amount of quenching can also be controlled by laser pump fluence. Our results exhibit potential applications of ferromagnet/heavy metal multilayered structures in spintronic devices and ultrafast optical manipulation of spin dynamics via SST for faster switching applications.

The hybrid systems allow for quantum transduction and coherent information transfer and to this end, quantum coupling of magnons with superconducting qubits, phonons, photons and magnons has been explored. Usually, such coupling is enhanced by the number of spins (N) in the systems and therefore continuous thin films and ferromagnetic microstructures have been mostly studied due to very large values of N. On the other hand, intermediate to strong magnon-magnon coupling in ferromagnetic nanostructure arrays can be boosted by microwave-pumped dipolar coupling between the nanoelements. This has opened a new avenue for attaining nanoscale hybrid magnonics. Keeping this in mind, here we have studied SW dynamics of triangular-shaped Py nanodot (having some edge deformation) arrays arranged in a square lattice with lattice constants of 395 nm and 305 nm and lengths 325 nm and 235 nm (S1 and S2), respectively using broadband FMR. Here, two low-frequency modes i.e., F1 and F2 modes show a clear mode repulsion, characteristic of anticrossing due to magnon-

magnon coupling. The cooperativity is found to be maximum at around 21.11 at 15º in-plane (InP) orientation of bias field (H) with $H \approx 845$ Oe for S2 sample. The mode repulsion occurs between F1 and F2 modes because of significant modification of the stray field of individual triangle. This anticrossing gap is also stable under external microwave power for both samples. This result will be useful for the design of integrated on-chip devices using planar hybrid systems towards new generation nanoscale magnonics.

Connected nanodots are promising systems because of their fundamental importance and potential applications in field of information communication and processing by aiding information transfer. The advantage of *connected dots* (CDs) array over 1D dot array of separated dots is its complex shape anisotropy and both dipole and exchange interactions which enable stabilization of different types of spin configurations in the system. As all the magnetic nanodots are physically connected where both exchange and magnetostatic interaction can play an important role in SW propagation, and provide channels for SW propagation while posing a periodic potential to the propagating SWs. In this work, we show reconfigurable magnonic band structure and band gap by a bias-field controlled spin texture in chains of connected $Ni_{80}Fe_{20}$ (permalloy, Py hereafter) submicron dots. Interestingly, we could attain two different spin textures and starkly different SW dynamics at the same bias-field magnitude of 330 Oe but reached by following two different magnetic histories, i.e., a 'field-bifurcation'. A first-order phase transition from the saturation to magnetic vortex state is found to drive this change, as opposed to a continuous change from a saturated state to an 'S' state.

Next, we have extended our study to explore the role of those magnetic spin textures in artificial spin ice (ASI) system. Here, we have employed the effects of magnetic field sweeping on magnetic microstates and the ensuing SW dynamics in a square ASI structure made of Py for different InP bias field orientations (φ). Rich SW spectra are observed in the system and a detailed SW dispersion with both the φ and H has been studied experimentally and by numerical simulations. We observe a transition from '*W*' shape to monotonous variation of low-frequency SW mode with the rearranging of the magnetic microstate by changing φ from 0° to 45°. Further, a sharp jump in the rest of SW modes is observed before '*W*' minima in negative H. This jump is correlated with the reversal field of the nanobars observed in the MOKE loops and the position is tuned by bias field orientation. The calculated SW mode profiles show a striking difference in power and phase profile due to changes in φ. Most of the power is localized either horizontal or vertical nanobars for φ = 0° whereas power is uniformly

distributed on both nanobars for φ = 45°. Furthermore, we have introduced a new technique to control topological defect states which can generate distinct SW modes in the spectra. Observation of such reconfigurability of dipolar mediated interaction on the number of SW mode, SW mode frequency and intensity would pave the way for the advancement of spin-texture driven magnonics.

9.2 Future Perspective:

The continuous and confined magnetic thin films are the building blocks for future storage devices with higher storage density, faster processing speed and energy-efficient communication devices. Therefore, an in-depth scientific understanding of ultrafast spin dynamics and control over different spin-related effects in these ferromagnetic continuous and confined films is one of the most crucial aspects of modern magnetism research. The study of spin dynamics in such systems can enhance the fundamental understanding as well as can resolve the issue of thermal loss due to the Joule heating effect in current complementary metal-oxide-semiconductor (CMOS) based devices. Nowadays, significant attention is being paid to enhancing the iDMI constant which is essential to stabilize chiral spin textures such as skyrmions and non-reciprocal SW dispersion. The HM/FM is a common choice for high iDMI systems but recently 2D-metal/FM interface promises an alternative choice to stabilize chiral spin textures. The most common HMs are Pt, Pd, W, Hf and Ta and FMs are Co, CoFeB, CoFe, and $Ni_{80}Fe_{20}$. The alternative 2D-metals are MoS_2, $MoSe_2$, graphene, WS_2, WSe_2. Furthermore, FM sandwiched between two different nonmagnet (NM) with opposite signs of the iDMI holds promise for the additive nature of the iDMI. Again, the study of ultrafast magnetization dynamics in various FM samples is another attractive aspect where the sub-ps response time of spin dynamics is crucial for developing ultrafast magnetic devices. Many theoretical and experimental research approached to divulge the underlying mechanism behind the nature of ultrafast demagnetization. Despite such great efforts, many questions remain unanswered. Apart from the ST between FM and NM, the ST between neighbouring domains is also found to be important in inducing ultrafast demagnetization. Very recently, new mechanisms of optical inter-site spin-transfer (OISTR) and TME have also been proposed to explain the unusual ultrafast demagnetization in the multi-domain system. Similar investigation can be extended to various samples to reveal the underlying mechanism and complete understanding of ultrafast magnetization dynamics.

Besides, quasiperiodicity in 1D, 2D even 3D nanomagnets offers new dimensionality in the design of collective spin-wave excitation spectra. Hybrid systems are to be considered as triggering candidates

using different carriers such as superconducting qubits, phonons, photons and magnons to boost the fundamental importance of nanoscience and nanotechnology. The study of avoided crossing in magnetic nanodots can open the door to developing magnon-based energy-efficient gigahertz frequency on-chip quantum devices. Here the magnon-magnon coupling strength in a single cavity or multi-cavity system can be efficiently tuned by varying various external and internal parameters such as the orientation of the bias magnetic field, size, shape, periodicity of the nanomagnet and exciting rf power. Furthermore, different spin textures, such as domains, quasi-uniform states, vortex, skyrmion, and antiskyrmion are nonuniform and ordered magnetic spin configurations, which are of increasing interest as active components in magnetic data storage and information processing. There are many limitations in sample fabrication in terms of achieving desired shape, size, geometry, dimension and inter-element separation. The periodic arrangement of those spin textures can fulfil those drawbacks by introducing an additional degree of controlling and scaling parameters toward nanoscale dimensions. The main degree of freedom of spin texture is to design an on-demand magnonic crystal using direct control of the external magnetic field and magnetic parameters of the system. At the end of this thesis, the frustration in any FM system gives rise to the disordered ground state with macroscopic degeneracy in ordered FM systems. These frustrations can form special kinds of spin textures, such that magnetic monopoles and antimonopoles in ASI structures. The frustrations can be further controlled by system geometry, magnetic history and magnetic parameters. This structure has a residual entropy even at very low temperature. The study of SW mode interaction with magnetic defects and the reconfigurability of those defects can give rise to novel types of SW dispersion. Also, the SW propagation through the monopoles in an ASI is very fascinating to explore by using imaging techniques such as micro-focused BLS, and X-ray tomography, which can add some new functionalities by modifying SW intensity and/or frequency. Such engineering of magnetization dynamics via different spin textures and dimensionality can play an important role in the understanding of the novel phenomena in these systems and their potential applications in future spintronics and magnonics technology.

Appendix A: Chapter 5

A. Characterization of Domain Configuration:

The power spectral density (PSD)for different domain configurations observed in the ferromagnetic multilayer thin film heterostructure Ta(1.5nm)/Pt(20nm)/[Co(3nm)/Pt(0.6nm)]$_{22}$/Pt(2.4nm) as described in the main articleare shown in Figures 5.1S(a)-(e).We have fitted those PSD using the

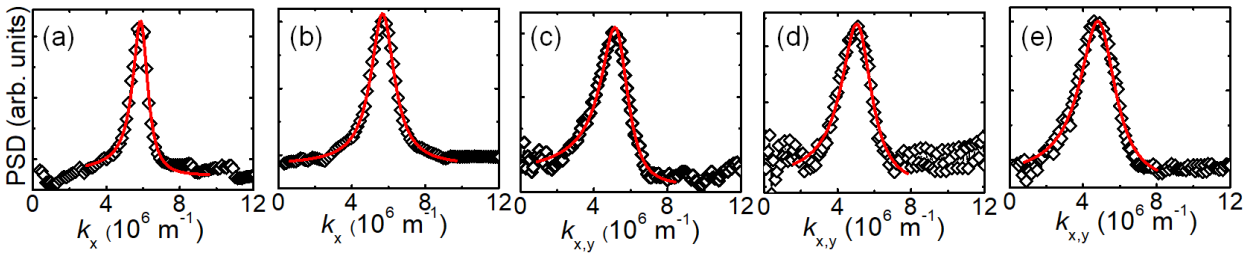

Figure 5.1S*:*(a)-(e) Power spectral density (PSD) of [S2], [S1], [S5], [S4] and [S3] domain configurations respectively.

asymmetric Lorentzian function and extracted the average wavenumber (k) and linewidth (Δk). Figures 5.1S(a)-(b) show only average k_x obtained from [S2] and [S1] domain configurations. Figures 5.1S(c)-(d) represent average wave number in both directions i.e., $k_{x,y}$ for[S5], [S4], and [S3] respectively.

B. TR-MOKE Trace and MFM Image After and Before Measurement:

Figure 5.2S(a) shows representative TR-MOKE trace obtained from nearly pure stripe domain configuration (at remanence after application of 2 kOe InP magnetic field) at pump and probe fluence of 1.50 mJcm^{-2} and 10.40 mJcm^{-2} respectively. This TR-MOKE trace consists of four-part (i) ultrafast demagnetization (ii) magnetization recovery along with transient magnetization enhancement (TME) region (iii) fast final magnetization recovery region and (iv) slow final magnetization recovery region. We have discussed the variation of different amplitude and time constant for different pump fluences in the main article. Figures 5.2S(b)-(c) represent two MFM images recorded before and after the ultrafast demagnetization measurement respectively showing invariance of the domain structure before and after ultrafast demagnetization measurement.

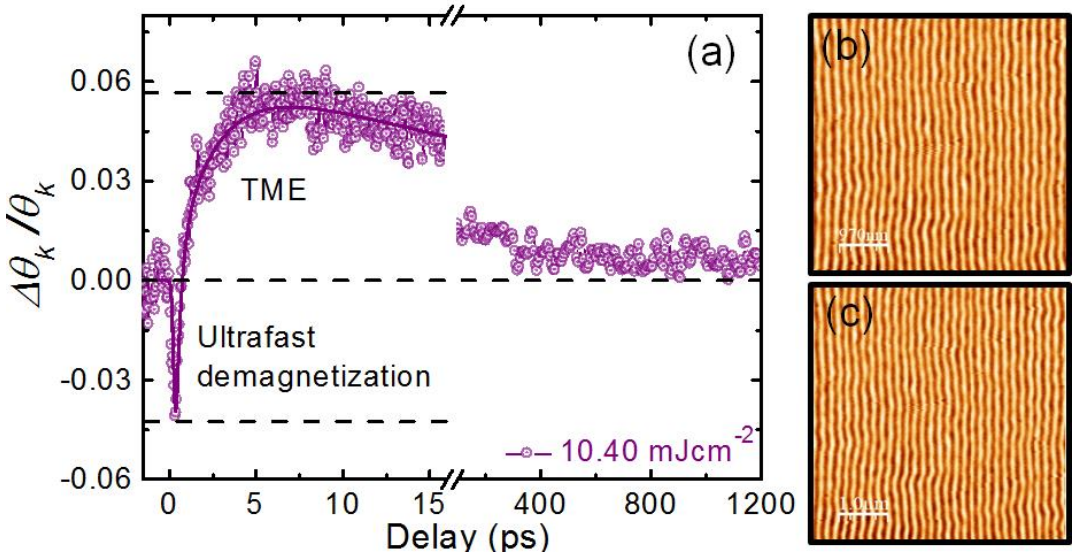

Figure 5.2S: (a)TR-MOKE signal for [S2] at pump fluence 10.40mJ cm^{-2} where different temporal regions are marked. The MFM images before (b) and after (c) TR-MOKE measurement.

C. Additional Ultrafast Demagnetization Result for [S1] and [S3] Domain Configuration:

Figures 5.3S(a)-(b) show representative ultrafast demagnetization traces recorded for [S1] and [S3] domain configurations with varying laser pump fluence. We have fitted our result with Equation (2) of the main article to extract the relevant time constants. Figures 5.3S(e)-(f) show the variation of those time constants with different pump fluences which shows a monotonic trend. Demagnetization amplitude and time constant for [S1] are a bit smaller than those for [S2]. The variation of ultrafast demagnetization amplitude and TME amplitude with different pump fluences is shown in Figure 5.3S(c) for [S1]. In case of [S3], we have only TME amplitude and time constants. The variation ofTME amplitude for [S3] is shown in Figure 5.3S(d).

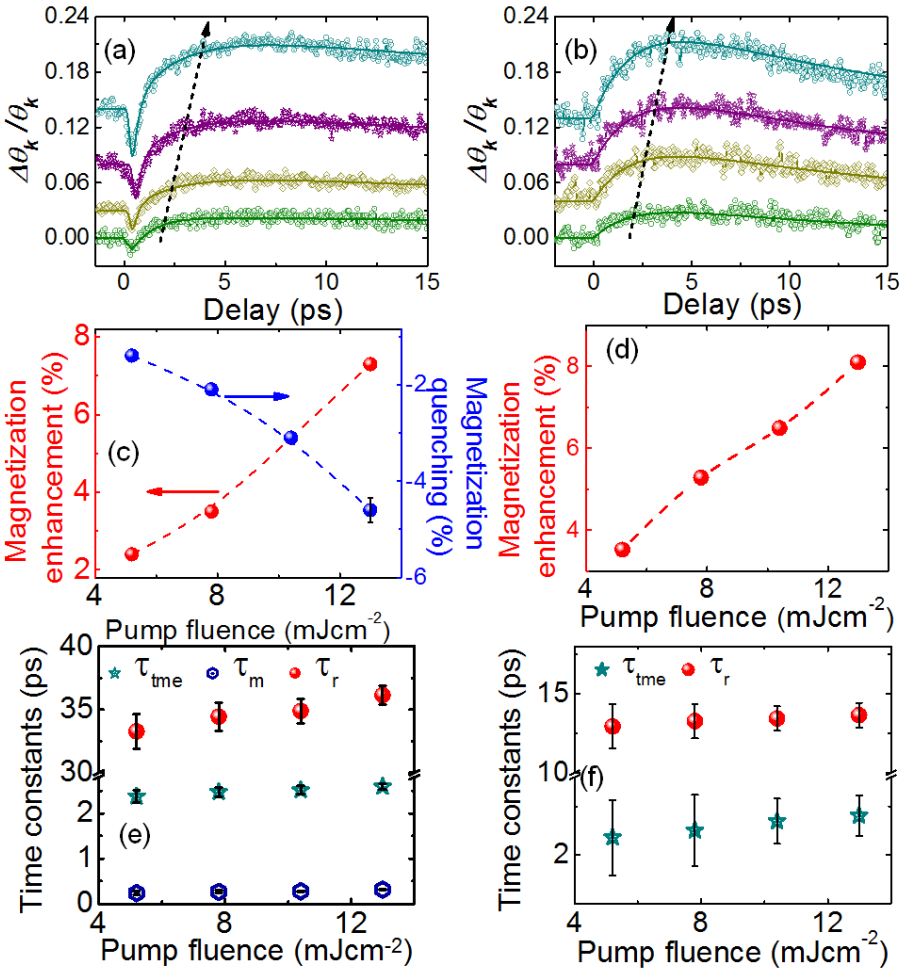

Figure 5.3S: (a)-(b) TR-MOKE signal for [S1] and [S3] domain configurations respectively for various pump fluences (Cyan: 12.99; Violet: 10.40; Gold: 7.80 and Olive: 5.2 mJ cm^{-2}). The variation of different amplitudes for [S1] (c) and [S2] (d) with different pump fluences. The variation of different time constants for [S1] (e) and [S2] (f) with different pump fluences.

Appendix B: Chapter 6

A. Ground State Spin Configuration for Different In-plane Bias Field Orientation:

Here we show the simulated ground state spin configuration along with three-dimensional (3D) surface

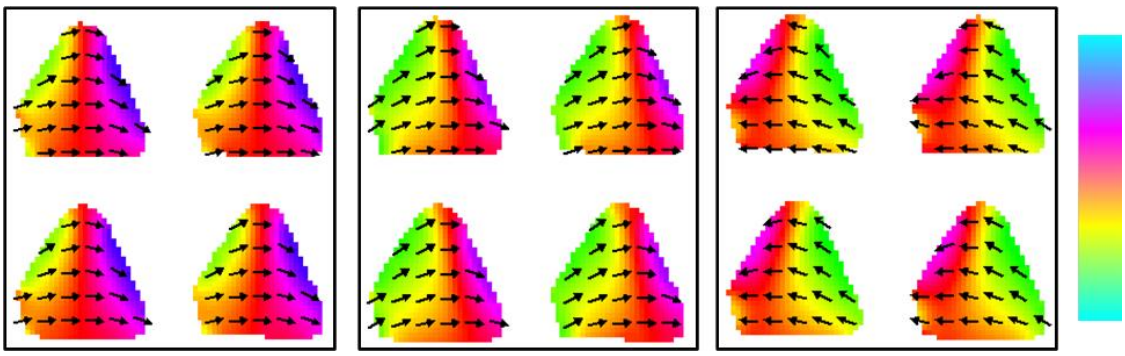

Figure 6.1S*:* Surface plot of magnetization and spin configuration for the bias field orientation (φ) of (a) 0º, (b) 15º and (c) 165º for sample S2 at *H* = 850 Oe.

plot of magnetization distribution for sample S2 at bias field orientation (φ) of (a) 0º, (b) 15º and (c) 165º at *H* = 850 Oe. In all cases they show quasi-uniform spin configurations forming C-like states.

B. Simulated Spin Wave Dynamics for Deformed Single Triangular Nanodot:

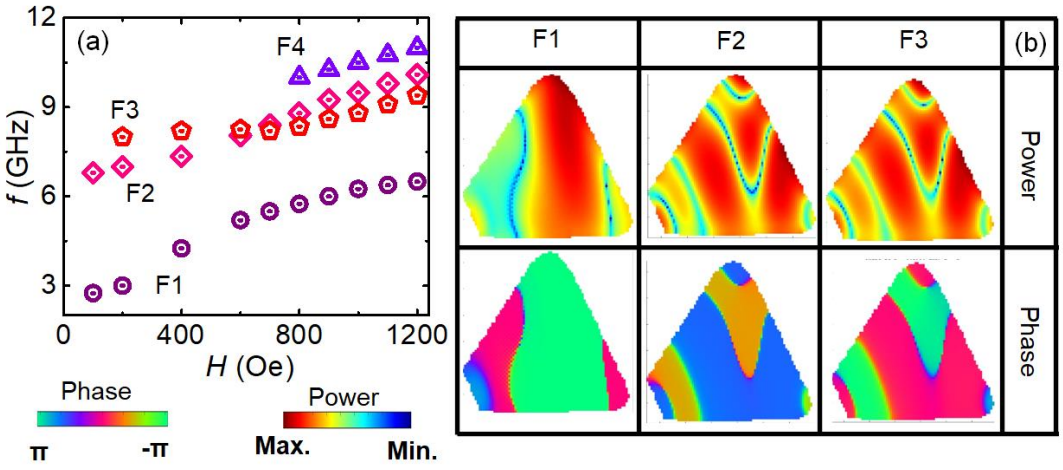

Figure 6.2S*:* (a) Simulated SW frequencies as a function of bias magnetic field at an orientation (φ) of 15º for deform single triangle. (b) Simulated spatial distribution of power and phase of the SW modes obtained at *H* = 700 Oe.

We have simulated spin-wave frequency variation with *H* for deformed single triangular nanodot at φ = 15º. Here, we have observed rich frequency variation for four prominent SW modes as shown in Fig. 6.2S(a). Clearly, two SW modes (F2 and F3) cross each other at *H* = 700 Oe, while an avoided crossing occurs between F1, and F2 or F3 modes around the same field value. Figure 6.2S(b) shows the power

and phase profiles of the three modes, which reveals quantized nature of the modes. The quantization number (*n*: backward volume, *m*: Damon Eshbach) of F1 mode is (4,1) whereas the same for F2 and F3 modes are (4,3). The simultaneous occurrence of two phenomena, i.e., magnon-magnon crossing and avoided crossing in the same system suppressed the phase coherence between F1 and F2, F3 modes. In case of deformed triangular dot array, the avoided crossing phenomena between F1 and F2 mode with no magnon-magnon crossing, enabled the system to revive the said phase coherence at the region of avoided crossing as discussed in the main article.

C. Simulated Stray and Internal Magnetic Field Distribution with Bias Field Orientation for S1:

Figures 6.3S(a)-(c) shows three representative stray field distribution at at φ = 0º, 15º, and 165º, respectively, at H = 900 Oe (i.e., in the avoided crossing regime). The linescan of stray field distribution

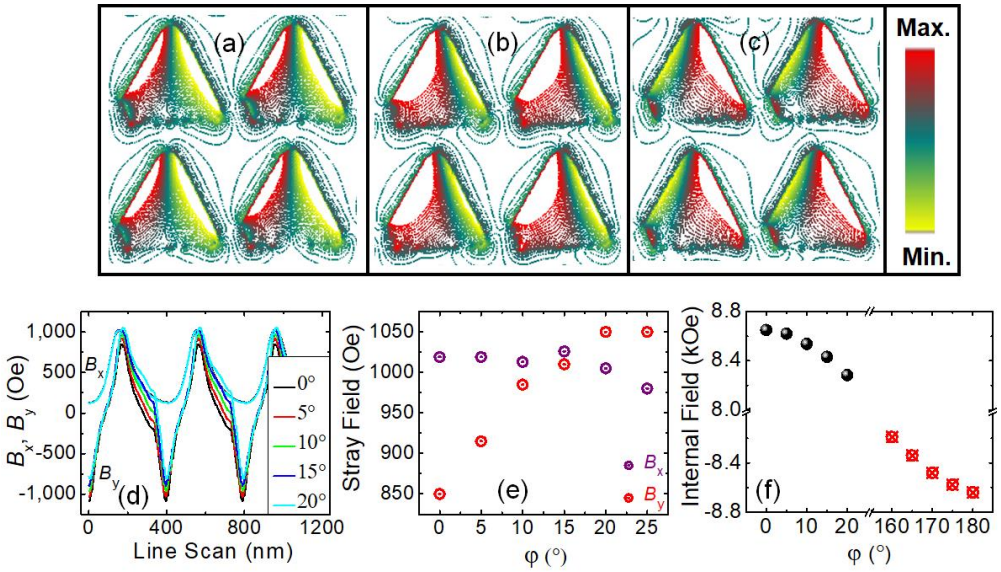

Figure 6.3S*:* Simulated magnetostatic field distribution at P = −15 dBm for φ = (a) 0°, (b) 15° and (c) 165°. (d) Linescans of the simulated magnetostatic fields (B_x, B_y). (e) Variation of stray magnetic field with φ. (f) Variation of internal field distribution with φ for sample S1.

(B_x, B_y) in the nonmagnetic region is shown in Fig. 3S(d) for S1. Figure 3S(e) is the variation of stray field, i.e., (B_x, B_y) with φ for S1. We have also calculated internal field for S1 and presented it in Fig. 3S(f). All these three quantities follow similar variations as mentioned in the article for S1 sample.

Appendix C: Chapter 7

A. Experimental and Simulated MFM Images at Remanence and at an Applied Magnetic Field:

Here we show the experimental MFM image for the studied sample with and without external magnetic field. Figure S1(a) represents the experimental MFM image in the remanent state after the magnetic field is reduced from the positive saturation field to zero. The simulated MFM image using LLG micromagnetic simulator at the remanent state using identical conditions as the experiment is shown in Fig. S1(b). We have also shown the simulated MFM image in Fig. S1(c) after the sample is AC demagnetized followed by increasing the magnetic field to 330 Oe, using the steps mentioned in the article. It shows shifted core magnetic vortex states in the dots.

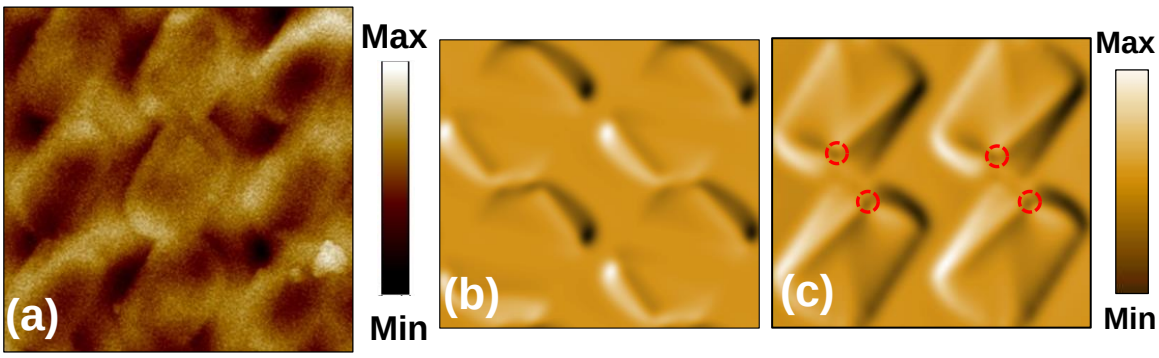

Figure 7.1S: (a) Experimental MFM image of the sample at the remanent state. Simulated MFM images at the (b) remanent state and (c) shifted core vortex state at H = 330 Oe (obtained by rising the magnetic field from the AC demagnetized state), respectively.

B. Supplemental Movie: We have simulated the static magnetic configurations of the sample at different bias magnetic field (H) values starting from the AC demagnetized state to saturated state, i.e. $0 \leq H \leq 500$ Oe at an interval of 5 Oe and collected the snapshots of the M_y component of magnetization to form a movie, **M1**. In this movie, we have shown the motion of the vortex core with the variation in H. To obtain a vortex state, first we simulated the AC demagnetized state. Subsequently, we have shown well controlled core movement with H. This result corresponds to a first order phase transition from vortex to leaf state at H = 465 Oe.

C. Reconfigurable Magnonics Mediated by Coupling Between Different Spin Textures in $Ni_{80}Fe_{20}$ Diatomic Nanodots: In the above investigations, we have shown that magnetic quasi-spin texture plays an important role in the magnonic band structure. Here, we have taken 25-nm-thick

$Ni_{80}Fe_{20}$ (permalloy: Py hereafter) made diatomic nanodots in a rectangular symmetry as shown in Fig. 2S(a). The circular-shaped Py diatomic nanodot array of 500 μm × 500 μm area, characterized by a

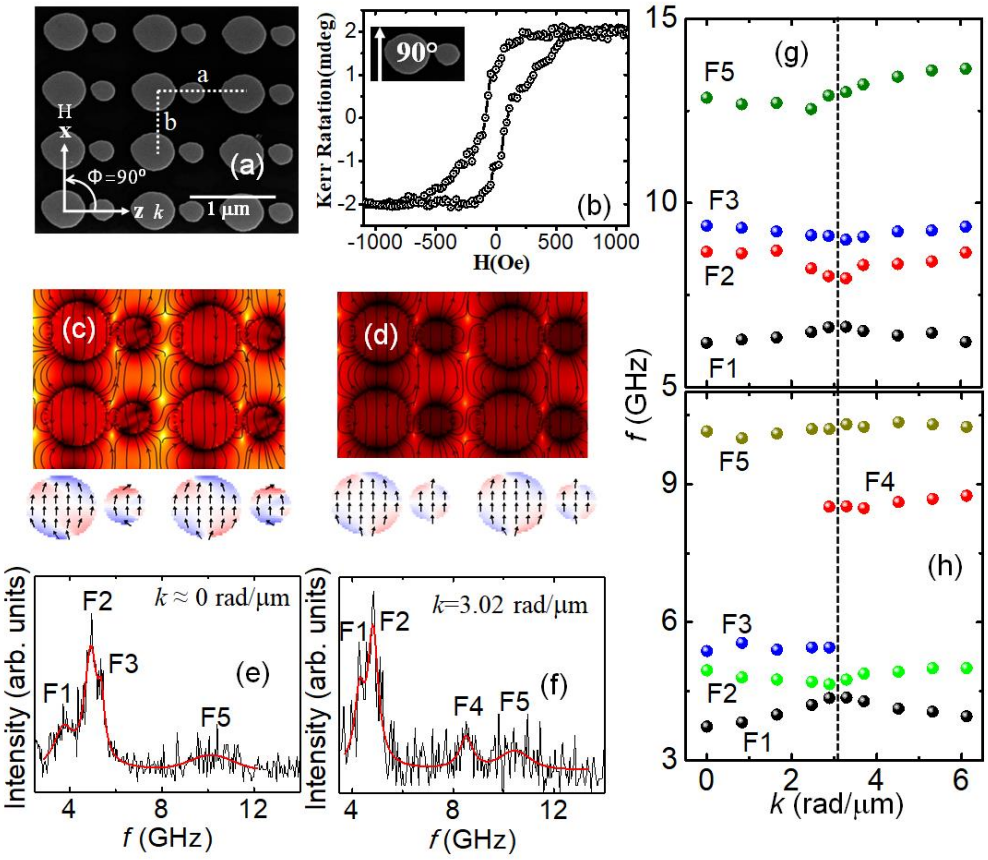

Figure 7.2S: (a) Scanning electron microscope (SEM) image and (b) experimental magnetic hysteresis loop of the sample. (c)-(d) Simulated demagnetization field distribution with spin texture coupling at two different bias magnetic field values, H_1 = 900 Oe (leaf state - leaf state coupling) and H_2 = 300 Oe (leaf state - C state coupling). (e)-(f) The Stokes side of BLS spectra taken at H_2 = 300 Oe at $k \approx 0$ and $k \approx 3.02$ rad/μm. (g)-(h) Magnonic band structure corresponding to two different coupled magnetic states, i.e. leaf-leaf and leaf-C coupling, respectively.

complex double-dot unit cell has been fabricated on self-oxidized Si [100] substrate using the same method discussed in chapter 7. The diameter of the larger and smaller dot of one unit is about 490 nm and 235 nm, respectively, as shown in the SEM image in Fig. 7.2S(a). The separation between the larger and the smaller dot (intra-unit) is about 60 nm, while the inter-unit separation is about 215 nm. The magnetic hysteresis loop measured by static magneto-optical Kerr effect at $\phi = 90^o$ is shown in Fig. 7.2S(b). The variation of demagnetization field distribution along with two different spin-texture couplings namely leaf state - leaf state coupling (H_1 = 900 Oe), and leaf state - C state coupling (H_2 = 300 Oe obtained by reducing the field from saturated state) are shown in Figs. 7.2S(c)-(d).

In Figs. 7.2S(e)-(f), we present two representative BLS spectra for $k \approx 0$ (centre of BZ) and $k = 3.02$ rad/μm (1^{st} BZ boundary, $k \approx \pi/a$) at H_2. The experimental SW dispersion relations for H_1 and H_2 fields are plotted in Figs. 7.2S(g)-(h). A significant change in spin wave dispersion is observed due to change in coupling of spin texture. A significant increment of unsaturated magnetic spin drives this change when field is reduced from H_1 and H_2, due to increment of dynamic dipolar interaction between the neighboring dots, as shown in Figs. 7.2S(d)-(e).

Observation of such reconfigurable band structure with external bias magnetic field and ensuing spin texture would pave way for the advancement of a new research field called spin-texture driven magnonics.

References:

[1] R. M. García Salvador, N. Novas, A. Alcayde, D. El Khaled, and F. G. Montoya, in *Electronics*2020).
[2] J. Bardeen and W. H. Brattain, Phys. Rev. **74**, 230 (1948).
[3] J. Bardeen and W. H. Brattain, Phys. Rev. **75**, 1208 (1949).
[4] G. E. Moore, Proceedings of the IEEE **86**, 82 (1998).
[5] R. K. Cavin, P. Lugli, and V. V. Zhirnov, Proceedings of the IEEE **100**, 1720 (2012).
[6] K. Molvig, M. S. Tekula, and A. Bers, Phys. Rev. Lett. **38**, 1404 (1977).
[7] Spintronics: Improving electronics with finer spin control, https://phys.org/news/2021-05-spintronics-electronics-finer.html.
[8] I. Žutić, J. Fabian, and S. Das Sarma, Rev. of Mod. Phys. **76**, 323 (2004).
[9] A. Hirohata and K. Takanashi, J. Phys. D: Appl. Phys. **47**, 193001 (2014).
[10] S. D. Bader and S. S. P. Parkin, Annu. Rev. of Condens. Matter Phys. **1**, 71 (2010).
[11] W. Gerlach and O. Stern, Z. Physik **9**, 349 (1922).
[12] G. E. Uhlenbeck and S. Goudsmit, Nature **117**, 264 (1926).
[13] P. A. M. Dirac and R. H. Fowler, Proceedings of the Royal Society of London. Series A, Containing Papers of a Mathematical and Physical Character **117**, 610 (1928).
[14] I. Dzyaloshinsky, J. Phys. Chem. Solids **4**, 241 (1958).
[15] T. Moriya, Phys. Rev. **120**, 91 (1960).
[16] J. Torrejon, J. Kim, J. Sinha, S. Mitani, M. Hayashi, M. Yamanouchi, and H. Ohno, Nat. Commun. **5**, 4655 (2014).
[17] H. T. Nembach, J. M. Shaw, M. Weiler, E. Jué, and T. J. Silva, Nat. Phys. **11**, 825 (2015).
[18] H. Yang *et al.*, Nat. Mater. **17**, 605 (2018).
[19] A. K. Mondal, S. Majumder, S. Sahoo, S. N. Panda, S. Sinha, and A. Barman, ACS Appl. Nano Mater. **5**, 5056 (2022).
[20] F. Ajejas *et al.*, Nano Lett. **18**, 5364 (2018).
[21] A. K. Chaurasiya, C. Banerjee, S. Pan, S. Sahoo, S. Choudhury, J. Sinha, and A. Barman, Sci. Rep. **6**, 32592 (2016).
[22] N. Taniguchi, Proc. Intl. Conf. Prod. Eng. Tokyo, Part II, Japan Society of Precision Engineering (1974).
[23] M. N. Baibich, J. M. Broto, A. Fert, F. N. Van Dau, F. Petroff, P. Etienne, G. Creuzet, A. Friederich, and J. Chazelas, Phys. Rev. Lett. **61**, 2472 (1988).
[24] G. Binasch, P. Grünberg, F. Saurenbach, and W. Zinn, Phys. Rev. B **39**, 4828 (1989).
[25] E. Grochowski, in *Holographic Data Storage*, edited by H. J. Coufal, D. Psaltis, and G. T. Sincerbox (Springer Berlin Heidelberg, Berlin, Heidelberg, 2000), pp. 447.
[26] M. Julliere, Phys. Lett. A **54**, 225 (1975).
[27] J. C. Slonczewski, J. Magn. Magn. Mater. **159**, L1 (1996).
[28] K. Yakushiji, T. Saruya, H. Kubota, A. Fukushima, T. Nagahama, S. Yuasa, and K. Ando, Appl. Phys. Lett. **97**, 232508 (2010).
[29] Y. Huai, AAPPS bulletin **18**, 33 (2008).
[30] K.-S. Lee, S.-W. Lee, B.-C. Min, and K.-J. Lee, Appl. Phys. Lett. **102**, 112410 (2013).
[31] K. Ando, S. Takahashi, K. Harii, K. Sasage, J. Ieda, S. Maekawa, and E. Saitoh, Phys. Rev. Lett. **101**, 036601 (2008).
[32] A. Chernyshov, M. Overby, X. Liu, J. K. Furdyna, Y. Lyanda-Geller, and L. P. Rokhinson, Nat. Phys. **5**, 656 (2009).
[33] See, f. example, D. C. Ralph, and M. D. Stiles, J. Magn. Magn. Mater. **320**, 1190 (2008).
[34] E. Saitoh, M. Ueda, H. Miyajima, and G. Tatara, Appl. Phys. Lett. **88**, 182509 (2006).
[35] J. E. Hirsch, Phys. Rev. Lett. **83**, 1834 (1999).
[36] Y. Tserkovnyak, A. Brataas, and G. E. W. Bauer, Phys. Rev. B **66**, 224403 (2002).

[37] K. Uchida, S. Takahashi, K. Harii, J. Ieda, W. Koshibae, K. Ando, S. Maekawa, and E. Saitoh, Nature **455**, 778 (2008).
[38] P. Barla, V. K. Joshi, and S. Bhat, J. Comput. Electron. **20**, 805 (2021).
[39] V. V. Kruglyak, S. O. Demokritov, and D. Grundler, J. Phys. D: Appl. Phys. **43**, 260301 (2010).
[40] A. Barman *et al.*, J. Phys.: Condens. Matter **33**, 413001 (2021).
[41] F. Bloch, Z. Phys. **61**, 206 (1930).
[42] L.-J. Chang *et al.*, Nano Lett. **20**, 3140 (2020).
[43] J. R. Eshbach, Phys. Rev. Lett. **8**, 357 (1962).
[44] F. Goedsche, Phys. Status Solidi B **39**, K29 (1970).
[45] S. Choi, K.-S. Lee, and S.-K. Kim, Appl. Phys. Lett. **89**, 062501 (2006).
[46] S. Mansfeld, J. Topp, K. Martens, J. N. Toedt, W. Hansen, D. Heitmann, and S. Mendach, Phys. Rev. Lett. **108**, 047204 (2012).
[47] S. O. Demokritov, A. A. Serga, A. André, V. E. Demidov, M. P. Kostylev, B. Hillebrands, and A. N. Slavin, Phys. Rev. Lett. **93**, 047201 (2004).
[48] V. Vlaminck and M. Bailleul, Science **322**, 410 (2008).
[49] S. Bandyopadhyay, J. Atulasimha, and A. Barman, arXiv:2107.08497 (2021).
[50] K. Yamada, S. Kasai, Y. Nakatani, K. Kobayashi, H. Kohno, A. Thiaville, and T. Ono, Nat. Mater. **6**, 270 (2007).
[51] S. Choudhury, A. K. Chaurasiya, A. K. Mondal, B. Rana, K. Miura, H. Takahashi, Y. Otani, and A. Barman, Sci. Adv. **6**, eaba5457 (2020).
[52] M. Mruczkiewicz and P. Gruszecki, in *Solid State Physics*, edited by R. E. Camley, and R. L. Stamps (Academic Press, 2021), pp. 1.
[53] A. Barman and J. Sinha, Springer International Publishing AG (2018).
[54] A. K. Chaurasiya, A. Kumar, R. Gupta, S. Chaudhary, P. K. Muduli, and A. Barman, Phys. Rev. B **99**, 035402 (2019).
[55] A. Kumar *et al.*, Appl. Phys. Lett. **116**, 232405 (2020).
[56] Z. Zhou *et al.*, ACS Appl. Mater. Interfaces **13**, 32579 (2021).
[57] A. Hallal, J. Liang, F. Ibrahim, H. Yang, A. Fert, and M. Chshiev, Nano Lett. **21**, 7138 (2021).
[58] A. Soumyanarayanan, N. Reyren, A. Fert, and C. Panagopoulos, Nature **539**, 509 (2016).
[59] W. Han, R. K. Kawakami, M. Gmitra, and J. Fabian, Nat. Nanotech. **9**, 794 (2014).
[60] H. Bangar, A. Kumar, N. Chowdhury, R. Mudgal, P. Gupta, R. S. Yadav, S. Das, and P. K. Muduli, ACS Appl. Mater. Interfaces **14**, 41598 (2022).
[61] J. Sinova, D. Culcer, Q. Niu, N. A. Sinitsyn, T. Jungwirth, and A. H. MacDonald, Phys. Rev. Lett. **92**, 126603 (2004).
[62] K. Shen, G. Vignale, and R. Raimondi, Phys. Rev. Lett. **112**, 096601 (2014).
[63] M. Belmeguenai, J.-P. Adam, Y. Roussigné, S. Eimer, T. Devolder, J.-V. Kim, S. M. Cherif, A. Stashkevich, and A. Thiaville, Phys. Rev. B **91**, 180405(R) (2015).
[64] K. Di, V. L. Zhang, H. S. Lim, S. C. Ng, M. H. Kuok, J. Yu, J. Yoon, X. Qiu, and H. Yang, Phys. Rev. Lett. **114**, 047201 (2015).
[65] A. Fert, V. Cros, and J. Sampaio, Nat. Nanotechnol. **8**, 152 (2013).
[66] A. Fert, N. Reyren, and V. Cros, Nat. Rev. Mater **2**, 17031 (2017).
[67] C. Moreau-Luchaire *et al.*, Nat. Nanotechnol. **11**, 444 (2016).
[68] K. Everschor-Sitte, J. Masell, R. M. Reeve, and M. Kläui, J. Appl. Phys. **124**, 240901 (2018).
[69] M. V. Kamalakar, C. Groenveld, A. Dankert, and S. P. Dash, Nat. Commun. **6**, 6766 (2015).
[70] I. G. Serrano, J. Panda, F. Denoel, Ö. Vallin, D. Phuyal, O. Karis, and M. V. Kamalakar, Nano Lett. **19**, 666 (2019).
[71] T. Y. Yang *et al.*, Phys. Rev. Lett. **107**, 047206 (2011).
[72] Z. Wang, C. Tang, R. Sachs, Y. Barlas, and J. Shi, Phys. Rev. Lett. **114**, 016603 (2015).
[73] D. Marchenko, A. Varykhalov, M. R. Scholz, G. Bihlmayer, E. I. Rashba, A. Rybkin, A. M. Shikin, and O. Rader, Nat. Commun. **3**, 1232 (2012).
[74] S. Das Sarma, S. Adam, E. H. Hwang, and E. Rossi, Rev. Mod. Phys. **83**, 407 (2011).

[75] N. Ligato, L. S. Caputi, and A. Cupolillo, Carbon **100**, 258 (2016).
[76] S. H. Cheng, K. Zou, F. Okino, H. R. Gutierrez, A. Gupta, N. Shen, P. C. Eklund, J. O. Sofo, and J. Zhu, Phys. Rev. B **81**, 205435 (2010).
[77] C. L. Kane and E. J. Mele, Phys. Rev. Lett. **95**, 226801 (2005).
[78] S.-H. Chen, B. K. Nikolić, and C.-R. Chang, Phys. Rev. B **81**, 035428 (2010).
[79] N. Rougemaille, A. T. N'Diaye, J. Coraux, C. Vo-Van, O. Fruchart, and A. K. Schmid, Appl. Phys. Lett. **101**, 142403 (2012).
[80] M.-H. Liu, J. Bundesmann, and K. Richter, Phys. Rev. B **85**, 085406 (2012).
[81] J. K. Dewhurst, P. Elliott, S. Shallcross, E. K. U. Gross, and S. Sharma, Nano Lett. **18**, 1842 (2018).
[82] M. Hofherr *et al.*, Sci. Adv. **6**, eaay8717 (2020).
[83] B. Koopmans, M. van Kampen, J. T. Kohlhepp, and W. J. M. de Jonge, Phys. Rev. Lett. **85**, 844 (2000).
[84] T. Jiang, X. Zhao, Z. Chen, Y. You, T. Lai, and J. Zhao, Mater. Today Phys. **26**, 100723 (2022).
[85] J. Wang, I. Cotoros, K. M. Dani, X. Liu, J. K. Furdyna, and D. S. Chemla, Phys. Rev. Lett. **98**, 217401 (2007).
[86] D. Rudolf *et al.*, Nat. Commun. **3**, 1037 (2012).
[87] E. Beaurepaire, J. C. Merle, A. Daunois, and J. Y. Bigot, Phys. Rev. Lett. **76**, 4250 (1996).
[88] G. Malinowski, F. Dalla Longa, J. H. H. Rietjens, P. V. Paluskar, R. Huijink, H. J. M. Swagten, and B. Koopmans, Nat. Phys. **4**, 855 (2008).
[89] M. Battiato, K. Carva, and P. M. Oppeneer, Phys. Rev. Lett. **105**, 027203 (2010).
[90] B. Vodungbo *et al.*, Nat. Commun. **3**, 999 (2012).
[91] M. Krauß, T. Roth, S. Alebrand, D. Steil, M. Cinchetti, M. Aeschlimann, and H. C. Schneider, Phys. Rev. B **80**, 180407 (2009).
[92] E. Turgut *et al.*, Phys. Rev. Lett. **110**, 197201 (2013).
[93] B. Koopmans, J. J. M. Ruigrok, F. D. Longa, and W. J. M. de Jonge, Phys. Rev. Lett. **95**, 267207 (2005).
[94] J.-Y. Bigot, M. Vomir, and E. Beaurepaire, Nat. Phys. **5**, 515 (2009).
[95] A. B. Schmidt *et al.*, Phys. Rev. Lett. **105**, 197401 (2010).
[96] B. Koopmans, G. Malinowski, F. Dalla Longa, D. Steiauf, M. Fähnle, T. Roth, M. Cinchetti, and M. Aeschlimann, Nat. Mater. **9**, 259 (2010).
[97] B. Pfau *et al.*, Nat. Commun. **3**, 1100 (2012).
[98] M. L. Lalieu, R. Lavrijsen, and B. Koopmans, Nat. Commun. **10**, 1 (2019).
[99] S. D. Bader, Rev. Mod. Phys. **78**, 1 (2006).
[100] S. A. Nikitov, P. Tailhades, and C. S. Tsai, J. Magn. Magn. Mater. **236**, 320 (2001).
[101] V. S. Tkachenko, A. N. Kuchko, M. Dvornik, and V. V. Kruglyak, Appl. Phys. Lett. **101**, 152402 (2012).
[102] H. Lin, M. Page, M. McConney, J. Jones, B. Howe, and N. Sun, MRS Bull. **43**, 841 (2018).
[103] F. Heussner, A. A. Serga, T. Brächer, B. Hillebrands, and P. Pirro, Appl. Phys. Lett. **111**, 122401 (2017).
[104] Q. Wang, P. Pirro, R. Verba, A. Slavin, B. Hillebrands, and A. V. Chumak, Sci. Adv. **4**, e1701517 (2018).
[105] H. Yu, G. Duerr, R. Huber, M. Bahr, T. Schwarze, F. Brandl, and D. Grundler, Nat. Commun. **4**, 2702 (2013).
[106] A. Khitun, D. E. Nikonov, and K. L. Wang, J. Appl. Phys. **106**, 123909 (2009).
[107] K. Vogt, F. Y. Fradin, J. E. Pearson, T. Sebastian, S. D. Bader, B. Hillebrands, A. Hoffmann, and H. Schultheiss, Nat. Commun. **5**, 3727 (2014).
[108] A. V. Chumak, A. A. Serga, and B. Hillebrands, Nat. Commun. **5**, 4700 (2014).
[109] D. Kumar, S. Barman, and A. Barman, Sci. Rep. **4**, 4108 (2014).
[110] S. Bandyopadhyay, Superlat. Microstruct. **22**, 411 (1997).
[111] R. Hertel, W. Wulfhekel, and J. Kirschner, Phys. Rev. Lett. **93**, 257202 (2004).
[112] M. Balynsky, D. Gutierrez, H. Chiang, A. Kozhevnikov, G. Dudko, Y. Filimonov, A. A. Balandin, and A. Khitun, Sci. Rep. **7**, 11539 (2017).
[113] A. K. Mondal, C. Banerjee, A. Adhikari, A. K. Chaurasiya, S. Choudhury, J. Sinha, S. Barman, and A. Barman, Phys. Rev. B **101**, 224426 (2020).
[114] C. Banerjee, S. Choudhury, J. Sinha, and A. Barman, Phys. Rev. Appl. **8**, 014036 (2017).

[115] G. Sietsema, T. Liu, and M. E. Flatté, SPIN **07**, 1740012 (2017).
[116] H. Yu, J. Xiao, and H. Schultheiss, Phys. Rep. **905**, 1 (2021).
[117] S. Choudhury, S. Saha, R. Mandal, S. Barman, Y. Otani, and A. Barman, ACS Applied Materials & Interfaces **8**, 18339 (2016).
[118] S. Saha, R. Mandal, S. Barman, D. Kumar, B. Rana, Y. Fukuma, S. Sugimoto, Y. Otani, and A. Barman, Adv. Funct. Mater. **23**, 2378 (2013).
[119] A. A. Clerk, K. W. Lehnert, P. Bertet, J. R. Petta, and Y. Nakamura, Nat. Phys. **16**, 257 (2020).
[120] B. Rana, A. K. Mondal, S. Bandyopadhyay, and A. Barman, Nanotechnology **33**, 082002 (2021).
[121] B. Zare Rameshti *et al.*, Phys. Rep. **979**, 1 (2022).
[122] Y. Li, W. Zhang, V. Tyberkevych, W.-K. Kwok, A. Hoffmann, and V. Novosad, J. Appl. Phys. **128**, 130902 (2020).
[123] Y. Tabuchi, S. Ishino, A. Noguchi, T. Ishikawa, R. Yamazaki, K. Usami, and Y. Nakamura, Science **349**, 405 (2015).
[124] Y. Tabuchi, S. Ishino, T. Ishikawa, R. Yamazaki, K. Usami, and Y. Nakamura, Phys. Rev. Lett. **113**, 083603 (2014).
[125] B. Rana, A. K. Mondal, S. Bandyopadhyay, and A. Barman, Nanotechnology **33**, 062007 (2021).
[126] I. A. Novikov, M. A. Kiryanov, P. K. Nurgalieva, A. Y. Frolov, V. V. Popov, T. V. Dolgova, and A. A. Fedyanin, Nano Lett. **20**, 8615 (2020).
[127] A. Kimel *et al.*, J. Phys. D: Appl. Phys. **55**, 463003 (2022).
[128] B. Bhoi and S.-K. Kim, in *Solid State Physics*, edited by R. L. Stamps (Academic Press, 2020), pp. 39.
[129] V. S. Bhat, F. Heimbach, I. Stasinopoulos, and D. Grundler, Phys. Rev. B **93**, 140401 (2016).
[130] F. H. D. Leeuw, R. V. D. Doel, and U. Enz, Rep. Prog. Phys. **43**, 689 (1980).
[131] T. H. E. Lahtinen, K. J. A. Franke, and S. van Dijken, Sci. Rep. **2**, 258 (2012).
[132] M. Weisheit, S. Fähler, A. Marty, Y. Souche, C. Poinsignon, and D. Givord, Science **315**, 349 (2007).
[133] T. H. E. Lahtinen, J. O. Tuomi, and S. van Dijken, Adv. Mater. **23**, 3187 (2011).
[134] O. Wojewoda *et al.*, Appl. Phys. Lett. **117**, 022405 (2020).
[135] C. Banerjee, P. Gruszecki, J. W. Klos, O. Hellwig, M. Krawczyk, and A. Barman, Phys. Rev. B **96**, 024421 (2017).
[136] F. Ma, Y. Zhou, H. B. Braun, and W. S. Lew, Nano Lett. **15**, 4029 (2015).
[137] N. Amos, R. Fernandez, R. Ikkawi, B. Lee, A. Lavrenov, A. Krichevsky, D. Litvinov, and S. Khizroev, J. Appl. Phys. **103**, 07E732 (2008).
[138] M. Hehn, S. Padovani, K. Ounadjela, and J. P. Bucher, Phys. Rev. B **54**, 3428 (1996).
[139] J. Yoon, S.-y. Park, Y. Jo, M.-H. Jung, C.-Y. You, T. Kim, J. R. Rhee, and Y. K. Kim, Curr. Appl. Phys. **9**, 688 (2009).
[140] M. Coïsson, C. Appino, F. Celegato, A. Magni, P. Tiberto, and F. Vinai, Phys. Rev. B **77**, 214404 (2008).
[141] D. Wu, T. Jin, Y. Lou, and F. Wei, Appl. Surf. Sci. **346**, 567 (2015).
[142] F. Luo, F. Zheng, G. Yin, D. Wu, and F. Wei, Appl. Phys. Express **6**, 073003 (2013).
[143] N. Vukadinovic, H. L. Gall, J. B. Y. V. Gehanno, A. Marty, Y. Samson, and B. Gilles, Eur. Phys. J. B **13**, 445 (2000).
[144] S. Woo *et al.*, Nat. Commun. **8**, 15573 (2017).
[145] S. Barman, S. Saha, S. Mondal, D. Kumar, and A. Barman, Sci. Rep. **6**, 33360 (2016).
[146] K. Y. Guslienko, J Nanosci Nanotechnol **8**, 2745 (2008).
[147] M. Jaafar, R. Yanes, D. Perez de Lara, O. Chubykalo-Fesenko, A. Asenjo, E. M. Gonzalez, J. V. Anguita, M. Vazquez, and J. L. Vicent, Phys. Rev. B **81**, 054439 (2010).
[148] K. S. Buchanan, P. E. Roy, M. Grimsditch, F. Y. Fradin, K. Y. Guslienko, S. D. Bader, and V. Novosad, Nat. Phys. **1**, 172 (2005).
[149] B. Van Waeyenberge *et al.*, Nature **444**, 461 (2006).
[150] L. Giovannini, F. Montoncello, F. Nizzoli, G. Gubbiotti, G. Carlotti, T. Okuno, T. Shinjo, and M. Grimsditch, Phys. Rev. B **70**, 172404 (2004).
[151] J. P. Park and P. A. Crowell, Phys. Rev. Lett. **95**, 167201 (2005).

[152] L. J. Cornelissen, J. Liu, B. J. van Wees, and R. A. Duine, Phys. Rev. Lett. **120**, 097702 (2018).
[153] S. Mayr *et al.*, Nano Lett. **21**, 1584 (2021).
[154] S. H. Skjærvø, C. H. Marrows, R. L. Stamps, and L. J. Heyderman, Nat. Rev. Phys. **2**, 13 (2020).
[155] J. C. Gartside, D. M. Arroo, D. M. Burn, V. L. Bemmer, A. Moskalenko, L. F. Cohen, and W. R. Branford, Nat. Nanotech. **13**, 53 (2018).
[156] M. Tanaka, E. Saitoh, H. Miyajima, T. Yamaoka, and Y. Iye, Phys. Rev. B **73**, 052411 (2006).
[157] C. F. Petersen, A. Farhan, S. Dhuey, Z. Chen, M. J. Alava, A. Scholl, and S. van Dijken, Appl. Phys. Lett. **112**, 092403 (2018).
[158] R. F. Wang *et al.*, Nature **439**, 303 (2006).
[159] G.-W. Chern and P. Mellado, Europhys. Lett. **114**, 37004 (2016).
[160] J. Sklenar, Y. Lao, A. Albrecht, J. D. Watts, C. Nisoli, G.-W. Chern, and P. Schiffer, Nat. Phys. **15**, 191 (2019).
[161] J. Park, B. L. Le, J. Sklenar, G.-W. Chern, J. D. Watts, and P. Schiffer, Phys. Rev. B **96**, 024436 (2017).
[162] L. Pauling, J. Am. Chem. Soc. **57**, 2680 (1935).
[163] M. J. Harris, S. T. Bramwell, D. F. McMorrow, T. Zeiske, and K. W. Godfrey, Phys. Rev. Lett. **79**, 2554 (1997).
[164] M. T. Kaffash, S. Lendinez, and M. B. Jungfleisch, Phys. Lett. A **402**, 127364 (2021).
[165] D. M. Arroo, J. C. Gartside, and W. R. Branford, Phys. Rev. B **100**, 214425 (2019).
[166] A. K. Chaurasiya, A. K. Mondal, J. C. Gartside, K. D. Stenning, A. Vanstone, S. Barman, W. R. Branford, and A. Barman, ACS Nano **15**, 11734 (2021).
[167] E. Iacocca, S. Gliga, R. L. Stamps, and O. Heinonen, Phys. Rev. B **93**, 134420 (2016).
[168] V. S. Bhat, S. Watanabe, K. Baumgaertl, A. Kleibert, M. A. W. Schoen, C. A. F. Vaz, and D. Grundler, Phys. Rev. Lett. **125**, 117208 (2020).
[169] M. Goryca, X. Zhang, J. Li, A. L. Balk, J. D. Watts, C. Leighton, C. Nisoli, P. Schiffer, and S. A. Crooker, Phys. Rev. X **11**, 011042 (2021).
[170] P. d. M. Petrus Peregrinus (of Maricourt), *The Letter of Petrus Peregrinus on the Magnet, A.D. 1269* (McGraw publishing Company, 1904), The Letter of Petrus Peregrinus on the Magnet, A.D. 1269.
[171] W. Gerlach and O. Stern, Z. Physik **9**, 353 (1922).
[172] W. Heisenberg, Z. Physik **38**, 411 (1926).
[173] P. Weiss, J. Phys. Theor. Appl. **6**, 661 (1907).
[174] C. Kittel, *Introduction to Solid State Physics* (Wiley, 2004).
[175] T. Kasuya, Prog. Theor. Phys. **16**, 58 (1956).
[176] M. A. Ruderman and C. Kittel, Phys. Rev. **96**, 99 (1954).
[177] H. A. Kramers, Physica **1**, 182 (1934).
[178] P. W. Anderson, Phys. Rev. **79**, 705 (1950).
[179] A. N. Bogdanov and U. K. Rößler, Phys. Rev. Lett. **87**, 037203 (2001).
[180] A. Bogdanov and D. Yablonskiui, Sov. Phys. JETP **68**, 101 (1989).
[181] S. Rohart and A. Thiaville, Phys. Rev. B **88**, 184422 (2013).
[182] J.-H. Moon, S.-M. Seo, K.-J. Lee, K.-W. Kim, J. Ryu, H.-W. Lee, R. D. McMichael, and M. D. Stiles, Phys. Rev. B **88**, 184404 (2013).
[183] A. H. Morrish, in *The Physical Principles of Magnetism* (R. E. Krieger Publishing Company, 1980).
[184] P. Bruno and J. P. Renard, Appl. Phys. A **49**, 499 (1989).
[185] P. Bruno and J. Seiden, J. Phys. Colloques. **49**, C8 (1988).
[186] W. Palmer, Phys. Rev. **131**, 1057 (1963).
[187] D. X. Chen, J. A. Brug, and R. B. Goldfarb, IEEE Trans. Magn. **27**, 3601 (1991).
[188] N. Nakajima *et al.*, Phys. Rev. Lett. **81**, 5229 (1998).
[189] S. Pal, B. Rana, O. Hellwig, T. Thomson, and A. Barman, Appl. Phys. Lett. **98**, 082501 (2011).
[190] A. D. Kent, Nat. Mater. **9**, 699 (2010).
[191] R. P. Cowburn, A. O. Adeyeye, and M. E. Welland, Phys. Rev. Lett. **81**, 5414 (1998).
[192] M. E. Schabes and H. N. Bertram, J. Appl. Phys. **64**, 1347 (1988).

[193] B. K. Mahato, S. Choudhury, R. Mandal, S. Barman, Y. Otani, and A. Barman, J. Appl. Phys. **117**, 213909 (2015).
[194] S. Jain, Y. Ren, A. O. Adeyeye, and N. Singh, Phys. Rev. B **80**, 132401 (2009).
[195] V. V. Kruglyak, P. S. Keatley, R. J. Hicken, J. R. Childress, and J. A. Katine, Phys. Rev. B **75**, 024407 (2007).
[196] A. B. a. A. Haldar, in *Time-domain study of magnetization dynamics in magnetic thin films and micro- and nanostructures* (Solid State Phys Elsevier Inc., 2014).
[197] S. Pan, O. Hellwig, and A. Barman, Phys. Rev. B **98**, 214436 (2018).
[198] L. Mayer, J. Appl. Phys. **29**, 1003 (1958).
[199] G. P. Zhang and W. Hübner, Phys. Rev. Lett. **85**, 3025 (2000).
[200] F. Dalla Longa, J. T. Kohlhepp, W. J. M. de Jonge, and B. Koopmans, Phys. Rev. B **75**, 224431 (2007).
[201] W. Hübner and G. P. Zhang, Phys. Rev. B **58**, R5920 (1998).
[202] E. Carpene, E. Mancini, C. Dallera, M. Brenna, E. Puppin, and S. De Silvestri, Phys. Rev. B **78**, 174422 (2008).
[203] C. Dornes *et al.*, Nature **565**, 209 (2019).
[204] P. Tengdin *et al.*, Sci. Adv. **6**, eaaz1100.
[205] L. D. Landau and E. Lifshitz, Phys. Z. Sowjetunion **8**, 153 (1935).
[206] T. L. Gilbert, Phys. Rev. **100**, 1243 (1955).
[207] M. C. Hickey and J. S. Moodera, Phys. Rev. Lett. **102**, 137601 (2009).
[208] H. Suhl, IEEE Trans. Magn. **34**, 1834 (1998).
[209] Y. Tserkovnyak, A. Brataas, and G. E. W. Bauer, Phys. Rev. Lett. **88**, 117601 (2002).
[210] V. Kamberský, Czech. J. Phys. **26**, 1366 (1976).
[211] R. J. Elliott, Phys. Rev. **96**, 266 (1954).
[212] Y. Yafet, in *Solid State Physics*, edited by F. a. T. Seitz, D.1963), pp. 1.
[213] C. Kittel and A. H. Mitchell, Phys. Rev. **101**, 1611 (1956).
[214] J. Kuneš and V. Kamberský, Phys. Rev. B **65**, 212411 (2002).
[215] V. Kamberský, Phys. Rev. B **76**, 134416 (2007).
[216] S. Qiao, W. Yan, S. Nie, J. Zhao, and X. Zhang, AIP Adv. **5**, 087170 (2015).
[217] J. Lindner, K. Lenz, E. Kosubek, K. Baberschke, D. Spoddig, R. Meckenstock, J. Pelzl, Z. Frait, and D. L. Mills, Phys. Rev. B **68**, 060102 (2003).
[218] S. N. Panda, S. Majumder, S. Choudhury, A. Bhattacharya, S. Sinha, and A. Barman, Nanoscale **13**, 13709 (2021).
[219] N.-H. Kim, J. Jung, J. Cho, D.-S. Han, Y. Yin, J.-S. Kim, H. J. M. Swagten, and C.-Y. You, Appl. Phys. Lett. **108**, 142406 (2016).
[220] C. H. Du, H. L. Wang, Y. Pu, T. L. Meyer, P. M. Woodward, F. Y. Yang, and P. C. Hammel, Phys. Rev. Lett. **111**, 247202 (2013).
[221] B. Heinrich, R. Urban, and G. Woltersdorf, IEEE Trans. Magn. **38**, 2496 (2002).
[222] L. Berger, Phys. Rev. B **54**, 9353 (1996).
[223] G. D. H. Hurdequint, J. Phys. Paris. Colloq. **49** (1988).
[224] A. B. Yaroslav Tserkovnyak, Gerrit E.W. Bauer, Bertrand I. Halperin, Rev. Mod. Phys., 1375 (2005).
[225] C. Kittel, Phys. Rev. **73**, 155 (1948).
[226] J. R. Eshbach and R. W. Damon, Phys. Rev. **118**, 1208 (1960).
[227] R. W. Damon and J. R. Eshbach, J. Appl. Phys. **31**, S104 (1960).
[228] B. A. Kalinikos and A. N. Slavin, J. Phys. C: Solid State Phys. **19**, 7013 (1986).
[229] R. Arias and D. L. Mills, Phys. Rev. B **60**, 7395 (1999).
[230] C. E. Patton, J. Appl. Phys. **39**, 3060 (1968).
[231] T. J. Silva, C. S. Lee, T. M. Crawford, and C. T. Rogers, J. Appl. Phys. **85**, 7849 (1999).
[232] J. Ding, M. Kostylev, and A. O. Adeyeye, Appl. Phys. Lett. **100**, 062401 (2012).
[233] K. Hoffmann and Z. Skvor, IEEE Trans. Microw. Theory Tech. **46**, 2520 (1998).
[234] R. S. Kwok and L. Ji-Fuh, IEEE Trans. Microw. Theory Tech. **47**, 111 (1999).
[235] R. N. Simons, in *Coplanar Waveguide Circuits, Components, and Systems* (Wiley, 2001), pp. 1.

[236] A. Barman, T. Kimura, Y. Otani, Y. Fukuma, K. Akahane, and S. Meguro, Rev. Sci. Instrum. **79**, 123905 (2008).
[237] M. Faraday, T. Martin, and R. I. o. G. Britain, *Faraday's Diary: Being the Various Philosophical Notes of Experimental Investigation Made by Michael Faraday, During the Years 1820-1862 and Bequeathed by Him to the Royal Institution of Great Britain, Now, by Order of the Managers, Printed and Published for the First Time, Under the Editorial Supervision of Thomas Martin ; with a Foreword by Sir William H. Bragg. Index* (G. Bell and sons, Limited, 1932).
[238] P. Bruno, Y. Suzuki, and C. Chappert, Phys. Rev. B **53**, 9214 (1996).
[239] R. V. T. W. McDaniel, in *Handbook of Magneto-Optical Data Recording: Materials, Subsystems, Techniques* (Elsevier Science, 1995).
[240] B. Ziaie, A. Baldi, and M. Z. Atashbar, in *Springer Handbook of Nanotechnology*, edited by B. Bhushan (Springer Berlin Heidelberg, Berlin, Heidelberg, 2010), pp. 231.
[241] K. E. Drexler, Engines of Creation: The Coming Era of Nanotechnology (Eric Dresler) (2000).
[242] G. Binnig, C. F. Quate, and C. Gerber, Phys. Rev. Lett. **56**, 930 (1986).
[243] D. McMullan, Scanning **17**, 175 (1995).
[244] D. E. N. Joseph I. Goldstein , Patrick Echlin , David C. Joy , Charles E. Lyman , Eric Lifshin , Linda Sawyer , Joseph R. Michael, in *Scanning Electron Microscopy and X-Ray Microanalysis* (Springer US, 2012).
[245] V. S. R. a. J. J. Beaudoin, in *Handbook of Analytical Techniques in Concrete Science and Technology: Principles, Techniques and Applications* (Springer, 2010), p. 231.
[246] H. H. a. H. P. Oepen, in *Magnetic Microscopy of Nanostructures* (Springer, 2005).
[247] S. Foner, Rev. Sci. Instrum. **30**, 548 (1959).
[248] Z. Q. Qiu and S. D. Bader, Rev. Sci. Instrum. **71**, 1243 (2000).
[249] S. Swann, Physics in Technology **19**, 67 (1988).
[250] J. Yang, W. Cui, Y. Li, G. Xie, N. Zhang, R. Wang, T. Hu, and H. Zhang, Appl. Surf. Sci. **382**, 88 (2016).
[251] M. W. Pyun, E. J. Kim, D. H. Yoo, and S. H. Hahn, Appl. Surf. Sci. **257**, 1149 (2010).
[252] C. Bishop, in *Electron Beam Evaporation, Vacuum Deposition onto Webs, Films and Foils* (Elsevier, 2011).
[253] Y. Chen, Microelectron. Eng. **135**, 57 (2015).
[254] M. A. Moram and M. E. Vickers, Rep. Prog. Phys. **72**, 036502 (2009).
[255] C. V. Raman, Nature **121**, 619 (1928).
[256] P. H. Gammon, H. Kiefte, and M. J. Clouter, J. Phys. Chem. **87**, 4025 (1983).
[257] F. Li, Q. Cui, Z. He, T. Cui, J. Zhang, Q. Zhou, G. Zou, and S. Sasaki, J. Chem. Phys. **123**, 174511 (2005).
[258] E. Courtens, J. Pelous, J. Phalippou, R. Vacher, and T. Woignier, Phys. Rev. Lett. **58**, 128 (1987).
[259] S. Reiß, G. Burau, O. Stachs, R. Guthoff, and H. Stolz, Biomed. Opt. Express **2**, 2144 (2011).
[260] J. R. Sandercock, in *Second Int. Conf. on Light Scattering in Solids*, edited by M. Balkanski (Flammarion, Paris, 1971).
[261] R. Mock, B. Hillebrands, and R. Sandercock, J. Phys. E: Sci. Instrum. **20**, 656 (1987).
[262] W. Wettling, R. S. Smith, W. Jantz, and P. M. Ganser, J. Magn. Magn. Mater. **28**, 299 (1982).
[263] W. W. J. R. Sandercock, IEEE Trans. Magn. **14** (1978).
[264] M. Cardona and G. Güntherodt, *Light Scattering in Solids VII: Crystal-field and magnetic excitations* 2000), Vol. 75, p.^pp. 201.
[265] J. R. Sandercock, in *Operator Manual for the Tandem Fabry-Perot Interferometer*1999).
[266] J. R. Sandercook, in *Operator manual of TANDEM FABRY-PEROT INTERFEROMETER TFP-1*2010).
[267] in *Operator's Manual, Libra-Ultrafast Amplifier Laser System* (Coherent, USA).
[268] in *Operator's Manual, SDG Elite-Synchronization and Delay Generator* (Coherent, USA).
[269] in *User's Manual, Model: Harmonic, HGS-T: Frequency Doubler and Pulse Selector* (Spectra-Physics, California, USA, 2002).
[270] V. P. Denysenkov and A. M. Grishin, Rev. Sci. Instrum. **74**, 3400 (2003).
[271] J. V. T. V. d. Broeck, in *1994 IEEE MTT-S International Microwave Symposium Digest*1994), p. 1069.

[272] F. S. A. Ferrero, U. Pisani, IEEE Trans. Microw. Theory Tech. **42**, 2455 (1994).
[273] V. K. T. L. A. Hayden, IEEE Trans. Microw. Theory Tech. **41**, 415 (1993).
[274] R. B. M. J. A. Jargon, D. K. Rytting, IEEE Trans. Microw. Theory Tech. **47**, 2008 (1999).
[275] V. T. A. Ferrero, in *IEEE MTT-S International Microwave Symposium Digest*2006), p. 1456.
[276] M. Donahue and D. G. Porter, **Version 1.0, https://www.nist.gov/publications/oommf-users-guide-version-10** (1999).
[277] A. Vansteenkiste, J. Leliaert, M. Dvornik, M. Helsen, F. Garcia-Sanchez, and B. V. Waeyenberge, AIP Advances **4**, 107133 (2014).
[278] M. R. Scheinfein and A. Price, **http://llgmicro.home.mindspring.com** (2003).
[279] M. Krawczyk and H. Puszkarski, Phys. Rev. B **77**, 054437 (2008).
[280] V. Laude, M. Wilm, S. Benchabane, and A. Khelif, Phys. Rev. E **71**, 036607 (2005).
[281] J. O. Vasseur, P. A. Deymier, B. Djafari-Rouhani, Y. Pennec, and A. C. Hladky-Hennion, Phys. Rev. B **77**, 085415 (2008).
[282] M. Krawczyk, S. Mamica, M. Mruczkiewicz, J. W. Klos, S. Tacchi, M. Madami, G. Gubbiotti, G. Duerr, and D. Grundler, J. Phys. D: Appl. Phys. **46**, 495003 (2013).
[283] M. Krawczyk, M. L. Sokolovskyy, J. W. Klos, and S. Mamica, Adv. Condens. Matter Phys. **2012**, 764783 (2012).
[284] J. Kaczér and L. Murtinová, Phys. Status Solidi A. **23**, 79 (1974).
[285] P. F. Carcia, A. D. Meinhaldt, and A. Suna, Appl. Phys. Lett. **47**, 178 (1985).
[286] A. Manchon, H. C. Koo, J. Nitta, S. M. Frolov, and R. A. Duine, Nat. Mater. **14**, 871 (2015).
[287] A. K. Geim and K. S. Novoselov, Nat. Mater. **6**, 183 (2007).
[288] V. V. Cheianov and V. I. Fal'ko, Phys. Rev. Lett. **97**, 226801 (2006).
[289] A. H. Castro Neto, F. Guinea, N. M. R. Peres, K. S. Novoselov, and A. K. Geim, Rev. Mod. Phys. **81**, 109 (2009).
[290] J. Fischer, B. Trauzettel, and D. Loss, Phys. Rev. B **80**, 155401 (2009).
[291] S. Sinha, S. Pan, S. Choudhury, J. Sinha, and A. Barman, J. Phys. Chem. C **121**, 17442 (2017).
[292] D. Ma, Z. Li, and Z. Yang, Carbon **50**, 297 (2012).
[293] A. H. Castro Neto and F. Guinea, Phys. Rev. Lett. **103**, 026804 (2009).
[294] B. Wang, J. Wang, and J. Zhu, ACS Nano **8**, 1862 (2014).
[295] T. Abtew, B.-C. Shih, S. Banerjee, and P. Zhang, Nanoscale **5**, 1902 (2013).
[296] G. Bertoni, L. Calmels, A. Altibelli, and V. Serin, Phys. Rev. B **71**, 075402 (2005).
[297] Y. Yao, F. Ye, X.-L. Qi, S.-C. Zhang, and Z. Fang, Phys. Rev. B **75**, 041401 (2007).
[298] X. Li, Z. Wu, and J. Liu, Sci. Rep. **7**, 6526 (2017).
[299] W. Han, APL Mater. **4**, 032401 (2016).
[300] A. J. Berger, W. Amamou, S. P. White, R. Adur, Y. Pu, R. K. Kawakami, and P. C. Hammel, J. Appl. Phys. **115**, 17C510 (2014).
[301] C. Du, H. Wang, F. Yang, and P. C. Hammel, Phys. Rev. B **90**, 140407(R) (2014).
[302] B. Do and H. Awano, Journal of Science: Advanced Materials and Devices **1**, 57 (2016).
[303] A. C. Ferrari *et al.*, Phys. Rev. Lett. **97**, 187401 (2006).
[304] L. G. Cançado *et al.*, Nano Lett. **11**, 3190 (2011).
[305] C. T. Chen, E. A. Casu, M. Gajek, and S. Raoux, Appl. Phys. Lett. **103**, 033109 (2013).
[306] A. K. Chaurasiya, S. Choudhury, J. Sinha, and A. Barman, Phys. Rev. Appl. **9**, 014008 (2018).
[307] K.-W. Kim, H.-W. Lee, K.-J. Lee, and M. D. Stiles, Phys. Rev. Lett. **111**, 216601 (2013).
[308] F. Freimuth, S. Blügel, and Y. Mokrousov, Phys. Rev. B **96**, 104418 (2017).
[309] C. H. Back, R. Allenspach, W. Weber, S. S. P. Parkin, D. Weller, E. L. Garwin, and H. C. Siegmann, Science **285**, 864 (1999).
[310] E. B. Myers, D. C. Ralph, J. A. Katine, R. N. Louie, and R. A. Buhrman, Science **285**, 867 (1999).
[311] P. Gambardella and I. M. Miron, Phil. Trans. R. Soc. A. **369**, 3175 (2011).
[312] A. Manchon, J. Železný, I. M. Miron, T. Jungwirth, J. Sinova, A. Thiaville, K. Garello, and P. Gambardella, Rev. Mod. Phys. **91**, 035004 (2019).
[313] M. Kurniawan, A. Perrin, P. Xu, V. Keylin, and M. McHenry, IEEE Magnetics Letters **7**, 1 (2016).

[314] M. M. Decker, M. S. Wörnle, A. Meisinger, M. Vogel, H. S. Körner, G. Y. Shi, C. Song, M. Kronseder, and C. H. Back, Physical Review Letters **118**, 257201 (2017).
[315] M. Fähnle, T. Tsatsoulis, C. Illg, M. Haag, B. Y. Müller, and L. Zhang, J. Supercond. Nov. Magn. **30**, 1381 (2017).
[316] Q. Zhang, A. V. Nurmikko, G. X. Miao, G. Xiao, and A. Gupta, Phys. Rev. B **74**, 064414 (2006).
[317] A. De, S. S. P. K. Arekapudi, L. Koch, F. Samad, S. N. Panda, B. Böhm, O. Hellwig, and A. Barman, ACS Appl. Mater. Interfaces **14**, 13970 (2022).
[318] G. M. Müller *et al.*, Nat. Mater. **8**, 56 (2009).
[319] S. Pan, S. Mondal, T. Seki, K. Takanashi, and A. Barman, Phys. Rev. B **94**, 184417 (2016).
[320] G. Ju, J. Hohlfeld, B. Bergman, R. J. M. van de Veerdonk, O. N. Mryasov, J.-Y. Kim, X. Wu, D. Weller, and B. Koopmans, Phys. Rev. Lett. **93**, 197403 (2004).
[321] S. A. McGill, R. I. Miller, O. N. Torrens, A. Mamchik, I. W. Chen, and J. M. Kikkawa, Phys. Rev. B **71**, 075117 (2005).
[322] S. N. Panda, B. Rana, Y. Otani, and A. Barman, Adv. Quantum Technol. **5**, 2200016 (2022).
[323] P. Agrawal, F. Büttner, I. Lemesh, S. Schlotter, and G. S. D. Beach, Phys. Rev. B **100**, 104430 (2019).
[324] U. Atxitia, O. Chubykalo-Fesenko, J. Walowski, A. Mann, and M. Münzenberg, Phys. Rev. B **81**, 174401 (2010).
[325] J. O. Vasseur, L. Dobrzynski, B. Djafari-Rouhani, and H. Puszkarski, Phys. Rev. B **54**, 1043 (1996).
[326] F. Hellman *et al.*, Rev. Mod. Phys. **89**, 025006 (2017).
[327] Y. Khivintsev, B. Kuanr, T. J. Fal, M. Haftel, R. E. Camley, Z. Celinski, and D. L. Mills, Phys. Rev. B **81**, 054436 (2010).
[328] K. Adhikari, S. Sahoo, A. K. Mondal, Y. Otani, and A. Barman, Phys. Rev. B **101**, 054406 (2020).
[329] X. S. Wang and X. R. Wang, J. Appl. Phys. **129**, 151101 (2021).
[330] X. S. Wang, H. W. Zhang, and X. R. Wang, Phys. Rev. Appl. **9**, 024029 (2018).
[331] G. S. Agarwal, Phys. Rev. Lett. **53**, 1732 (1984).
[332] S. Klingler *et al.*, Phys. Rev. Lett. **120**, 127201 (2018).
[333] C. Dai, K. Xie, Z. Pan, and F. Ma, J. Appl. Phys. **127**, 203902 (2020).
[334] D. MacNeill, J. T. Hou, D. R. Klein, P. Zhang, P. Jarillo-Herrero, and L. Liu, Phys. Rev. Lett. **123**, 047204 (2019).
[335] Y. Shiota, T. Taniguchi, M. Ishibashi, T. Moriyama, and T. Ono, Phys. Rev. Lett. **125**, 017203 (2020).
[336] J. Chen, C. Liu, T. Liu, Y. Xiao, K. Xia, G. E. W. Bauer, M. Wu, and H. Yu, Phys. Rev. Lett. **120**, 217202 (2018).
[337] Y. Li *et al.*, Phys. Rev. Lett. **124**, 117202 (2020).
[338] K. Adhikari, S. Choudhury, S. Barman, Y. Otani, and A. Barman, Nanotechnology **32**, 395706 (2021).
[339] S.-K. Kim, K.-S. Lee, and D.-S. Han, Appl. Phys. Lett. **95**, 082507 (2009).
[340] A. Haldar, D. Kumar, and A. O. Adeyeye, Nat. Nanotech. **11**, 437 (2016).
[341] Y. Au, M. Dvornik, O. Dmytriiev, and V. V. Kruglyak, Appl. Phys. Lett. **100**, 172408 (2012).
[342] J. P. Gianvittorio and Y. Rahmat-Samii, IEEE Antennas Propag. Mag. **44**, 20 (2002).
[343] R. Fabiha, J. Lundquist, S. Majumder, E. Topsakal, A. Barman, and S. Bandyopadhyay, Adv. Sci. **9**, 2104644 (2022).
[344] A. V. Chumak *et al.*, IEEE Trans. Magn. **58**, 0800172 (2022).
[345] P. P. Horley, A. Sukhov, J. Berakdar, and L. G. Trápaga-Martínez, Eur. Phys. J. B **88**, 165 (2015).
[346] V. Novosad, K. Y. Guslienko, H. Shima, Y. Otani, S. G. Kim, K. Fukamichi, N. Kikuchi, O. Kitakami, and Y. Shimada, Phys. Rev. B **65**, 060402 (2002).
[347] G. Gubbiotti, G. Carlotti, T. Okuno, M. Grimsditch, L. Giovannini, F. Montoncello, and F. Nizzoli, Phys. Rev. B **72**, 184419 (2005).
[348] Z. Liu, R. D. Sydora, and M. R. Freeman, Phys. Rev. B **77**, 174410 (2008).
[349] A. Adhikari, C. Banerjee, A. Kumar Mondal, A. Kumar Chaurasiya, S. Choudhury, J. Sinha, S. Barman, and A. Barman, Mater. Sci. Eng. B **272**, 115385 (2021).
[350] F. Montoncello and F. Nizzoli, J. Appl. Phys. **107**, 023906 (2010).

[351] B. K. Mahato, B. Rana, D. Kumar, S. Barman, S. Sugimoto, Y. Otani, and A. Barman, Appl. Phys. Lett. **105**, 012406 (2014).
[352] S. Barman, A. Barman, and Y. Otani, J. Phys. D: Appl. Phys. **43**, 335001 (2010).
[353] S. Barman, A. Barman, and Y. Otani, IEEE Trans. Mag. **46**, 1342 (2010).
[354] H. T. Nembach, J. M. Shaw, T. J. Silva, W. L. Johnson, S. A. Kim, R. D. McMichael, and P. Kabos, Phys. Rev. B **83**, 094427 (2011).
[355] D. Kumar, O. Dmytriiev, S. Ponraj, and A. Barman, J. Phys. D: Appl. Phys. **45**, 015001 (2011).
[356] S. Choudhury, S. Majumder, S. Barman, Y. Otani, and A. Barman, Phys. Rev. Appl. **10**, 064044 (2018).
[357] X. Chen, C. Zheng, S. Zhou, Y. Liu, and Z. Zhang, Magnetochemistry **8**, 7 (2022).
[358] X. Zhang, C.-L. Zou, L. Jiang, and H. X. Tang, Phys. Rev. Lett. **113**, 156401 (2014).
[359] I. Žutić, J. Fabian, and S. Das Sarma, Rev. Mod. Phys. **76**, 323 (2004).
[360] A. V. Chumak, V. I. Vasyuchka, A. A. Serga, and B. Hillebrands, Nat. Phys. **11**, 453 (2015).
[361] Z. K. Wang, V. L. Zhang, H. S. Lim, S. C. Ng, M. H. Kuok, S. Jain, and A. O. Adeyeye, ACS Nano **4**, 643 (2010).
[362] R. Mandal *et al.*, ACS Nano **6**, 3397 (2012).
[363] S. Tacchi, G. Duerr, J. W. Klos, M. Madami, S. Neusser, G. Gubbiotti, G. Carlotti, M. Krawczyk, and D. Grundler, Phys. Rev. Lett. **109**, 137202 (2012).
[364] A. Vogel, M. Martens, M. Weigand, and G. Meier, Appl. Phys. Lett. **99**, 042506 (2011).
[365] D. Bhowmik, L. You, and S. Salahuddin, Nat. Nanotech. **9**, 59 (2014).
[366] D. B. Carlton, N. C. Emley, E. Tuchfeld, and J. Bokor, Nano Lett. **8**, 4173 (2008).
[367] A. Imre, G. Csaba, L. Ji, A. Orlov, G. H. Bernstein, and W. Porod, Science **311**, 205 (2006).
[368] H. Jung, Y.-S. Choi, K.-S. Lee, D.-S. Han, Y.-S. Yu, M.-Y. Im, P. Fischer, and S.-K. Kim, ACS Nano **6**, 3712 (2012).
[369] S. Saha, S. Barman, J. Ding, A. O. Adeyeye, and A. Barman, Appl. Phys. Lett. **103**, 242416 (2013).
[370] M. Giglio, S. Musazzi, and U. Perini, Phys. Rev. Lett. **47**, 243 (1981).
[371] S. H. Strogatz and M. Dichter, *Nonlinear Dynamics and Chaos, 2nd ed. SET with Student Solutions Manual* https://doi.org/10.1201/9780429492563 (Avalon Publishing, 2016).
[372] R. P. Cowburn, D. K. Koltsov, A. O. Adeyeye, M. E. Welland, and D. M. Tricker, Phys. Rev. Lett. **83**, 1042 (1999).
[373] See Supplemental Material at http://link.aps.org/supplemental/10.1103/PhysRevB.101.224426 for additional experimental and simulated MFM images and a simulated movie (M1) for vortex core motion in the sample with magnetic field.
[374] K. Wagner, A. Kákay, K. Schultheiss, A. Henschke, T. Sebastian, and H. Schultheiss, Nat. Nanotech. **11**, 432 (2016).
[375] F. Garcia-Sanchez, P. Borys, R. Soucaille, J.-P. Adam, R. L. Stamps, and J.-V. Kim, Phys. Rev. Lett. **114**, 247206 (2015).
[376] K. Adhikari, S. Barman, R. Mandal, Y. Otani, and A. Barman, Phys. Rev. Appl. **10**, 044010 (2018).
[377] X. Zhou, G.-L. Chua, N. Singh, and A. Adeyeye, Advanced Functional Materials **Adv. Funct. Mater.**, n/a (2016).
[378] V. M. Parakkat, G. M. Macauley, R. L. Stamps, and K. M. Krishnan, Phys. Rev. Lett. **126**, 017203 (2021).
[379] S. Ladak, D. E. Read, G. K. Perkins, L. F. Cohen, and W. R. Branford, Nat. Phys. **6**, 359 (2010).
[380] S. Sahoo, A. May, A. van Den Berg, A. K. Mondal, S. Ladak, and A. Barman, Nano Letters **21**, 4629 (2021).
[381] C. Nisoli, R. Wang, J. Li, W. F. McConville, P. E. Lammert, P. Schiffer, and V. H. Crespi, Phys. Rev. Lett. **98**, 217203 (2007).
[382] V. S. Bhat, F. Heimbach, I. Stasinopoulos, and D. Grundler, Phys. Rev. B **96**, 014426 (2017).
[383] S. Lendinez and M. B. Jungfleisch, J. Phys.: Condens. Matter **32**, 013001 (2020).
[384] Y. Li *et al.*, J. Appl. Phys. **121**, 103903 (2017).
[385] M. Taghipour Kaffash, W. Bang, S. Lendinez, A. Hoffmann, J. B. Ketterson, and M. B. Jungfleisch, Phys. Rev. B **101**, 174424 (2020).

[386] M. B. Jungfleisch, J. Sklenar, J. Ding, J. Park, J. E. Pearson, V. Novosad, P. Schiffer, and A. Hoffmann, Phys. Rev. Appl. **8**, 064026 (2017).
[387] S. Gliga, A. Kákay, R. Hertel, and O. G. Heinonen, Physical Review Letters **110**, 117205 (2013).
[388] R. Negrello, F. Montoncello, M. T. Kaffash, M. B. Jungfleisch, and G. Gubbiotti, APL Materials **10**, 091115 (2022).
[389] Y. Li *et al.*, J. Phys. D: Appl. Phys. **50**, 015003 (2017).
[390] J. C. Gartside, K. D. Stenning, A. Vanstone, H. H. Holder, D. M. Arroo, T. Dion, F. Caravelli, H. Kurebayashi, and W. R. Branford, Nat. Nanotechnol. **17**, 460 (2022).
[391] T. Dion, J. C. Gartside, A. Vanstone, K. D. Stenning, D. M. Arroo, H. Kurebayashi, and W. R. Branford, Phys. Rev. Research **4**, 013107 (2022).
[392] J. C. Gartside, A. Vanstone, T. Dion, K. D. Stenning, D. M. Arroo, H. Kurebayashi, and W. R. Branford, Nat. Commun. **12**, 2488 (2021).
[393] Á. Papp, W. Porod, and G. Csaba, Nat. Commun. **12**, 6422 (2021).
[394] J. Grollier, D. Querlioz, K. Y. Camsari, K. Everschor-Sitte, S. Fukami, and M. D. Stiles, Nat. Electron. **3**, 360 (2020).
[395] Y.-L. Wang, Z.-L. Xiao, A. Snezhko, J. Xu, L. E. Ocola, R. Divan, J. E. Pearson, G. W. Crabtree, and W.-K. Kwok, Science **352**, 962 (2016).
[396] S. Lendinez, M. Taghipour Kaffash, and M. B. Jungfleisch, Appl. Phys. Lett. **118**, 162407 (2021).
[397] A. V. Chumak, A. A. Serga, and B. Hillebrands, J. Phys. D: Appl. Phys. **50**, 244001 (2017).